

https://dspace.org/

Characterising the Molecular and Functional Phenotypes of RAW264.7 Macrophages under Cannabidiol (CBD) and Tamoxifen Treatment

Mackade, Thabang

2025

University of the Witwatersrand, Johannesburg

https://hdl.handle.net/10539/49880

Mackade, Thabang. (2025). Characterising the Molecular and Functional Phenotypes of RAW264.7 Macrophages under Cannabidiol (CBD) and Tamoxifen Treatment [Master's dissertation, University of the Witwatersrand, Johannesburg]. WIReDSpace. https://hdl.handle.net/10539/49880

Downloaded from a DSpace repository. https://dspace.org/

Characterising the Molecular and Functional Phenotypes of RAW264.7 Macrophages under Cannabidiol (CBD) and Tamoxifen Treatment



WITS
UNIVERSITY

Thabang Mackade
1692568

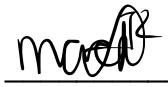
A dissertation submitted in fulfilment of the requirements for the Degree of Master of Science in Medicine (MSc.Med).

DEPARTMENT OF ANATOMICAL SCIENCES, FACULTY OF HEALTH SCIENCES,
UNIVERSITY OF THE WITWATERSRAND, JOHANNESBURG

8 July 2025

Declaration

I, Thabang Mackade, declare that this dissertation entitled “Characterising the Molecular and Functional Phenotypes of RAW264.7 Macrophages under Cannabidiol (CBD) and Tamoxifen Treatment” is my own, unaided work. It is being submitted for the Degree of Master of Science in Medicine at the University of the Witwatersrand, Johannesburg. It has not been submitted before for any degree or examination at any other University.



Thabang Mackade

8th day of July 2025 in Johannesburg

Dedication

I dedicate this work to the Almighty God, whose grace and guidance have illuminated my path. I am eternally grateful to my Ancestors, whose sacrifices and prayers have paved the way for my success. Finally, I express my deepest gratitude to my mom (Phumzile Zwane), dad (Kingsley Mackade), brother (Thato Mackade) and my entire family whose unwavering love and support have been my constant source of strength. We did it! Sekunjalo! Thokozani eMakhosini!!

Presentations Arising from this Dissertation

Oral Presentations

Thabang Mackade, Tanya Augustine, Sindisiwe Buthelezi and Kutlwano Xulu. "Developing a 3-Dimensonal *in vitro* System for Investigating Macrophage-Mediated Tumour Interactions." 49th Surgical Research Society of Southern Africa Meeting (Hybrid), GE Conference Centre, Melrose Estate, Johannesburg, 8th July 2022.

Thabang Mackade, Tanya Augustine, Sindisiwe Buthelezi and Kutlwano Xulu. "Developing a 3-Dimensonal *in vitro* System for Investigating Macrophage-mediated Tumour Interactions." Faculty of Health Sciences Research Day and Postgraduate Expo 2022, University of the Witwatersrand, Johannesburg, 15th September 2022.

Augustine TN, Mackade T, Altriche N, Xulu KR, Buthelezi S. "Polarisation of Macrophages toward an Anti-Tumour Phenotype: A Role for Cannabidiol in Enhancing Tamoxifen Efficacy *in vitro.*" 51st Meeting of the Surgical Research Society of Southern Africa, Bloemfontein, University of the Free State. 21st June 2024. (presented by supervisor since Mackade could not attend).

Abstract

Breast cancer remains a major global health concern. While standard treatments like Tamoxifen have been effective, limitations such as side effects and drug resistance necessitate the exploration of novel therapeutic approaches. Cannabidiol, a non-psychoactive cannabinoid, has emerged as a promising agent with potential anti-cancer properties. Macrophages, key players in the tumour microenvironment, can be polarised into M1 and M2 phenotypes. M1 macrophages exhibit potent anti-tumour activity, while M2 macrophages promote tumour growth and metastasis. Understanding how to modulate macrophage polarisation could offer new therapeutic avenues. This study aimed to investigate the synergistic effects of CBD and Tamoxifen on breast cancer cell growth and macrophage activation. By utilising MCF7 breast cancer cells and RAW264.7 macrophages, the study sought to elucidate the underlying molecular mechanisms that contribute to these compounds' anticancer and immunomodulatory effects.

The present study employed a combination of functional assays and proteomic analysis to explore the mechanisms underlying both macrophage polarisation and the effects of CBD and Tamoxifen on MCF7 and RAW264.7 cells. The results demonstrate that CBD and Tamoxifen, particularly in combination, can induce M1 macrophage polarisation. This is characterised by increased nitric oxide production and upregulation of protein pathways associated with inflammation, including those involved in cytokine production and cellular metabolic processes, which collectively support the anti-tumour functions of M1 macrophages. Additionally, these treatments enhanced RAW264.7 macrophage phagocytosis of MCF7 breast cancer cells. The findings of this study suggest that CBD and Tamoxifen may synergistically modulate the tumour microenvironment. By promoting M1 macrophage polarisation and inhibiting tumour cell growth, this combination therapy holds promise as a novel approach for breast cancer treatment. Further research is warranted to fully elucidate the underlying molecular mechanisms and to explore the clinical potential of CBD and Tamoxifen in breast cancer therapy.

Acknowledgments

Funding and Laboratory Resources

I would like to express my utmost gratitude to the National Research Foundation (NRF) (Prof Augustine, Grant number 121263), the Friedel Sellschop Award, Wits (Prof Augustine), and the Postgraduate Merit Award Scholarship (Wits) for their generous financial support, which made this research possible. I am also grateful to the Council for Scientific and Industrial Research (CSIR) for providing funding (Dr S Buthelezi) and access to their facilities. Finally, I would like to thank the Department of Anatomical Sciences (Wits) and its staff for the use of their laboratories and for their invaluable assistance.

Supervisors

I would like to express my sincere gratitude to my supervisors, Prof. Tanya Augustine, Dr Sindisiwe Buthelezi and Dr Kutlwano Xulu. Your meticulous guidance and unwavering support have been instrumental in shaping this research. I am deeply grateful for the invaluable skills and knowledge you have imparted, pushing me beyond my limits and fostering my academic growth. Your patience and encouragement have been truly inspiring.

My Colleagues

- Nastassia Altriche (Stassi), my exceptional lab partner! Your unwavering support, positive spirit and invaluable insights have made this journey truly memorable. I am grateful for the countless hours we spent together, both in and out of the lab (especially at McDonald's and the fields on education campus!!).
- Sinegugu Dubazana, I am deeply indebted to you. Thank you for your patient guidance and expertise in proteomics. Your invaluable knowledge and support have been instrumental in the success of this research.

- Lehlogonolo Marakalla, Simone Gallant and Derushka Arnachellen, thank you for your constant support and encouragement. Your friendship and camaraderie have made this experience truly enjoyable.

Table of Contents

Declaration ..... *i*
Dedication ..... *ii*
Presentations Arising from this Dissertation ..... *iii*
Abstract ..... *iv*
Acknowledgments ..... *v*
List of Abbreviations ..... *vi*
List of Figures ..... *xi*
List of Tables ..... *xiii*
Chapter 1 ..... *1*
Introduction and Literature Review *1*
1.1.1. Epidemiology of Breast Cancer 1
1.1.2. Classification of Breast Cancer 2
1.1.3. Breast Cancer Therapy 4
1.1.4. The Breast Tumour Microenvironment 6
1.1.5. Effects of Tamoxifen on Immune Activity in the TME 10
1.1.6. Cannabidiol as a Promising Adjuvant Therapy for ER+ Breast Tumours 12
1.1.7. Macrophage Phenotyping by Proteomics 16
1.2. Rationale for the Study 22
1.3. Aims and Objectives 23
Chapter 2 ..... *25*
Materials and Methods *25*
2.1. Cell Culture 25
2.2. Assessing the Impact of Duration on the Polarisation of M0 RAW264.7 Macrophages into the M1 and M2 Phenotypes 26
2.2.1. Data Analysis 27
2.3. Optimisation of CBD Treatment Concentration, Duration of Treatment and Treatment Model 28
2.3.1. Plating Cells for Experimentation 28
2.3.2. Drug Preparations and Treatment 28
2.3.3. Neutral red Assay 30
2.3.4. MTT Assay 31
2.3.5. Data Analysis 31
2.4. Evaluation of the impact of the Optimised Treatment Regimen on RAW264.7 Macrophages 32

2.4.1. Data Analysis 34
2.5. Proteomic Analysis of RAW264.7 Macrophages 34
2.5.1. Sample Preparation for Mass Spectrometry: 34
2.5.2. Liquid Chromatography-Mass Spectrometry (LC-MS) Data Acquisition 36
2.5.3. SWATH-MS Data Processing and Statistical Analysis 36
2.5.4. Functional Analysis: 37
2.6. Assessing the interactions between RAW264.7 macrophages and MCF7 breast cancer cells using fluorescence microscopy and the Griess Reagent 37
2.6.1. Data Analysis 38
Chapter 3 ..... *39*
Results *39*
3.1. Influence of Polarisation Duration on RAW264.7 Macrophage Phenotype 39
3.1.1. Evaluation of Nitrite Production 39
3.1.2. Temporal Proteomic Profiling of Macrophage Polarisation 42
3.1.3. Determination of Optimal Conditions for Subsequent Experimentation 44
3.2. The Cytotoxic Effects of CBD and Tamoxifen against MCF7 Cells 55
3.2.1. Effects of CBD and Tamoxifen on Cell Viability 55
3.2.2. Effects of CBD and Tamoxifen on Growth Inhibition 61
3.2.3. Determination of Optimal Conditions for Subsequent Experimentation 64
3.3. Assessment of the Cytotoxic Potential of Optimised CBD and Tamoxifen Treatment on RAW264.7 Macrophages 65
3.3.1. Impact on Cell Viability and Growth 65
3.3.2. Impact on Protein Expression 67
3.4. Impact of Tamoxifen and CBD on Macrophage Phagocytosis of Breast Cancer Cells 80
Chapter 4 ..... *83*
Discussion and Conclusion *83*
4.1. Macrophage Polarisation and Phenotypic Characterisation 83
4.1.1. The Role of Morphology in Defining Macrophage Phenotypes 84
4.1.2. Nitric Oxide Production as a Marker of Macrophage Polarisation 85
4.1.3. Molecular Mechanisms of Macrophage Polarisation 87
4.2. The Cytotoxic Effects of CBD and Tamoxifen against MCF7 Breast Cancer Cells 103
4.3. Impact of CBD-Tamoxifen Synergy on Macrophage Behaviour 109
4.4. A Novel Role for CBD and Tamoxifen: Enhancing Macrophage Phagocytosis 119
4.5. Conclusions 125
4.6. Limitations of the Current Study 126
References *127*
Appendices *163*

List of Abbreviations

Abbreviation	
ADDG	Gamma-adducin
AMP	Adenosine monophosphate
AMPD3	AMP deaminase 3
ANOVA	Analysis of Variance
ANXA3	Annexin A3
APOBR	Apolipoprotein B receptor
APOL2	Apolipoprotein 2
APOL3	Apolipoprotein 3
Arg-1	Arginase 1
Arg-2	Arginase 2
ATGL	Adipose triglyceride lipase
ATP	Adenosine triphosphate
B2CL1	Bcl-2-like protein 1
BCA	Bicinchoninic acid
BMDMs	Bone-marrow derived macrophages
C1QBP	Complement component 1 Q subcomponent-binding protein
CALM1	Calmodulin-1
CALM2	Calmodulin-2
CALM3	Calmodulin-3
CATD	Cathepsin D
CATL1	Cathepsin L1
CBD	Cannabidiol
CBG	Cannabigerol
CBN	Cannabinol
CBR	Cannabinoid receptors
CCL2	C-C motif chemokine ligand 2
CCL3	C-C motif chemokine ligand 3
CEBPβ	CCAAT/enhancer-binding protein beta
CO_2	Carbon dioxide
COX-2	Cyclooxygenase-2
CSIR	Council for Scientific and Industrial Research
CTLs	Cytotoxic T lymphocytes
CY24A	Cytochrome b-245 alpha chain
DAPI	4',6-diamidino-2-phenylindole
DCIS	Ductal carcinoma *in situ*
DEGS1	Sphingolipid delta (4)-desaturase
DIA	Data-Independent Acquisition
DMEM	Dulbecco's Modified Eagles Medium

DMSO	Dimethyl sulfoxide
DTT	Dithiothreitol
ECM	Extracellular matrix
EDTA	Ethylenediaminetetraacetic
EGF	Epidermal growth factor
EGFR	Epidermal growth factor receptor
ENOG	Enolase 2
ER	Oestrogen receptor
ERO1A	Endoplasmic reticulum oxidoreductin-1-like protein alpha
FABP5	Fatty acid-binding protein 5
FBS	Foetal Bovine Serum
FCGR1	High affinity immunoglobulin gamma Fc receptor I
FCGR2	Low affinity immunoglobulin gamma Fc region receptor II
FCGR3	Low affinity immunoglobulin gamma Fc region receptor III
FDR	False discovery rate
FPPS	Farnesyl pyrophosphate synthase
FYB1	FYN-binding protein 1
GBA1	Lysosomal acid glucosylceramidase
GBG2	Guanine nucleotide-binding protein
GBP3	Guanylate-binding protein 3
GM-CSF	Granulocyte macrophage-colony stimulating factor
GR	Glucocorticoid receptor
GRN	Progranulin
GSTP1	Glutathione S-transferase P 1
HER2	Human epidermal growth factor receptor 2
HILIC	Hydrophilic interaction liquid chromatography
HK2	Hexokinase 2
HK3	Hexokinase 3
HMCS1	Hydroxymethylglutaryl-CoA synthase
hMDMS	Human monocyte-derived macrophages
HMGA1	High mobility group protein A1
HMGA2	High mobility group protein A2
HMOX-1	Heme oxygenase-1
Hrs	Hours
HS74L	Heat shock 70 kDa protein 4L
HSP	Heat shock proteins
IAA	Iodoacetamide
IAH1	Isoamyl acetate-hydrolyzing esterase 1
IC	Invasive carcinoma
IC_{50}	Half-maximal (50%) inhibitory concentration
IDC	Invasive ductal carcinoma

IDO1	Tryptophan catabolising enzyme
IFI	Interferon-activable proteins
IFIT	Interferon-inducible proteins
IFITM	Interferon-induced transmembrane
IFN-γ	Interferon-gamma
IL-10	Interleukin-10
IL-12	Interleukin-12
IL-13	Interleukin-13
IL-1α	Interleukin-1 alpha
IL-1β	Interleukin -1β
IL-2	Interleukin-2
IL-4	Interleukin-4
IL-6	Interleukin-6
IL-8	Interleukin-8
ILC	Invasive lobular carcinoma
IMP	Inosine monophosphate
iNOS	Inducible nitric oxide synthase
iPSC	Induced pluripotent stem cells
IRF-1	Interferon regulatory factor 1
IRG1	Aconitate decarboxylase 1
IS	In situ
ISGs	Interferon stimulated genes
ITAL	Integrin alpha-L
ITAM	Integrin alpha-M
ITB2	Integrin beta-2
ITGA5	Integrin alpha-5
JAK-STAT	Janus kinase-signal transducer and activator of transcription
JNK	c-Jun N-terminal kinase
JUPI2	Jupiter microtubule associated homolog 2
KCC1D	Calcium/calmodulin-dependent protein kinase
KIME	Mevalonate kinase
LC-MS/MS	Liquid chromatography coupled with tandem mass spectrometry
LCIS	Lobular carcinoma *in situ*
LDH	Lactate dehydrogenase
LPS	Lipopolysaccharides
M-CSF	Monocyte colony stimulating factor
MAPK	Mitogen-activated protein kinase
MeCN	Acetonitrile
MEF2C	Myocyte-specific enhancer factor 2C
MHC	Major histocompatibility complex
ml	Millilitre

MRC1	Mannose receptor C-type-1
MS	Mass spectrometry
MS1	First mass analyser
MS2	Second mass analyser
MSR1	Macrophage scavenger receptor types I
MT1	Metallothionein-1
MT2	Metallothionein-2
MTT	Thiazolyl Blue Tetrazolium Bromide
MVD1	Diphosphomevalonate decarboxylase
NADPH	Nicotinamide adenine dinucleotide phosphate
NCF4	Neutrophil cytosol factor 4
NED	N-(1-naphthyl) ethylenediamine
NK	Natural killer
nm	Nanometer
NO	Nitric oxide (NO)
NOX	NADPH oxidase
NRF2	Nuclear factor erythroid 2-related factor 2
OASL1	5'-oligoadenylate synthase (OAS)-like protein 1
OXPHOS	Oxidative phosphorylation
P/S	Penicillin/Streptomycin
P2RX4	P2X purinoceptor 4
PA1B3	Platelet-activating factor acetylhydrolase IB subunit alpha1
PAFA2	Platelet-activating factor acetylhydrolase 2
PAI2	Plasminogen activator inhibitor 1
PBS	Phosphate Buffered Saline
PCA	Principle component analysis
PGH2	Prostaglandin G/H synthase 2
PI3K/Akt/mTOR	Phosphoinositide 3 kinase/Akt/mammalian target of rapamycin
PKC	Protein kinase C
PMVK	Phosphomevalonate kinase
PPARγ	Peroxisome proliferator-activated receptor gamma
PR	Progesterone receptor
PRDX1	Peroxiredoxin-1
PRDX2	Peroxiredoxin-2
PTMs	Post-translational modifications
RETR1	Reticulophagy regulator 1
RIPK3	Receptor-interacting serine/threonine-protein kinase
RN185	RING finger protein 185
RNS	Reactive nitrogen species
ROS	Reactive oxygen species
RPM	Rotations per minute

S100a13	Protein S10AD
SDS	Sodium dodecyl sulphate
SERM	Selective oestrogen receptor modulator
SFM	Serum-free media
SODM	Superoxide dismutase 2
STAT1	Signal transducer and activator of transcription 1
SWATH-MS	Sequential Window Acquisition of all Theoretical Mass Spectra
TAMs	Tumour-associated macrophages
TAP2	Antigen peptide transporter 2
TDLU	Terminal ductal lobulo-alveolar/lobular unit
TGF-β	Transforming growth factor-beta
TGM2	Protein-glutamine gamma-glutamyltransferase 2
Th1	Type 1 T helper cell
Th2	Type 2 T helper cell
THC	Tetrahydrocannabinol
TLR	Toll-like receptor
TME	Tumour microenvironment
TNBC	Triple-negative breast cancers
TNF-α	Tumour necrotic factor-alpha
TPSN	Tapasin
Tregs	Regulatory T cells
TRPV	Transient receptor potential vanilloid
VEGF	Vascular endothelial growth factor
WHO	World Health Organisation
ZYX	Zyxin
µl	Microliter
µM	Micromolar

List of Figures

		Page number:
Figure 1.1	The breast structure	3
Figure 1.2	Macrophage polarisation into M1 and M2 phenotypes	8
Figure 1.3	Schematic of a general proteomic workflow	19
Figure 1.4	Common markers associated with M1 and M2 macrophage phenotypes	21
Figure 1.5	Flow diagram showing an overview of methodology	24
Figure 3.1.1	Impact of duration on the polarisation of M0 RAW264.7 macrophages to the M1 and M2 phenotypes	41
Figure 3.1.2	Overview of identifications from the proteome of M0, M1and M2 RAW264.7 macrophage phenotypes	46
Figure 3.1.3A	PCA plot demonstrating the variation in protein expression among RAW264.7 macrophage phenotypes	47
Figure 3.1.3B	PCA plot demonstrating the variation in protein expression among RAW264.7 macrophage phenotypes	48
Figure 3.1.3C	PCA plot demonstrating the variation in protein expression among RAW264.7 macrophage phenotypes	49
Figure 3.1.4A	Volcano plot demonstrating the differential protein expression among RAW264.7 macrophage phenotypes	50
Figure 3.1.4B	Volcano plot demonstrating the differential protein expression among RAW264.7 macrophage phenotypes	51
Figure 3.1.5A	String-enrichment analysis	53
Figure 3.1.5B	String-enrichment analysis	54
Figure 3.2.1	Representative images showing Neutral Red Uptake by MCF7 cells in control groups and 2 μM Tamoxifen	57
Figure 3.2.2	Representative images showing Neutral Red Uptake by MCF7 cells treated with increasing concentrations of CBD	58

Figure 3.2.3	Representative images showing Neutral Red Uptake by MCF7 cells treated with CBD and Tamoxifen	59
Figure 3.2.4	Graphical representations of changes in cell viability of MCF7 cells treated with CBD and Tamoxifen across time	60
Figure 3.2.5	Graphical representations of changes in growth inhibition of MCF7 cells treated with CBD and Tamoxifen across time	63
Figure 3.3.1	Cytotoxic effects of Tamoxifen and CBD treatment on RAW 264.7 macrophages assessed using the Neutral Red and MTT assays	66
Figure 3.3.2	Morphological assessments of RAW264.7 macrophages treated with CBD and/or Tamoxifen	70
Figure 3.3.3	Overview of identifications from the proteome of RAW264.7 macrophages treated with CBD and/or Tamoxifen	71
Figure 3.3.4	PCA plot demonstrating the variation in protein expression among RAW264.7 macrophages treated with CBD and/or Tamoxifen	72
Figure 3.3.5A	Differential expression of proteins in RAW264.7 cells treated with 2 μM Tamoxifen	73
Figure 3.3.5B	Differential expression of proteins in RAW264.7 cells treated with 5 μM CBD	74
Figure 3.3.5C	Differential expression of proteins in RAW264.7 cells treated with CBD and Tamoxifen	75
Figure 3.3.6A	String-enrichment analysis	77
Figure 3.3.6B	String-enrichment analysis	78
Figure 3.3.6C	String-enrichment analysis	79
Figure 3.4	Phagocytic assay using CellTracker green dye and the Griess reagent	82
Figure 4.1	Proposed mechanism for LPS and IFN-γ signalling in activated M1 macrophages	90

Figure 4.2	Overview of the activation and crosstalk of Cannabinoid signalling pathways.	107
Figure 4.3	Anti-tumour effects of M1 macrophages	123

List of Tables

		Page number:
Table 2.1	Treatments administered to MCF7 cells during optimisation	29
Table 2.2	Treatments administered to RAW264.7 cells during Neutral Red and MTT experimentation	33
Table 3.1	The enriched pathways and proteins M1 polarised RAW264.7 macrophages (relative to M0 phenotype)	52
Table 3.2	The enriched pathways and proteins M2 polarised RAW264.7 macrophages (relative to M0 phenotype)	52
Table 3.3	The enriched pathways and proteins in Tamoxifen-treated RAW264.7 macrophages (relative to untreated cells)	76
Table 3.4	The enriched pathways and proteins in CBD-treated RAW264.7 macrophages (relative to untreated cells)	76
Table 3.5	The enriched pathways and proteins in Tamoxifen-CBD treated RAW264.7 macrophages (relative to untreated cells)	76

Chapter 1

Introduction and Literature Review

1.1.1. Epidemiology of Breast Cancer

Despite the significant advancements in breast cancer research and treatment in recent decades, this disease remains a global health concern. Breast cancer is a leading cause of cancer-related deaths in women worldwide ranking second in Africa and Southeast Asia and fifth in the Western Pacific region (Azamjah, Soltan-Zadeh and Zayeri, 2019; Arzanova and Mayrovitz, 2022). In 2019, the World Health Organisation (WHO) ranked cancer as one of the two major causes of death in 112 out of 183 countries (Azamjah, Soltan-Zadeh and Zayeri, 2019; Sung *et al*., 2021; Arzanova and Mayrovitz, 2022). Estimates from the WHO's International Agency for Research on Cancer revealed that in 2018, South Africa had 107 467 cancer cases and 57 373 deaths of which, 14 097 were breast cancer cases (Dlamini *et al.,* 2023). As of 2020, breast cancer has been reported as the most diagnosed cancer worldwide, surpassing prostate and lung cancers (Sung *et al*., 2021; Arzanova and Mayrovitz, 2022). In addition, 2.3 million women were diagnosed with breast cancer, and 685 000 deaths occurred worldwide, in the year 2020 (Agyemang and Achiaa, 2020; Sung *et al*., 2021; Arzanova and Mayrovitz, 2022).

Due to the variation in risk factors, screening approaches and access to newer treatments, the trends of breast cancer vary across countries (Lu and Ma, 2020; Dlamini *et al.,* 2023; Bray *et al*., 2024). Globally, breast cancer cases continue to steadily increase (Lu and Ma, 2020; Dlamini *et al.,* 2023; Bray *et al*., 2024). This increase may be ascribed partly to the improved detection methods, particularly in less developed countries it may also be related to female fertility shifts and lifestyle changes (Lu and Ma, 2020; Arzanova and Mayrovitz, 2022; Dlamini *et al.,* 2023; Bray *et al*., 2024). Developed countries are faced with the highest incidences of breast cancer but mortality rates vary significantly depending on the geographical region

(Agyemang and Achiaa, 2020; Arzanova and Mayrovitz, 2022; Dlamini *et al.,* 2023). The highest mortality rates are commonly reported in socio-economically disadvantaged regions, and this mostly reflects limited access to early detection and timely treatment options (Agyemang and Achiaa, 2020; Arzanova and Mayrovitz, 2022; Dlamini *et al.,* 2023; Bray *et al.*, 2024). However, even within developed countries, evident disparities in the mortality rate are observed among black and white women which highlights existing health inequalities (Agyemang and Achiaa, 2020; Arzanova and Mayrovitz, 2022; Dlamini *et al.,* 2023; Bray *et al.*, 2024).

1.1.2. Classification of Breast Cancer

Anatomically, breasts are classified as modified tubulo-alveolar apocrine sweat glands consisting of skin, subcutaneous tissue and stroma (Tharmapalan *et al.,* 2019; Neagu *et al.,* 2021). The structural organisation of the mammary gland is composed of a network of branching ducts and terminal secretory lobules (**Figure 1.1**). There are 15 to 20 lobes emerging from the breast nipple and each lobe comprises of approximately 20 to 30 clusters of alveoli containing mammary secretory cells of epithelial origin (Tharmapalan *et al.,* 2019; Neagu *et al.,* 2021)**.** All the alveoli that lead into the same terminal duct form the terminal ductal lobulo-alveolar/lobular unit (TDLU), this is where the majority of breast tumours arise (Tharmapalan *et al.,* 2019; Neagu *et al.,* 2021; **Figure 1.1**).

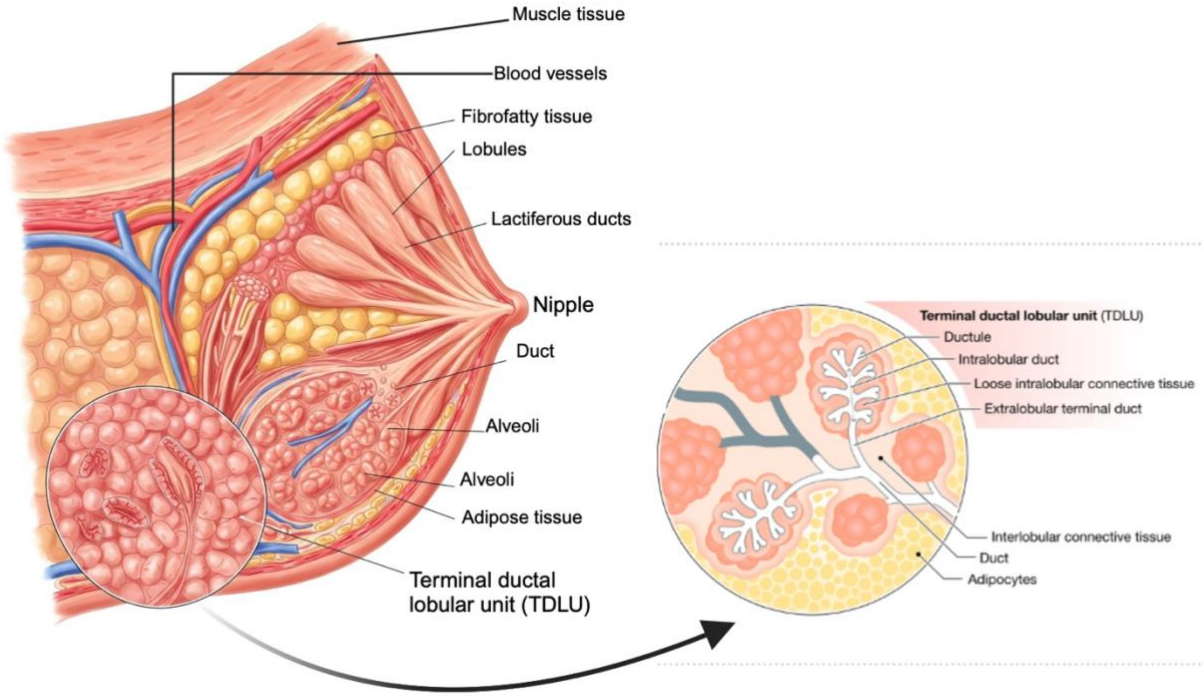


Figure 1.1: The breast structure. A schematic of the human breast showing terminal ductal lobular units (TDLUs), the functional units of breast. Most cancers emanate within the epithelial cells lining the TDLUs. Adapted from Tharmapalan *et al*., 2019. Created with BioRender.com.

From a histological standpoint, breast ducts and TDLUs consist of two layers with specific breast cell populations that present with particular patterns in their normal protein expression (Tharmapalan *et al.,* 2019; Neagu *et al.,* 2021). The innermost layer includes a luminal layer lined by epithelial cells which assist in securing milk secretion during lactation, with cuboidal cells that express cytokeratin 8, cytokeratin 18, oestrogen receptor (ER), progesterone receptor (PR) and the human epidermal growth factor receptor 2 (HER2) (Tharmapalan *et al.,* 2019; Neagu *et al.,* 2021). The outermost layer is a contractile myoepithelial layer, resting on a basement membrane that distinguishes the breast epithelium from the surrounding stroma (Tharmapalan *et al.,* 2019; Neagu *et al.,* 2021). Proteins expressed by cells within this layer include p63, located in the nuclei, cytoplasmic proteins such as cytokeratin 5 and 14, and the smooth muscle actin that provides contractile forces for the ejection of milk (Tharmapalan *et al.,* 2019; Neagu *et al.,* 2021).

Breast cancer is a multifactorial disease and researchers across the globe are actively engaged in developing accurate and effective methods for classifying the disease (Onitilo *et al*., 2009; Toss *et al*., 2017). Building on existing research, several studies have presented an integrated approach for identifying breast cancer subtypes (Onitilo *et al*., 2009; Toss *et al*., 2017). The main categories of breast tumours are characterised as *in situ*/non-invasive (IS) and invasive carcinoma (IC). Both types consist of a ductal or lobular origin and can be further classified as ductal carcinoma *in situ* (DCIS), lobular carcinoma *in situ* (LCIS), invasive lobular carcinoma (ILC) and invasive ductal carcinoma (IDC) (Toss *et al*., 2017; Neagu *et al.,* 2021). Based on protein profiles, breast tumours have been additionally classified according to specific molecular subtypes: luminal A and luminal B tumours, identified by the expression of luminal/epithelial biomarkers and characterised by positive expression of oestrogen receptors (ER+) and/or progesterone receptors (PR+), the HER2-enriched tumours, with HER2/neu tyrosine kinase receptor overexpression and triple-negative breast cancers (TNBC), that do not express ER, PR and HER2 (Onitilo *et al*., 2009; Toss *et al*., 2017; Neagu *et al.,* 2021).

1.1.3. Breast Cancer Therapy

Notably, different subtypes of breast cancer exhibit varying risks for progression, treatment response and overall survival (Agyemang and Achiaa, 2020; Arzanova and Mayrovitz, 2022). Luminal A and B tumours are hormone-dependent, primarily growing in response to oestrogen and/or progesterone signalling (Onitilo *et al*., 2009; Toss *et al*., 2017; Neagu *et al.,* 2021). These tumours display low recurrence risks. However, they still present risks for treatment resistance and secondary complications arising from therapy (Onitilo *et al*., 2009; Toss *et al*., 2017; Neagu *et al.,* 2021). Clinically, patients presenting with luminal A or B breast cancer are often subjected to hormone therapy (Onitilo *et al*., 2009; Toss *et al*., 2017; Neagu *et al.,* 2021). For decades, Tamoxifen has been the cornerstone of treatment for hormone-receptor positive breast tumours (Onitilo *et al*., 2009; Toss *et al*., 2017; Neagu *et al.,* 2021; Howell and Howell, 2023). Tamoxifen is classified as a selective oestrogen receptor

modulator (SERM), which acts as an oestrogen-receptor antagonist by binding to ERs with high affinity, thus preventing oestrogen binding. This further inhibits oestrogen function and prevents oestrogen-dependent cell growth in breast tissue (Onitilo *et al*., 2009; Toss *et al*., 2017; Neagu *et al.,* 2021; Howell and Howell, 2023). Tamoxifen has demonstrated significant clinical efficacy in reducing the risk of breast cancer recurrence and mortality by approximately 50% and 31%, respectively, in patients with ER+ breast cancer (Onitilo *et al*., 2009; Toss *et al*., 2017; Howell and Howell, 2023).

Breast cancers positive for HER2 are characterised as fast-growing and aggressive compared to luminal A and B tumours (Agyemang and Achiaa, 2020; Arzanova and Mayrovitz, 2022). However, the prognosis of these cancers has improved significantly following the establishment of therapies targeting the HER2 protein, including trastuzumab, an anti-HER2 antibody (Agyemang and Achiaa, 2020; Arzanova and Mayrovitz, 2022). TNBC breast tumours are commonly associated with poor prognosis, poor survival rates and high recurrence. This subtype is typically treated with a combination of surgery, radiation and chemotherapy (Arzanova and Mayrovitz, 2022; Hao *et al*., 2023).

The current study primarily focuses on hormone-dependant tumours, specifically luminal A, constituting approximately 70% of all diagnosed breast cancers (Li *et al*., 2019; Agyemang and Achiaa, 2020). Tamoxifen has been used in the management of breast cancer for over 30 years, and the drug has been reported to effectively reduce the mortality rate in individuals with oestrogen receptor-positive breast cancer (Howell and Howell, 2023). While it holds undeniable value and remains a mainstay in breast cancer treatment, the efficacy of Tamoxifen is often limited by systemic side effects, cytotoxicity and drug resistance (Li, Tsang and Tse, 2021; Mishra *et al*., 2021; Rostami, Tafvizi, and Manjili, 2022). Overcoming the limitations and improving the efficacy of traditional cancer therapies continues to be a crucial challenge. Recently the landscape of cancer research is increasingly recognising the tumour microenvironment (TME), a dynamic ecosystem surrounding cancer cells, as a treatment target (Roma-Rodrigues *et al*., 2019; Xiao *et al*., 2021; Babar *et al*., 2023). This innovative approach has now emerged as a promising strategy with several potential benefits including harnessing the immune response and overcoming

resistance, both of which may contribute to improving treatment response and patient outcomes (Roma-Rodrigues *et al*., 2019; Xiao *et al*., 2021; Bai and Cui, 2022; Bilotta, Antignani, and Fitzgerald, 2022; Babar *et al*., 2023).

1.1.4. The Breast Tumour Microenvironment

Tumour progression not only depends on neoplastic cells but also on significant alterations in the surrounding TME (Papanicolaou *et al*., 2022; Li, Tsang and Tse, 2021). In breast cancer, the TME plays significant roles in tumour behaviour and treatment response thus making its pathologic exploration important for disease management (Onal *et al*., 2020; Li, Tsang and Tse, 2021). The TME in breast cancer can be classified according to cellular and soluble components (Li, Tsang and Tse, 2021; Babar *et al*., 2023). The cellular components can be further divided into local (intra-tumoural), regional (breast) and metastatic compartments (Li, Tsang and Tse, 2021; Babar *et al*., 2023). The local compartment depicts the biological characteristics of tumour cells and tumour infiltrating inflammatory cells, including plasma cells, lymphocytes, macrophages, dendritic cells and neutrophils (Segovia-Mendoza and Morales-Montor, 2019; Li, Tsang and Tse, 2021). The regional compartment describes the interactions between tumour cells and neighbouring cells in the stroma, these involve stromal fibroblasts, myoepithelial cells, adipocytes, vascular and lymphatic endothelial cells (Segovia-Mendoza and Morales-Montor, 2019). The metastatic compartment includes host cells at lymph nodes and distant organs, which form metastatic sites, thus creating new TME (Segovia-Mendoza and Morales-Montor, 2019).

Various soluble factors are involved in cancer progression in the breast and at distant sites. These include enzymes, growth factors and cytokines. Within the complex TME, each component considerably impacts breast cancer progression (Mehta *et al*., 2021). Macrophages, which are pivotal players in the tumour's inflammatory infiltrate, have attracted particular attention (Segovia-Mendoza and Morales-Montor, 2019; Mehta *et al*., 2021). Their diverse functions within the TME include promoting and suppressing tumour growth under certain conditions, thus making them fascinating targets for

understanding and potentially manipulating cancer progression (Segovia-Mendoza and Morales-Montor, 2019; Mehta *et al*., 2021).

Tumour-Associated Macrophages (TAMs) in Breast Cancer

As actionable targets within the TME are continuously being identified, a promising therapeutic approach involves combining cancer cell elimination strategies with targeted modulation of the TME. This combinatorial approach may achieve synergistic effects in cancer treatment (He *et al*., 2021; Li, Tsang and Tse, 2021; Eligini *et al*., 2023). Macrophages, highly plastic and heterogenous cells, play a pivotal role in shaping the TME (Mehta *et al*., 2021). They demonstrate remarkable pluripotency, polarising into distinct functional subsets with heterogenous roles in the immune response (Li, Tsang and Tse, 2021). Importantly, macrophages can be polarised from an initial, relatively undifferentiated state (often referred to as M0) into distinct functional subsets: classically activated macrophages (M1) and alternatively activated macrophages (M2) (Boutilier and Elsawa, 2021; Chen *et a*l., 2023; **Figure 1.2**).

M1 macrophages participate in positive immune responses by secreting inflammatory cytokines and chemokines, playing a role in immune surveillance (Mehta *et al*., 2021). This polarisation is driven by signals from type 1 T-helper (Th1) cells, such as interferon-γ (IFN-γ) and tumour necrosis factor-α (TNF-α), as well as by exposure to microbial products like lipopolysaccharides (LPS) (Boutilier and Elsawa, 2021; Mas-Rosario *et a*l., 2023; Zhang and Sioud, 2023). Following these stimuli, M0 macrophages differentiate into the M1 phenotype, acquiring the ability to kill bacterial and viral pathogens and, eliminate tumour cells via enhanced phagocytosis and the production of inflammatory factors such as reactive nitrogen species (RNS) and reactive oxygen species (ROS), interleukin-2 (IL-2), interleukin-6 (IL-6), interleukin-12 (IL-12) and TNF-α (Oshi *et a*l., 2020; Mehta *et al*., 2021; Augustine, Nweke and Fru, 2022; **Figure 1.2**). Conversely, M0 macrophages differentiate into the M2 phenotype following exposure to cytokines secreted by type 2 T-helper (Th2) cells, such as interleukin-4 (IL-4), interleukin-10 (IL-10) and interleukin-13 (IL-13) (Mehta *et al*., 2021; Augustine, Nweke and Fru, 2022; **Figure 1.2**). The M2 macrophage phenotype

exhibits pro-tumour characteristics by initiating responses related to tissue repair and remodelling, and immune suppression (Mehta *et al*., 2021; Kerneur, Cano and Olive, 2022; Zhang and Sioud, 2023).

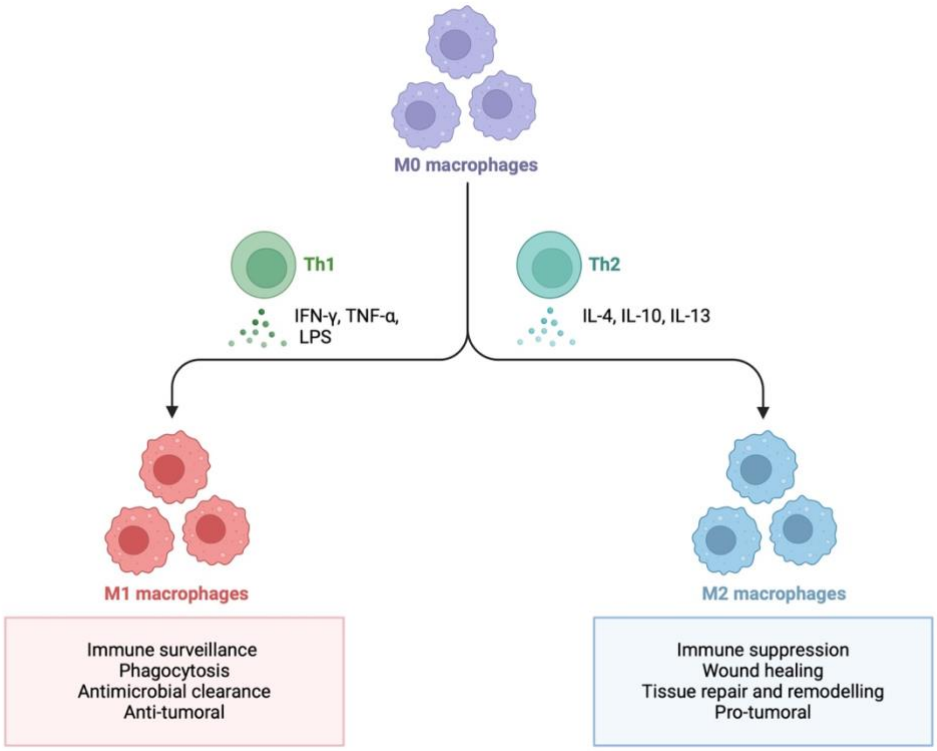


Figure 1.2: Macrophage polarisation into M1 and M2 phenotypes. Macrophage polarisation from the M0 state is initiated by signals released by T-helper cells (Th). M1 macrophage polarisation is induced by cytokines like IFN-γ and TNF-α. While polarisation towards the M2 phenotype is stimulated by IL-4, IL-10 and IL-13. Created with BioRender.com.

Maintaining a balance between M1 and M2 macrophage activation is crucial for sustaining tissue homeostasis (Li, Tsang and Tse, 2021). Imbalances in this equilibrium have significant pathological consequences (Boutilier and Elsawa, 2021; Li, Tsang and Tse, 2021). Excessive M1 activation is associated with the onset of various inflammatory and autoimmune diseases including arthritis, diabetes and atherosclerosis (Li, Tsang and Tse, 2021; Eligini *et al*., 2023; Kulakova *et al*., 2024). This unchecked inflammation can lead to chronic inflammatory autoimmune diseases,

characterised by persistent inflammation and irreversible tissue damage (Li, Tsang and Tse, 2021; Eligini *et al*., 2023; Kulakova *et al*., 2024). Conversely, an overabundance of M2 macrophages can contribute to tumour progression by stimulating tumour cell proliferation, invasion and angiogenesis, while simultaneously suppressing anti-tumour responses (Mehta *et al*., 2021; Chen *et al*., 2023). These findings emphasise the crucial role of macrophage polarisation in diverse disease contexts.

Within the intricate milieu of breast cancer, tumour-associated macrophages (TAMs) emerge as key players, significantly influencing tumour progression and patient outcomes (Mas-Rosario *et al*., 2023; Zhang *et al*., 2024a). TAMs originate from both resident tissue macrophages and circulating monocytes that are recruited to the tumour site (Zhou *et a*l., 2020; Li *et al*., 2023). These cells, predominantly of the M2 phenotype represent a considerable portion of the infiltrate of immune cells within breast tumours (Mehta *et al*., 2021; Li *et al*., 2023). Importantly, the induction of M2 macrophages commonly coincides with an increase in CD4+ T-cell-derived cytokines and correlates with poor patient survival outcomes (Mehta *et a*l., 2021; Zhan *et al.,* 2023). As benign cells transform into invasive cancerous cells, the TME undergoes a dramatic shift. Instead of a pro-inflammatory environment that is characterised by Th1 immune cells, it becomes dominated by Th2-driven immunosuppression fueled by several growth factors and cytokines, derived from both tumour and non-tumour cells in the TME (Lee, 2019; Mehta *et al*., 2021). This shift results in M1 macrophages polarising into M2 macrophages and the preferential accumulation of M2 macrophages within the TME (Lee, 2019; Mehta *et a*l., 2021; Dominguez-Cejudo *et al*., 2023).

While M2 macrophages dominate the breast TME, it is possible that enhancing the activity of M1 macrophages can lead to the inhibition of tumour growth (Murray, 2017; Petty *et al*., 2021; Stavrou and Constantinidou, 2024). Interestingly, transforming M2 macrophages back to M1 or blocking their ability to secrete tumour-promoting molecules offers promising avenues for therapy targeted towards the immune system (Stavrou and Constantinidou, 2024). This could involve strategies like reprogramming TAMs to an anti-tumour phenotype to enhance immune responses against tumour

cells, inhibiting TAM recruitment to the tumour to reduce their pro-tumourigenic effects and by developing TAM-targeted therapies (Petty *et al*., 2021; Zhou *et al*., 2020; Augustine, Nweke and Fru, 2022; Eligini *et al*., 2023; Stavrou and Constantinidou, 2024). TAMs are a complex and important component of the TME in breast cancer. Understanding their role in tumour progression is critical for developing effective therapies that can improve outcomes for patients with this disease.

1.1.5. Effects of Tamoxifen on Immune Activity in the TME

Early studies from the 1980s and 1990s report that Tamoxifen has no apparent influence on immune function (Behjati, 2009). However, there is growing evidence from research that suggests the contrary (Behjati, 2009; Pepe *et al*., 2021; Sfogliarini *et al*., 2022). Tamoxifen has been reported to have the ability to partially eliminate immune tolerance induced by oestrogen and its receptors, in oestrogen receptor-positive breast cancer (Pepe *et al*., 2021; Sfogliarini *et al*., 2022). Tamoxifen has also been revealed to promote the expression of α-lactalbumin in breast tumour cells. This lactation molecule is known as a target for immunotherapy in breast cancer treatment, and is commonly downregulated during tumorigenesis (Huang *et al*., 2021). Tamoxifen was also found to increase the cytotoxic capacity of natural killer (NK) cells, which were reported to decrease the breast cancer risk in women who are highly susceptible (Huang *et al*., 2021).

In vitro studies have revealed that Tamoxifen treatment upregulates IFN-γ associated genes in normal human mammary epithelial cells. This upregulation can promote macrophage activation towards the M1 phenotype, potentially contributing to enhanced immune surveillance within normal breast tissue (Schild-Hay *et al*., 2009; Huang *et al*., 2021). In a murine breast cancer model, Tamoxifen induced a shift of CD4+ T-lymphocytes from a Th1 anti-tumour phenotype towards a Th2 pro-tumour phenotype, thus illustrating its ability to impair anti-tumour immunity (Sfogliarini *et al*., 2022). Furthermore, it has been observed that Tamoxifen-induces transforming growth factor-beta (TGF-β) production in MCF7 cells resulting in a decreased cytotoxic

effect of CD8+ cytotoxic T lymphocytes (CTLs) and an increase in the polarisation of CD4+ T-lymphocytes into regulatory T cells (Tregs) (Moisand *et al*., 2023).

Limited research has explored Tamoxifen's effects on innate immune cells, such as macrophages, nevertheless, our knowledge of the mechanisms involved in these interactions between Tamoxifen and macrophages has evolved (Sfogliarini *et al*., 2022). Initially, researchers suggested that Tamoxifen's impact on macrophages involved increased activity of specific proteins like protein kinase C (PKC) and transcription factors such as the peroxisome proliferator-activated receptor gamma (PPARγ), glucocorticoid receptor (GR) and signal transducer and activator of transcription 1 (STAT1) (Pepe *et al*., 2021; Sfogliarini *et al*., 2022). However, recent studies performed on murine macrophages suggest that Tamoxifen activates additional transcription factors such as nuclear factor erythroid 2-related factor 2 (NRF2) and interacts with the PI3K (phosphatidylinositol 3-kinase)/AKT) pathway (He, Ru and Wen, 2020; Pepe *et al*., 2021; Sfogliarini *et al*., 2022). These events are reported to increase the expression of NRF2 genes, responsible for regulating the cell's defense against oxidative stress and toxic insults, including heme oxygenase 1 (HMOX-1) and vascular endothelial growth factor A (VEGF-A), while promoting immune polarisation markers such as arginase 1 (ARG-1) and interleukin-1β (IL-1β) (He, Ru and Wen, 2020; Pepe *et al*., 2021; Sfogliarini *et al*., 2022).

Unlike its cytotoxic effects in other cells including epithelial or hepatic cells, Tamoxifen has been reported to not stimulate macrophage cell death in murine models (Pepe *et al*., 2021). Instead, earlier studies demonstrate that it influences cholesterol and lipid metabolism of macrophages, even helping to prevent atherosclerosis (Sfogliarini *et al*., 2022). Recently, Tamoxifen was shown to impact immune-metabolic responses, promoting the M1 macrophage phenotype, enhancing phagocytosis and even activating caspase-1 (Pepe *et al*., 2021). Importantly, upon caspase-1 activation, macrophages secrete IL-1β. While caspase-1 can ultimately contribute to cell death, IL-1β secretion can occur independently of cell lysis (Pepe *et al*., 2021; Sfogliarini *et al*., 2022). This mechanism has been reported for Tamoxifen, which stimulates the formation of active caspase-1 in macrophages without compromising cell viability (Pepe *et al*., 2021; Sfogliarini *et al*., 2022).

While Tamoxifen can activate beneficial immune responses, as mentioned previously, macrophages can contribute to drug resistance in cancer patients (Chen *et al*., 2023; Zhang *et al*., 2024b). In breast cancer, TAMs can constitute over 50% of the TME and the M2 macrophage phenotype is particularly linked to tumour malignancy and Tamoxifen resistance (Mas-Rosario *et al*., 2023). Mechanisms underlying macrophage-mediated Tamoxifen resistance in breast cancer cells are currently unclear, but research suggests that macrophages promote resistance via secretion of various chemokines which stimulate the PI3K/Akt/mTOR signalling pathway, that is commonly associated with resistance to hormone therapy (Mishra *et al*., 2021; Howell and Howell, 2023). Furthermore, results from a previous study also confirmed that patients with high M2 macrophage infiltration tend to develop resistance to hormone therapy, including Tamoxifen (Zhang *et al.,* 2024b). While standard traditional breast cancer therapies, like Tamoxifen, have demonstrated efficacy, their primary mode of action was developed to target cancer cells directly. However, growing evidence suggests that these therapies can also indirectly influence the TME and immune cell populations, including macrophages (Li, Tsang and Tse, 2021; Mishra *et al*., 2021; Howell and Howell, 2023; Zhang *et al.,* 2024b). While these interactions have been observed, a deeper understanding of the precise mechanisms and the extent of their impact on therapeutic outcomes is still needed.

1.1.6. Cannabidiol as a Promising Adjuvant Therapy for ER+ Breast Tumours

The preferential accumulation of TAMs within the breast TME is a major contributor to establishing metastatic and malignant tumours (Mehta *et al*., 2021). Thus, TAM-targeted therapies are now being explored and developed (Zhou *et al*., 2020; Amaral *et al*., 2021; Zhan *et al*., 2023). As emerging therapeutic compounds, cannabinoids are gaining attention for their anti-tumour properties, with Cannabidiol (CBD) being the most promising (Amaral *et al*., 2021). Cannabinoids have been utilised historically in palliative cancer treatment owing to their ability to modulate side effects associated with standard cancer therapy including, pain, nausea, appetite, mood swings and

sleep disturbances (Dobovišek *et al.,* 2022; Buijs *et a*l., 2023). Recently, they have been recognised for their anti-tumorigenic effects in various cancer types including breast cancer and their clinical interest has been rising over the years with some cannabinoid-based medicines already being approved for clinical use. These approved medications primarily address conditions like appetite loss and weight loss associated with HIV/AIDS and chemotherapy, as well as epilepsy (Silva *et al*., 2020; 2021; Almeida *et al*., 2023; Yndart-Arias *et al*., 2023; Suttithumsatid, Sukketsiri and Panichayupakaranant, 2023).

CBD is the non-psychoactive constituent of the cannabinoid family and is derived from the *Cannabis sativa* plant (Massi *et al*., 2013; Mangal *et al*., 2021). The biological activities of CBD are mainly mediated by G protein-coupled cannabinoid receptors (CBRs), CB1 and CB2. Particularly, CB-Rs are distributed throughout the nervous, gastrointestinal, cardiovascular and immune systems (Kisková *et al.*, 2019; Mangal *et a*l., 2021). Furthermore, they are involved in biological processes such as pain regulation, energy metabolism and inflammation (Kisková *et al.*, 2019; Mangal *et al*., 2021). In breast cancer, CB1 is expressed moderately and CB2 expression is relatively upregulated, this is associated with tumour aggressiveness and as a result, this receptor is gradually emerging as a target for treatment (Kisková *et al*., 2019). Additionally, CBD signalling may occur via other receptors including the transient receptor potential vanilloid (TRPV) and, in receptor-independent pathways such as interactions with membrane channels (Kisková *et al.*, 2019; Mangal *et al*., 2021).

CBD has been reviewed as a potent anticancer agent based on its *in vitro* and *in vivo* activities against tumour cells (Seltzer *et al*., 2020; Mangal *et al*., 2021). Although the molecular mechanisms of action for CBD have not been fully characterised, several studies report on its ability to decelerate tumour progression (Shrivastava *et al.,* 2011; Kisková *et al.*, 2019; Dobovišek *et al*., 2020). In breast cancer cell lines, including ER+ MCF7 and T47D cells, and the ER- MDA-MB-231 cells, CBD was found to have antineoplastic effects such as inducing cell death mechanisms (Shrivastava *et al.,* 2011; Kisková *et al.*, 2019; Dobovišek *et al*., 2020). McAllister *et al.* (2011) revealed that CBD has the ability to inhibit the proliferation of cancer cells by inducing mitochondrial damage and increasing the production of ROS. Shrivastava *et al.* (2011)

also observed that CBD treatment causes an increase in ROS production and induces endoplasmic reticulum stress in breast cancer cell lines, which further led to the activation of autophagy and apoptosis. In addition, another study found that CBD treatment in mice breast cancer models resulted in a significant reduction of primary tumour growth and metastasis (Garcia-Morales *et al*., 2023).

Research has shown that CBD can modulate the immune microenvironment in breast cancer (Dobovišek *et al*., 2022). In 2015, Elbaz *et al* documented CBD's *in vitr*o and *in viv*o effects in breast cancer cell lines including ER- breast cancer. This study revealed that CBD has the ability to inhibit growth and metastatic or migratory processes in breast cancer cells by modulating the TME, and also through the inhibition of epidermal growth factor (EGF)-induced tumourigenesis. These findings were especially significant because it is well established that the overexpression of EGF and its receptor (EGFR) are associated with negative prognosis, particularly for patients with triple-negative breast cancer (Elbaz *et al*., 2015). Notably, in murine models, CBD has been shown to regulate tumour-secreted cytokines such as macrophage colony-stimulating factor (M-CSF) (Kisková *et al.*, 2019; Muthumalage *et al*., 2019). By decreasing M-CSF levels, CBD inhibits the recruitment and polarisation of monocytes into macrophages within the TME (Mehta *et al.*, 2021; Mas-Rosario *et al*., 2023). This reduction in macrophage infiltration subsequently suppresses angiogenesis, thereby restricting the supply of nutrients and oxygen essential for tumour growth (Mehta *et al.*, 2021; Mas-Rosario *et al*., 2023).

Furthermore, CBD was also shown to inhibit the recruitment of total macrophage and M2-phenotype macrophage populations to primary and secondary metastatic regions in cancer models (Elbaz *et al*., 2015; Deng *et al*., 2022). This observation suggests that CBD may have the ability to alter the cytokine profile secreted from the cancer cells, leading to the decreased infiltration of macrophages within tumour sites (Elbaz *et al*., 2015; Deng *et al*., 2022). Cytokine-profile analyses from 4T1.2 cells (breast cancer cell line derived from mice mammary gland tissue) treated with CBD revealed that CBD inhibits C-C motif chemokine ligand 3 (CCL3) and M-CSF secretion. CCL3 plays a pivotal role in the biological process of macrophage recruitment and high levels

of M-CSF are associated with macrophage-induced tumour metastasis and poor prognosis (Elbaz *et al*., 2015; Mehta *et al*., 2021; Mas-Rosario *et al*., 2023).

CBD exerts significant influence on macrophage function, in human mononuclear cells, CBD has been shown to upregulate inflammatory cytokines like TNF-α, IFN-γ and IL-1α, thus contributing to an M1 phenotype (Nichols and Kaplan, 2020; Boutilier and Elsawa, 2021; Mas-Rosario *et a*l., 2023). Studies have demonstrated that CBD can regulate nitric oxide (NO) secretion in peritoneal macrophages in response to various inflammatory stimuli (Yekhtin *et al*., 2022). In diabetic mice, CBD treatment has been shown to alter the secretion of TNF-α and IL-6 by macrophages (Weiss *et al*., 2007; Gonzalez-Mariscal *et al*., 2022). Moreover, it has been shown that CBD has the ability to decrease infiltration of macrophages in models of pulmonary inflammation (Nichols and Kaplan, 2020).

Given that immune cells, including macrophages, produce the inflammatory cytokine, IL-6, it is noteworthy that CBD has been shown to regulate circulating IL-6 in various inflammatory models, such as diabetes, cancer, asthma and hepatitis (Weiss *et al*., 2007; Gonzalez-Mariscal *et al*., 2022; Zaiachuk *et al*., 2023). *In vitro* studies have revealed that CBD and its metabolites can modulate inflammatory responses by modulating the generation of ROS, TNF-α and other inflammatory cytokines, as well as transcription factors such as nuclear factor kappa beta (NF-κB), IL-1β, IL-2, IL-6 and IL-8 (Kisková *et al*., 2019; Dobovišek *et al*., 2020; Yan *et al*., 2023). These findings collectively suggest that CBD can modulate macrophage function and influence the inflammatory response. This makes it a potential adjuvant therapy for diseases like breast cancer, which often involve complex and dynamic inflammatory processes. By potentially enhancing the immunomodulatory effects of standard treatments like Tamoxifen, CBD could offer a promising therapeutic strategy.

1.1.7. Macrophage Phenotyping by Proteomics

While it is established that various macrophage phenotypes coexist within the TME, their precise characteristics and functions remain incompletely understood. Recently, several approaches have been employed to characterise the phenotype, localisation, and distribution of macrophages within the tumour. Notably, extensive research has focused on macrophage polarisation, often utilising transcriptomic approaches (Li *et al*., 2021; Liu *et al*., 2022; Eligini *et al*., 2023). Although transcriptomics provides valuable insights into gene expression profiles, it is crucial to acknowledge that mRNA levels do not always directly match protein abundance due to post-transcriptional processing and post-translational mechanisms, such as mRNA stability, protein degradation and post-translational modifications (PTMs) (Oshi *et al*., 2020; Murugesan *et al*., 2022; Eligini *et al*., 2023).

Proteomics, the large-scale study of proteins, has surfaced as a remarkable tool for characterising macrophage phenotypes in breast cancer (Neagu *et al*., 2021; Kusebauch *et al*., 2023). By analysing differentially expressed proteins in M1 and M2 macrophages, proteomics provides valuable insights into the molecular mechanisms underlying macrophage polarisation and their impact on tumour progression (Eligini *et al*., 2023; Mas-Rosario *et al.,* 2023). Several proteomic technologies are available and are constantly evolving. Recent advances in mass spectrometry (MS) have significantly improved our ability to comprehensively profile the proteome of TAMs (Li *et al*., 2021; Eligini *et al*., 2023; Kusebauch *et al*., 2023). Among these technologies, liquid chromatography coupled with tandem mass spectrometry (LC-MS/MS) is the most widely used MS-based method for unbiased protein quantitation from biological samples (Matallana-Surget, Leroy and Wattiez, 2010; Li *et al*., 2021; Eligini *et al*., 2023). This high-throughput analytical technique combines the separation power of liquid chromatography with the detection and identification capabilities of mass spectrometry, enabling comprehensive and unbiased protein profiling (Eligini *et al*., 2023; Kusebauch *et al*., 2023).

The LC-MS/MS workflow comprises of a multidimensional separation of peptides in complex biological samples (Sinha and Mann, 2020; Neagu *et al*., 2021; Shuken,

2023; **Figure 1.3**). Briefly, proteins are extracted from cells or tissues using appropriate buffers and lysis techniques (Sinha and Mann, 2020; Neagu *et al*., 2021; Shuken, 2023). Thereafter, the proteins are enzymatically digested (often with trypsin) into peptides, which are then cleaned to remove salts, detergents and other contaminants that can interfere with the LC-MS/MS analysis. Peptides are separated based on their physiochemical properties using a chromatographic column. The separated peptides are then ionized and introduced into the mass spectrometer. The first analyser (MS1) scans a specific mass range to detect all peptide ions present in the sample. Selected precursor peptide ions from MS1 are fragmented in a collision cell, and the resulting fragment ions are detected by the second mass analyser (MS2) (Old *et al*., 2005; Matallana-Surget, Leroy and Wattiez, 2010; Li *et a*l., 2021; Meyer, 2021; Eligini *et al*., 2023; Kusebauch *et al*., 2023).

Various data acquisition and processing approaches have been described. Data-Independent Acquisition (DIA) with its variant Sequential Window Acquisition of all Theoretical Mass Spectra (SWATH-MS) has emerged as a robust data acquisition strategy (Meyer, 2021; Neagu *et al*., 2021; Kusebauch *et al*., 2023). DIA/SWATH-MS significantly enhances the detection and accurate quantification of a large portion of the proteome by combining deep proteome coverage and high reproducibility across samples. Its performance has been successfully validated and standardised across multiple laboratories (Meyer, 2021; Kusebauch *et al*., 2023). This approach divides the entire mass range into overlapping mass windows, and MS/MS spectra are acquired for all precursor ions within each window. Software algorithms identify and characterise peptide peaks in MS1 and MS2 spectra (Meyer, 2021; Kusebauch *et al*., 2023). Peptide sequences are matched to a protein database using search engines like Mascot, Sequest or Spectronaut (Matallana-Surget, Leroy and Wattiez, 2010). These engines analyse the LC-MS/MS data to quantify protein abundance. To identify differentially expressed proteins between experimental conditions, statistical tests are employed (Sinha and Mann, 2020; Neagu *et al*., 2021; Shuken., 2023). However, due to the multiple comparisons inherent in proteomics, rigorous statistical methods are crucial to minimise the risk of false discoveries.

The false discovery rate (FDR) is a statistical method used to control the proportion of false positives among the identified differentially expressed proteins (Karp *et al*., 2007; Lai, 2017; Sinha and Mann, 2020; Shuken, 2023). It calculates the expected proportion of false discoveries among all proteins declared significant. The q-value is the minimum FDR threshold at which a given protein can be considered significant (Karp *et al*., 2007; Lai, 2017; Sinha and Mann, 2020; Shuken, 2023. By controlling the FDR and using q-values, researchers can ensure that the identified protein changes are statistically robust and not simply due to random chance (Karp *et al*., 2007; Lai, 2017; Sinha and Mann, 2020; Shuken, 2023). Following statistical analysis, softwares like Cytoscape can be employed to visualise protein-protein interaction networks and identify key players in biological processes (Doncheva *et al*., 2019; Sinha and Mann, 2020; Neagu *et al*., 2021; Shuken, 2023). This network analysis provides valuable insights into the interconnectedness of proteins and their potential roles in cellular pathways.

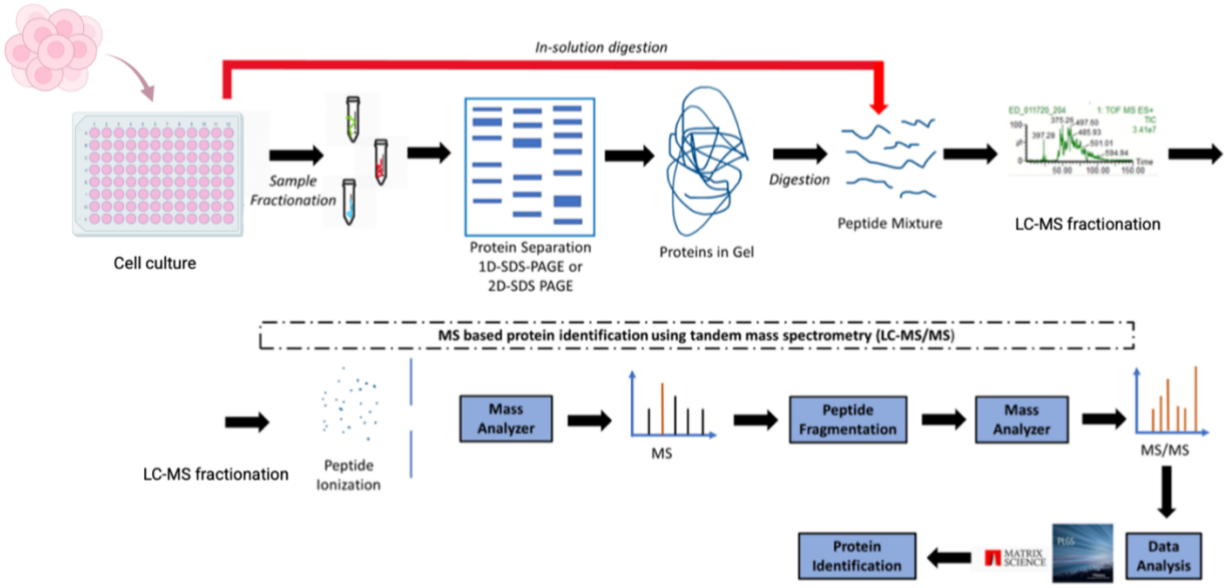


Figure 1.3: Schematic of a general proteomic workflow. The sample undergoes fractionation (for example, by electrophoresis) and is subsequently digested by trypsin, either in-gel or in-solution. The resulting peptide mixture is then ionised and separated by liquid chromatography (LC). Peptides are then ionised and their corresponding mass-to-charge ratios (m/z) are measured in the mass spectrometer. Data analysis, typically using dedicated proteomics software, leads to the identification of peptides, which in turn allows for the identification of the corresponding proteins. Adapted from Neagu *et al*., 2021. Created with BioRender.com.

Several studies have utilised LC-MS/MS to investigate the proteomic changes associated with macrophage polarisation in breast cancer (Oates *et al*., 2023; Gudgeon *et al*., 2025; **Figure 1.4**). While M1 and M2 macrophages exhibit distinct protein expression profiles, it is crucial to recognise that macrophage polarisation is not a simple binary switch. Instead, there is growing evidence supporting the concept of a continuum of macrophage activation states (Augustine, Nweke and Fru, 2022; Eligini *et al*., 2023; Zhang *et al*., 2024a). Research on human and murine macrophage cell lines has demonstrated that M1 protein profiles are linked to inflammatory mediators such as TNF-α, IL-1β and inducible nitric oxide synthase (iNOS), while M2 macrophages are associated with IL-10, TGF-β and arginase-1 (McWhorter *et al*.,

2013 Boutilier and Elsawa, 2021; Munir *et al*., 2021; Wang *et al*., 2022a; Gudgeon *et al*., 2025; **Figure 1.4**). Additionally, PTMs such as phosphorylation and acetylation, can regulate macrophage function and with LC-MS/MS widely used to identify and quantify these PTMs in macrophage proteins, these techniques can provide insights into the signalling pathways that drive macrophage polarisation (Oates *et al*.,2023; Gudgeon, Marín-Rubio and Trost, 2022). Macrophages also undergo metabolic reprogramming during polarisation. Studies have shown that M1 macrophages exhibit a glycolytic phenotype, while M2 macrophages favour oxidative phosphorylation. LC-MS/MS can be used to analyse the metabolic enzymes and metabolites associated with metabolic shifts during polarisation (Viola *et a*l., 2019; Rattigan *et al*., 2018; Wang *et al*., 2022a). Ultimately, LC-MS/MS can help researchers understand the complex mechanisms underlying tumour-associated macrophage function and identify novel therapeutic targets.

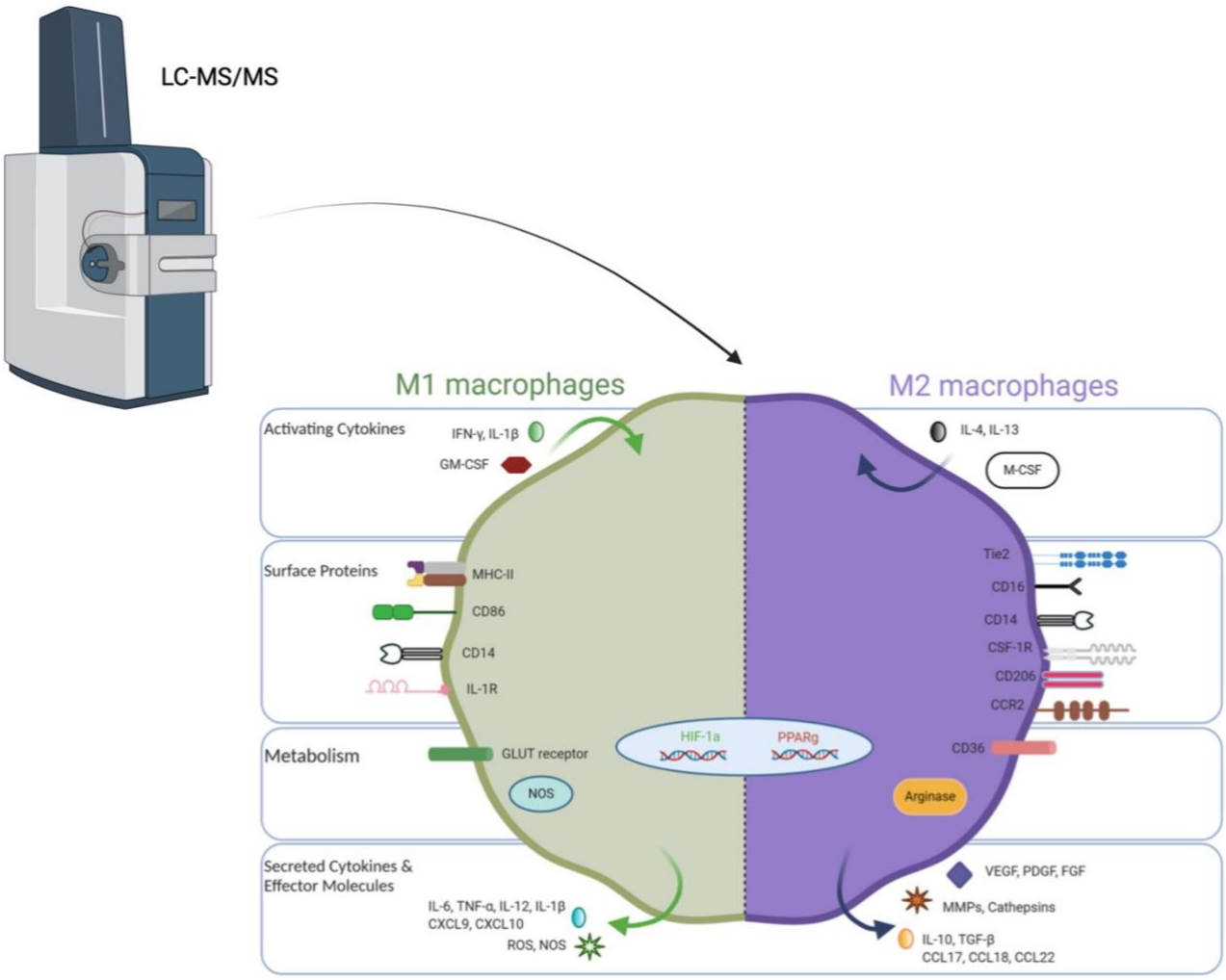


Figure 1.4: Common markers associated with M1 and M2 macrophage phenotypes. Figure illustrates key polarisation markers linked with M1 and M2 macrophages, that have been identified utilising various techniques including LC-MS/MS based proteomics. Adapted from Mehta *et al*., 2021. Created using BioRender.com.

1.2. Rationale for the Study

Breast cancer continues to be a major public health concern, with oestrogen receptor-positive breast cancer representing a substantial portion of cases. While conventional therapies like Tamoxifen have been effective, many patients develop resistance, notwithstanding delayed recurrence. This underscores the need for innovative approaches, including those targeting the TME. Macrophages, play a critical role in shaping the TME and can promote tumour growth, angiogenesis, and metastasis. Therefore, targeting macrophages offers a promising therapeutic strategy.

CBD has emerged as a potential therapeutic agent with immunomodulatory properties. However, the precise mechanism underlying its effects on macrophages and its potential synergy with conventional therapies like Tamoxifen remain unclear. Proteomic analysis using LC-MS/MS can provide valuable insights into the molecular mechanisms by which CBD and Tamoxifen influence macrophage phenotype and function. By identifying differentially expressed proteins, we can gain a better understanding of the pathways associated with macrophage polarisation and their impact on breast tumour progression. This may pave the way for novel combination therapies to improve patient outcomes.

1.3. Aims and Objectives

Aim:

The current study aimed to assess the mechanisms of macrophage polarisation of RAW264.7 macrophages in response to CBD and Tamoxifen, in the context of breast cancer. The experimental design is briefly outlined in **Figure 1.5**.

Objectives:

- To characterise the time-dependent polarisation of M0 RAW264.7 macrophages into M1 and M2 phenotypes using the Griess reagent and spectrophotometry to quantify nitrite production, phase-contrast microscopy to visualise morphological changes, and mass spectrometry to analyse differential protein expression profiles.
- To determine the optimal concentration and exposure duration of CBD in combination with 2 μM Tamoxifen on MCF7 breast cancer cells by measuring cell viability with the Neutral red assay and evaluating growth inhibition using the MTT assay.
- To evaluate the cytotoxic and polarising effects of the optimised CBD and 2 μM Tamoxifen treatment on RAW264.7 macrophages by assessing cytotoxicity using Neutral red and MTT assays and investigating proteomic changes through mass spectrometry.
- To investigate the interaction between RAW264.7 macrophages and MCF7 breast cancer cells following optimised CBD and 2 μM Tamoxifen treatment by assessing macrophage phagocytosis of MCF7 cells using fluorescence microscopy and measuring nitrite production in co-cultures using the Griess reagent.
- To integrate functional, morphological and proteomic data to elucidate the synergistic immunomodulatory effects of CBD and Tamoxifen on macrophage behaviour in the context of breast cancer.

Experimental Design

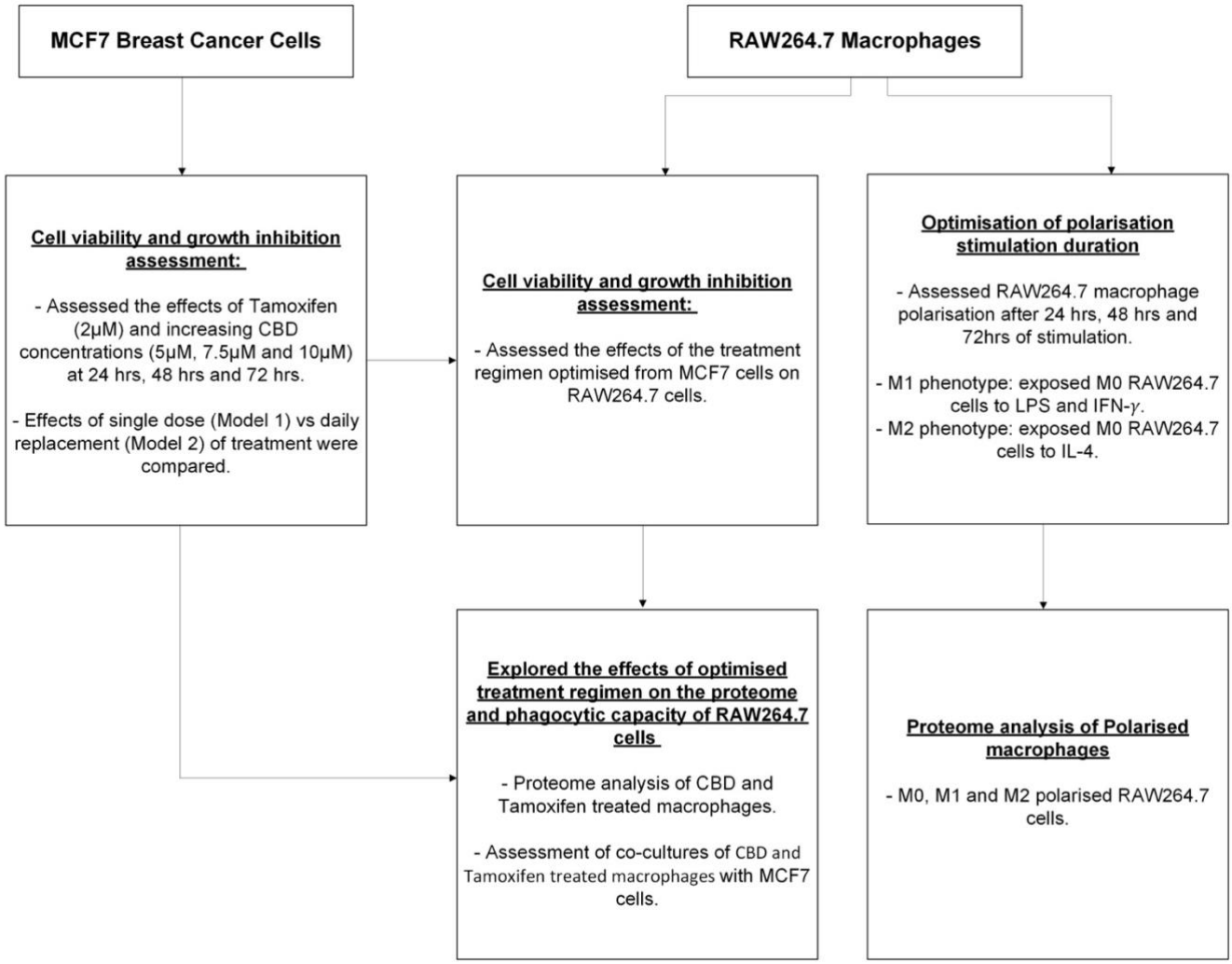


Figure 1.5: Flow diagram showing an overview of the methodology. The effects of CBD and Tamoxifen were assessed on both MCF7 and RAW264.7 cell lines. Thereafter, analysis relating to the polarisation, proteome and phagocytic activity of RAW264.7 macrophages was performed.

Chapter 2

Materials and Methods

Human Research Ethics Waiver was obtained from the Human Ethics Research Committee (Medical), University of the Witwatersrand, Waiver Certificate Number: W-CBP-220617-01 (**Appendix A0**).

2.1. Cell Culture

Cell Culture:

MCF7 breast cancer cells (luminal A phenotype) at passage numbers 12-14 (obtained from Cellonex, South Africa) were cultured in Dulbecco's Modified Eagles Medium (DMEM) (Separation Scientific, P04-03590) supplemented with 5% (v/v) foetal bovine serum (FBS) (Separation Scientific, P30-3302) and 0.1% (w/v) penicillin/streptomycin (P/S) (Thermofisher Scientific, 15140148), henceforth referred to as complete culture medium. The RAW264.7 macrophage cell line (ATCC1TIB-71™, obtained from Cellonex, South Africa, CCL-240) at passage numbers 11-15, was cultured in DMEM supplemented with 10% (v/v) FBS, henceforth referred to as complete culture medium. Both cell lines were propagated in T75 tissue culture flasks (Greiner Bio-one, 658170) and incubated at 5% CO_2 and 37^oC in a Heracell 160i CO_2 incubator (Thermofisher Scientific). Cultured samples of MCF7 and RAW264.7 cells were subsequently tested for mycoplasma contamination. The cultures tested negative for mycoplasma following staining with 4',6-diamidino-2-phenylindole (DAPI) (Sigma-Aldrich; D9542) (**Appendix A1**).

Subculture:
Upon reaching ~75% confluency, MCF7 cells were washed with 0.1 M phosphate buffered saline (PBS) (pH 7.4, **Appendix A2**) and detached from the flask using 0.25% trypsin/ethylenediaminetetraacetic (EDTA) (Separation Scientific, P10-019500). The reaction was neutralised with the addition of 4 mL of complete media. The RAW 264.7 cells were detached in PBS by gently scraping the bottom of the flask with a cell

scraper (Sigma Aldrich, C5981). The resulting cell suspensions were transferred into 15 mL centrifuge tubes (Lasec, 188261) and centrifuged using a Rotafix 32A centrifuge (Labotech) at 400×*g* for 5 minutes. Thereafter, the supernatants were discarded and the cell pellets were resuspended in 1 mL complete media. Cells were counted and viability was assessed using the Trypan Blue Exclusion method using a TC20 Automated Cell Counter (BioRad). The cells were cryopreserved at $1x10^6$ cells/mL in their respective freezing down media (**Appendix A2**) at -80°C until subsequent experimentation.

2.2. Assessing the Impact of Duration on the Polarisation of M0 RAW264.7 Macrophages into the M1 and M2 Phenotypes

To distinguish the different RAW264.7 macrophage phenotypes (M0, M1 and M2), nitrite production was quantified using the Griess Reagent Kit (ThermoFisher Scientific, G7921). Macrophages (M0) with a viability of ~80% were seeded in duplicate (1×10^5 cells/well) for the induction of each phenotype and cultured to ~75% confluency. Unstimulated RAW264.7 cells (cultured in DMEM and 10% (v/v) FBS) were used as the M0 control. The M1 phenotype was generated by exposing cells to the following stimulants (**Appendix B1**); 100 ng/mL lipopolysaccharides (LPS) (Sigma-Aldrich, L2880) and 20 ng/mL interferon-gamma (IFN-γ) (Sigma-Aldrich, SRP3058). For M2 polarisation, the cells were exposed to 20 ng/mL interleukin-4 (IL-4) (Sigma-Aldrich, SRP3093). These stimuli and their concentrations have been previously established as effective inducers of the respective macrophage phenotypes (Deci *et al*., 2019; Khabipov *et al*., 2019; Heaster *et al*., 2020; Shi *et al*., 2020; Liang *et al*., 2022; Liu *et al*., 2022). The cells were subjected to a single, prolonged exposure to the respective stimuli for a period of 72 hours, consistent with previous studies (Deci *et al*., 2019; Khabipov *et al*., 2019; Heaster *et al*., 2020; Shi *et al*., 2020; Liang *et al*., 2022; Liu *et al*., 2022).

To study the effects of duration in response to stimulation on macrophage polarisation, the morphology of the macrophages and nitrite production from the macrophages in

cultures were assessed at 24-hour intervals over a 72-hour period. To assess the nitrite production, 50 µL of the culture supernatants were transferred to 96-well plates and mixed with 30 µL of deionized water and 20 µL of the Griess reagent which constitutes 10 µL of N-(1-naphthyl) ethylenediamine (NED) and 10 µL of sulfanilic acid. The plates were incubated for 30 minutes at room temperature, protected from light. Following incubation, the absorbance was measured at 560 nm using the Promega Glomax spectrophotometer. Serum-free media was used as a blank control and was subtracted from all absorbance values to obtain the corrected absorbance. The concentration of nitrite formation was assessed from a nitrite standard reference curve. The curve was generated by performing 6 serial twofold dilutions of sodium nitrite (100, 50, 25, 12.5, 6.25, 3.13 and 1.56 µM) (**Appendix B2**) (Palmieri *et al*., 2020; Drehmer *et al*., 2022).

2.2.1. Data Analysis

Experimentation was conducted three times. Microsoft Excel (version 16.77) was utilised to manage numerical data and generate graphs. Statistical analyses were performed using Statistica (version 14.0.1). The distribution of the data was analysed using the Shapiro-Wilk test of normality. The Kruskal-Wallis One-Way Analysis of Variance (ANOVA) by Ranks test was conducted to determine differences in polarisation between the different phenotypes and the Friedman One-Way ANOVA by Ranks test was performed to measure the differences across the time-points. The appropriate post-hoc tests were then performed to determine whether these differences were significant ($p<0.05$) (**Appendix B3**).

2.3. Optimisation of CBD Treatment Concentration, Duration of Treatment and Treatment Model

Anticancer drug candidates are typically initially screened on cell lines to reveal their biological effects and underlying molecular mechanisms (Olivas-Aguirre *et al*., 2022). Human tumour cell lines are essential tools for developing and testing anti-cancer drugs (Olivas-Aguirre *et al*., 2022). The MCF7 cell line, isolated from a woman with metastatic breast cancer, is one of the most widely used breast cancer cell line due to its high expression of oestrogen receptors, which closely mimics oestrogen receptor-positive breast cancers (Olivas-Aguirre *et al*., 2022; Schlottmann *et al*., 2022). Thus, to evaluate the efficacy of CBD and/or Tamoxifen treatment, we utilised MCF7 cells as an *in vitro* model for oestrogen-receptor positive breast cancer.

2.3.1. Plating Cells for Experimentation

MCF7 breast cancer cells were harvested using trypsin/EDTA and enumerated using the Trypan Blue Exclusion method. Cells with a viability of ~80% were utilised for experimentation. The cells were seeded at a density of 1 x 10^5 cells/well in 24-well plates and complete culture medium was added to a final volume of 300 µL/well. Thereafter, cells were incubated at 5% CO_2 and 37^{o}C for 24 hours to achieve ~75% confluency. Cells were seeded in duplicate for each treatment group (**Table 2.1**).

2.3.2. Drug Preparations and Treatment

Tamoxifen (Sigma Aldrich; T5648) and CBD (Biocom Africa; 90080) were dissolved in 100% methanol to a final concentration of 1 mg/mL. The drug stock solutions were further diluted in complete culture medium to achieve working concentrations required for experimentation (**Appendix C1**). Tamoxifen was observed at 2 µM, its use was based on a previous study performed by Dr Kyrtania Pather (2020) in our laboratory (Pather and Augustine, 2020). In this study, Tamoxifen was tested on MCF7 breast cancer cells using concentrations ranging from 0.5 to 2.5 µM, using the lactate

dehydrogenase (LDH) and Neutral red cytotoxicity assays. A concentration of 2 µM was selected as it exhibited suboptimal cytotoxic effects by inducing cell death *in vitro* at approximately 50% (half-maximal inhibitory concentration, (IC_{50})), thus allowing for the investigation of cellular responses without causing excessive cell death. These results align with previous cellular studies, in which the *in vitro* concentration of 2 µM mimicked treatment regimens administered to women with breast cancer (Ryden *et al*., 2005; Pawlak and Wiebe, 2007; Pike *et al*., 2015; Hassan *et al*., 2017). In the present study, CBD was tested at concentrations obtained from literature (5 µM, 7.5 µM and 10 µM,) (Shrivastava *et al*., 2011; Sultan, Marie and Sheweita, 2018; Dobovišek *et al*., 2022). Upon reaching confluency, cells were washed with PBS and incubated with 300 µL of the working concentrations of the respective treatments, according to two treatment models (model 1 and model 2, to be described below).

Given the recent advancements in understanding the impact of different treatment regimens (Patwardhan *et al*., 2021), two models were employed to evaluate the efficacy of our drug treatments *in vitro*, using MCF7 cells. Model 1 involved a single dose of drugs over a 72-hour period, while model 2 utilised a regimen of a daily drug replacement for a total of 72 hours. The cytotoxic effects of these treatment regimens were assessed using the Neutral red and MTT assays at 24, 48 and 72 hours post-treatment. Experiments were repeated for three independent measures.

Table 2.1: Treatments administered to MCF7 cells during optimisation

Treatment group	Treatment components
Media control (untreated cells)	Complete media (DMEM + 5% (v/v) FBS + 0.1% (w/v) P/S)
Diluent control (0.4% methanol)	0.4% (v/v) methanol in complete media
2 µM Tamoxifen	2 µM Tamoxifen in complete media
5 µM CBD	5 µM CBD in complete media
7.5 µM CBD	7.5 µM in complete media
10 µM CBD	10 µM in complete media

2 µM Tamoxifen + 5 µM CBD	2 µM Tamoxifen + 5 µM CBD in complete media
2 µM Tamoxifen + 7.5 µM CBD	2 µM Tamoxifen + 7.5 µM CBD in complete media
2 µM Tamoxifen + 10 µM CBD	2 µM Tamoxifen + 10 µM CBD in complete media

2.3.3. Neutral red Assay

Following 24, 48 and 72 hours of treatment with Tamoxifen and/or CBD as per section 4.3.2, the Neutral red assay was performed to determine the effects of the treatment regimens on the viability of MCF7 cells. The cells were washed with PBS three times and incubated with 100 µg/mL neutral red dye (Gurr BDH Chemicals, Poole, England, 340564A) (**Appendix C1**) dissolved in complete culture medium, for 3 hours at 37^{o}C and 5% CO_2. After the 3 hours of incubation, cells were assessed for dye uptake using an Olympus IX51 microscope with CellSense V11 software. The Neutral red medium was then removed, and cells were washed with PBS. Subsequently, 150 µL of desorb solution (1% acetic acid in 50% ethanol) (**Appendix C1**) was added to each well to extract the dye and the 24-well plates were placed on a Micromixer Mx2 microplate shaker (FINEPCR) at 400 rotations per minute (rpm) for 60 minutes. The supernatant was then transferred into corresponding wells of a 96-well plate and absorbance levels were measured at a wavelength of 560 nm and a reference wavelength of 600 nm on a Promega Glomax spectrophotometer (Anatech). Serum-free media was used as a blank control and was subtracted from all absorbance values to obtain the corrected absorbance. The absorbance of the untreated cells (media control) was considered as 100% viable and the cell viabilities of the experimental samples were calculated using the formula below (Gomez-Gutierrez *et al*., 2021).

$$Cell\ viability\ (\%) = \frac{corrected\ mean\ absorbance\ (sample)}{corrected\ mean\ absorbance\ (media\ control)} \times 100$$

2.3.4. MTT Assay

To provide additional information on cytotoxicity and cell proliferation, the Thiazolyl Blue Tetrazolium Bromide (MTT) (Sigma-Aldrich; M5655-1G) assay was also conducted on MCF7 breast cancer cells. The MTT labelling reagent was prepared by dissolving Thiazolyl Blue Tetrazolium Bromide to a final concentration of 5 mg/mL in PBS (**Appendix C1**). In the last four hours of treatment, the cells were incubated at 37°C and 5% CO_2 with 30 µL/well of MTT. At the end of each treatment duration (24, 48 and 72 hours), the solutions were aspirated and 500 µL of dimethyl sulfoxide (DMSO) (Thermofisher Scientific, 20688) was added into each well. Following this, the solubilised solution was transferred to corresponding wells of a 96-well plate and the absorbance of the soluble formazan product was quantified using the Promega Glomax spectrophotometer at a wavelength of 560 nm. Likewise, the absorbance of the untreated cells (media control) was considered as 100% viable. To assess the minimal growth conditions of the cells, serum-free media was used as a basal media control and 0.1% Triton-X-100 (Sigma-Aldrich, X100) (**Appendix C1**) was used as a positive control for cell death. The cytotoxic effects of the drug treatments were calculated in terms of growth inhibition percentage, according to the formula below (Suttithumsatid, Sukketsiri and Panichayupakaranant, 2023).

$$Growth\ inhibition\ (\%) = \left(100 - \left(\frac{corrected\ mean\ absorbance\ (sample)}{corrected\ mean\ absorbance\ (media\ control)}\right)\right) \times 100$$

2.3.5. Data Analysis

Numerical data was managed in Microsoft Excel (version 16.77). Graphs were also generated in Microsoft Excel to assess the cell viability and growth inhibition at the different time intervals. Dose-response curves were generated using GraphPad Prism (version 10) and were used to calculate the half-maximal (50%) inhibitory concentration (IC_{50}) of CBD in MCF7 cells. Statistical analyses were performed using

Statistica (version 14.0.1) The Shapiro-Wilk test, used to assess the distribution of the data, showed that that the data did not follow a normal distribution ($p>0.05$). As a result of the non-normal distribution of the data and small sample size, non-parametric tests were subsequently conducted. The Kruskal-Wallis One-Way ANOVA by Ranks test was performed to determine the differences in cell viability and growth inhibition between the treatment groups. The Friedman One-Way ANOVA by Ranks test was performed to measure the differences in cell viability across the different time intervals. Additionally, appropriate post-hoc tests for Kruskal-Wallis and Friedman tests were used to determine whether the variances observed were significant. Furthermore, the Mann-Whitney U test was conducted to assess whether the effect of treatment was significantly altered between the two different treatment models. For all analyses, $p<0.05$ was regarded as statistically significant (**Appendix C3-4).**

2.4. Evaluation of the impact of the Optimised Treatment Regimen on RAW264.7 Macrophages

Tumour cells and cells within the tumour microenvironment, including macrophages, engage in complex reciprocal interactions (Zhan *et al*., 2023). In this study, we explored how the behaviour of RAW264.7 macrophages was influenced by Tamoxifen and CBD, optimised for their effects on MCF7 breast cancer cells, and reciprocal interactions with MCF7 cells. RAW264.7 macrophages are derived from BALB/c mice transfected with the Abelson leukaemia virus and are a widely used model for macrophage-associated immunological studies (Li *et al*., 2021). They exhibit similarities to primary macrophages such as human monocyte-derived macrophages (hMDMs), bone-marrow derived macrophages (BMDMs) and their human counterparts (THP-1 and U937), in terms of genotype and phenotype (Taciak *et al*., 2018; Khabipov *et al*., 2019; Li *et al*., 2021; Shuster, 2023).

RAW264.7 macrophages (M0) were harvested and enumerated using the Trypan Blue Exclusion method. Cells with a viability of ~80% were utilised for experimentation. The cells were seeded at a density of 1 x 10^5 cells/well in 24-well plates and complete

culture medium was added to a final volume of 400 µL/well. Thereafter, cells were incubated at 5% CO_2 and 37°C for 24 hours to achieve ~75% confluency. Once cells were confluent, they were incubated with 400 µL of the working concentrations of the respective treatments, shown in **Table 2.2**. Based on the quantitative and qualitative analyses (results section 3.2.), it was determined that 5 µM CBD would be the optimal concentration to be used for subsequent experiments in combination with 2 µM Tamoxifen. It was established that the duration of treatment would be 72 hours, following model 2, in which treatments were administered daily.

Following the optimisation of treatment and treatment duration on MCF7 cells, the effects of 5 µM CBD, 2 µM Tamoxifen and combination of both drugs were assessed in RAW264.7 macrophages over 72 hours, utilising treatment model 2. The Neutral red and MTT assays were performed to assess the cytotoxic effects of treatment. The experimental protocols for both assays were followed as outlined in sections 2.3.3 and 2.3.4. Experimentation was carried out in duplicate for each treatment group (**Table 2.2**) and repeated for three independent measures.

Table 2.2: Treatments administered to RAW264.7 cells during Neutral red and MTT experimentation

TREATMENT GROUP	TREATMENT COMPONENTS
MEDIA CONTROL (UNTREATED CELLS)	Complete media (DMEM + 10% (v/v) FBS)
DILUENT CONTROL (0.2% METHANOL)	0.2% (v/v) methanol in complete media
2 µM TAMOXIFEN	2 µM Tamoxifen in complete media
5 µM CBD	5 µM CBD in complete media
2 µM TAMOXIFEN + 5 µM CBD	2 µM Tamoxifen + 5 µM CBD in complete media

2.4.1. Data Analysis

Data was managed in Microsoft Excel (version 16.77). Statistical analyses were performed using Statistica (version 14.0.1). The Shapiro-Wilk test of normality revealed that the data was not normally distributed ($p>0.05$). The Kruskal-Wallis One-Way ANOVA by Ranks test was conducted to determine whether there were significant differences in cell viability and growth inhibition across the different treatment groups. A post-hoc test was also performed to determine whether these differences were significant ($p<0.05$) (**Appendix C4).**

2.5. Proteomic Analysis of RAW264.7 Macrophages

The proteome of RAW264.7 macrophages (M0, M1 and M2) that were polarised according to section 2.2 above and, those exposed to optimised CBD and Tamoxifen treatment (section 2.4) were assessed. Following stimulation and/or treatment, as per sections 2.2 and 2.4, the cells were harvested, snap-frozen in liquid nitrogen and stored at -80ºC until mass spectrometry analysis at the Council for Scientific and Industrial Research (CSIR). Experimentation was conducted in triplicates for each treatment group.

2.5.1. Sample Preparation for Mass Spectrometry:

Stored samples were thawed on ice and re-suspended in 75 µL extraction buffer containing 50 mM Tris-HCl buffer and 2% sodium dodecyl sulphate (SDS), pH 8. The buffer is required to maintain a stable pH for protein stability and, to denature and solubilise the proteins (Meyer, 2021; Neagu *et al*., 2021; Kusebauch *et al*., 2023). Thereafter, samples were loaded into 96-well microplates which were placed into the Pixul Multi-Sample Sonicator (Active Motif, Carlsbad, CA) for cell homogenisation and protein extraction. The cells were then sonicated under the settings: Pulse = 50; PRF = 1; Process time = 5; Burst = 20. After completion of the extraction cycles, the

samples were transferred into 2 mL Eppendorf tubes. To degrade nucleic acids (DNA and RNA), the nuclease enzyme, benzonase was added, followed by the addition of 2M MgCl and incubation at 37°C for 30 minutes. After incubation the samples were centrifuged at 15 000×*g* for 10 minutes to remove cell debris and supernatants were transferred into fresh tubes. Protein quantities were measured using the Pierce Bicinchoninic Acid (BCA) Protein Assay (ThermoFisher Scientific, Massachusetts, USA). Aliquots of protein solution were then stored at -80ºC until further processing.

Protein samples were thawed and 20 µg per sample was incubated with 10 mM dithiothreitol (DTT) at 60°C for 30 minutes, to reduce disulphide bonds in proteins formed by the oxidation of sulfhydryl groups (Meyer, 2021; Neagu *et al*., 2021; Kusebauch *et al*., 2023). Samples were then alkylated with 40 mM iodoacetamide (IAA) at room temperature in the dark for 30 minutes, to stabilise free sulfhydryl groups and improve protein yield (Meyer, 2021; Neagu *et al*., 2021; Kusebauch *et al*., 2023). Subsequently, the reaction was quenched with 10 mM DTT. The samples were then purified of detergents and salts by binding them to magnetic hydrophilic interaction liquid chromatography (HILIC) beads (MagReSyn™ HILIC microparticles; ReSyn Biosciences Edenvale, South Africa) and digested with trypsin (1:20; enzyme: protein) and LysC (1:100; enzyme: protein). Protein digestion was subsequently performed in a 96 deep-well plate, for automated sample preparation employing the KingFisher Duo™ magnetic handling station (Thermo Fisher Scientific).

Briefly, magnetic hydrophilic affinity microparticles (20 µL, 200 µg) were equilibrated in 200 µL of 100mM ammonium acetate pH 4.5 comprising 15% acetonitrile (MeCN). Microparticles were then moved to 100 µL of protein binding solution (all protein samples were adjusted to 50 µL utilizing 1% SDS and added to 50 µL of 200 mM ammonium acetate pH 4.5 containing 30% MeCN) and mixed for 30 minutes at room temperature. The captured proteins were then washed twice in 200 µL of 95% MeCN, transferred to 200 µL of 25 mM ammonium bicarbonate containing 2 µg of sequencing grade trypsin (Promega, Madison, USA) and mixed for 4 hours digestion at 47°C. After digestion, the beads were removed, and the resultant peptide samples were transferred to 2 mL LoBind tubes and were dried overnight using the CentriVap speed vacuum dryer to remove the buffer through sublimination while still preserving the

chemical and biological structure of the peptides (Neagu *et al*., 2021; Kusebauch *et al*., 2023). Peptide concentrations were quantified using the Pierce Quantitative Colorimetric Peptide Assay Kit (Thermo Fisher Scientific, Massachusetts, USA).

2.5.2. Liquid Chromatography-Mass Spectrometry (LC-MS) Data Acquisition

Proteome profiles were generated using an EvosepOne (Evosep Biosystems) system coupled with a timsTOF HT mass spectrometer (Bruker) with a peptide loading mass of 500 ng and an LC gradient (60 SPD). All data were acquired under the dia-PASEF (default short gradient) mode, with an MS1 scan range of 100–1700 *m*/*z*. Twelve isocratic *m*/*z* and IM windows were selected for serial MS2 fragmentation ranging from 390 to 1250 *m*/*z* and 0.84 to 1.31 1/K0 for mass and IM range, respectively.

2.5.3. SWATH-MS Data Processing and Statistical Analysis

Raw Swath (.wiff) data files were imported into Spectronaut v19 software (Biognosys Inc) and were examined alongside the murine UniProt sequence database accompanied with a list of familiar contaminating proteins. The default direct DIA identification and quantification settings were used for data processing and included: trypsin, IAA based alkylation and comprehensive exploration effort with biological alterations permitted. The false discovery rate (FDR) analysis was set at 0.01 (1%) at the peptide level. Spectronaut v19 software (Biognosys Inc) performed an unpaired comparison (two-sample t-test) between samples labelled according to experimental conditions, based on the $\log_2$ ratios of individual intensities of peptides of a protein. Kernel Density Estimator was selected as the P value estimator, corrected for multiple testing using the q-value threshold set at ≤ 0.01 to control the overall FDR. A $\log_2$ fold change cut-off of 0.58 was used to select peptides for protein group quantitation. Cross run global normalisation was enabled, and individual runs were normalised using the median quantities of all peptides selected for normalisation (**Appendix D1**). Furthermore, a principal component analysis (PCA) was conducted using Spectronaut

v19 software (Biognosys Inc) on the dysregulated proteins between the samples. Samples from polarised macrophages (M0, M1 and M2) and those treated with optimised CBD and Tamoxifen were pooled separately and analysed under the previously described conditions. This quality control step ensured that any observed differences were biological and not due to technical factors (**Appendix D2**).

2.5.4. Functional Analysis:

Unpaired comparisons (two-sample t-test) were performed using Spectronaut v19 software (Biognosys Inc), to determine differentially expressed proteins between samples at an FDR of 0.01 (1%) and q-value of 0.01. A list of the dysregulated proteins with corresponding log_2 ratios representing differential abundance (0.01 q-value cut-off) was imported directly into the Cytoscape software (v3.10.2) with the STRING plug-in, to demonstrate network interactions between dysregulated proteins (Doncheva *et al*., 2018). For the STRING analyses, a high-confidence protein interaction score of 0.7 was used and p-values were corrected for multiple testing making use of the Benjamini-Hochberg procedure (Glueck *et al*., 2008; Doncheva *et al*., 2019).

2.6. Assessing the interactions between RAW264.7 macrophages and MCF7 breast cancer cells using fluorescence microscopy and the Griess Reagent

To quantify macrophage phagocytosis of MCF7 breast cancer cells in response to optimised Tamoxifen and/or CBD treatment, a combination of the CellTracker Green CMFDA dye (Thermofisher Scientific, C2925) and Griess reagent assay (ThermoFisher Scientific, G7921) was employed. MCF7 cells with a viability of ~80% were seeded in duplicates in 24-well plates at a density of 5 x 10^4 cells/well and cultured to ~75% confluency. The cells were then labelled with CellTracker Green CMFDA at a concentration of 2.5 µM for 60 minutes in 5% CO_2 at 37°C. Thereafter, the breast cancer cells were washed with PBS, pH 7.4 and co-incubated with 5 x 10^4

RAW264.7 macrophages (M0) (1:1 ratio, RAW264.7:MCF7 cells). The optimal labelling concentration and cell ratio were determined in preliminary experiments (**Appendix E1**) (Wang *et al*., 2013; Jaiswal, 2017; Joshi *et al*., 2018; Candas-Green *et al*., 2020; Sun *et al*., 2022a).

The co-cultures were then treated (according to Table 2.2, section 2.4) with 2 μM Tamoxifen, 5 μM CBD or combination of both, according to treatment model 2 which involved repeated treatments every 24 hours over a 72-hour duration. At 72 hours, phagocytosis was visualised by phase contrast microscopy using an Olympus IX51 microscope with CellSense V11 software, at a wavelength of 488 nm for green fluorescence and overlaid with phase contrast. Additionally, nitrite levels were assessed from supernatants obtained from the co-cultures using the Griess reagent (as per section 2.2). Background nitrite production from MCF7 cells was subtracted from the measured values. Co-cultures with RAW264.7 macrophages stimulated to an M1 phenotype (using 100 ng/ml lipopolysaccharides (LPS) and 20 ng/ml interferon-gamma (IFN-γ)), as per section 2.2, were used as a positive control for phagocytosis (Xu *et al*., 2023).

2.6.1. Data Analysis

Experimentation was conducted three times. Microsoft Excel (version 16.77) was utilised to manage numerical data and generate graphs. Statistical analyses were performed using Statistica (version 14.0.1). The distribution of the data was analysed using the Shapiro-Wilk test of normality. The Kruskal-Wallis One-Way ANOVA by Ranks test was conducted to determine differences in the nitrite production between the treatment groups for co-cultures involving both M0 and M1 macrophage phenotypes. Furthermore, the Mann-Whitney U test was conducted to assess whether the nitrite production was different between co-cultures containing M0 and M1 macrophages. The appropriate post-hoc tests were also performed to determine whether these differences were significant. For all analyses, $p<0.05$ was regarded as statistically significant (**Appendix E2**).

Chapter 3

Results

3.1. Influence of Polarisation Duration on RAW264.7 Macrophage Phenotype

3.1.1. Evaluation of Nitrite Production

Nitrite production, a marker of inducible nitric oxide synthase (iNOS) activity, was quantified in RAW264.7 culture supernatants using the Griess reagent assay (Palmieri *et al*., 2020; Drehmer *et al*., 2022). This spectrophotometric technique relies on a diazotization reaction that was originally described by Griess in 1879 (Palmieri *et al*., 2020; Drehmer *et al*., 2022) In this chemical reaction sulphanilamide and *N*-1-napthylethylenediamine dihydrochloride (NED) are used to convert nitic oxide to nitrite, which can be detected in different biological and experimental matrices such as plasma, urine, and cell culture medium (Palmieri *et al*., 2020; Drehmer *et al*., 2022). Untreated RAW264.7 cells were used as M0 macrophages (DMEM + 10% (v/v) FBS). The M0 macrophages were polarised into an M1 phenotype (using 100 ng/mL LPS and IFN-γ 20 ng/mL) and M2 phenotype (using 20 ng/mL IL-4) for 24, 48 and 72 hours according to previously described methods (section 2.2.)

After polarisation, heterogeneous cell populations were observed across all experimental groups and time points (**Figure 3.1.1 A**). Unstimulated (M0) macrophages maintained a consistent M0 phenotype over the 72-hour period, characterised by the prevalence of rounded cells with smooth surfaces (**Figure 3.1.1. A1-3**). At the 24-hour time point, both stimulated and unstimulated macrophages exhibited similar morphological characteristics, with a predominance of rounded cell shapes (**Figure 3.1.1. A1, A4, A7**). Distinct morphological alterations were observed in the stimulated groups (M1 and M2) at 48 and 72 hours. Compared to the M0 control, LPS and IFN-γ-stimulated cells (M1) exhibited increased cell size and developed dendritic morphologies characterised by extensive surface ruffling and the prominence of pseudopodia and microvilli (**Figure 3.1.1. A4-6**). These morphological changes suggest polarisation of the cells toward an M1 macrophage phenotype. Conversely,

IL-4-treated cells (M2) presented with an enlarged and spread-out morphology, indicative of an M2 macrophage phenotype (**Figure 3.1.1. A7-9**). The results of cellular morphologies presented in Figure 3.1.1 A are consistent with previous findings (McWhorter *et al*., 2013; Wu *et al*., 2014; Heinrich *et al*., 2017; Liang *et al*., 2022).

Quantitative evaluation revealed a progressive increase in nitrite production over time in all macrophage phenotypes. M1 macrophages showed elevated nitrite concentrations compared to M0 and M2 cells across all time-points, specifically at 48 hours following stimulation. However, this difference was not statistically significant ($p>0.05$; **Figure 3.1.1 B**). The M2 phenotype evinced a particularly significant time-dependant increase in nitrite levels, particularly by 72 hours post-stimulation ($p<0.05$; **Figure 3.1.1 B**). Notably, both M1 and M2 groups produced comparable nitrite levels at the 72-hour time point, surpassing those of the M0 control ($p>0.05$; **Figure 3.1.1 B**).

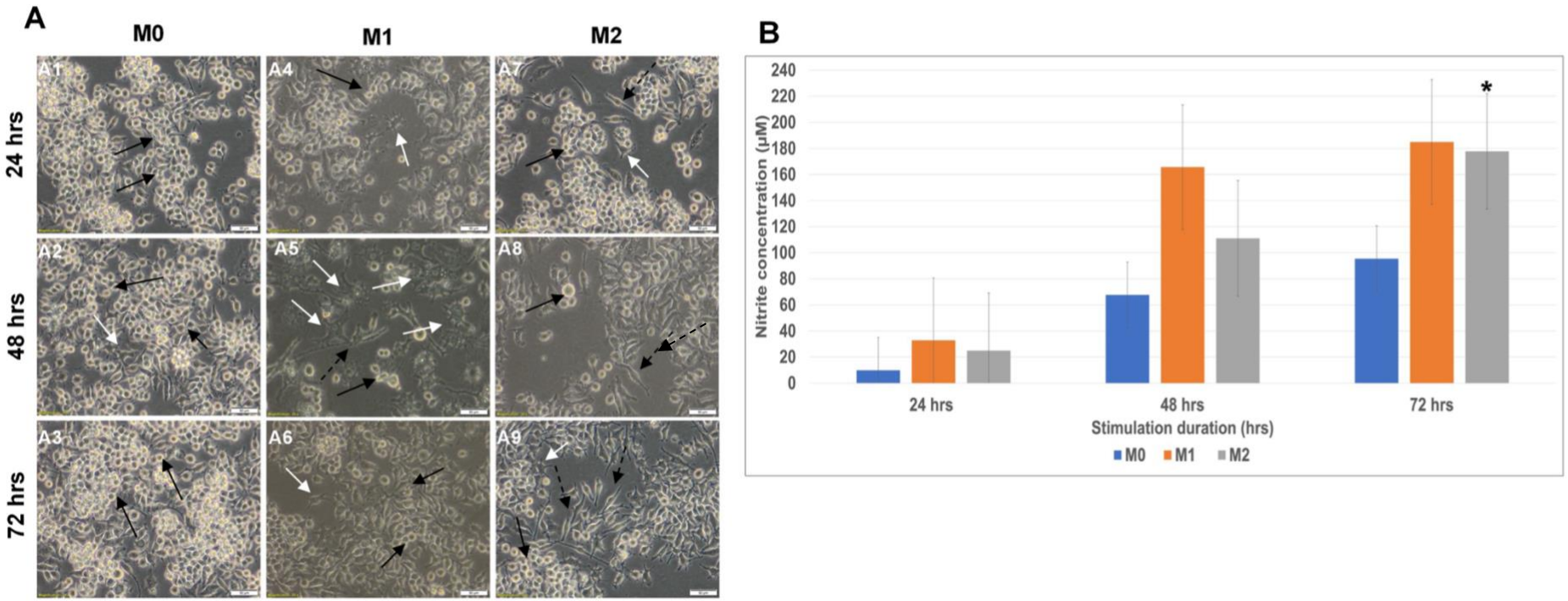


Figure 3.1.1: Impact of duration on the polarisation of M0 RAW264.7 macrophages to the M1 and M2 phenotypes. Key: A) Representative images of RAW264.7 cells following 24, 48 and 72 hours of stimulation; **A1-3)** M0 control – unstimulated cells (DMEM + 10% FBS); **A4-6**) M1 - cells stimulated with LPS (100 ng/mL) and IFN-γ (20 ng/mL); **A7-9**) M2 – cells stimulated with IL-4 (20 ng/ml); **B**) Plot showing nitrite concentration (µM) of stimulated RAW264.7 over a 72-hour period. Error bars indicate the standard error of mean. A heterogeneous population of macrophages was observed across all groups and durations. Unstimulated macrophages (M0) revealed an abundance of rounded cells (solid black arrows) across all time intervals (**A1-3**). Cells stimulated with LPS and IFN-γ (M1) initially evinced an abundance of rounded cells (solid black arrows) and the formation of few dendritic (white arrows) and spindle-shaped (black dashed arrows) cells (**A4**). However, by 48 and 72 hours, the majority of these cells exhibited an activated phenotype characterised by membrane ruffling and pseudopodia formation (white arrows)(**A5-6**). IL-4-treated cells (M2) also demonstrated a shift from a predominantly rounded morphology at 24 hours, to a more spread-out phenotype (black dashed arrows) at 48 and 72-hour time points (**A7-9**). Images captured at 20X magnification (scale bar – 50 µm). A time-dependant increase in nitrite production was observed across all phenotypic group (**B**). This increase was significant in M2 macrophages ($p<0.05$). While M1 macrophages produced higher nitrite levels compared to M0 and M2 cells, particularly at 48 hours, this difference was not statistically significant ($p>0.05$). At 72 hrs both M1 and M2 groups produced comparable and elevated nitrite levels relative to the M0 control, however, this observation was statistically non-significant ($p>0.05$). (*** $p<0.05$ relative to unstimulated cells (M0)**).

3.1.2. Temporal Proteomic Profiling of Macrophage Polarisation

Macrophages are characterised by their remarkable inherent plasticity, which allows them to polarise into distinct phenotypes in response to environmental stimuli both *in vivo* and *in vitro* (Kerneur, Cano and Olive, 2022). Developing *in vitro* models of macrophage polarisation is crucial for understanding their diverse functions and contributions to various physiological and pathological processes (Purcu *et al*., 2022). However, the expression of macrophage markers is significantly influenced by the duration of stimulation (Purcu *et al*., 2022). Therefore, this study employed a time-course proteomic analysis to investigate the dynamic changes in protein expression profiles associated with M0, M1 and M2 polarisation of RAW264.7 macrophages *in vitro*.

Using label-free quantification (FDR of 0.01 (1%) and q-value of 0.01), a total of 85 044 peptides and 6 694 protein groups were identified across all phenotypes (**Figure 3.1.2**). The average numbers of peptides and protein groups in each phenotype following 24, 48 and 72 hours of stimulation are indicated in **Figure 3.1.2**. Principal component analysis (PCA) was performed to visualise the variation among the protein expression profiles of RAW264.7 macrophage phenotypes in response to the different stimulation durations (**Figure 3.1.3 A-C**). Notably, the most striking observation was the clear separation between M0 macrophages and the M1/M2 phenotypes which was observed across all timepoints (**Figure 3.1.3 A-C**). This indicated that the stimulation conditions (LPS and IFN-γ for M1 phenotype, IL-4 for M2 phenotype) and stimulation durations (24, 48 and 72 hours) induced significant changes in the proteomic profiles of the macrophages compared to the unstimulated control (M0).

The first two principal components generated for the 24-hour interval, PC1 (31.11%) and PC2 (22.58%), together accounted for 53.69% of the total variance (**Figure 3.1.3 A**). PC1 primarily drove the separation between the unstimulated M0 macrophages and the stimulated M1/M2 groups. PC2 further distinguished between M1 and M2 phenotypes. While some separation between M1 and M2 groups was observed, there

was significant overlap, indicating that 24 hours of stimulation may not be sufficient for complete and robust polarisation into distinct M1 and M2 phenotypes.

At the 48-hour timepoint a clear separation between M0, M1 and M2 macrophages was observed (**Figure 3.1.3 B)**. PC1 (36.42%) and PC2 (18.12%) both accounting for 54.54% of the total variance, were the primary drivers of this separation. PC1 primarily distinguished unstimulated M0 macrophages from the stimulated M1 and M2 groups, while PC2 further differentiated between M1 and M2 phenotypes. Notably, the protein expression profiles of M1 and M2 cells did overlap at this timepoint. This observation further supports the successful polarisation of RAW264.7 macrophages into M1 and M2 phenotypes upon 48 hours of stimulation, as previously observed in section 5.1.1.

Following 72 hours of stimulation, RAW264.7 macrophages clustered according to the three phenotypes (M0, M1 and M2) (**Figure 3.1.3 C)**. This separation was influenced by PC1 (46.27%) and PC2 (17.22%), together accounting for 63.49% of the total variance. Likewise, PC1 separated unstimulated M0 macrophages from the stimulated M1 and M2 groups, while PC2 differentiated between M1 and M2 phenotypes. Interestingly, the M1 and M2 groups clustered more closely compared to the M0 group, suggesting that stimulation, regardless of the polarisation direction, induces a more similar protein expression profile in these cells compared to the resting M0 state after 72 hours. This observation suggests that 72 hours of stimulation may not be sufficient to fully induce distinct M1 and M2 macrophage phenotypes.

After confirming the polarisation of M0 RAW264.7 macrophages, a comparative proteomic analysis was conducted between M0, M1 and M2 phenotypes at the 48-hour time point (**Figure 3.1.4 A-B**). The analysis revealed significant differences in protein expression profiles among M1 and M2 phenotypes. Compared to the unstimulated macrophages (M0), M1 macrophages revealed dysregulation of 416 proteins, including upregulation of 264 and downregulation of 152 proteins (**Figure 3.1.4 A**). While the differential expression in M2 macrophages (compared to M0) involved a total of 270 proteins with 171 upregulated and 99 downregulated proteins (**Figure 3.1.4 B**). The complete list indicating the differentially expressed proteins within each macrophage phenotype is shown in **Appendix F2**. Notably, as depicted

by the grey nodes in the volcano plots (**Figure 3.1.4 A-B**), a majority of the proteins were not considered significant, primarily due to the stringent FDR and q-value cut-offs. These statistical measures effectively control the false discovery rate, minimising the proportion of false positives among the identified differentially expressed proteins. This provides greater confidence in the biological significance of the observed protein expression differences (Karp *et al*., 2007; Lai, 2017).

Protein-protein interaction network analyses were constructed using the identified differentially expressed proteins (**Figure 3.1.5 A-B**). For M1 macrophages the analysis revealed pathways involved in cellular metabolic processes, regulation of cytokine production, phagocytosis and, ROS and RNS production (**Figure 3.1.5 A**). For M2 macrophages, the differentially expressed proteins were shown to interact with proteins involved in cellular metabolic processes, detoxification of ROS, cell adhesion and migration and, regulation of cell proliferation (**Figure 3.1.5 B**). **Tables 3.1 and 3.2** show some of the proteins involved in the respective pathways regulating the polarisation of RAW264.7 macrophages into M1 and M2 phenotypes.

3.1.3. Determination of Optimal Conditions for Subsequent Experimentation

Nitrite, a stable metabolite of nitric oxide (NO), serves as a key marker of M1 macrophage activation (Palmieri *et al*., 2020; Drehmer *et al*., 2022). Our analysis revealed the highest nitrite production in M1 macrophages at 48 hours, indicative of peak NO production and M1 activation. By contrast, unstimulated (M0) and stimulated M2 macrophages exhibited lower nitrite levels at this time point. Intriguingly, at 72 hours, nitrite production was comparable between M1 and M2 macrophages. This unexpected convergence suggests that prolonged *in vitro* culture conditions can influence macrophage phenotype and function, potentially inducing a phenotypic and functional switch. Consistent with this, proteomic analysis via PCA revealed substantial overlap between M1 and M2 phenotypes at 24 and 72 hours, with M0 macrophages exhibiting some overlaps. This further indicates that full polarisation into distinct M1 and M2 phenotypes may not have been achieved at these times. However, at 48 hours post-stimulation, the PCA plot clearly delineated M0, M1 and M2 phenotypes, confirming successful polarisation and corroborating our functional and

morphological findings. Therefore, to establish well-characterised M1 and M2 populations for subsequent experiments, RAW264.7 cells were stimulated for 48 hours with 100 ng/mL LPS and 20 ng/mL IFN-γ for M1 polarisation, or 20 ng/mL IL-4 for M2 polarisation. This 48-hour stimulation ensures robust and distinct M1 and M2 phenotypes for downstream analyses.

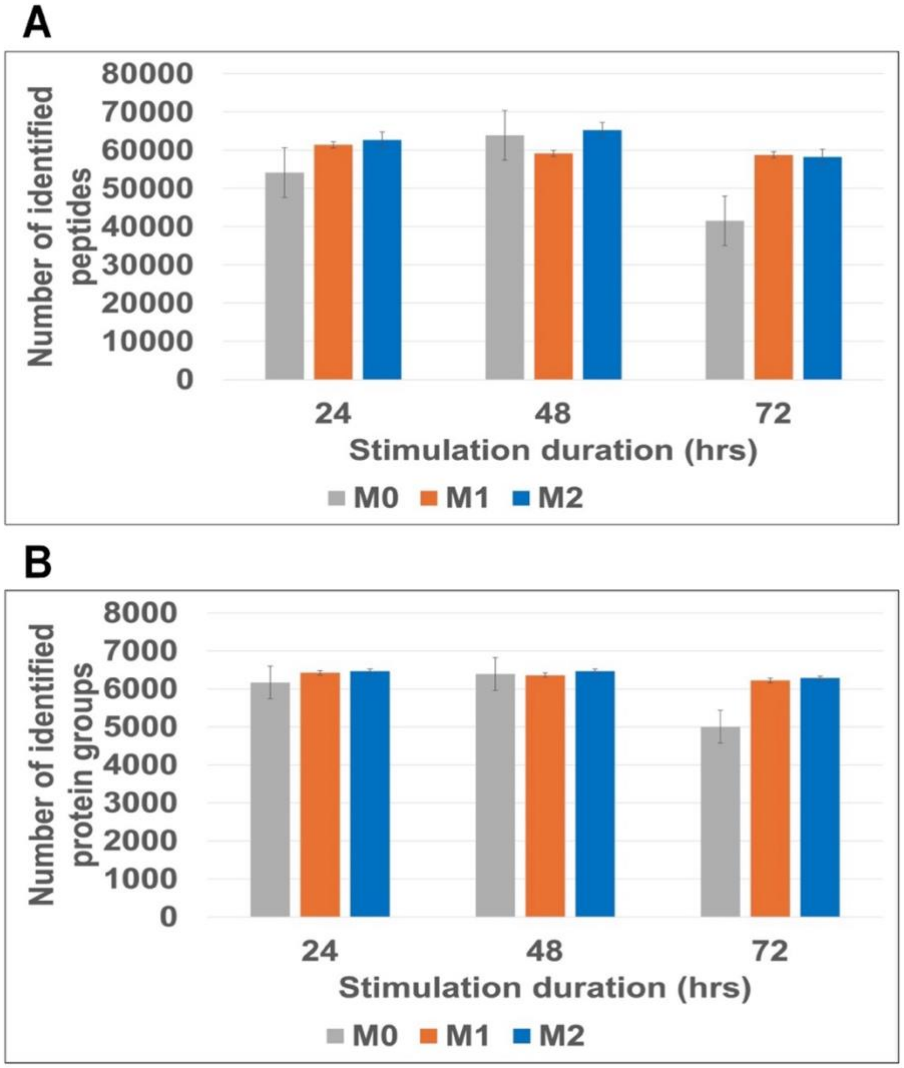


Figure 3.1.2: Overview of identifications from the proteome of M0, M1and M2 RAW264.7 macrophage phenotypes. Bar graphs showing the average number of identified **A)** peptides and **B)** protein groups across triplicates of each phenotypic group. Error bars indicate the standard error of mean.

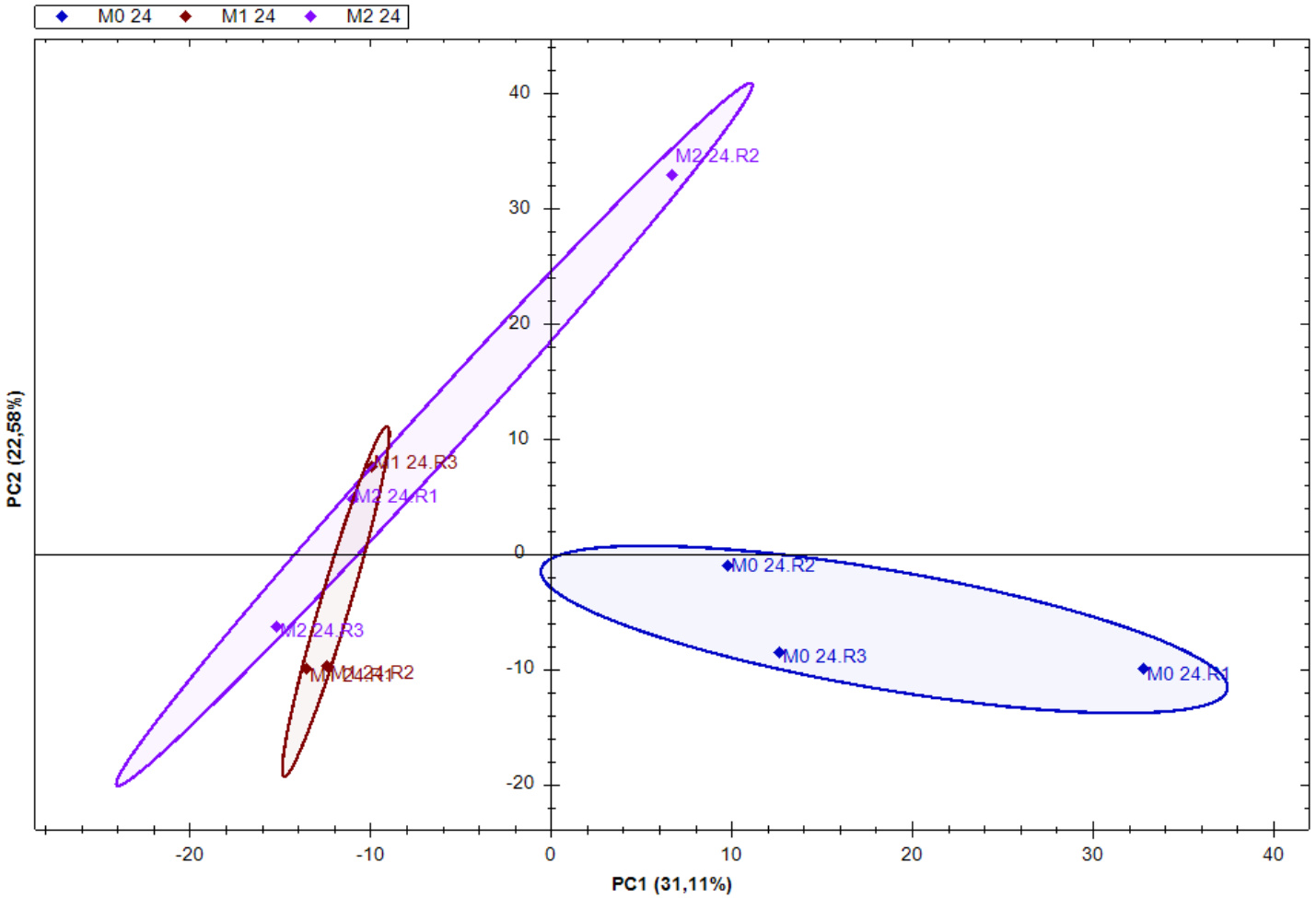


Figure 3.1.3A: PCA plot demonstrating the variation in protein expression among RAW264.7 macrophage phenotypes. Plot representing the relationships between the different RAW264.7 phenotypes (M0, M1 and M2) at 24 hours post-stimulation, based on their principal component scores (R1-R3 represents the triplicates from each group). PC1 explains 31.11% of the total variation, while PC2 explains 22.58%. The cells clustered into different groups according to the macrophage phenotypes (M0, M1 and M2). A clear separation between M0 macrophages and M1/M2 macrophages was observed. M1 and M2 phenotypes demonstrated evident overlap at 24 hours, suggesting inadequate polarisation into the respective phenotypes. Spectronaut v19 software was used to generate the plot using an FDR of 0.01 (1%) and q-value of 0.01.

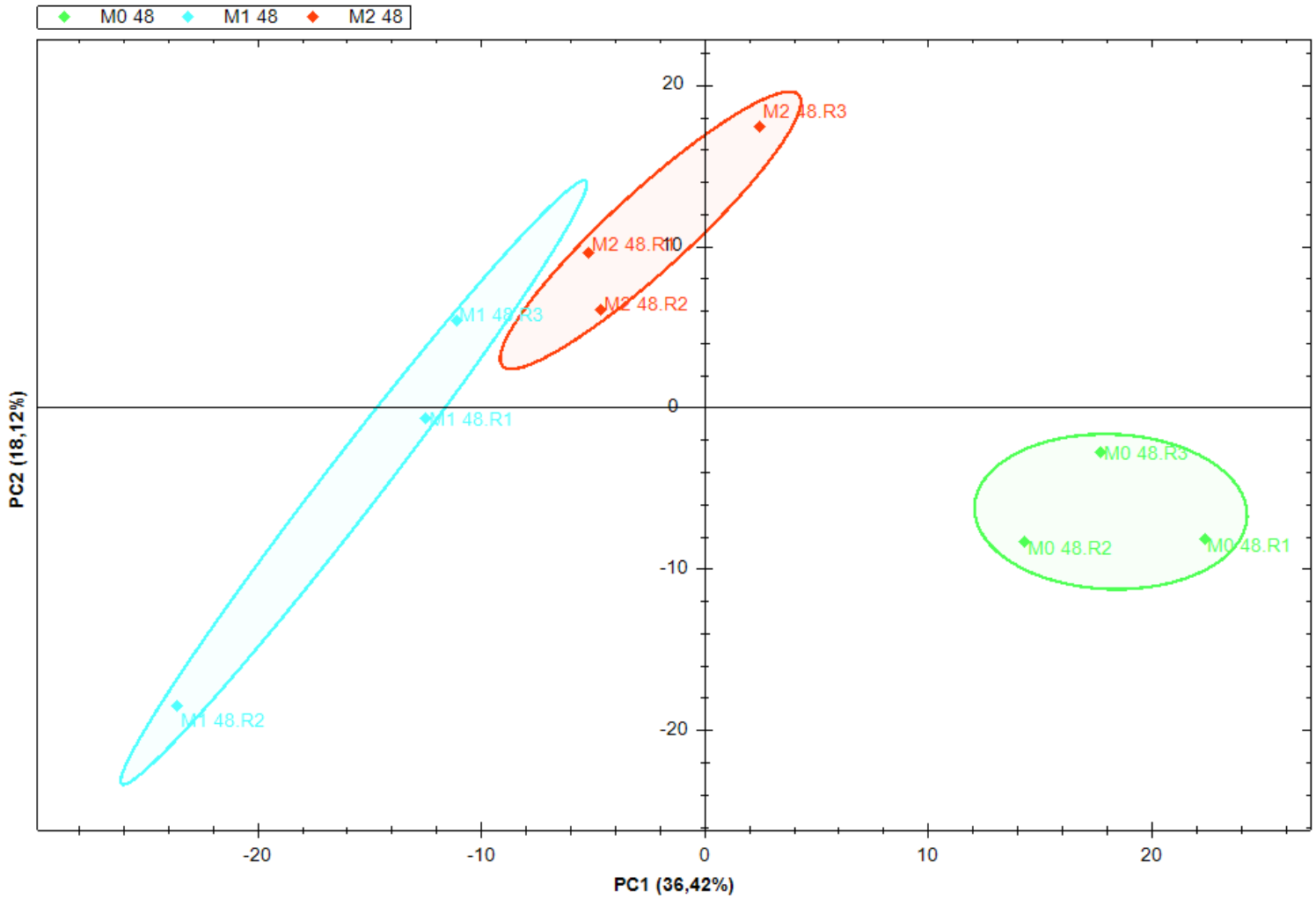


Figure 3.1.3B: PCA plot demonstrating the variation in protein expression among RAW264.7 macrophage phenotypes. Plot representing the relationships between the different RAW264.7 phenotypes (M0, M1 and M2) at 48 hours post-stimulation based on their principal component scores (R1-R3 represents the triplicates from each group). PC1 explains 36.42% of the total variation, while PC2 explains 18.12%. The cells clustered into different groups according to the macrophage phenotypes (M0, M1 and M2). A clear separation between M0 macrophages and M1/M2 macrophages was observed. At 48 hours, a clear distinction is seen between M1 and M2 phenotypes, suggesting successful polarisation. Spectronaut v19 software was used to generate the plot using an FDR of 0.01 (1%) and q-value of 0.01.

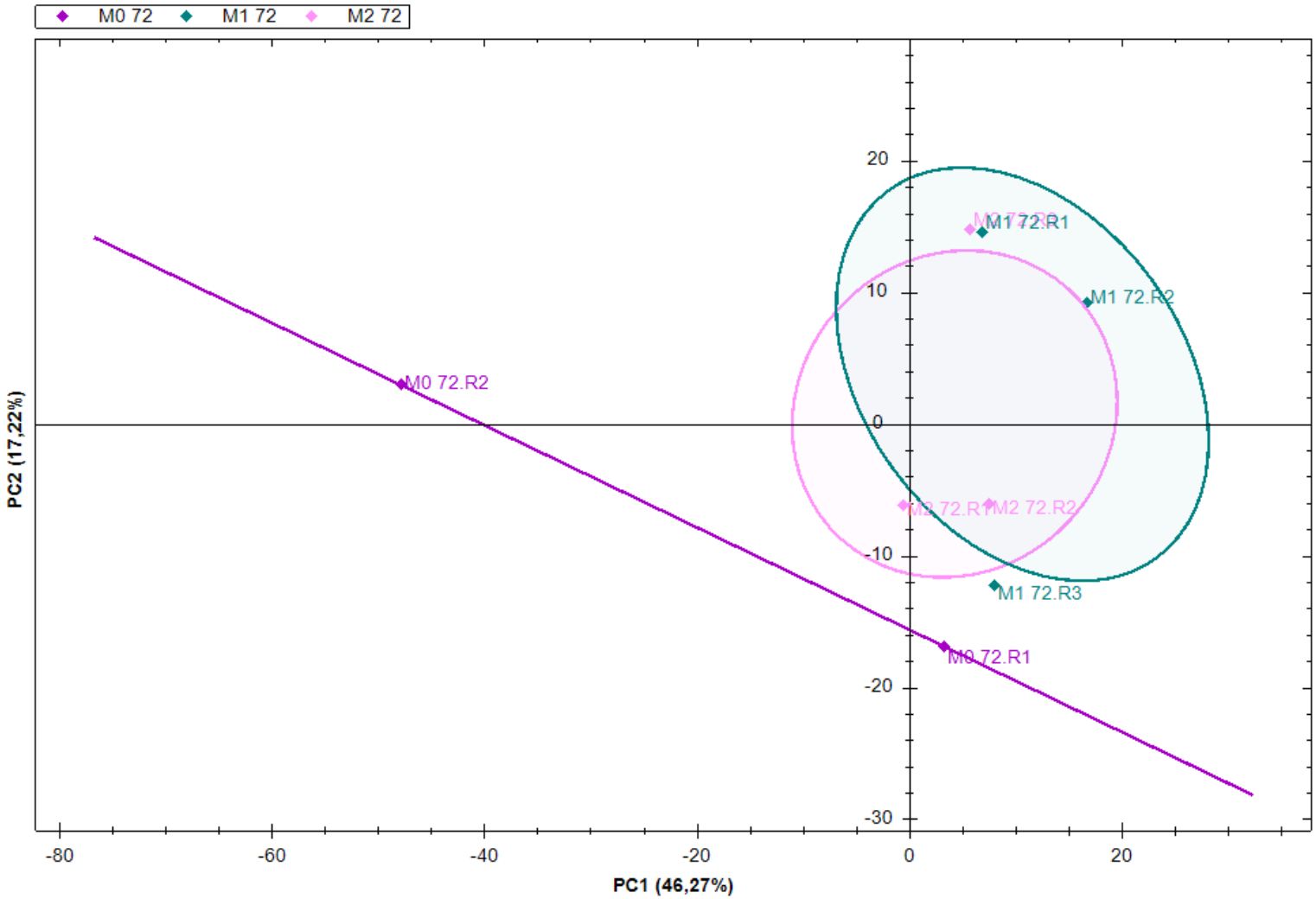


Figure 3.1.3C: PCA plot demonstrating the variation in protein expression among RAW264.7 macrophage phenotypes. Plot representing the relationships between the different RAW264.7 phenotypes (M0, M1 and M2) at 72 hours post-stimulation based on their principal component scores (R1-R3 represents the triplicates from each group). PC1 explains 46.27% of the total variation, while PC2 explains 17.22%. The cells clustered into different groups according to the macrophage phenotypes (M0, M1 and M2). A clear separation between M0 macrophages and M1/M2 macrophages was observed. M1 and M2 phenotypes clustered more closely compared to M0 macrophages, suggesting insufficient polarisation at this time point. Spectronaut v19 software was used to generate the plot using an FDR of 0.01 (1%) and q-value of 0.01.

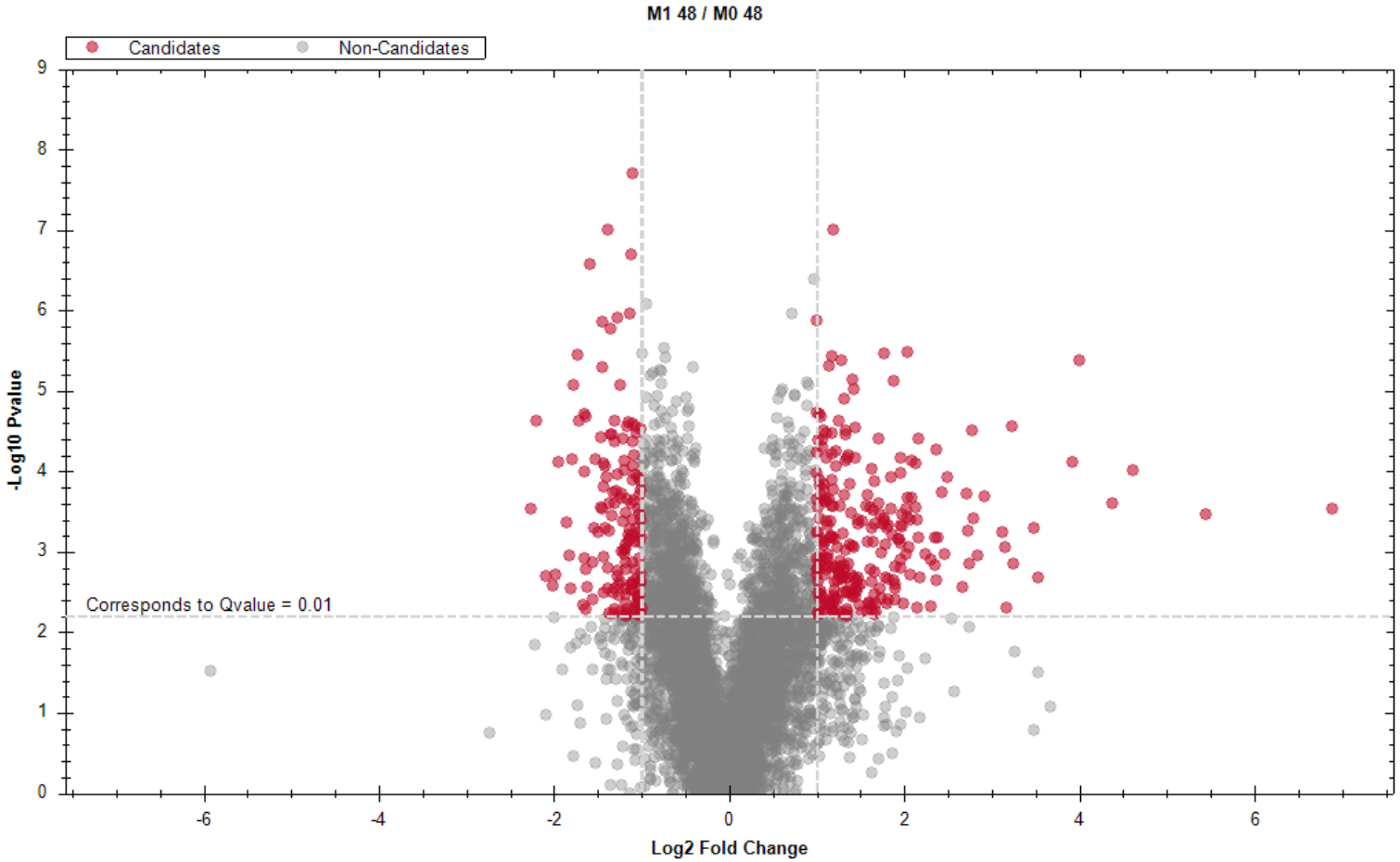


Figure 3.1.4A: Volcano plot demonstrating the differential protein expression among RAW264.7 macrophage phenotypes. Plots indicates the dysregulated proteins in M1 macrophages (compared to M0) following polarisation over 48 hours; X-axis shows the log_2 fold change; Y-axis shows the significance ($-log_{10}$ p-value). Red nodes - significantly dysregulated proteins between the macrophage phenotypes, those located in the negative x-axis are significantly downregulated and those in the positive x-axis are significantly upregulated. Grey nodes indicate proteins that exhibited no significant changes in protein expression. Spectronaut v19 software was used to generate the plot using an FDR of 0.01 (1%) and q-value of 0.01.

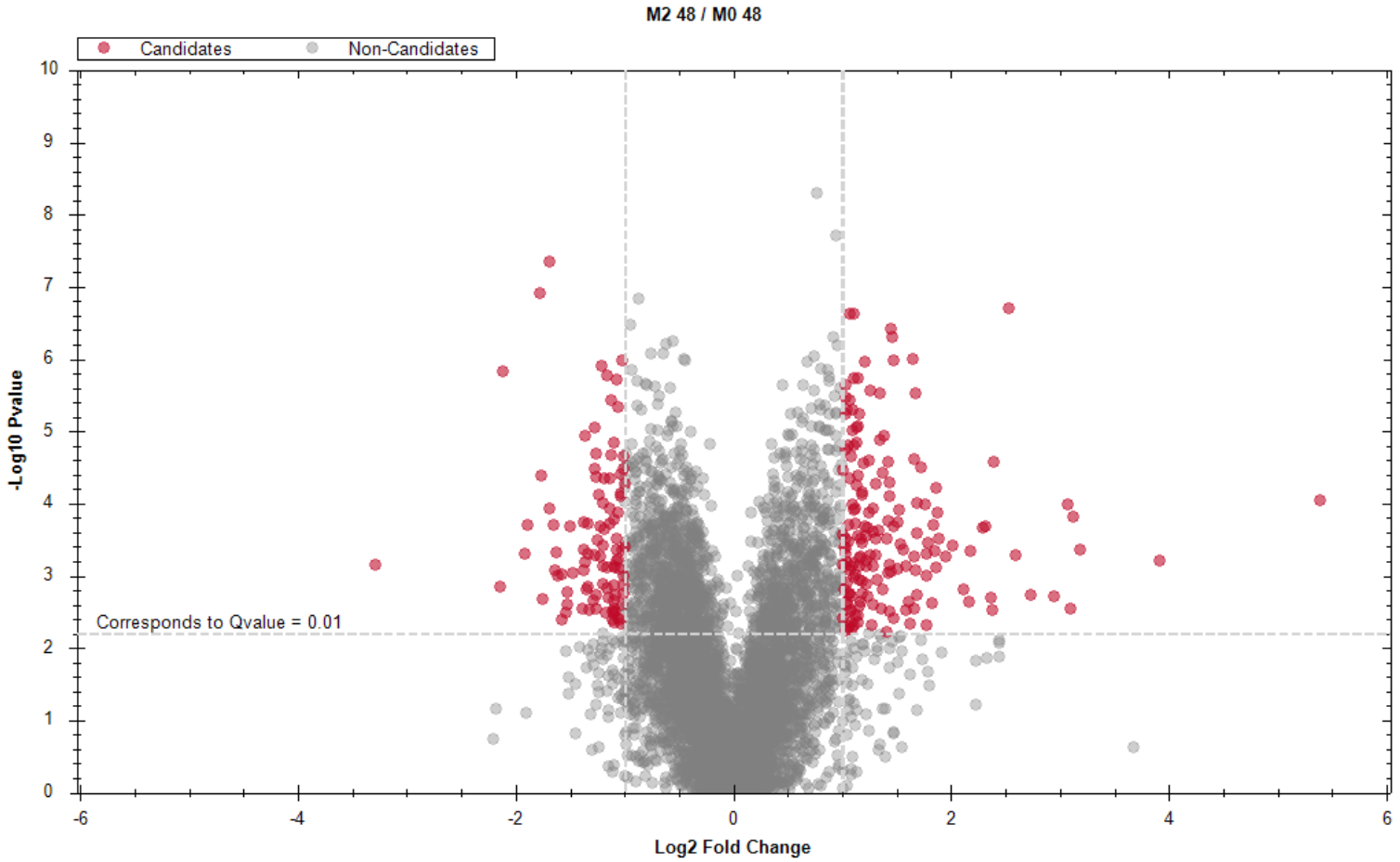


Figure 3.1.4B: Volcano plot demonstrating the differential protein expression among RAW264.7 macrophage phenotypes. Plots indicates the dysregulated proteins in M2 macrophages (compared to M0) following polarisation over 48 hours; X-axis shows the $\log_2$ fold change; Y-axis shows the significance ($-\log_{10}$ p-value). Red nodes - significantly dysregulated proteins between the macrophage phenotypes, those located in the negative x-axis are significantly downregulated and those in the positive x-axis are significantly upregulated. Grey nodes indicate proteins that exhibited no significant changes in protein expression. Spectronaut v19 software was used to generate the plot using an FDR of 0.01 (1%) and q-value of 0.01.

Table 3.1: The enriched pathways and proteins M1 polarised RAW264.7 macrophages (relative to M0 phenotype)

Pathway name	False discovery rate (FDR)	Proteins within pathway
Cellular metabolic processes	1.31×10^{-10}	HXK3, GLPK, PA1B3, PAFA2, APOBR
Regulation of cytokine production	9.50×10^{-4}	IFI2, IFI20, IFI5B, IFM3, OASL1, ISG15, GBP3, C/EBPβ, CCL2, IRG1, PAI2, PTGS2
Phagocytosis	1.12×10^{-2}	CD44, FCGR1, FCGR2, FCGR3, MSR1, H2-L, ITA5, ITAL, HS74L
ROS and RNS production	4.38×10^{-2}	CY24A, RETR1, RN185, CATL1, GBA1, TAP2, TPSN

Table 3.2: The enriched pathways and proteins M2 polarised RAW264.7 macrophages (relative to M0 phenotype)

Pathway name	False discovery rate (FDR)	Proteins within pathway
Cellular metabolism	1.31×10^{-10}	PGH2, DEGS1, AMPD3,UPP1
Detoxification of ROS	8.00×10^{-3}	ARGI2, GSTP1, PRDX1, PRDX5, SODM, CY24A, NCF4, ERO1A
Cell adhesion	3.52×10^{-2}	ITAM, FYB1, ZYX, CATD
Cell migration	1.80×10^{-4}	ANXA3, GRN, MEF2C, P2RX4
Regulation of cell proliferation	8.40×10^{-3}	B2CL1, GBG2, HMGA1, HMGA2

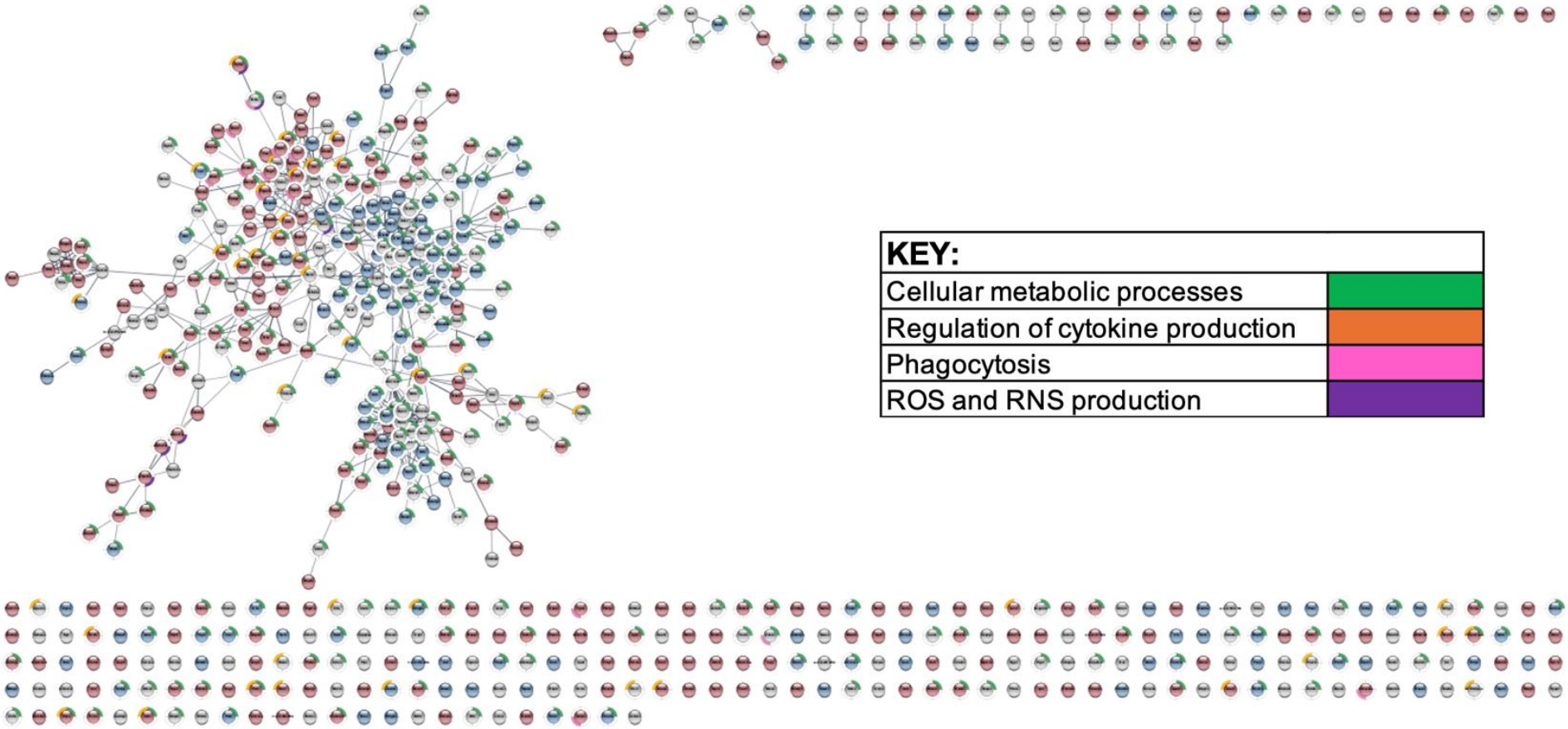


Figure 3.1.5A: String-enrichment analysis. Plot shows protein-protein interactions between differentially expressed proteins in the M1 RAW264.7 macrophage phenotype compared to M0, following 48 hours of stimulation with IFNγ and LPS. Nodes: blue indicates downregulation, red indicates upregulation, grey indicates no significant difference in protein expression following stimulation. Singleton proteins (shown at the bottom) do not directly interact with other identified proteins but contribute to the enriched pathways. Key shows respective pathways proteins are involved in. Cytoscape software (v3.10.2) was used to generate pathway, with an FDR of 0.01 (1%) and high-confidence protein interaction score of 0.7 was used (Doncheva *et al*., 2019).

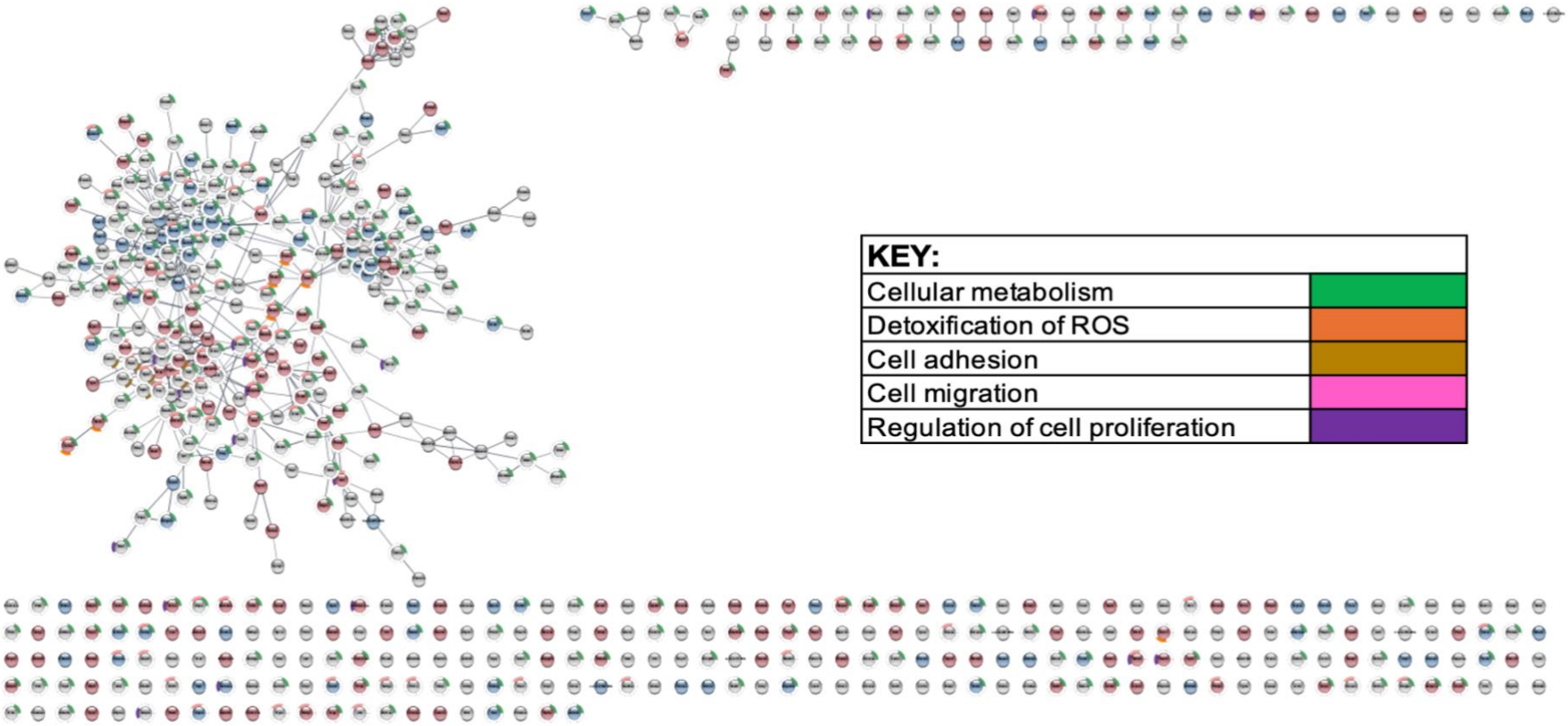


Figure 3.1.5B: String-enrichment analysis. Plot shows protein-protein interactions between differentially expressed proteins in the M2 RAW264.7 macrophage phenotype compared to M0, following 48 hours of stimulation with IL-4. Nodes: blue indicates downregulation, red indicates upregulation, grey indicates no significant difference in protein expression following stimulation. Singleton proteins (shown at the bottom) do not directly interact with other identified proteins but contribute to the enriched pathways. Key shows respective pathways proteins are involved in. Cytoscape software (v3.10.2) was used to generate pathway, with an FDR of 0.01 (1%) and high-confidence protein interaction score of 0.7 was used (Doncheva *et al*., 2019).

3.2. The Cytotoxic Effects of CBD and Tamoxifen against MCF7 Cells

Following the establishment of the polarisation protocol for distinct M1 and M2 macrophage phenotypes, subsequent experiments investigated the effects of CBD and Tamoxifen on both MCF7 breast cancer cells and RAW264.7 macrophages. Treatment conditions were initially optimised in MCF7 cells, consistent with standard anticancer drug screening practices (Olivas-Aguirre *et al*., 2022). The impact of the optimised treatments on macrophage-breast cancer cell interactions was also explored.

3.2.1. Effects of CBD and Tamoxifen on Cell Viability

The combined effects of CBD and Tamoxifen on the cell viability of MCF7 cells were assessed using the Neutral red assay. This method measures the ability of viable cells to accumulate the Neutral red dye within lysosomal compartments (Gomez-Gutierrez *et al*., 2021). Morphological assessments exhibited robust uptake of the dye in control cells (media and diluent controls) over time in both treatment models 1 (single dose, prolonged treatment) model 2 (daily dose, repeated treatment) (**Figure 3.2.1 A1 - A6, B1 - B6**). These densely populated cells exhibited typical adherent, spindle-shaped morphology, with distinct cytoplasmic and nuclear boundaries (**Figure 3.2.1 A1 - A6, B1 - B6**). A decrease in cell density and viability was observed when cells were under the single treatments of Tamoxifen (**Figure 3.2.1 C1-C6**) and CBD (**Figure 3.2.2**), and when Tamoxifen treatment was combined with CBD (**Figure 3.2.3**). These qualitative observations were supported by the quantitative assessment of Neutral red uptake (**Figure 3.2.4**).

Negligible effects of the diluent (0.4% methanol) on MCF7 cell viability were noted in both treatment models across time ($p>0.05$, **Figure 3.2.4**), whereas exposure to Tamoxifen and CBD, individually or in combination, elicited variable cellular responses indicative of cell stress and death (**Figure 3.2.1 – 3.2.4**). While no overt differences in both cell morphology and viability were apparent at the 24-hour timepoint, subsequent assessments at 48 and 72 hours revealed distinct trajectories for the two treatment models under CBD and Tamoxifen treatment (**Figure 3.2.1 – 3.2.4**). Even though

morphologies consistent with cell stress, including cell shrinkage were present, cells exposed to treatment model 1, in which only a single dose of treatment was administered and prolonged over 72 hours, exhibited signs of recovery across all treatment groups by 48 and 72 hours. These signs were characterised by increased cell density and improved viability, particularly in cells treated with 5 µM CBD or 2 µM Tamoxifen over 72 hours ($p<0.05$; **Figure 3.2.1 - 3.2.4**). However, cells at higher doses of 7.5 µM and 10 µM showed some recovery till 48 hours and plateaued thereafter (**Figure 3.2.2 - 3.2.4**). When 2 µM Tamoxifen was combined with CBD, the cell viability percentage was lower than the single treatments, with 2 µM Tamoxifen and 10 µM CBD significantly reducing cell viability by 72 hours, compared to the diluent control ($p<0.05$; **Figure 3.2.4**). Thus, indicating that higher doses of CBD induced higher levels of cytotoxicity.

MCF7 cells under treatment model 2, in which treatment was repeated daily over 72 hours, displayed progressive morphological alterations that were accompanied by a dose-dependent decline in cell viability across all treatment groups (**Figure 3.2.1 - 3.2.4**). Morphological changes included shrinkage of cells causing them to appear more rounded, loss of cell-cell adhesion, accumulation of cell debris because of dead cells and increased intercellular spaces due to cell loss (**Figure 3.2.1 - 3.2.3**). Cell viability percentages were notably reduced relative to the diluent control for all single and co-treatments for treatment model 2 (**Figure 3.2.4**). These reductions were significant by 72 hours in cells treated with 2 µM Tamoxifen alone and in combination with 7.5 µM and 10 µm CBD ($p<0.05$, **Figure 3.2.4**). Additionally, treatment with 10 µM CBD alone and in combination with 2 µM Tamoxifen significantly reduced cell viability relative to the diluent control at 72 hours ($p<0.05$; **Figure 3.2.4**). Notably, no significant differences in cytotoxicity were observed between the two treatment models across the different time points, but the trend indicated that cell recovery occurred in treatment model 1 which was not evident in cells treated according to model 2.

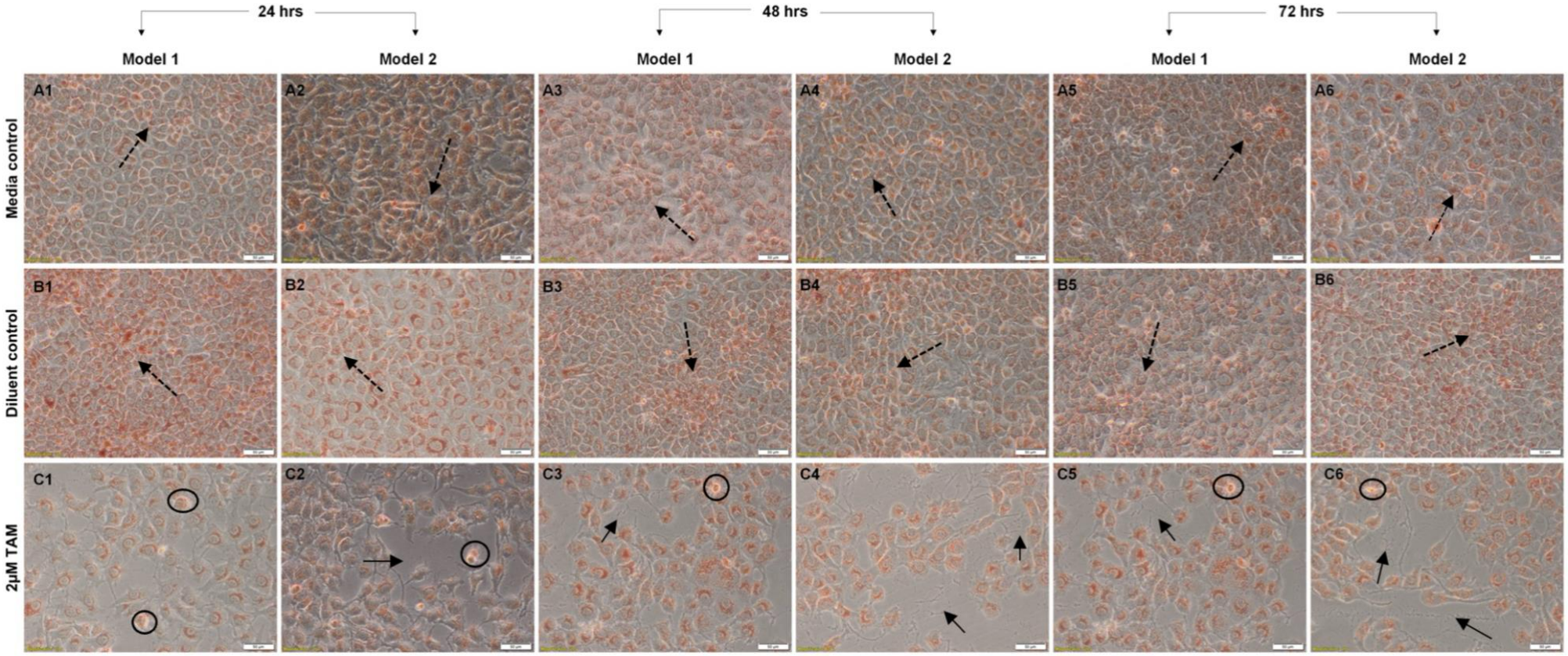


Figure 3.2.1: Representative images showing Neutral red Uptake by MCF7 cells in control groups and 2 μM Tamoxifen. Treatment models 1 and 2 showed positive staining for the Neutral red dye across the different time points (24, 48 and 72 hours), in controls (media and diluent), and cells treated with 2 μM Tamoxifen (2 μM TAM). Control cells maintained a healthy adherent morphology with distinct cytoplasmic and nuclear boundaries. Cell density increased over time, leading to clumping (dashed black arrows) (**A1-A6; B1-B6**). Cells exposed to 2 μM Tamoxifen in treatment model 1 exhibited signs of recovery over time, shown by the increase in cell density (**C1, C3, C5**). While cells in treatment model 2 demonstrated a progressive loss in cell number, indicated by intercellular spaces and cell debris (solid black arrows) (**C2, C4, C6**). Additionally, cell shrinkage (encircled) was evident, indicating cell death (**C2, C4, C6**). Images were captured at 20X magnification (scale bar – 50 μm).

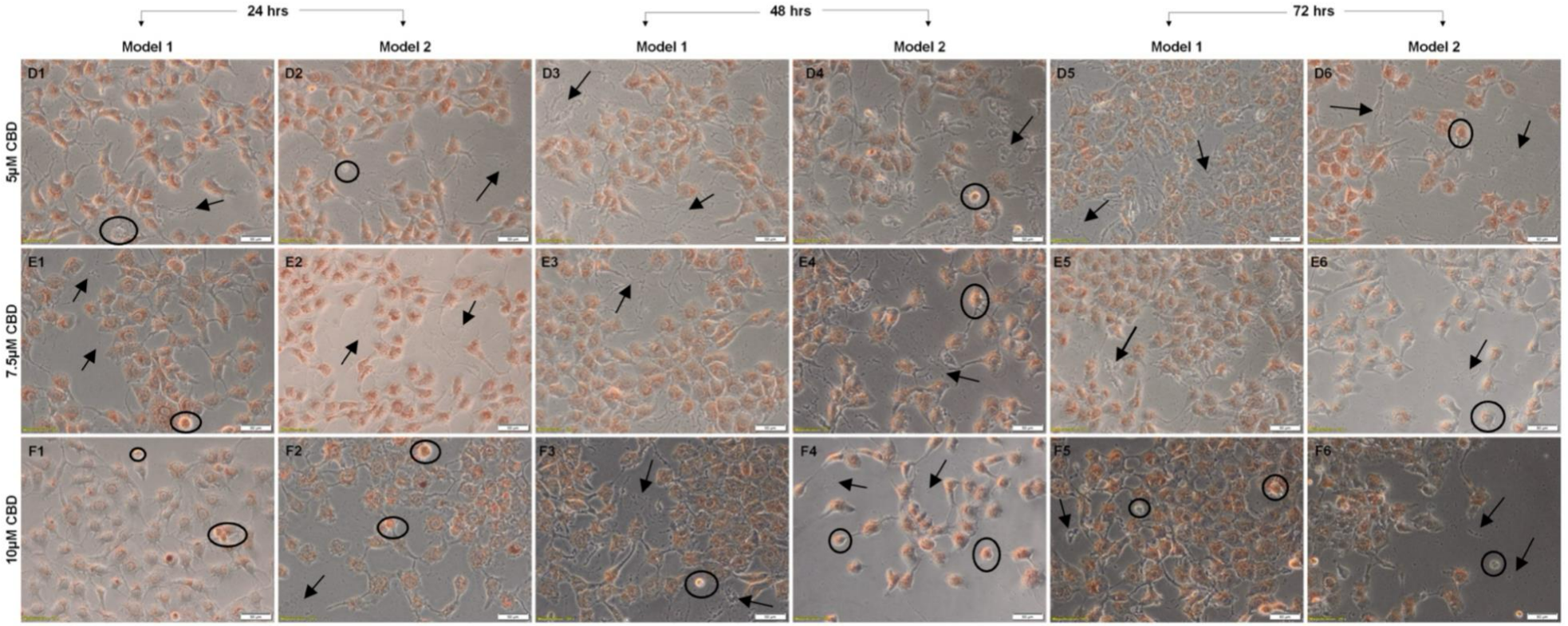


Figure 3.2.2: Representative images showing Neutral red Uptake by MCF7 cells treated with increasing concentrations of CBD. Neutral red staining was evident for all CBD concentrations across the treatment models and time intervals. By 72 hours of treatment, cells exposed to treatment model 1 for all the three concentrations (5, 7.5 and 10 μM) revealed an increase in cell density and less evident signs of cell death (membrane blebbing, shrunken cells) (**D5, E5**, **F5**). Cells under treatment model 2, exhibited a dose-dependent decrease in cell density across time which led to properties of cell death including rounded cells (encircled) and intercellular spaces with cell debris (solid black arrows) (**D-F**). Images captured at 20X magnification (scale bar – 50 μm).

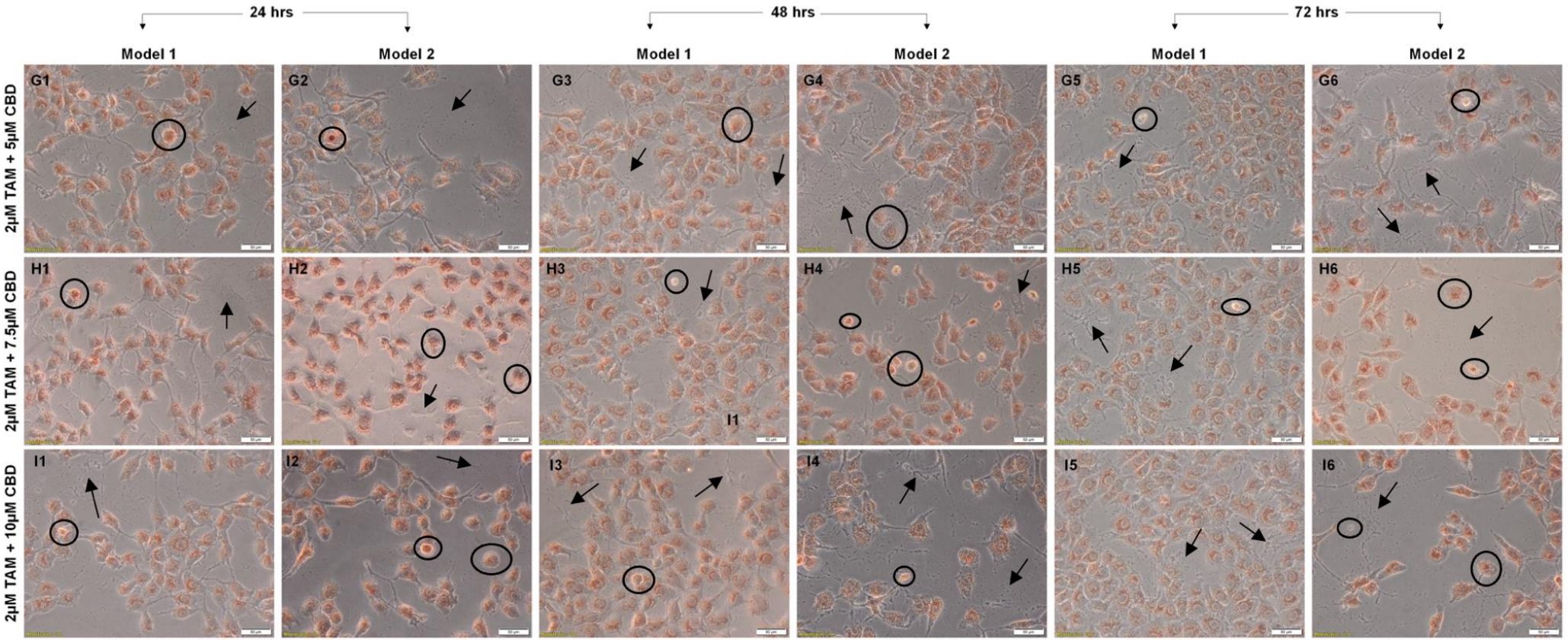


Figure 3.2.3: Representative images showing Neutral Red Uptake by MCF7 cells treated with CBD and Tamoxifen. Red cytoplasmic staining, indicating uptake of the Neutral Red dye was observed for the co-treatments across the treatment models and time points. All the treatment groups showed characteristics of cell death (**G-I**). By 48 and 72 hrs, cells in treatment model 1 presented signs of recovery characterised by increased cell density (**G3, H3, I3, G5, H5, I5**). Treatment with CBD and Tamoxifen using model 2 induced a dose-dependent and time-dependent reduction in cell density (**G2, H2, I2; G4, H4, I4; G6, H6, I6**). Signs of cell death were more apparent in this model, indicated by rounded up cells (encircled) and, cell debris or dead cells (solid black arrows). Images captured at 20X magnification (scale bar – 50 µm).

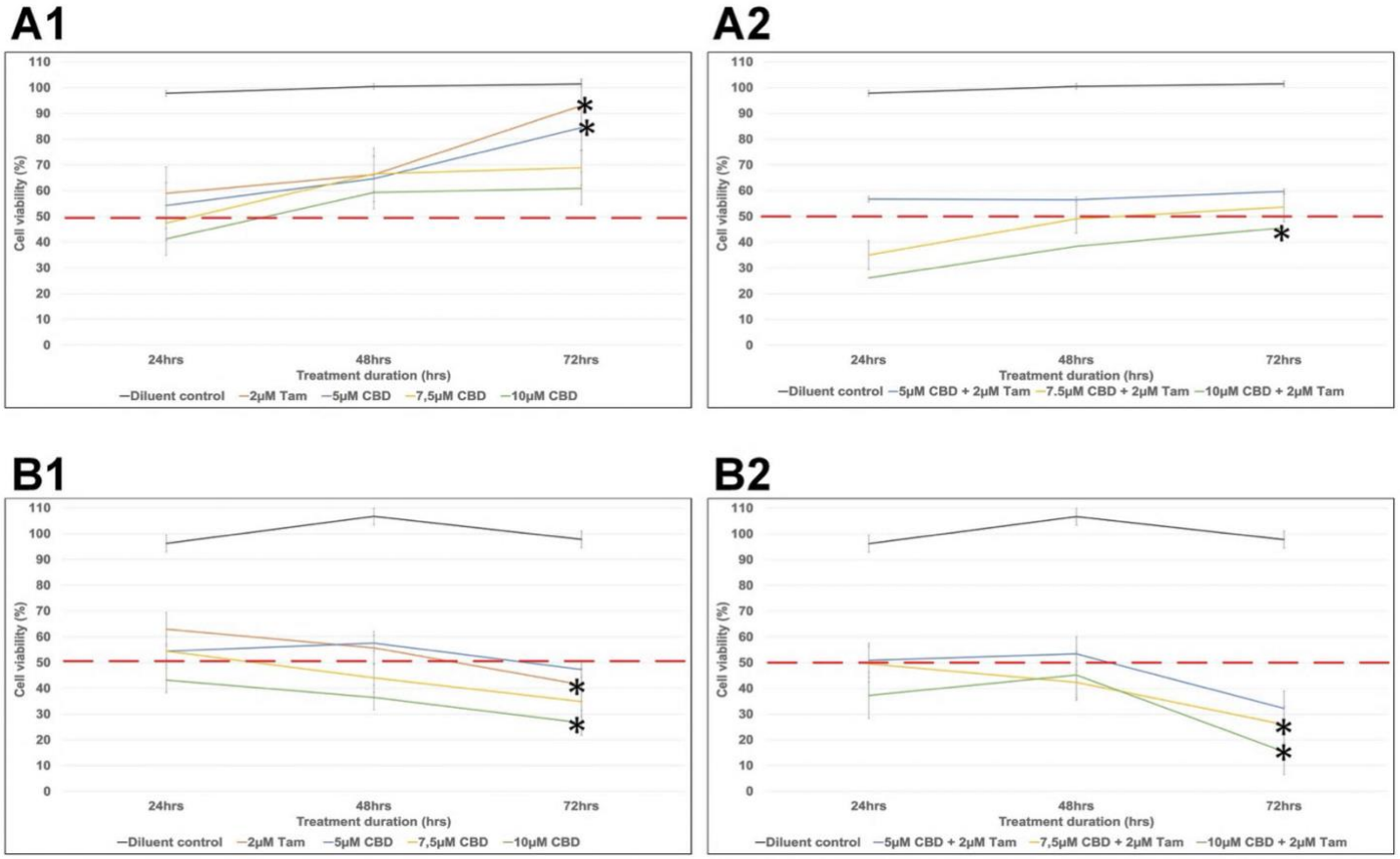


Figure 3.2.4: Graphical representations of changes in cell viability of MCF7 cells treated with CBD and Tamoxifen across time. Key: A) Treatment model 1; **B)** Treatment model 2; **1)** CBD alone; **2)** CBD + Tamoxifen. Y-axis – Cell viability (%), X-axis – Treatment duration (hrs). The red dashed lines represent the IC_{50} of treatment. Error bars indicate the standard error of mean. In both treatment models, cells exposed to the diluent control (0.4% methanol) maintained cell viabilities close to 100%. Cells under treatment model 1 exhibited an increase in cell viability over time, which was significant in cells treated with 5 μM CBD alone ($p<0.05$; **A1-2**). Cells treated with 2 μM Tamoxifen alone and in combination with 10μM CBD revealed a significant increase in cell viability compared to the diluent control ($p<0.05$; **A1-2**). Treatment model 2 displayed a dose-dependent decline in cell viability across the time points (**B1-2**). Statistical analyses indicated significant reductions in cell viability for 2 μM Tamoxifen alone, 10 μm CBD alone and, the 7 μM and 10 μm co-treatment groups ($p<0.05$; **B1-2**). Treatment with 10μM CBD alone and in combination with Tamoxifen also significantly reduced cell viability relative to the diluent control ($p<0.05$; **B1-2**). No significant differences in cytotoxicity were observed between the two treatment models across the different time points (*** p<0.05 relative to the diluent control**).

3.2.2. Effects of CBD and Tamoxifen on Growth Inhibition

Growth inhibition in response to CBD and Tamoxifen treatment was quantified using the 3-(4,5-Dimethylthiazol-2-yl)-2,5-diphenyltetrazolium bromide (MTT) assay. This colorimetric technique detects the reduction of MTT to formazan in active mitochondria of viable cells and has been used successfully to quantitate cell survival and proliferation (Shahneh *et al.,* 2013; Suttithumsatid, Sukketsiri and Panichayupakaranant, 2023). Control groups (diluent) in both treatment models exhibited stable proliferative patterns across time. Consistent with the Neutral red assay, the diluent (0.4% methanol) had no significant impact on cell growth (**Figure 3.2.5**). MCF7 cells exposed to serum-free media (SFM) served as a baseline for minimal growth conditions and findings indicate that SFM did not induce substantial reductions in cellular growth (**Figure 3.2.5**). Conversely, Triton-X-100 (0.1%), served as a positive control for cytotoxicity and findings show that cellular exposure to 0.1% Triton-X-100 markedly inhibited cell growth, with a significant effect in treatment model 2 ($p<0.05$; **Figure 3.2.5 B**).

The growth inhibition induced by CBD and Tamoxifen, administered individually or in combination diminished over time in treatment model 1, where cells were given a single dose of treatment over 72 hours (**Figure 3.2.5 A**). These results confirmed the results of the Neutral red assay, where cellular recovery was observed over the 72-hour treatment period. Notably, the cytotoxic effects of 2 µM Tamoxifen were significantly attenuated relative to the potent cytotoxic control, Triton-X-100 (0.1%) following 72 hours of treatment ($p<0.05$; **Figure 3.2.5 A**). This indicated substantive cell recovery. Furthermore, the diluent exhibited significantly lower growth inhibitory properties than Triton-X-100 over 72 hours in both models ($p<0.05$; **Figure 3.2.5**). In contrast, in treatment model 2, in which cells were given repeated doses of treatments every 24 hours over a 72-hour period, there was a progressive increase in growth inhibition across all treatment groups (**Figure 3.2.5 B**). The combination of 2 µM Tamoxifen with 5 µM CBD or 7.5 µM CBD significantly inhibited cell growth at 72 hours ($p<0.05$; **Figure 3.2.5 B**). No significant differences in growth inhibition were observed between the two treatment models across the different time points, however, the trend indicated that cells were able to recover from the single prolonged exposure of

treatment (model 1) more rapidly than from repeated doses (model 2) of treatment over 72 hours.

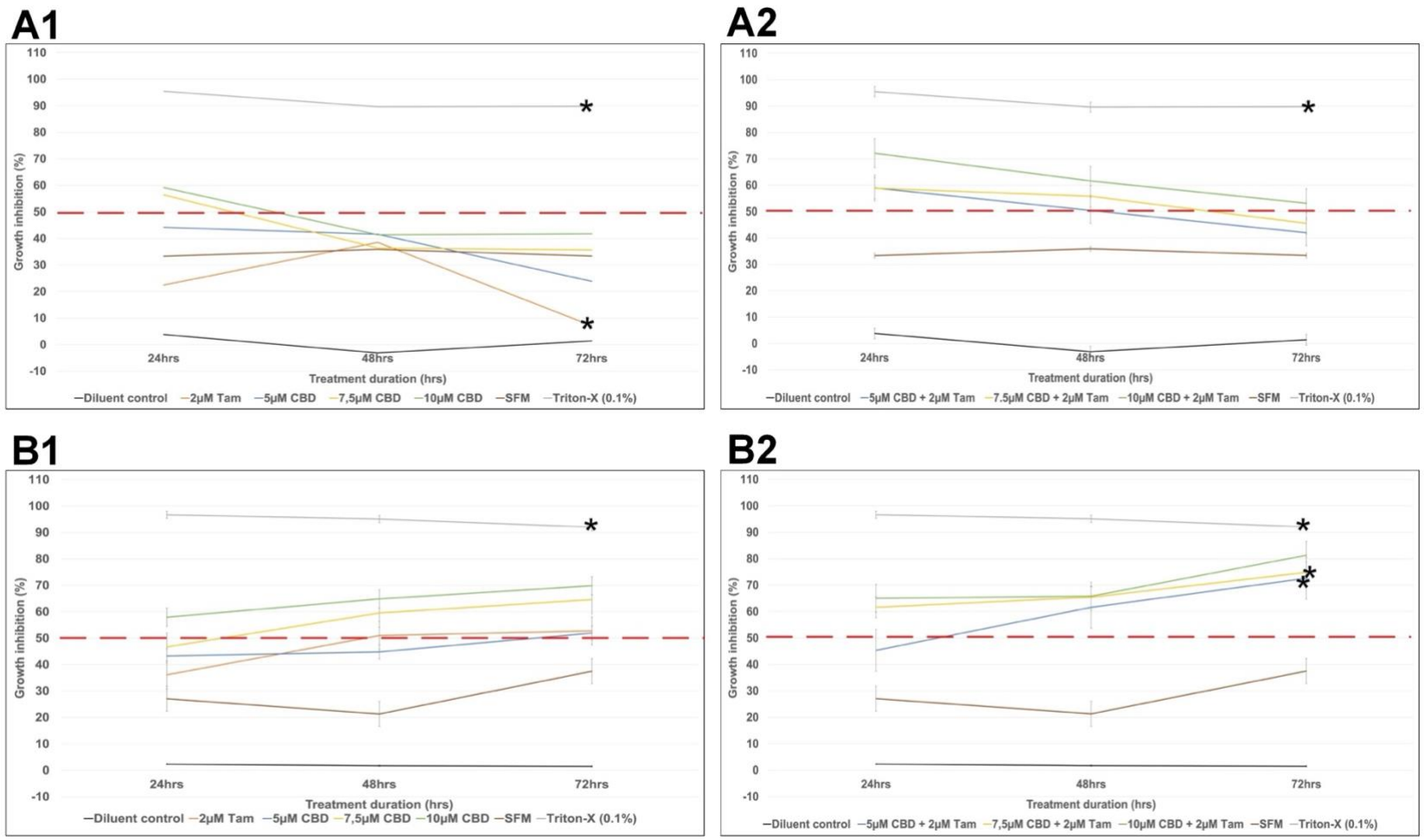


Figure 3.2.5: Graphical representations of changes in growth inhibition of MCF7 cells treated with CBD and Tamoxifen across time. Key: A) Treatment model 1; **B)** Treatment model 2; **1)** Single control treatments; **2)** CBD + Tamoxifen combined treatments. Y-axis – Growth inhibition (%), X-axis – Treatment duration (hrs). The red dashed lines represent the IC_{50} of treatment. Error bars indicate the standard error of mean. Control groups in both treatment models revealed similar proliferative trends across time. The diluent and serum-free media (SFM) had no significant effects on cell growth, while Triton-X significantly inhibited cell growth in both treatment models by 72 hours ($p<0.05$). In model 1, CBD alone and in combination with Tamoxifen resulted in growth inhibition, but cell recovery was evident by 72hours (**A1-2**). However, the cytotoxic effects of 2 μM Tamoxifen were significantly attenuated ($p<0.05$; **A1-2**). In treatment model 2, a dose-dependent increase in growth inhibition was evident across all treatment groups. The combination of 2 μM Tamoxifen with 5 μM CBD or 7.5 μM CBD significantly inhibited cell growth ($p<0.05$; **B1-2**) (*** p<0.05 relative to the diluent control**).

3.2.3. Determination of Optimal Conditions for Subsequent Experimentation

To optimise CBD treatment conditions, we considered the balance between inducing cytotoxic effects and allowing for the observation of long-term cellular responses. As previously observed, CBD concentrations used in single treatments and in combination with 2 μM Tamoxifen induced cell recovery in MCF7 cells in treatment model 1 (single dose, prolonged exposure to treatment) by 72 hours. However, in treatment model 2 (daily dose, repeated treatment), increasing CBD concentrations (5, 7.5, 10 μM) progressively reduced cell viability and increased growth inhibition over time.

Based on these findings, treatment model 2 was selected for further experiments. A concentration of 5 μM CBD, both alone and in combination with 2 μM Tamoxifen, demonstrated suboptimal cytotoxicity across time and at 72 hours, by reducing cell viability and inhibiting growth by approximately 50% at 72 hours. This concentration allowed for the observation of cellular behaviour while maintaining a therapeutically relevant cytotoxic effect *in vitro*. Therefore, it was deemed to be the most suitable concentration and time period to study the effects of CBD and Tamoxifen in this study

To further support this finding, IC_{50} values calculated across the different time points (**Appendix C3**), quantitatively assessed the potency of CBD alone and in combination with 2 μM Tamoxifen. The lowest IC_{50} values for both CBD alone and in combination with Tamoxifen were observed in treatment model 2 at 72 hours (**Appendix C3**). This suggests that a 72-hour treatment regimen combining 5 μM CBD and 2 μM Tamoxifen, with daily replacement (model 2), may offer a synergistic effect with Tamoxifen without inducing excessive cytotoxicity, thus allowing for the observation of cellular behaviour over time, *in vitro*.

3.3. Assessment of the Cytotoxic Potential of Optimised CBD and Tamoxifen Treatment on RAW264.7 Macrophages

3.3.1. Impact on Cell Viability and Growth

The 72-hour treatment regimen (optimised on MCF7 cells) combining 5 µM CBD and 2 µM Tamoxifen, with daily replacement (model 2) was evaluated in M0 RAW264.7 macrophages, to assess its impact on macrophage cell viability and proliferation. Control cells (media and diluent) displayed dense populations of cells with characteristic rounded morphology, with a few dendritic and spindle-shaped cells (**Figure 3.3.1 A1, A2**). These cells further exhibited positive and intense staining with the Neutral red dye (**Figure 3.3.1 A6, A7),** and this correlated with negligible effects on cell viability ($p>0.05$; **Figure 3.3.1 B1),** and growth inhibition ($p>0.05$; **Figure 3.3.1 B2**). Treatment with Tamoxifen, CBD or their combination resulted in heterogeneous macrophage phenotypes characterised by a mixture of rounded, dendritic and spindle-shaped morphologies, suggestive of M0, M1 and M2 macrophage phenotypes, respectively (**Figure 3.3.1 A3-5**) (McWhorter *et al*., 2013; Wu *et al*., 2014; Heinrich *et al*., 2017; Liang *et al*., 2022). These cells also demonstrated positive staining with Neutral red (**Figure 3.3.1 A8-10**). While a slight reduction in cell viability and density was observed across all treatment groups, these changes were not statistically significant ($p>0.05$, **Figure 3.3.1**). In addition, treatments (CBD and/or Tamoxifen) showed negligible effects in inducing cytotoxicity or growth inhibition, as measured using the MTT assay, compared to serum-free media (SFM) and 0.1% Triton-X-100 ($p>0.05$; **Figure 3.3.1 B2**).

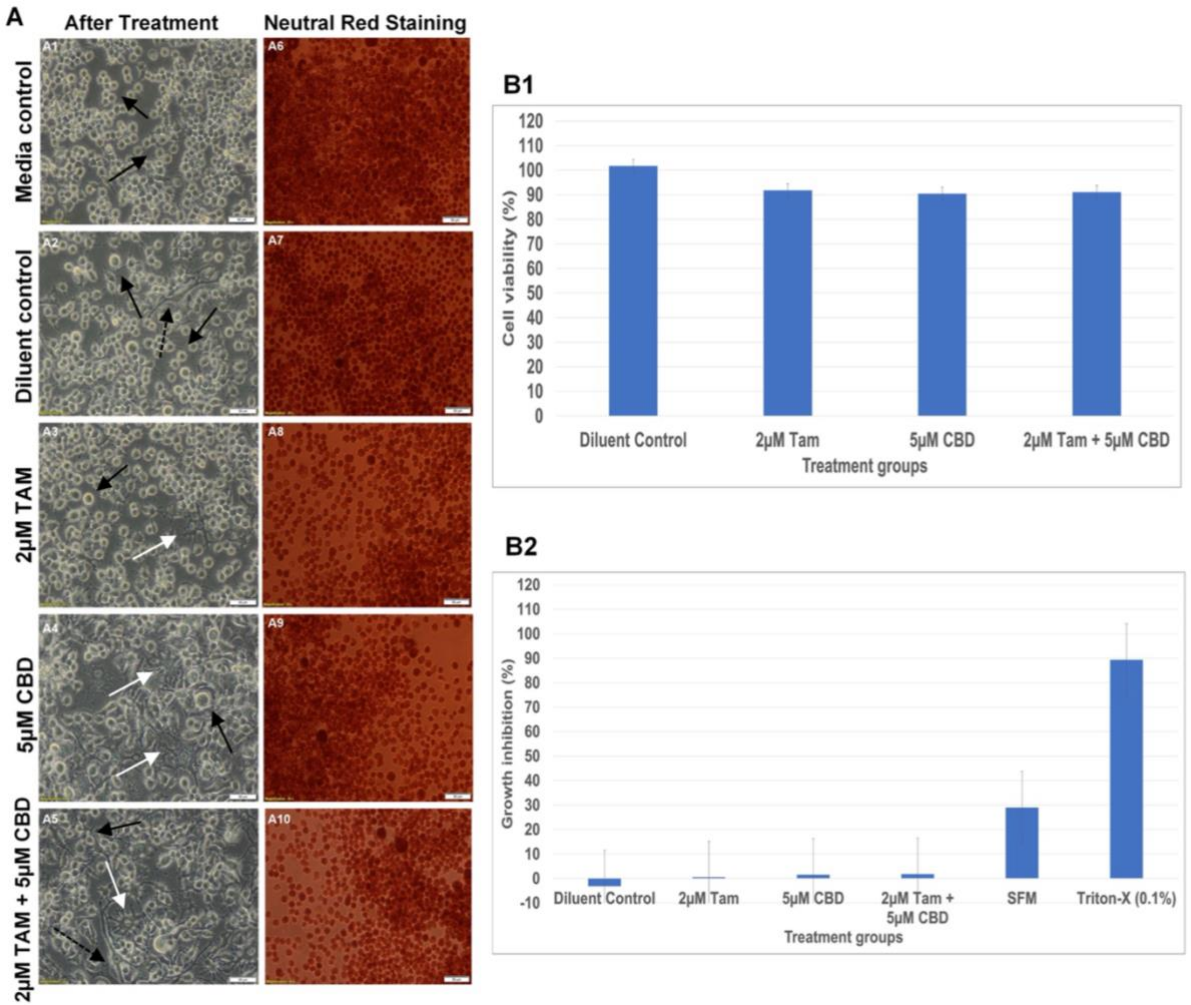


Figure 3.3.1: Cytotoxic effects of CBD and Tamoxifen treatment on RAW 264.7 macrophages assessed using the Neutral red and MTT assays. Key: A) Representative photomicrographs of RAW264.7 cells, following 72 hours of treatment and staining with Neutral red. **B1)** Graph illustrating Cell viability (%) across treatment groups; **B2)** Graph showing growth inhibition (%) across the treatment groups. Error bars indicate the standard error of mean. RAW264.7 cells revealed a heterogeneous population of cells (**A**). Cells exhibited a predominantly rounded morphology (solid black arrows) with a few dendritic cells (white arrows) and spindle-shaped cells (dashed black arrows). Following treatment with Tamoxifen, CBD and combination of both, an increased number of dendritic cells was evident (**A3-5**). Cells showed little signs of stress in response to treatment. Qualitative analysis of Neutral red Uptake showed increased red cytoplasmic staining across all treatment groups, suggesting elevated viability (**A6-10**). Quantitative analyses revealed treatment with CBD alone and in combination with Tamoxifen to have negligible effects on cell viability and inhibition of growth ($p>0.05$; **B**). Images captured at 20X magnification (scale bar – 50 μm).

3.3.2. Impact on Protein Expression

To elucidate the molecular mechanisms underlying the synergistic effects of optimised CBD and Tamoxifen treatment a proteomic analysis of RAW264.7 macrophages following 72 hours of treatment was conducted. Corresponding morphological assessments showed that control cells exposed to the diluent (0.2% methanol) demonstrated a mixed population of rounded cells with spindle and dendritic-shaped cells (**Figure 3.3.2 A1**). Macrophages treated with 2 µM Tamoxifen (**Figure 3.3.2 A2**), 5 µM CBD (**Figure 3.3.2 A3**) and their combination (**Figure 3.3.2 A4**) induced a shift in the macrophage population towards an M1-like phenotype characterised by the increased presence of cells with extended processes (**Figure 3.3.2 A2-4**). This morphological change aligns with previous reports (McWhorter *et al*., 2013; Wu *et al*., 2014; Heinrich *et al*., 2017; Liang *et al*., 2022). Suggesting a potential transition from the M0 to M1-activated phenotype. Thereafter, proteomic analysis was conducted on the RAW264.7 cells treated with 2 µM Tamoxifen, 5 µM CBD or a combination of both.

Using relative quantification, implementing the label-free method, a total of 81 067 peptides and 6 572 protein groups were identified (**Figure 3.3.3**). The average numbers of peptides and protein groups identified in each treatment group following 72 hours of treatment are indicated in Figure 3.3.3. A principle component analysis (PCA) was conducted to reduce data dimensionality and identify patterns of variation within the data that could distinguish between macrophages treated with optimised CBD and/or Tamoxifen (**Figure 3.3.4**). Two principal components (PCs) were generated, accounting for 55.18% of the variation (PC1 – 36.95% and PC2 – 18.23%). The PCA revealed distinct clustering of cells into four groups corresponding to each treatment: diluent control (RDC), 2 µM Tamoxifen (RT), 5 µM CBD (RCB) and the combination treatment (RTCB). PC1 was the primary factor influencing the separation between groups, with RDC having lower PC1 scores and RTCB having higher PC1 scores. PC2 also contributed to the separation, especially between RTCB and RT groups. Interestingly, some overlap was observed between RAW264.7 cells exposed to the diluent control (RDC), reflecting the heterogeneity in the population, and those treated with both CBD and Tamoxifen (RTCB).

The expressed proteins in Tamoxifen and CBD-treated cells (RT and RCB, respectively), were analysed in pairwise comparisons to the untreated group (diluent control - RDC) to trace for differences in expression that may be associated with the immunomodulatory effects of the individual treatments (**Figure 3.3.5 A-B**). To highlight the possible synergistic mechanisms, the expressed proteins in the combination treatment (Tamoxifen and CBD – RTCB) were analysed in pairwise comparisons to the untreated cells (diluent control – RDC) (**Figure 3.3.5 C**). The analysis demonstrated a total of 116 proteins that were significantly dysregulated in Tamoxifen-treated macrophages (compared to the diluent control), including 31 upregulated and 85 downregulated proteins (**Figure 3.3.5 A**). CBD-treated cells demonstrated differential regulation of 80 proteins (compared to the diluent control), with 48 upregulated and 32 downregulated (**Figure 3.3.5 B**). In the Tamoxifen-CBD combination group, 77 proteins were dysregulated (compared to the diluent control), with 44 upregulated and 33 downregulated (**Figure 3.3.5 C**). We then focused on the proteins that were upregulated in RAW264.7 cells in each treatment group (**Table 5-7**). The complete list indicating the differentially expressed proteins in the macrophages in each treatment group is shown in **Appendix F3**. Notably, the majority of the proteins were not considered significant, primarily due to the stringent FDR and q-value cut-offs, as shown by the numerous grey nodes in Figures 3.3.5A-C. This minimised the proportion of false positives among the identified differentially expressed proteins. Thus providing greater confidence in the biological significance of the observed protein expression differences (Karp *et al*., 2007; Lai, 2017).

The String enrichment analysis identified networks of predicted associations for the dysregulated proteins in the pairwise comparisons (**Figure 3.3.6 A-C**). The analysis for Tamoxifen-treated cells revealed the involvement of these proteins in crucial cellular processes such as the immune response, lipid and cholesterol metabolism, (**Figure 3.3.6 A**). For CBD-treated cells, the differentially expressed proteins were shown to interact with other proteins involved in several cellular processes including, defence responses, regulation of phagocytosis, regulation of the MAP kinase pathway and IFN-γ signalling (**Figure 3.3.6 B**). For cells treated with the CBD-Tamoxifen combination, protein-protein interaction analysis revealed enrichment of pathways involved in cellular metabolism, regulation of cytokine signalling and NO-mediated

signal transduction (**Figure 3.3.6 C**). **Tables 3.3 – 3.5** below show some of the proteins involved in the respective pathways for each treatment group.

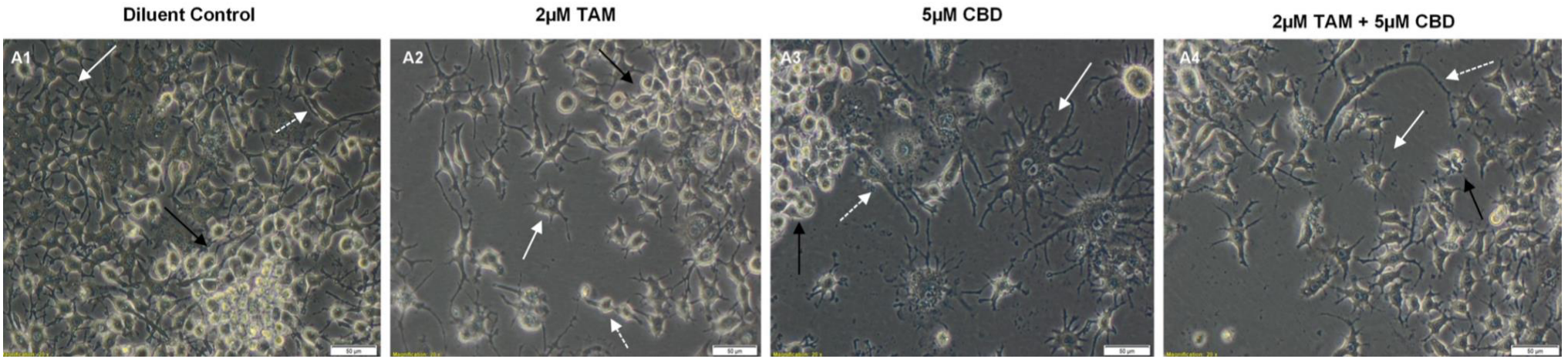


Figure 3.3.2: Morphological assessments of RAW264.7 macrophages treated with CBD and/or Tamoxifen. Representative photomicrographs of RAW264.7 cells, following 72 hours of treatment. Cells exposed to the diluent control (0.2% methanol, **A1**) revealed a heterogeneous population of cells. While, cells exposed to Tamoxifen alone (**A2**), CBD alone (**A3**) and Tamoxifen in combination with CBD (**A4**) exhibited a shift towards dendritic morphology characterised by numerous cellular extensions (solid white arrows) with reduced prevalence of rounded (black arrows) and spindle-shaped cells (white dashed arrows). Images captured at 20X magnification (scale bar – 50 μm).

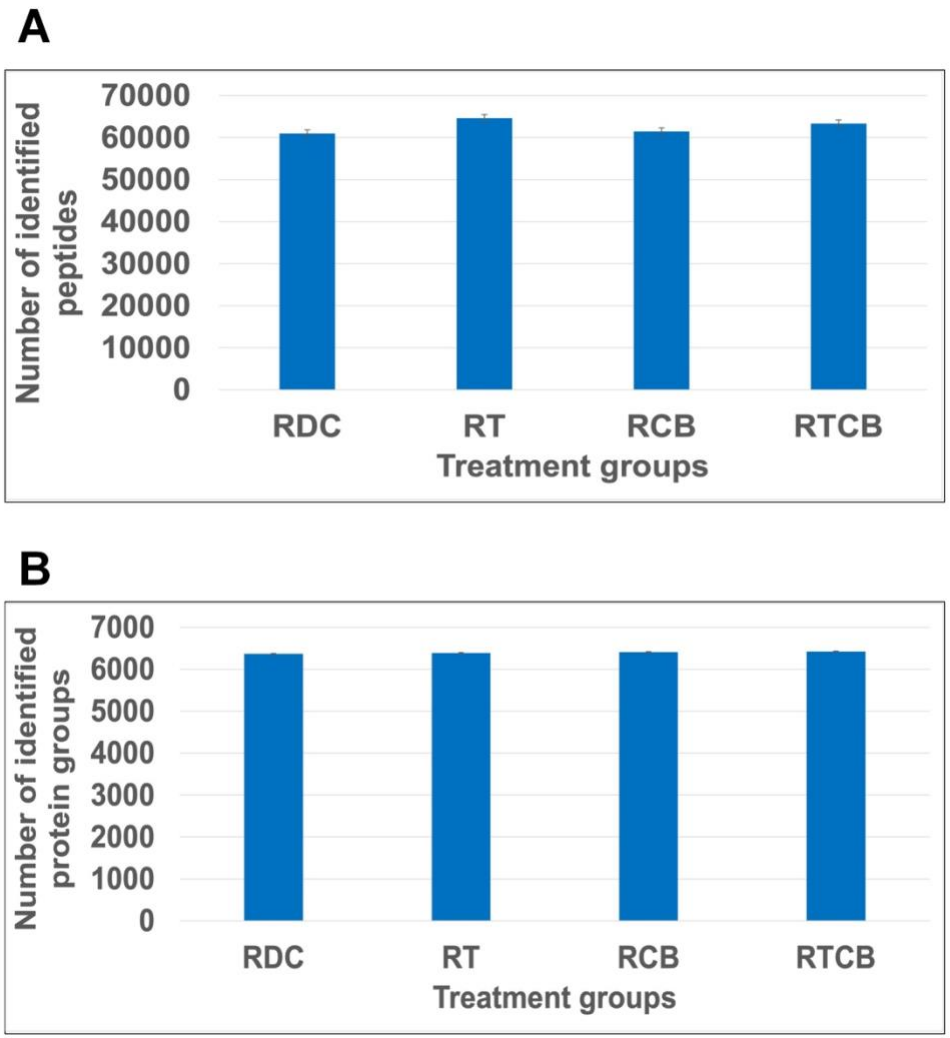


Figure 3.3.3: Overview of identifications from the proteome of RAW264.7 macrophages treated with CBD and/or Tamoxifen. Bar graphs showing the average number of identified **A)** peptides and **B)** protein groups across triplicates of each treatment group. Error bars indicate the standard error of mean. **RDC-diluent control, RT-2 µM Tamoxifen, RCB-5 µM CBD, RTCB-combination treatment**.

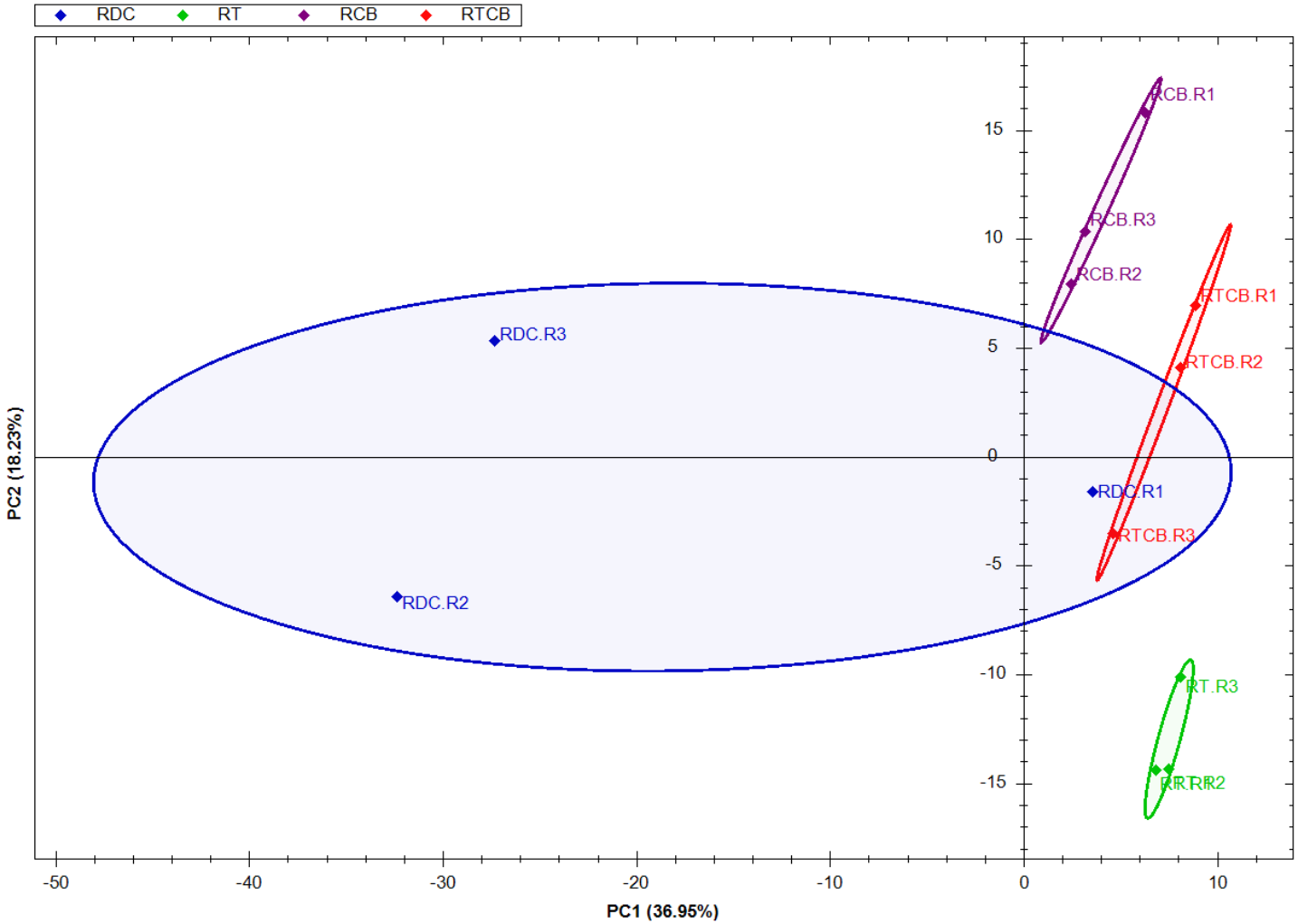


Figure 3.3.4: PCA plot demonstrating the variation in protein expression among RAW264.7 macrophages treated with CBD and/or Tamoxifen. PCA plot representing the relationships between RAW264.7 cells in the different treatment groups (**RDC-diluent control, RT-2μM Tamoxifen, RCB-5μM CBD, RTCB-combination treatment**), based on their principal component scores (R1-R3 represents the triplicates from each group). The values of the first and second PCs are shown for three repeats of each treatment group, PC1 explains 36.95% of the total variation and PC2 explains 18.23% of the variation. The cells appeared to cluster into four distinct groups representing each treatment group. Spectronaut v19 software generated the plot using an FDR of 0.01 (1%) and a q-value of 0.01.

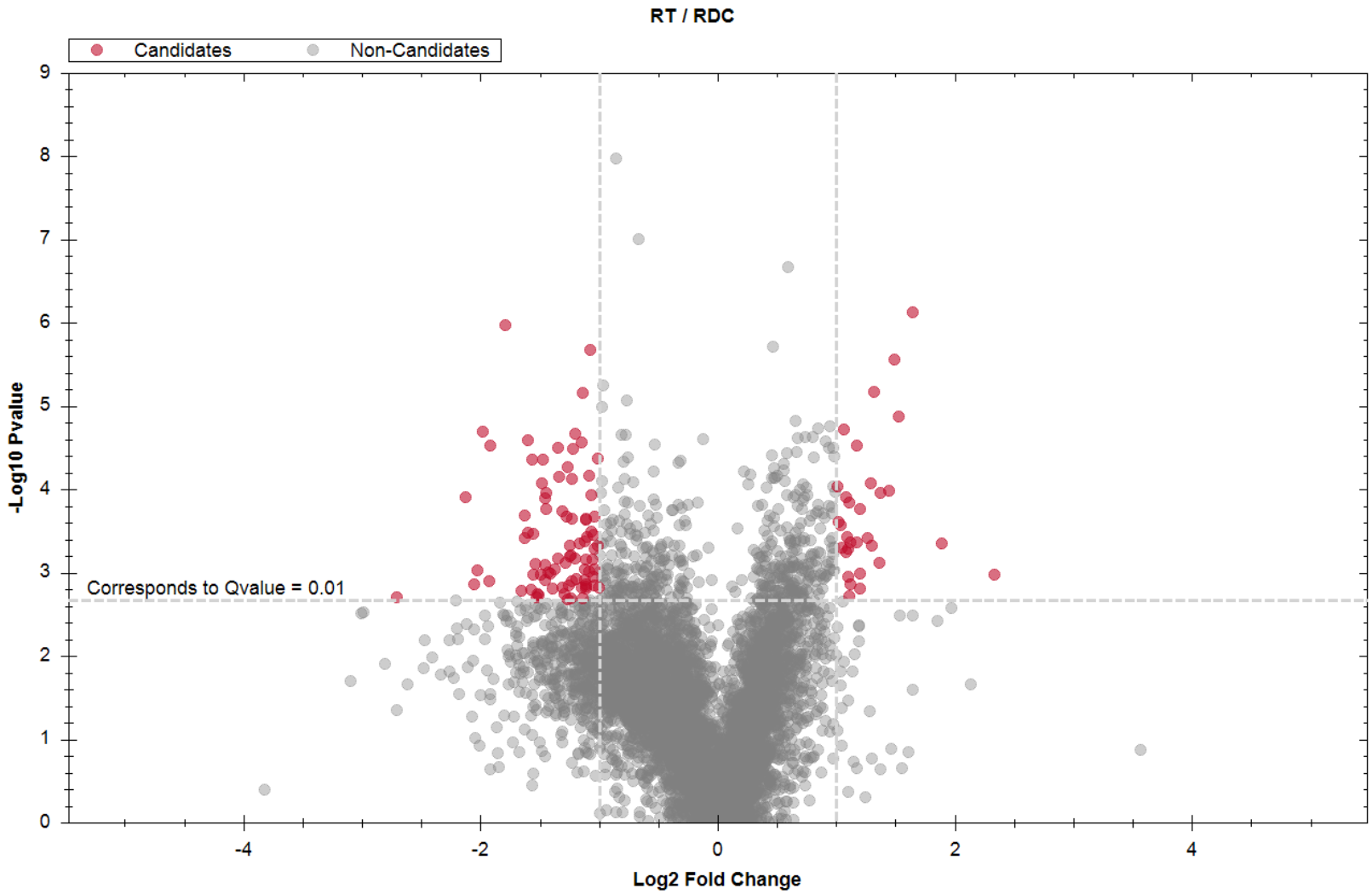


Figure 3.3.5A: Differential expression of proteins in RAW264.7 cells treated with 2 µM Tamoxifen. Pairwise volcano plot indicating dysregulated proteins following Tamoxifen treatment compared to untreated cells; X-axis shows the $\log_2$ fold change; Y-axis shows the significance ($-\log_{10}$ p-value). **RT – 2µM Tamoxifen; RDC – diluent control (untreated cells).** Red nodes - significantly dysregulated proteins between the treatment groups, those located in the negative x-axis are significantly downregulated and those in the positive x-axis are significantly upregulated. Grey nodes indicate proteins that exhibited no significant changes inexpression. Spectronaut v19 software was used to generate the plot using an FDR of 0.01 (1%) and Q-value of 0.01.

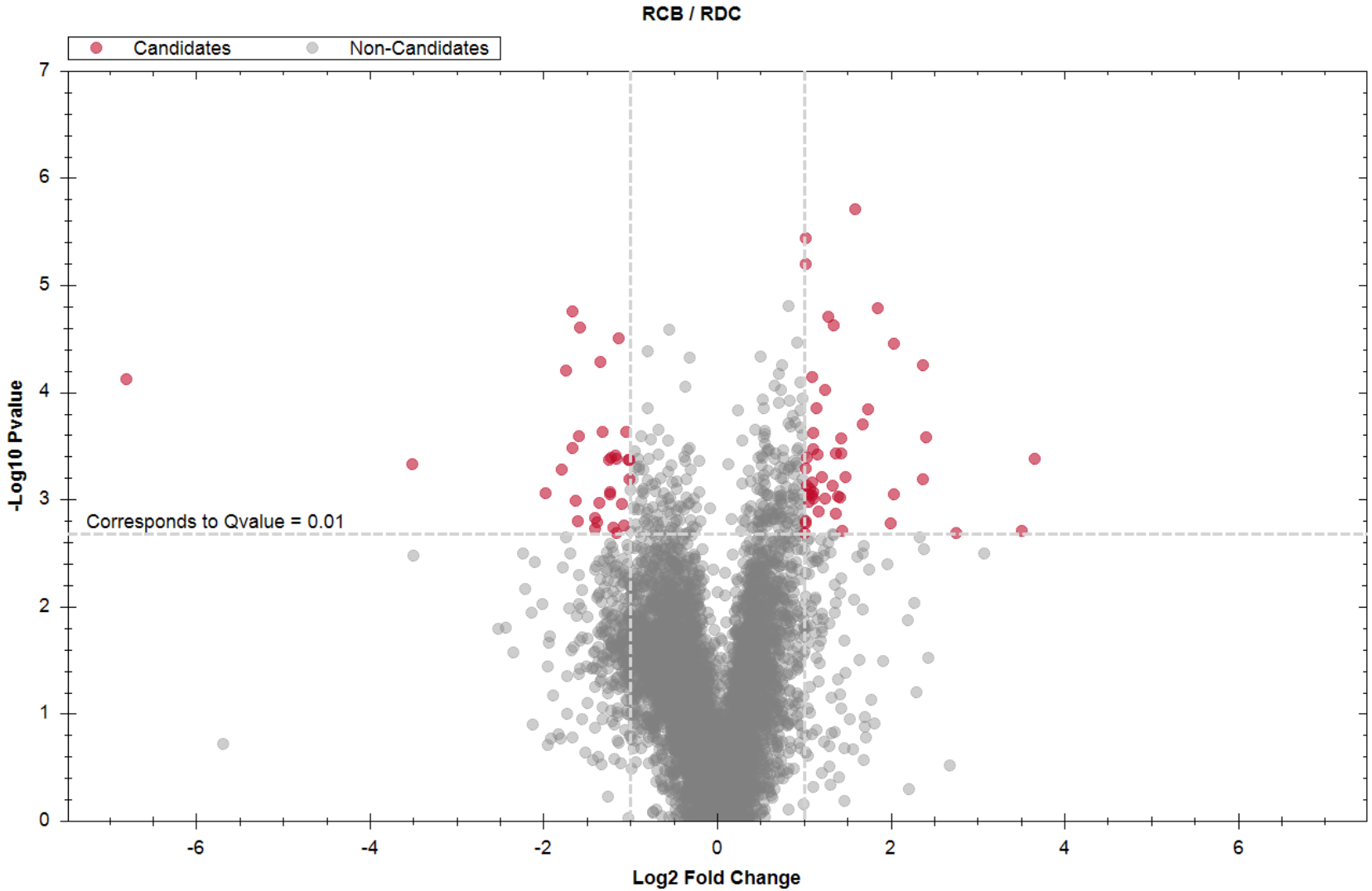


Figure 3.3.5B: Differential expression of proteins in RAW264.7 cells treated with 5 µM CBD. Pairwise volcano plot indicating dysregulated proteins following CBD treatment compared to untreated cells; X-axis shows the log_2 fold change; Y-axis shows the significance ($-log_{10}$ p-value). **RCB – 5µM CBD; RDC – diluent control (untreated cells**). Red nodes - significantly dysregulated proteins between the treatment groups, those located in the negative x-axis are significantly downregulated and those in the positive x-axis are significantly upregulated. Grey nodes indicate proteins that exhibited no significant changes inexpression. Spectronaut v19 software was used to generate the plot using an FDR of 0.01 (1%) and q-value of 0.01.

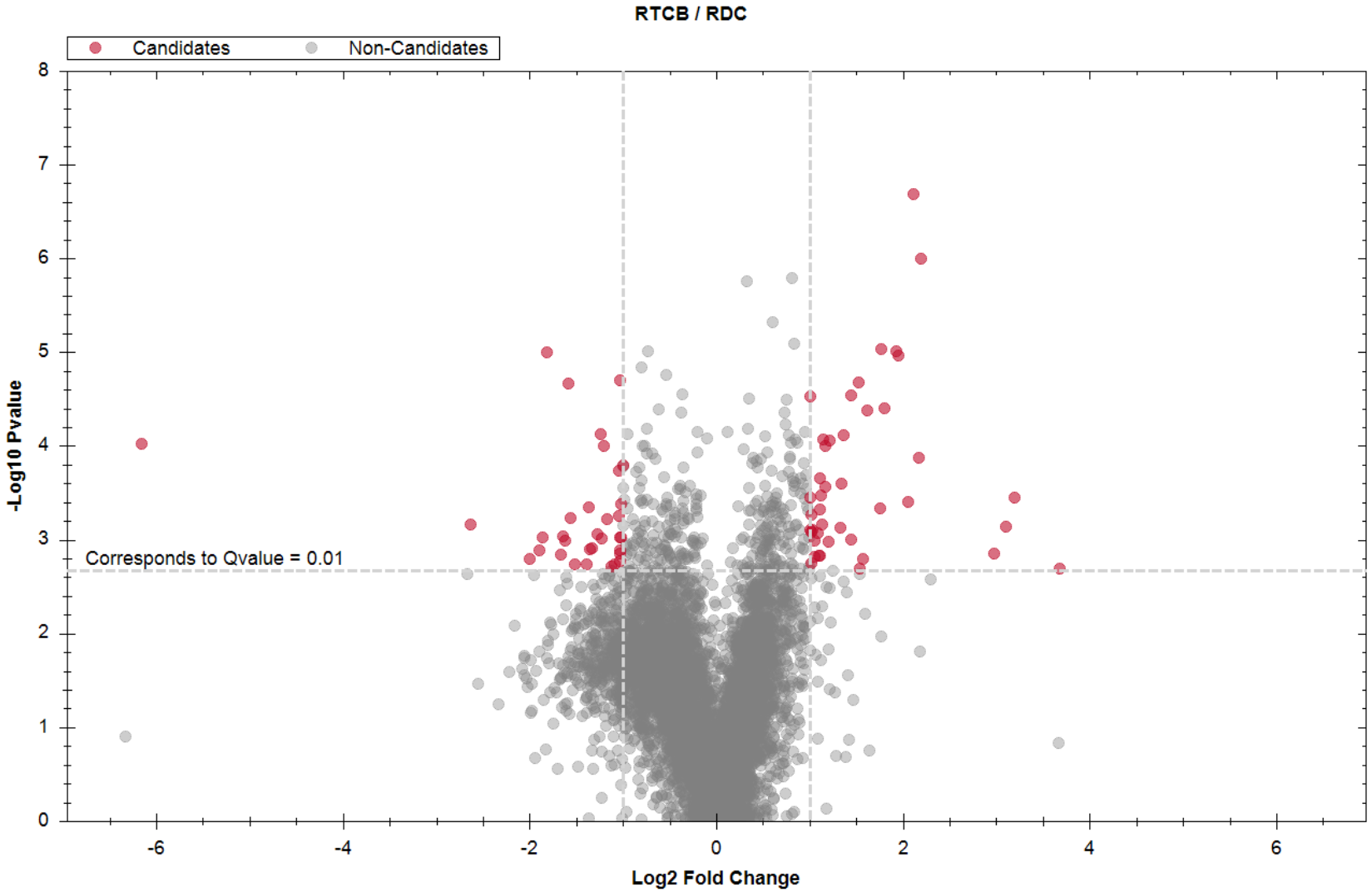


Figure 3.3.5C: Differential expression of proteins in RAW264.7 cells treated with CBD and Tamoxifen. Pairwise volcano plot indicating dysregulated proteins following CBD and Tamoxifen treatment compared to untreated cells; X-axis shows the $\log_2$ fold change; Y-axis shows the significance ($-\log_{10}$ p-value). **RTCB – 2μM Tamoxifen + 5μM CBD; RDC – diluent control (untreated cells).** Red nodes - significantly dysregulated proteins between the treatment groups, those located in the negative x-axis are significantly downregulated and those in the positive x-axis are significantly upregulated. Grey nodes indicate proteins that exhibited no significant changes in expression. Spectronaut v19 software was used to generate the plot using an FDR of 0.01 (1%) and a q-value of 0.01.

Table 3.3: The enriched pathways and proteins in Tamoxifen-treated RAW264.7 macrophages (relative to untreated cells)

Pathway name	False discovery rate (FDR)	Proteins in pathway
Immune system	1.31×10^{-13}	KCC1D, MP2K5, LAMP2, SRC, ATR
Metabolism of lipids	3.68×10^{-8}	FABP5, THIC, ASAH1,
Cholesterol biosynthesis	9.39×10^{-7}	FPPS, HMCS1, MVD1, KIME, PMVK

Table 3.4: The enriched pathways and proteins in CBD-treated RAW264.7 macrophages (relative to untreated cells)

Pathway name	False discovery rate (FDR)	Proteins in pathway
Defence response	2.20×10^{-3}	CD44, PAI1, HMOX1, VIM
Regulation of phagocytosis	2.20×10^{-3}	CD63, ADDG, C1QBP, CD47,
Regulation of MAP kinase pathway	1.35×10^{-2}	C/EBPβ, PAI2, Protein S10AD, JUPI2,
IFN-γ signalling	1.94×10^{-2}	CD47, VIM, AIF1, CCL2, IFM2

Table 3.5: The enriched pathways and proteins in Tamoxifen-CBD treated RAW264.7 macrophages (relative to untreated cells)

Pathway name	False discovery rate (FDR)	Proteins in pathway
Cellular metabolism	3.97×10^{-13}	ENOG, FPPS, IAH1, THIOM
Regulation of cytokine signalling	1.30×10^{-4}	Protein S10AD, CALM1, CALM2, CALM3, RIPK3
NO-mediated signal transduction	2.56×10^{-2}	ADDG, CD63, MT1, MT2

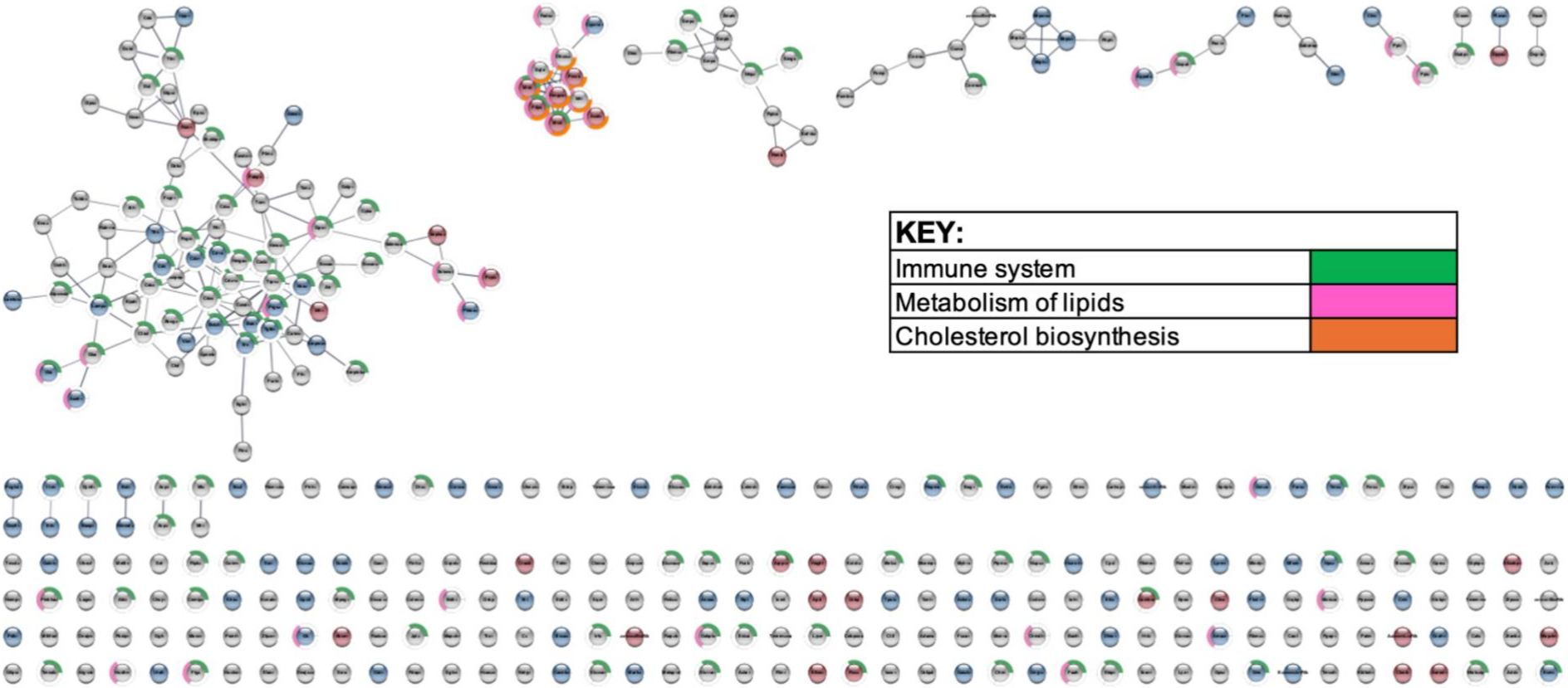


Figure 3.3.6A: String-enrichment analysis. Plot shows the protein-protein interactions between differentially expressed proteins in RAW264.7 cells exposed to 2 μM Tamoxifen. Nodes: blue indicates downregulation, red indicates upregulation and grey indicates no significant difference in protein expression. The singleton proteins (shown at the bottom) do not directly interact with other identified proteins but contribute to the enriched pathways. Key shows respective pathways proteins are involved in. Cytoscape software (v3.10.2) was used to generate pathway, FDR of 0.01 (1%) and high-confidence protein interaction score of 0.7 was used (Doncheva *et al*., 2019).

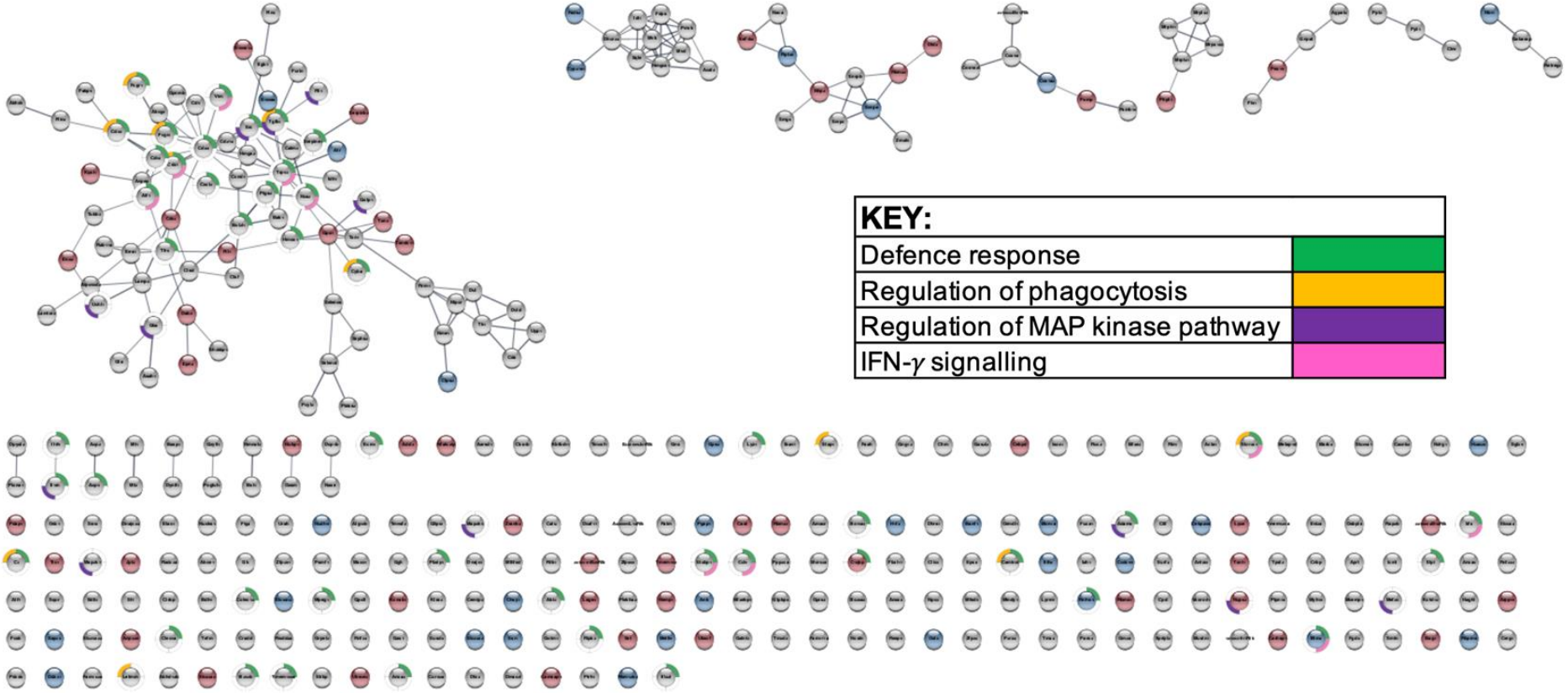


Figure 3.3.6B: String-enrichment analysis Plot shows the protein-protein interactions between differentially expressed proteins in RAW264.7 cells exposed to 5 μM CBD. Nodes: blue indicates downregulation, red indicates upregulation and grey indicates no significant difference in protein expression. The singleton proteins (shown at the bottom) do not directly interact with other identified proteins but contribute to the enriched pathways. Key shows respective pathways proteins are involved in. Cytoscape software (v3.10.2) was used to generate pathway, FDR of 0.01 (1%) and high-confidence protein interaction score of 0.7 was used (Doncheva *et al*., 2019).

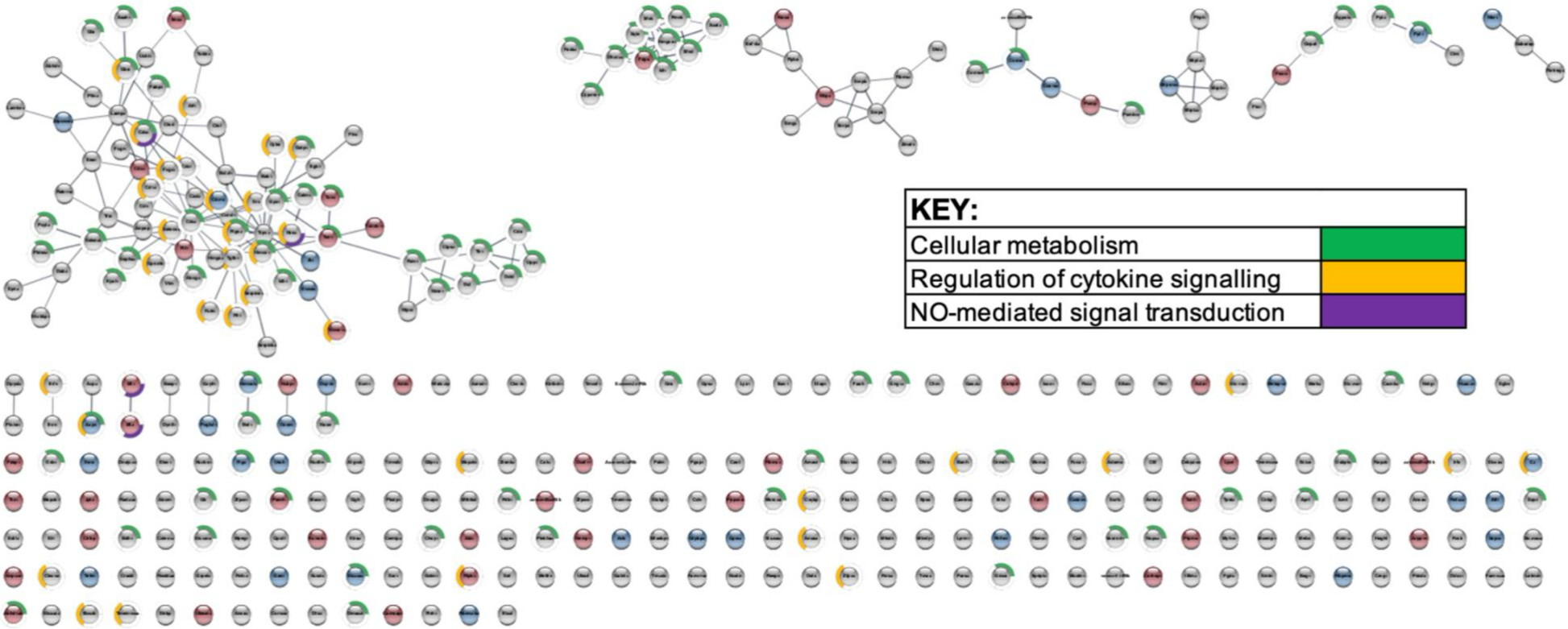


Figure 3.3.6C: String-enrichment analysis. Plot shows the protein-protein interactions between differentially expressed proteins in RAW264.7 cells exposed to 5 μM CBD and 2 μM Tamoxifen. Nodes: blue indicates downregulation, red indicates upregulation and grey indicates no significant difference in protein expression. The singleton proteins (shown at the bottom) do not directly interact with other identified proteins but contribute to the enriched pathways. Key shows respective pathways proteins are involved in. Cytoscape software (v3.10.2) was used to generate pathway, FDR of 0.01 (1%) and high-confidence protein interaction score of 0.7 was used (Doncheva *et al*., 2019).

3.4. Impact of Tamoxifen and CBD on Macrophage Phagocytosis of Breast Cancer Cells

Macrophage-mediated engulfment of cancer cells is a crucial cellular process in the innate immune response (Nam *et al*., 2019). To assess whether optimised Tamoxifen (2 μM) and CBD (5 μM) treatment could enhance this process, we co-cultured M0 RAW264.7 cells with MCF7 cells. The breast cancer cells were labelled with the CellTracker green dye to trace their uptake by the macrophages, which were left unstained. Additionally, we measured the nitrite production within the co-cultures using the Griess reagent assay. Macrophages polarised over 48 hours into an M1 phenotype (100 ng/mL LPS, and IFN-γ 20 ng/mL) as per section 4.2, were used as a positive control for phagocytosis (Xu *et al*., 2023).

Overlays of phase contrast images and fluorescence images of the co-cultures demonstrated a notable uptake of MCF7 cell fragments by RAW264.7 macrophages, regardless of their initial phenotype (M0 or M1) (**Figure 3.4 A**). While the presence of rounded macrophages was observed post 72 hours of treatment, all treatment groups exhibited a morphological shift in M0 macrophages towards a more activated M1-like phenotype, characterised by the development of cellular extensions (**Figure 3.4 A1-5**). Interestingly, the majority of M0 macrophages exposed to 5 μM CBD maintained a predominantly rounded morphology, however, the reappearance of dendritic cells was observed in cells treated with the combination of Tamoxifen (2 μM) and CBD (5 μM) (**Figure 3.4 A4-5**). Macrophages stimulated to the M1 phenotype revealed a higher prevalence of dendritic cells across all treatment groups (**Figure 3.4 A6-10**). Evidently, these macrophages displayed greater uptake of MCF7 cell fragments compared to the M0 macrophages. The results of cellular morphologies presented in Figure 3.4 A are consistent with previous findings (McWhorter *et al*., 2013; Wu *et al*., 2014; Heinrich *et al*., 2017; Liang *et al*., 2022).

An assessment of the nitrite levels from the co-cultures, consisting of initial M0 macrophages and MCF7 cells, revealed a progressive increase in nitrite concentrations across all treatment groups (**Figure 3.4 B**). Specifically, co-cultures

treated with a combination of Tamoxifen and CBD evidenced significantly higher nitrite concentrations compared to those exposed to media alone ($p<0.05$; **Figure 3.4 B**). Co-cultures involving initial M1 macrophages maintained comparable nitrite concentrations across all treatment groups, with slightly higher levels observed in the combined treatment group. However, this difference was not statistically significant ($p>0.05$; **Figure 3.4 B**). M1-containing cultures generally exhibited much higher nitrite concentrations compared to those containing M0 macrophages. However, no significant differences in nitrite levels were observed across the treatment groups between both M0 and M1 phenotypes ($p>0.05$; **Figure 3.4 B**).

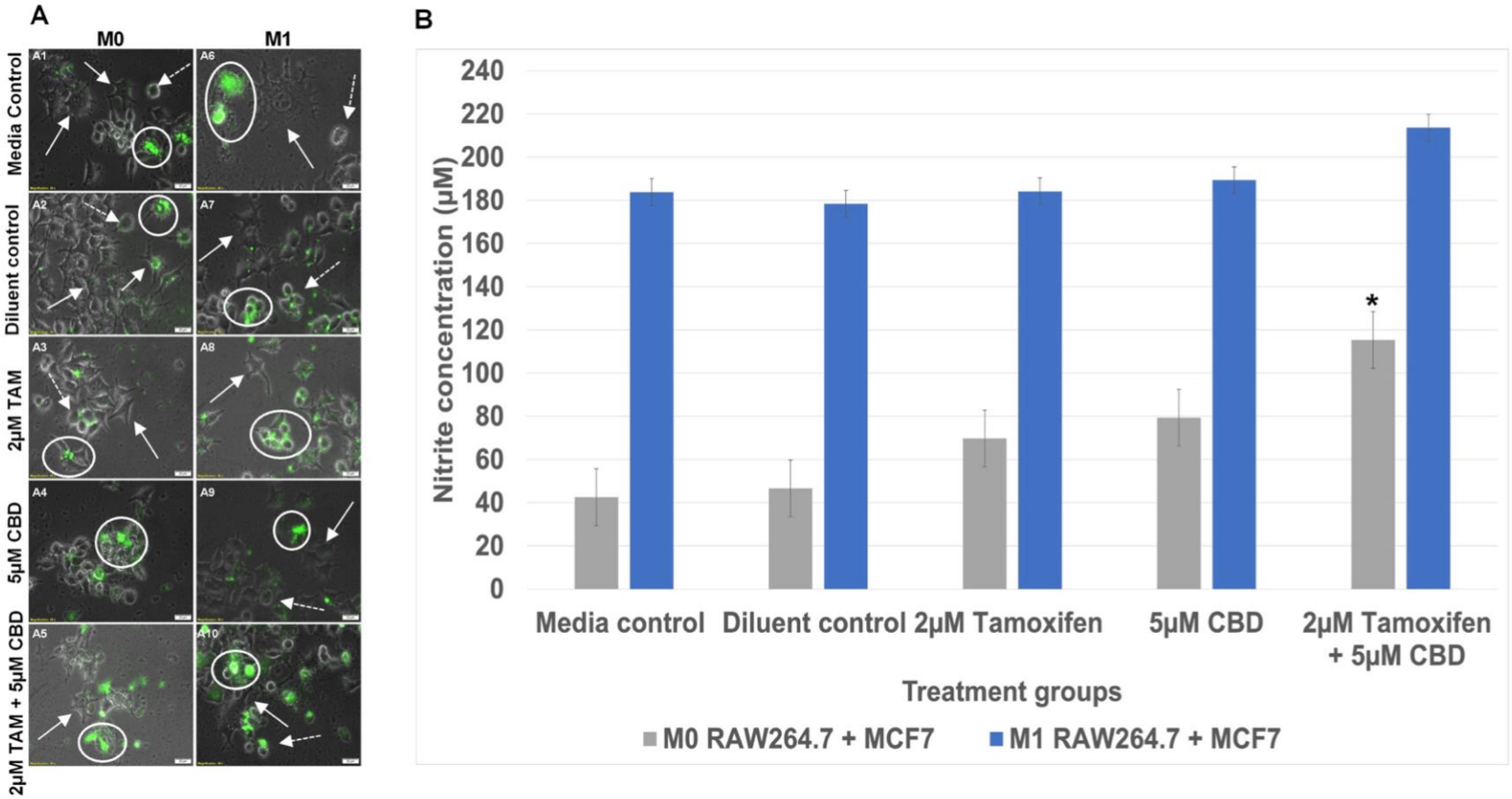


Figure 3.4: Phagocytic assay using CellTracker green dye and the Griess reagent. **A)** Fluorescence microscopic images of co-cultures containing MCF7 and RAW264.7 cells treated with optimised Tamoxifen and/or CBD. The MCF7 cells were labelled with 2.5 μM of CellTracker green dye and can be seen localised within the cytoplasm of the RAW264.7 macrophages. **A1-5)** M0 – Unstimulated macrophages **A6-10**) M1 – macrophages stimulated with LPS (100 ng/ml) and IFN-γ (20 ng/ml), used as positive controls for phagocytosis. **B)** Nitrite production from MCF7 and RAW264.7 co-cultures following treatment. Error bars indicate standard error of mean. Uptake of MCF7 cells was evidenced by the localisation of the green dye (encircled), within the macrophages for both phenotypes (M0 and M1) across all treatment groups. Dendritic morphologies (solid white arrows) were observed across all treatment groups regardless of the phenotype. However, in co-cultures containing M0 macrophages, exposed to 5 μM CBD, cells retained mostly rounded phenotypes (dashed white arrows). Images captured at 40X magnification (scale bar – 20 μm), at a wavelength of 488 nm. Nitrite production analysis revealed a progressive increase across all treatment groups involving M0 cells, with a significant elevation observed between the media control and combined treatment ($p<0.05$). M1-containing cultures demonstrated similar nitrite levels across treatment groups, with slightly elevated levels in the combination treatment group. However, this difference was not statistically significant ($p>0.05$). Co-cultures involving M1 macrophages showed higher nitrite concentrations compared to the M0 cultures, but this was not significant ($p>0.05$) (***p<0.05 relative to media control**).

Chapter 4

Discussion and Conclusion

Macrophages, as important components within the immune system, demonstrate significant plasticity, differentiating into distinct phenotypes with diverse functions (Oshi *et al*., 2020; Jiang *et al*., 2021; Mehta *et al*., 2021; Mas-Rosario *et al*., 2023). Within the tumour microenvironment (TME), macrophage polarisation plays a crucial role in shaping tumour progression (Sun *et al*., 2023). While M1 macrophages exhibit anti-tumour properties, promoting inflammation and tumour cell killing, M2 macrophages often support tumour growth and metastasis through immunosuppressive functions (Augustine, Nweke and Fru, 2022; Zhan *et al*., 2023). This study aimed to investigate the impact of CBD and Tamoxifen, both with potential anticancer properties, on cell growth and macrophage polarisation and function in the context of breast cancer.

4.1. Macrophage Polarisation and Phenotypic Characterisation

To delve into the functional and molecular characteristics of the different macrophage phenotypes, this study employed the RAW264.7 macrophage cell line. These macrophages are derived from BALB/c mice transfected with the Abelson leukaemia virus and are widely used in various macrophage-associated studies (Martinez-Martin *et al*., 2017; Taciak *et al*., 2018; Khabipov *et al*., 2019; Li *et al*., 2021). To optimise *in vitro* macrophage polarisation, a multifaceted approach was employed. This crucial step ensured reliable and physiologically relevant data in subsequent experiments. Firstly, morphological changes and nitric oxide (NO) production were analysed in induced M1 and M2 macrophages. Secondly, the proteomic profiles of these polarised macrophages were assessed, relative to M0 macrophages. These analyses were conducted across different time points (24, 48, and 72 hours), to determine the optimal polarisation duration. Unstimulated RAW264.7 macrophages, representing the M0 phenotype, were polarised towards the M1 phenotype using IFN-γ (20 ng/mL) and LPS (100 ng/mL), while IL-4 (20 ng/mL) was used to stimulate the M2 phenotype.

These stimuli and their concentrations have been well-established as potent inducers of the respective macrophage phenotypes (Deci *et al*., 2019; Khabipov *et al*., 2019; Heaster *et al*., 2020; Shi *et al*., 2020; Liang *et al*., 2022; Liu *et al*., 2022).

4.1.1. The Role of Morphology in Defining Macrophage Phenotypes

A key observation in this study was the inherent heterogeneity observed within each macrophage population (M0, M1 and M2) across all time points. This finding aligns with the concept that macrophage polarisation is a continuum rather than a binary switch between distinct M1 and M2 phenotypes (Heinrich *et al*., 2017; Li *et al*., 2021). This complexity arises from the dynamic nature of macrophage activation, influenced by various microenvironmental cues and the inherent plasticity of these cells (Heinrich *et al*., 2017; Purcu *et a*l., 2022; Eligini *et al*., 2023). Despite this heterogeneity, clear morphological differences became evident by 48 hours post-stimulation. While unstimulated (M0) macrophages exhibited a predominantly rounded morphology, M1 polarisation induced a pronounced shift towards a dendritic phenotype characterised by numerous pseudopodia and microvilli. Conversely, M2 polarisation favoured an elongated, spindle-shaped morphology.

These observations are consistent with previous studies utilising various macrophage cell lines. Studies on RAW264.7 macrophages have reported mainly roundish cells in the untreated control group (M0 phenotype). While polarisation towards the M1 phenotype induced a flattened, pancake-like morphology with cellular extensions and M2 polarisation led to cellular elongation within 48 hours of stimulation (McWhorter *et al*., 2013; Wu *et al*., 2014; Li *et a*l., 2021; Liang *et al*., 2022). Similarly, studies on THP-1 cells, a human macrophage cell line, revealed distinct phenotypic changes upon activation with IFN-γ and LPS (M1 phenotype) and IL-4 (M2 phenotype) for 48 hours. M0 macrophages exhibited a spherical shape, M1 macrophages displayed increased pseudopodia and, M2 macrophages appeared as elongated and stretched-out cells (Zhang *et al*., 2015; Li *et a*l., 2022). These results were consistent with a previous study performed on monocytes from human peripheral blood mononuclear cells that were stimulated to M1 and M2 macrophages (Reales-Calderon *et al*., 2014). These

findings suggest that 48 hours of stimulation provides sufficient time to induce characteristic morphological changes associated with M1 and M2 polarisation in macrophage cell lines. Notably, Heinrich *et al.* (2017) utilising canine macrophages, also observed distinct morphological changes upon polarisation. In this study, M0 macrophages appeared small and roundish with minimal cytoplasmic extensions, while M1 macrophages presented with numerous fibrillary cytoplasmic extensions on the cellular surface. M2 macrophages, in turn, exhibited bipolar spindleoid morphologies with elongated cell bodies (Heinrich *et al*., 2017). This study further supports the generalisability of these findings across different species.

These observations collectively highlight the significance of morphological analysis as a valuable tool for assessing macrophage polarisation. While reflecting the inherent plasticity and heterogeneity of macrophage populations, the observed morphological shifts provide valuable insights into the cellular adaptations associated with distinct activation states.

4.1.2. Nitric Oxide Production as a Marker of Macrophage Polarisation

M1-activated macrophages are recognised for their robust production of NO, a critical mediator of antimicrobial and anti-tumour responses (Zhang *et al*., 2015; Jiang *et al*., 2021). In this study, the levels of NO production in polarised RAW264.7 cells were measured indirectly as the amount of nitrite, a stable degradation product of NO, at various time points (Zhang *et al*., 2015; Jiang *et al*., 2021). Nitrite production was thus used as a potential marker to distinguish between the macrophage phenotypes. As expected, M1 macrophages exhibited higher nitrite production compared to both M0 and M2 macrophages, particularly at 48 hours post-stimulation. This difference in nitrite production at 48 hours effectively differentiated M1 macrophages from M0 and M2 populations, serving as a key indicator of successful M1 polarisation.

This finding aligns with other studies, where the authors demonstrated elevated NO concentrations within 48 hours in RAW264.7 macrophages stimulated towards the M1 phenotype, compared to the M0 and M2 phenotypes (Aldridge *et al.,* 2008; Wang *et*

al., 2015; Mas-Rosario *et al*., 2023). Similarly, Jiang *et al.* (2021) reported higher NO production in IFN-γ/LPS-treated RAW264.7 macrophages (M1) compared to the control group (M0). Other studies observed that NO production was markedly elevated in THP-1 M1 macrophages and decreased in M2 macrophages following a 48-hour stimulation with LPS plus IFN-γ or IL-4 (Zhang *et al*., 2015; Chen *et al*., 2023).

Interestingly, in this study a notable increase in nitrite production was observed in M2 macrophages at the 72-hour time point, an unexpected finding given the generally low NO production associated with this phenotype (Lee *et al*., 2015; Zhang *et al*., 2015; Huang *et al*., 2018; Pérez and Rius-Pérez, 2022). This observation may suggest a potential shift in macrophage phenotype over time, with M2 macrophages potentially acquiring certain M1-like characteristics during prolonged *in vitro* culture. This phenomenon highlights the inherent plasticity and dynamic nature of macrophage activation, which can be affected by several factors, including culture conditions and duration (Heinrich *et al*., 2017; Li *et a*l., 2021; Eligini *et al*., 2023).

Therefore, the observed differences in nitrite production at 48 hours of stimulation indicated that we successfully derived M1 and M2 macrophages from M0 RAW264.7 cells. However, the finding of increased nitrite production in the M2 phenotype is intriguing and warrants further investigation. While elevated nitrite production is typically associated with M1 macrophage activation, the observed increase of nitrite in M2 macrophages at 72 hours suggests a more complex interplay between macrophage phenotypes and the effects of prolonged *in vitro* culture. This phenomenon may not be a universal characteristic of M2 macrophages and may be specific to RAW264.7 cells or particular culture conditions. Further studies are required to validate this observation and to explore the underlying mechanisms.

4.1.3. Molecular Mechanisms of Macrophage Polarisation

The M1/M2 paradigm, while useful, is a simplified representation of the complex spectrum of macrophage phenotypes. This simplification may not fully capture the intricate biological processes underlying macrophage polarisation (Heinrich *et al*., 2017; Li *et al*., 2021). Recognising this limitation, this study employed a high-throughput proteomics approach to explore the molecular mechanisms driving activation of RAW264.7 macrophages towards M1 and M2 phenotypes.

The development of *in vitro* models for macrophage polarisation has significantly advanced our understanding of macrophage biology (Purcu *et a*l., 2022). While effective inducers for specific macrophage phenotypes are well-established, the optimal duration of stimulation remains a critical consideration (Liu *et al*., 2022; Purcu *et al.,* 2022). To further expand our temporal analysis of macrophage polarisation, this study assessed proteomic profiles of M1 and M2 phenotypes (using the M0 phenotype as baseline) at 24-, 48- and 72-hours post-stimulation.

Proteomic analysis revealed distinct temporal variations in protein expression across the different time points. Principle component analysis of the quantified proteins demonstrated a clear separation of M0, M1 and M2 phenotypes at 48 hours, suggesting that this time point provides the most distinct proteomic signatures for these polarised states. This observation aligns with our previous findings, where 48 hours of stimulation emerged as a critical time point for distinguishing between macrophage phenotypes. Morphological analysis at 48 hours revealed the most pronounced differences and nitrite production (a marker of M1 activation) was higher in M1 macrophages compared to both M0 and M2 macrophages at this time point.

The findings of this study demonstrate that 48 hours represents an optimal time point for assessing distinct macrophage phenotypes and are supported by previous literature utilising RAW264.7, THP-1 and human monocyte-derived macrophages (MDMs) (Zhang *et al* ., 2015; Li *et al*., 2021; Purcu *et al.,* 2022). Studies investigating the temporal expression of key polarisation markers have demonstrated significant upregulation of M1 markers, such as IL-12 and the tryptophan catabolising enzyme,

IDO1, at 48 hours post-stimulation at the mRNA level (Zhang *et al*., 2015; Li *et al*., 2021; Purcu *et al.,* 2022). Similarly, M2 markers, including mannose receptor C-type 1 (MRC1/CD206), transglutaminase 2 (TGM2) and C-C motif ligand 2 (CCL2), showed significant upregulation by 48 hours, but not at earlier time points (Zhang *et al*., 2015; Li *et al*., 2021; Purcu *et al.,* 2022). Furthermore, flow cytometry analysis performed by Liu *et al.* (2022) and Purcu *et a*l. (2022) confirmed the increased expression of surface markers associated with M1 (CD64) and M2 (CD206, CD163, CD200R) phenotypes at this time point. These findings, collectively, demonstrate that 48 hours of stimulation provides a robust and reliable time point for characterising distinct M1 and M2 macrophage phenotypes *in vitro,* providing a strong foundation for subsequent proteomic and functional analyses.

A detailed quantitative understanding of the dynamic changes associated with M1 and M2 polarisation remains elusive. To comprehensively characterise the successful polarisation of RAW264.7 macrophages following 48 hours of stimulation, the findings from morphological analyses and nitrite production assessments were integrated with a comprehensive proteomic analysis. Our proteomic analysis revealed distinct protein expression profiles in M1 and M2 polarised RAW264.7 macrophages, providing valuable insights into the molecular mechanisms underlying their distinct functional roles in several biological processes.

A. Molecular Signatures of M1 Macrophage Polarisation

Pathway analysis revealed that the differentially expressed proteins in the M1 phenotype (compared to M0) were mainly enriched in pathways involving regulation of cytokine production and signalling, phagocytosis, production of reactive oxygen species (ROS) and reactive nitrogen species (RNS), and cellular metabolism. These pathways further provided insights into the molecular underpinnings of the M1 phenotype.

Regulation of Cytokine Production and Signalling

The findings of the current study align with previous studies demonstrating the importance of cytokine signalling pathways in the activation of the M1 macrophage phenotype (Huang *et al*., 2018; Li *et al.,* 2021; Murugesan *et a*l., 2022). Utilising mass spectrometry-based proteomics, Li *et al.* (2021) also observed upregulation of proteins involved in toll-like receptor (TLR) signalling, IFN-γ-mediated signalling pathway and defence responses to antimicrobial particles in M1-polarised RAW264.7 and THP-1 macrophages. Within the TLR signalling pathway, toll-like receptor 4 (TLR4) activation by LPS triggers intracellular signalling cascades, resulting in the production of inflammatory cytokines and chemokines, thereby initiating an immune response to clear pathogens (Shea-Donohue, Zhao and Antalis, 2014; Murugesan *et al*., 2022; **Figure 4.1**). In the IFN-γ-mediated signalling pathway, IFN-γ signals via the JAK-STAT pathway and synergistically activates NF-κB, upregulating the interferon regulatory factor 1 (IRF-1) and subsequently driving the transcription of numerous interferon-stimulated genes (ISGs), which participate in defence responses (Huang *et al*., 2018; Li *et al*., 2021; **Figure 4.1**). ISGs, a large family of proteins, play a crucial role in priming cells for defence against viruses and bacteria. Their expression is upregulated by either type I interferons (including IFN-α and -β), type II interferons (IFN-γ), or type III interferons (IFN-λ1 to IFN-λ4) (Murugesan *et al.,* 2022). Thus, the upregulation of ISGs in M1 macrophages can be attributed to the synergistic effects of IFN-γ and LPS stimulation (Huang *et al*., 2018; Li *et a*l., 2021; Murugesan *et a*l., 2022; **Figure 4.1**).

Previous studies have reported the upregulation of various ISGs in M1-activated macrophages, including interferon-inducible proteins (IFIT1, IFIT2 and IFIT3), and 2'-5'-oligoadenylate synthase (OAS)-like protein 1 (OASL1) (Huang *et al*., 2018; Li *et al*., 2021; Murugesan *et a*l., 2022). This study observed the upregulation of several ISGs including OASL1, interferon-activable proteins 202, 204, and 205B (IFI2, IFI4, IFI5B) and interferon-induced transmembrane protein 3 (IFM3). This research, along with that of others, revealed protein-protein interaction networks involving these ISGs and other upregulated proteins such as ISG15, guanylate-binding protein 3 (GBP3) and

the IL-6 binding protein, CCAAT/enhancer-binding protein beta (C/EBPβ), a key regulator of macrophage polarisation (Huang *et al*., 2018; Li *et al*., 2021; Murugesan *et a*l., 2022). These proteins collectively orchestrate the polarisation and inflammatory responses of M1 macrophages, making them potential valuable biomarkers.

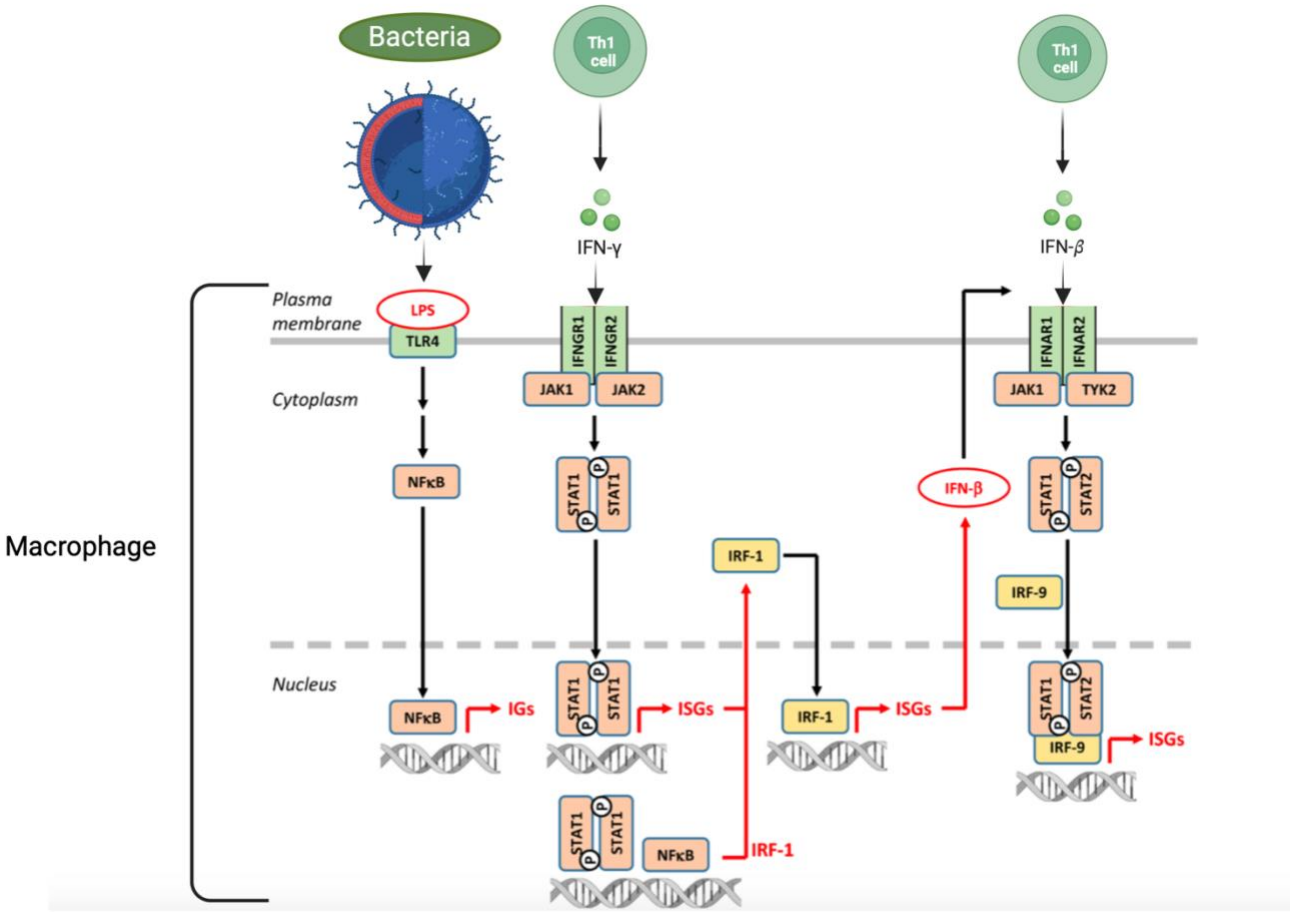


Figure 4.1: Proposed mechanism for LPS and IFN signalling in activated M1 macrophages. Figure depicts the key signalling pathways activated in macrophages upon stimulation with LPS (from gram-negative bacteria) and IFN-γ/β (from Th1 cells). These signalling cascades involve several transcription factors (NF-κB, IRF-1, IRF-9), ultimately leading to the transcription of inflammatory genes (IGs) and production of ISGs. Thus contributing to the M1 macrophage phenotype. Adapted from Huang *et al.,* 2018. Created using BioRender.com.

Among proteins that were upregulated in M1 macrophages in this study, proteins including CCL2, cis-aconitate decarboxylase 1 (IRG1), the plasminogen activator inhibitor type 2 (PAI-2/SerpinB2), and prostaglandin synthase 2 (PGH2/COX-2) have been reported as M1 biomarkers or cytokines/chemokines in previous studies (Reales-Calderon *et al*., 2014; Shea-Donohue, Zhao and Antalis, 2014; Gschwandtner, Derler and Midwood, 2019; Li *et al*., 2021; Murugesan *et al*., 2022). The C-C motif chemokine, CCL2, has been established as a marker of M1 polarisation (Murugesan *et al.,* 2022). It plays a vital role in monocytes and macrophages recruitment to sites of inflammation by inducing the production of inflammatory cytokines such as TNF-α and IL-6 (Gschwandtner, Derler and Midwood, 2019; Zhou *et al*., 2020). TNF-α, a potent cytokine, is essential for eliminating pathogens and inhibiting tumour growth (Li *et al*., 2023). IL-6, on the other hand, activates the STAT3 signalling pathway, a key driver of M1 macrophage polarisation (Chen *et al*., 2023). IRG1 is an enzyme that converts cis-aconitate, a crucial intermediate in the tricarboxylic acid (TCA) cycle, to itaconic acid (Wu *et al*., 2014; Murugesan *et a*l., 2022). Increased IRG1 and itaconic acid production are hallmarks of activated macrophages *in vitro* and *in vivo* (Wu *et al*., 2014). Itaconic acid exerts a spectrum of immunomodulatory effects, including antimicrobial activity and inhibition of the growth of intracellular pathogens (Wu *et al*., 2014; Murugesan *et al.,* 2022).

Furthermore, PAI-2/SerpinB2 is an important regulator of inflammatory responses, and its induction is critical during viral, bacterial and parasitic infections (Reales-Calderon *et al*., 2014). Shea-Donohue, Zhao and Antalis (2014) reported that PAI-2 expression is upregulated in macrophages following LPS stimulation through an NF-κB-dependant mechanism. This upregulation is crucial for maintaining TLR4 activation and preventing premature macrophage death, thereby ensuring the persistence of innate immune responses (Shea-Donohue, Zhao and Antalis, 2014; Li *et al*., 2021). PGH2/COX-2 is highly expressed in M1 macrophages and plays an important role in producing prostaglandins (Sheppe *et al*., 2018; Jia *et al*., 2023). Prostaglandins are crucial inflammatory mediators which promote the expression of key M1 markers (Sheppe *et al*., 2018; Jia *et al*., 2023). These molecules are involved in bacterial infections, likely contributing to bacterial clearance by macrophages (Sheppe *et al*., 2018; Jia *et al*., 2023). The presence of these well-characterised M1 markers in this

study provides strong support for the successful induction and activation of the M1 macrophage phenotype in RAW264.7 cells.

Phagocytosis

M1 macrophage activation induced by IFN-γ and LPS is characterised by the robust production of ROS and RNS, crucial for antimicrobial and antitumour activities (Pérez and Rius-Pérez, 2022). These reactive molecules play a pivotal role in activating redox-sensitive signalling pathways, including NF-κB and mitogen-activated protein kinase (MAP kinase), driving the inflammatory response (Tan *et al*., 2016; Griess *et al*., 2020; Pérez and Rius-Pérez, 2022). Nicotinamide adenine dinucleotide phosphate (NADPH) oxidases (NOXs), a large family of proteins, are primary drivers of ROS production (Pérez and Rius-Pérez, 2022). Specifically, NOX2 has been reported to be upregulated in M1 macrophages (Kumar *et al*., 2016; Pérez and Rius-Pérez, 2022). The current study observed increased expression of cytochrome b-245 alpha chain (CY24A), a crucial component of the NOX2 complex responsible for superoxide generation (Pérez and Rius-Pérez, 2022). This type of ROS is directly released inside phagocytic vesicles and is essential for killing bacteria and pathogens (Senevirathne *et al*., 2023). NOX2-dependant ROS production is not only essential for direct pathogen killing within phagocytic vesicles but also plays a critical role in activating autophagy, a key cellular process for pathogen clearance which is stimulated by TLRs in M1 macrophages (Deretic, 2012; Pérez and Rius-Pérez, 2022). This is supported by the upregulation of autophagy-related proteins such as Reticulophagy regulator 1 (RETR1) and RING finger protein 18 (RN185), in M1 macrophages in this study (Tang *et al*., 2011; Wilson and McCormick, 2024).

Furthermore, M1 macrophage activation triggers the production of NO through the activation of cytokine signalling pathways, including IFN-γ, TNF-α and TLR signalling (Huang *et al*., 2012; Pérez and Rius-Pérez, 2022). NO production significantly enhances the phagocytic and cytotoxic capabilities of M1 macrophages, enabling them to effectively eliminate pathogens and tumour cells (Hibbs *et al*., 1988; Huang *et al*., 2012; Pérez and Rius-Pérez, 2022). These findings are supported by our

observations of increased NO production and enrichment of IFN-γ, TNF-α and TLR signalling pathways in RAW264.7 macrophages stimulated to the M1 phenotype. Overall, these observations highlight the critical role of ROS and RNS production in M1 macrophage function, emphasising their importance in antimicrobial defence and immune responses.

Phagocytosis of pathogens and apoptotic cells is additionally mediated by several receptors such as CD14, CD36, CD44, CD206, CD163, high-affinity immunoglobulin gamma Fc receptor 1 (FCGR1), macrophage scavenger receptor 1 (MSR1), and major histocompatibility complex (MHC) molecules (Onodera *et al*., 1997; Huang *et al*., 2012; Martinez-Martin *et al*., 2017; Murugesan *et al*., 2022). In Murugesan *et al.* (2022) study where quantitative proteomics was performed using human induced pluripotent stem cells (iPSC)-derived macrophages, the expression of CD14, FCGR1, CD44, MHC class I molecules (HLA-A, -B, -C, -E and -F) and MHC class II molecules (HLA-DR, -DM, -DP and -DQ) were increased in M1 iPSC-derived macrophages. Consistent with these findings, this study observed increased expression of key phagocytic receptors including CD44, FCGR1, low-affinity immunoglobulin gamma Fc region receptor 2 (FCGR2), low-affinity immunoglobulin gamma Fc region receptor 3 (FCGR3), MSR1 and MHC class I molecule, H2-L in M1 RAW264.7 macrophages.

CD44 is a transmembrane adhesion molecule known to facilitate macrophage recruitment and activation of M1 macrophages (Sun *et al*., 2022b). This process enhances inflammation and triggers macrophages to ingest large particles and clear apoptotic cells (Sun *et al*., 2022b). Fc receptors are a family of cell surface receptors that bind to the Fc region of antibodies. They play a crucial role in phagocytosis by recognising and binding to antibody-coated pathogens or particles (Onodera *et al*., 1997; Bournazos, Wang and Ravetch, 2016; Martinez-Martin *et al*., 2017). The binding triggers a cascade of signalling events that lead to the internalisation and degradation of the target (Onodera *et al*., 1997; Bournazos, Wang and Ravetch, 2016; Martinez-Martin *et al*., 2017, Mendoza-Coronel and Ortega, 2017; Junker, Gordon and Qureshi, 2020). MSR1 is a phagocytic receptor that recognises a variety of pathogen-associated molecular patterns (PAMPs). MSR1 signals through JNK, TLR2 and TLR4 to induce the production of inflammatory cytokines which mediate phagocytosis (Guo

et al., 2019; Gudgeon, Marín-Rubio and Trost, 2022; Sheng and Zhang, 2022). H2-L is involved in the processing and presentation of foreign antigens to the immune system via MHC class I molecules (Bournazos, Wang and Ravetch, 2016; Huang *et al*., 2018).

Transmembrane glycoproteins, including integrins, contribute to the multifaceted functions of M1 macrophages. They aid in immune defence through processes like antigen presentation, phagocytosis, and immunosurveillance (Bournazos, Wang and Ravetch, 2016). The findings of this study further revealed increased expression of integrins, including integrin beta-2 (ITB2), integrin alpha-5 (ITA5) and integrin alpha-L (ITAL) in M1 RAW264.7 macrophages. Moreover, heat shock proteins (HSPs) are essential for antigen processing and presentation, as well as immune responses (Zhang *et al*., 2015). These intracellular signalling molecules can be internalised by antigen-presenting cells and facilitate the presentation of antigenic peptides to T cells (Zhang *et al*., 2015). The current study demonstrated increased expression of the heat shock 70 kDa protein 4L (HS74L) in M1 macrophages compared to M0 macrophages, aligning with previous reports on IFN-γ and LPS-induced HS74L expression (Zhang *et al*., 2015). Furthermore, the upregulation of additional proteins involved in antigen processing and presentation, such as cathepsin L1 (CATL1), lysosomal acid glucosylceramidase (GBA1), antigen peptide transporter 2 (TAP2) and tapasin (TPSN), observed in this study, further supports the enhanced antigen-presenting capacity of M1 macrophages. Taken together, these findings underscore the established role of M1 macrophages as potent phagocytes and key players in immune defence.

Cellular Metabolic Processes

Macrophage differentiation and polarisation are intricately linked to metabolic pathways (Reales-Calderon *et al*., 2014; Mehta *et al*., 2021). Specifically, M1 macrophages exhibit a shift towards glycolysis and lipid biosynthesis (Lee *et al*., 2015; Li *et al*., 2021; Murugesan *et a*l., 2022; Pérez and Rius-Pérez, 2022). These macrophages utilise glucose as the primary energy source to fuel their robust

inflammatory functions, including phagocytosis and the production of NO and ROS (Lee *et al*., 2015; Batista-Gonzalez *et al*., 2020; Li *et al*., 2021; Murugesan *et a*l., 2022). This metabolic shift is exemplified by increased glycolytic flux, as evidenced by the upregulation of key enzymes such as hexokinase 3 (HK3) in this study. HK3, along with hexokinase 2 (HK2) as reported by Court *et al*. (2017), catalyse the initial and rate-limiting step of glycolysis, converting glucose to glucose-6-phosphate (Patra *et al*., 2013; Seiler *et al*., 2022). Furthermore, we observed the upregulation of glycerol kinase (GLPK) in M1 RAW264.7 macrophages. GLPK catalyses the conversion of glycerol to glycerol-3-phosphate, which can enter glycolysis or contribute to lipid biosynthesis (Tang *et al.,* 2023).

Beyond glycolysis, M1 macrophages exhibit enhanced lipid biosynthesis, providing metabolic intermediates for the synthesis of inflammatory mediators such as NO and ROS (Lee *et al*., 2015; Batista-Gonzalez *et al*., 2020; Li *et al*., 2021; Murugesan *et al*., 2022). Newly synthesised lipids are also utilised for building cellular membranes and storing energy within lipid droplets (Remmerie and Scott, 2018; Batista-Gonzalez *et al*., 2020). This study's analyses revealed increased expression of key enzymes involved in lipid metabolism, including platelet-activating factor acetylhydrolase IB subunit alpha1 (PA1B3) and platelet-activating factor acetylhydrolase 2 (PAFA2) (Carman and Han, 2006; Xu *et al*., 2021; Dong *et al*., 2024). Moreover, we observed upregulation of apolipoprotein B receptor (APOBR) in M1 RAW264.7 macrophages. Apolipoproteins such as apolipoprotein L2 (APOL2) and apolipoprotein L3 (APOL3), identified in M1 iPSC-derived macrophages, by Murugesan *et al.* (2022), play crucial roles in lipid and cholesterol metabolism and can also modulate immune responses (Murugesan *et al*., 2022). APOBR, by facilitating lipoprotein uptake, may influence lipid metabolism and contribute to the inflammatory phenotype of M1 macrophages (Georgila, Vyrla and Drakos, 2019; Murugesan *et al*., 2022). Therefore, the findings of this study further support the metabolic reprogramming observed in M1 macrophages, where glycolysis and lipid biosynthesis are crucial for their inflammatory functions.

B. Molecular Pathways associated with M2 Macrophage Polarisation

The upregulated proteins identified in this study for M2 polarised macrophages (compared to M0) were mainly involved in metabolism, detoxification of ROS, cell adhesion and migration, and regulation of cell proliferation. These pathways provided deeper insights into the molecular mechanisms influencing the M2 phenotype.

Metabolism

M1 and M2 macrophages exhibit different programs of metabolic processes. While M1 macrophages primarily rely on glycolysis, M2 macrophages utilise fatty acid oxidation to fuel mitochondrial oxidative phosphorylation (OXPHOS) (Huang *et al*., 2014; Murugesan *et al*., 2022). This metabolic shift in M2 macrophages is driven by IL-4 induced signalling pathways, particularly those involving the transcription factor STAT6 (Huang *et al*., 2014; He, Ru and Wen, 2020; Li *et al*., 2021; Murugesan *et al*., 2022). While fatty acid oxidation is crucial for M2 macrophage function, the precise source of these fatty acids remains an area of active investigation (Huang *et al*., 2014). Studies suggest that fatty acids for energy production are primarily derived from lipolysis of intracellular lipid droplets, a process initiated by adipose triglyceride lipase (ATGL) (Zechner *et al*., 2012; Kienesberger *et al*., 2013; Huang *et al*., 2014). Interestingly, this study revealed that both M1 and M2 macrophages exhibit active lipid biosynthetic pathways, suggesting that *de novo* lipid synthesis contributes to the lipid pool utilised for energy production. This highlights the importance of lipids as a crucial energy source for both macrophage phenotypes, despite their distinct metabolic routes (Huang *et al*., 2014; Batista-Gonzalez *et al*., 2020).

However, in M2 macrophages, this study observed the upregulation of key enzymes involved in lipid metabolism including cyclooxygenase-2 (COX-2/PGH2) and sphingolipid delta(4)-desaturase (DEGS1). COX-2 plays a multifaceted role in macrophage function, exhibiting context-dependent effects on inflammation (Na *et al*.,

2013; Li *et al*., 2015; Jia *et al*., 2023). In M2 macrophages, COX-2 stimulates fatty acid uptake and oxidation, contributing to an anti-inflammatory state characterised by the reduced production of pro-inflammatory mediators that are associated with M1 macrophages (Li *et al*., 2015; Pan *et al*., 2022; Vassiliou and Farias-Pereira, 2023). These metabolic shifts facilitate the M2 macrophage phenotype, promoting tissue repair and wound healing processes (Li *et al*., 2015; Pan *et al*., 2022; Vassiliou and Farias-Pereira, 2023). Notably, COX-2 overexpression in M2 macrophages has been implicated in promoting breast cancer cell proliferation and survival both *in vitro* and *in vivo* (Li *et al*., 2015).

Our previous analysis demonstrated COX-2 upregulation in M1 polarised macrophages. This observation, along with reports of COX-2 expression in both M1 and M2 macrophages, suggests a dual role for this enzyme (Na *et al*., 2013; Li *et al*., 2015; Jia *et al*., 2023). COX-2 can contribute to both pro-inflammatory (M1) and anti-inflammatory (M2) responses depending on the cellular context and the prevailing signalling environment, further highlighting plasticity and complexity of macrophage function (Na *et al*., 2013; Li *et al*., 2015; Gao *et al*., 2023). Moreover, DEGS1, an enzyme involved in sphingolipid metabolism, also contributes to the M2 macrophage preference for fatty acid oxidation as an energy source (Batista-Gonzalez *et al*., 2020; de Simone *et al*., 2023). These findings underscore the complexity of macrophage metabolism and highlight the importance of lipid metabolism in shaping the functional characteristics of both M1 and M2 macrophage phenotypes.

Detoxification of ROS

M1 macrophages, characterised by robust ROS and NO production prioritise pathogen elimination (Pérez and Rius-Pérez, 2022). However, as the phagocytic phase subsides, the focus shifts towards tissue repair and remodelling (Pérez and Rius-Pérez, 2022). In contrast, M2 macrophages exhibit a distinct profile with poor ROS and NO production (Pérez and Rius-Pérez, 2022). A key factor contributing to this shift is the upregulation of arginase-2 (ARGI2) in M2 macrophages (Barra *et a*l., 2011; Tan *et al.,* 2016). This enzyme metabolises L-arginine to L-ornithine and urea,

depleting the intracellular pool of L-arginine, a substrate essential for NO synthesis by inducible nitric oxide synthase (iNOS), leading to decreased NO production and a shift towards an anti-inflammatory phenotype (Reales-Calderon *et al*., 2014; Lee *et al*., 2015; Huang *et al*., 2018). The resulting L-ornithine supports the wound healing function of M2 macrophages, by promoting cell proliferation and tissue repair through the production of polyamines and collagen (Reales-Calderon *et al*., 2014; Lee *et al*., 2015; Huang *et al*., 2018). While essential for tissue repair, these processes can also contribute to tumour progression by promoting tumour-associated stromal remodelling, essentially leading to invasion and metastasis (Barra *et al.,* 2011; Mehta *et al*., 2021; Pérez and Rius-Pérez, 2022). Studies by Barra *et al.* (2011) and Tan *et al.* (2016) have shown that IL-4-mediated polarisation of RAW264.7 macrophages towards the M2 phenotype leads to increased arginase activity. Consistent with these findings, this study observed increased ARGI2 expression in M2 RAW264.7 macrophages.

The transition from the M1 to M2 macrophage phenotype is characterised by a reduction in ROS production (Pérez and Rius-Pérez, 2022). This shift is largely mediated by the inhibition of NOX2, as demonstrated in RAW264.7 cells by Von Knethen *et al*. (2007), resulting in decreased superoxide generation and impaired phagocytic function (Von Knethen *et al*., 2007; Pérez and Rius-Pérez, 2022). Furthermore, IL-4 exposure in macrophages has been shown to downregulate NOX2 expression, promoting their shift towards a wound-repair and tissue-remodelling phenotype (Balce *et al*., 2011; Pérez and Rius-Pérez, 2022). Consistent with these observations, this study showed increased expression of key ROS detoxification enzymes in M2 macrophages, including glutathione S-transferase P 1 (GSTP1), peroxiredoxin-1 (PRDX1) and peroxiredoxin-5 (PRDX5). GSTP1 conjugates glutathione to electrophilic compounds (Singh and Reindl, 2021; Chen *et al*., 2023). PRDX1 and PRDX5 are peroxidases which catalyse the reduction of hydrogen peroxide and organic hydroperoxides to water and alcohols, respectively (O'flaherty *et al*., 2020). These enzymes effectively neutralise ROS, preventing oxidative damage and contributing to the M2 phenotype (O'flaherty *et al*., 2020; Singh and Reindl, 2021; Chen *et al*., 2023).

Evidently, this study revealed the upregulation of mitochondrial superoxide dismutase 2 (SODM) in M2 macrophages. While SODM converts superoxide anions to hydrogen peroxide, potentially contributing to oxidative stress, emerging evidence suggests a more nuanced role for ROS in M2 polarisation (Ming *et al*., 2012; Reales-Calderon *et al.*, 2014; He *et al*., 2013; Huang *et al*., 2018; Li *et al*., 2021; Pérez and Rius-Pérez, 2022). He *et al*. (2013) demonstrated that SOD-dependent hydrogen peroxide production could contribute to M2 macrophage polarisation. Furthermore, literature suggests that ROS may be implicated in the early stages of M2 polarisation (He *et al*., 2013; Zhang *et al*., 2013; Pérez and Rius-Pérez, 2022). Consistent with this, the current study identified the upregulation of several other proteins involved in ROS generation in M2 RAW264.7 macrophages including cytochrome b-245 alpha chain (CY24A), a crucial component of the NOX2 complex responsible for superoxide generation (Pérez and Rius-Pérez, 2022). Interestingly, CY24A, previously implicated in M1 polarisation in our analysis, appears to play a dual role in macrophage polarisation (Pérez and Rius-Pérez, 2022).

Other upregulated proteins found in M2 macrophages in the current study include neutrophil cytosol factor 4 (NCF4) and endoplasmic reticulum oxidoreductin-1-like protein alpha (ERO1A). NCF4 is a component of NOXs, thus participates in generating reactive oxidant intermediates (He *et al*., 2021). ERO1A is an oxidoreductase which is involved in disulfide bond formation within the endoplasmic reticulum, leading to the production of ROS in this cellular compartment (Shergalis *et al*., 2020; Zhang and Sioud, 2023). These findings highlight a complex interplay between ROS generation and detoxification in shaping the M2 macrophage phenotype. While M2 macrophages exhibit a generally reduced oxidative environment, ROS appear to play a crucial, albeit potentially paradoxical role in their differentiation and function.

Cell Adhesion and Migration

Integrin signalling, also observed in our M1 macrophage analysis, plays a pivotal role in M2 macrophage function, particularly in regulating cell adhesion, migration and the acquisition of a pro-tissue repair phenotype (He *et al*., 2021; Li *et al*., 2022). These

functions are crucial for M2 macrophages to effectively participate in wound healing and tissue remodelling by facilitating their interaction with the extracellular matrix (ECM) and responding to environmental cues (Shu *et al*., 2020; Liu *et al*., 2024). Integrins are recognised as key regulators of M2 polarisation, particularly in disease contexts such as cancer, where they are often associated with angiogenesis and immune suppression (Martinez *et al*., 2013; Liu *et al.*, 2020; Shu *et al*., 2020; Li *et al*., 2022). By mediating cell-ECM interactions, integrins enable M2 macrophage migration to sites of injury and facilitate their participation in wound healing processes (Martinez *et al*., 2013; Liu *et al*., 2020; Shu *et al*., 2020; Li *et al*., 2022).

Integrin alpha-M (ITAM) is a well-characterised integrin that promotes M2 polarisation by activating the JAK1/STAT6 pathway, enabling M2 macrophages to perform functions related to tissue repair, angiogenesis and immune tolerance (He *et al*., 2021; Li *et al*., 2022). ITAM interacts with ligands such as fibrinogen and complement proteins to regulate cellular adhesion and migration (Martinez *et al*., 2013; Li *et al*., 2022). Martinez *et al.* (2013) and Li *et al.* (2022) confirmed the upregulation of ITAM in IL-4 activated human and mouse macrophages (M2 phenotype), which is consistent with the results of the present study.

Furthermore, the bioinformatic analyses of this study identified additional upregulated proteins in M2 macrophages that are implicated in integrin-mediated signalling, including FYN-binding protein 1 (FYB1) and zyxin (ZYX). FYB1 acts as a key adaptor protein in integrin signalling, facilitating cell adhesion and migration by linking integrin receptors to downstream signalling pathways (Geng *et al*., 2001; Wen *et al*., 2020). ZYX is a crucial component of focal adhesions, structures that connect cells to the ECM. This protein plays a vital role in cell adhesion and migration by regulating the actin cytoskeleton and facilitating cell attachment to the ECM (Geng *et al*., 2001; Wen *et al*., 2020). Thus, the current study has shown that integrin signalling plays crucial roles in both M1 and M2 macrophage functions. In M1 macrophages, integrin signalling facilitates processes like phagocytosis, while in M2 macrophages, it plays a pivotal role in regulating adhesion, migration and the acquisition of a pro-tissue repair phenotype.

These findings suggest a complex and intricate interplay of integrin signalling pathways in shaping the distinct functional phenotypes of M1 and M2 macrophages.

This study further identified increased expression of proteins that mediate cell adhesion and migration in M2 macrophages, independent of the canonical integrin pathway. These include cathepsin D (CATD), annexin A3 (ANXA3), progranulin (GRN), myocyte-specific enhancer factor 2C (MEF2C) and P2X purinoceptor 4 (P2RX4). CATD, reported to be overexpressed in M2 macrophages in Zhang *et al.* (2015) and Li *et al.* (2022) study, is a lysosomal protease involved in protein degradation. It can degrade components of the ECM such as collagen and proteoglycans, this ECM remodelling can influence cell adhesion and migration by altering cell-matrix interactions (Zhang *et al*., 2015; Li *et al*., 2022). Studies have demonstrated that increased CATD expression promotes breast cancer cell migration and invasion (Zhang *et al*., 2015). As a calcium-dependent-phospholipid-binding protein, ANXA3 interacts with actin cytoskeletal proteins, influencing cell shape and motility (Du *et al*., 2018). GRN is a growth factor which plays a role in wound healing, involving cell migration and tissue repair (Dong *et al*., 2021). MEF2C is a transcription factor which regulates the expression of genes involved in cell adhesion and migration, such as integrins and cytoskeletal proteins (Li *et al*., 2023). P2RX4 is a ligand-gated ion channel activated by ATP (Ledderose *et al*., 2018). Activation of this protein can trigger several cellular processes, including changes in intracellular calcium levels, which can influence cell adhesion and migration (Ledderose *et al.,* 2018). Thus, this study demonstrated that M2 macrophage cell adhesion and migration are regulated by a complex network of proteins, including integrins and a diverse set of integrin-independent mechanisms.

Regulation of Cell Proliferation

M2 macrophages are key contributors to tumour progression, promoting cancer cell proliferation through mechanisms such as direct cell-cell contact or by releasing growth factors like IL-10, epidermal growth factor (EGF), transforming growth factor beta (TGF-β) and vascular endothelial growth factor (VEGF) (Fujiwara *et al*., 2011;

Boutilier and Elsawa, 2021; Kerneur, Cano and Olive, 2022). This study identified several upregulated proteins associated with the regulation of cell proliferation by M2 RAW264.7 macrophages, including Bcl-2-like protein 1 (B2CL1), CAAT/enhancer-binding protein beta (C/EBPβ), Guanine nucleotide-binding protein (GBG2), high mobility group A1 (HMGA1) and high mobility group A2 (HMGA2). B2CL1 is an anti-apoptotic protein that plays a crucial role in preventing cell death. By inhibiting apoptosis, B2CL1 indirectly promotes cell proliferation and survival. Overexpression of B2CL1 is frequently observed in various cancers, contributing to tumour growth and resistance to therapy (Qian *et al*., 2022). C/EBPβ is a transcription factor involved in regulating numerous genes, including those involved in the cell cycle, proliferation, differentiation and inflammation (Wang *et al*., 2022b). This protein's influence extends to macrophage polarisation, where it plays a complex, context dependant role, contributing to both M1 and M2 activation (Ruffell *et al*., 2009; Li *et al*., 2021; Wang *et al*., 2022b). C/EBPβ interacts with NF-kβ on inflammatory genes (M1) and with STAT factors on anti-inflammatory genes (M2) (Ruffell *et al*., 2009; Li *et al*., 2021; Wang *et al*., 2022b). Our observation of C/EBPβ in both our M1 and M2 macrophage polarisation analyses underscores its involvement in these macrophage phenotypes (Ruffell *et al*., 2009; Li *et al*., 2021; Wang *et al*., 2022b). GBG2 is a subunit of heterotrimeric G proteins, which play essential roles in signal transduction pathways including cell proliferation, differentiation and migration (Luo, Xiao and Yang, 2025). HMGA1 and HMGA2 are chromatin-binding proteins that regulate the expression of genes involved in the cell cycle, DNA replication and cell proliferation. Aberrant expression of HMGA1 and HMGA2 is frequently observed in various cancers, contributing to tumorigenesis and progression (Campos Gudiño, McManus and Hombach-Klonisch, 2023). These findings provide further evidence for the critical role of M2 macrophages in supporting tumour growth and highlight the complex regulatory mechanisms involved in their pro-proliferative functions.

Overall, the current study provides a comprehensive proteomic analysis of M1 and M2 polarised RAW264.7 macrophages, revealing significant protein expression changes that characterise these distinct phenotypes. Importantly, this study also established 48 hours as an optimal stimulation duration for inducing robust distinct M1 and M2 phenotypes *in vitro*. Collectively, the findings of this study provide a strong foundation

for further investigations into the molecular mechanisms underlying macrophage polarisation and their functional consequences. The differentially expressed proteins identified in this study have the potential to serve as valuable biomarkers for macrophage-associated diseases, including potentially predicting the course of cancer in future pre-clinical and clinical research.

4.2. The Cytotoxic Effects of CBD and Tamoxifen against MCF7 Breast Cancer Cells

The TME is a complex ecosystem comprising cancer cells, immune cells (of which macrophages are the most abundant), fibroblasts, endothelial cells and the extracellular matrix (Segovia-Mendoza and Morales-Montor, 2019). The response of cancer cells to therapeutic agents can significantly influence the behaviour of other cells within the TME (He *et al*., 2021; Li *et al*., 2021; Mehta *et al*., 2021; Olivas-Aguirre *et al*., 2022). Therefore, this study investigated the potential anticancer effects of CBD in combination with Tamoxifen on MCF7 cells, a representative oestrogen receptor-positive breast cancer cell line. This approach allows for a focused evaluation of the direct effects of the drug combination on cancer cell viability and proliferation before investigating their impact on the complex interactions within the TME, including macrophage activation and polarisation.

Many breast cancers are oestrogen receptor-positive and are often treated with Tamoxifen, a selective oestrogen receptor modulator (Dobovišek *et al*., 2020; Buijs *et a*l., 2023). While Tamoxifen remains a gold standard in the treatment of oestrogen receptor-positive breast cancer, its efficacy is often limited by undesirable side effects, acquired resistance and a significant impact on quality of life (Dobovišek et al., 2022; Mokoena, George and Abrahamse, 2024). To address these limitations, novel strategies are being explored to enhance the efficacy of standard cancer therapies. CBD, a phytocannabinoid traditionally used for palliative care, has emerged as a potential anticancer therapeutic agent with promising preclinical evidence (Dobovišek *et al*., 2022; Buijs *et al.*, 2023). *In vitro* and *in vivo* studies have demonstrated that

CBD can induce apoptosis, autophagy, and modulate the immune system in various cancer cell lines and animal models (Shrivastava *et al.,* 2011; Sultan, Marie and Sheweita, 2018; Kiskova *et al.,* 2019; Dobovišek *et al.,* 2020; Seltzer *et al.,* 2020; Mangal *et al.,* 2021; Dobovišek *et al.,* 2022; Ma *et al.,* 2024).

To evaluate the cytotoxic effects of CBD and Tamoxifen, MCF7 cells were treated with increasing concentrations of CBD (5, 7.5, 10 µM) alone and in combination with 2 µM Tamoxifen. This Tamoxifen concentration was previously determined in our laboratory and demonstrated the ability to induce cytotoxicity in approximately 50% of MCF7 cells, thus establishing its efficacy in reducing cell viability *in vitro* (Pather and Augustine, 2020). Recent preclinical and clinical advances have emphasised the impact of different treatment regimens (Patwardhan *et al*., 2021), thus, two models were employed to understand the efficacy of our drug treatments *in vitro*. Model 1 involved a single dose with prolonged exposure to the treatments over a 72-hour period. Model 2 utilised a regimen of daily drug replacement for a total of 72 hours. These models were selected to explore the potential effects of both once-off drug exposure and daily treatment, which may mimic different clinical scenarios and provide valuable insights into the efficacy of treatment (Patwardhan *et al*., 2021; Yadav *et al*., 2021).

In treatment model 1, where a single dose of 2 µM Tamoxifen was administered alone or in combination with various CBD concentrations (5, 7.5, 10 µM), signs of cell recovery were observed by 72 hours. This observation is consistent with the expected decline in drug concentrations due to drug metabolism and clearance within the MCF7 cells (Doyle *et al*., 1998; Cao *et al*., 2021; Zhao *et al*., 2021). Consequently, the observed cell recovery is likely primarily attributed to the diminishing cytotoxic effects of the drugs over time rather than specific synergistic or antagonistic interactions between CBD and Tamoxifen. Some studies have suggested that CBD may enhance the sensitivity of certain cancer cells to chemotherapy, but its effect on Tamoxifen-treated MCF7 cells is not yet fully understood (Almeida *et al*., 2023; Ma *et al*., 2024). To further investigate the potential interaction between CBD and Tamoxifen, we monitored the cell behaviour of MCF7 cells exposed to the daily drug replacement treatment regimen (model 2).

Early stages of cell death are often characterised by a reduction in cell size (Shrivastava *et al.,* 2011; Yan, Elbadawi and Efferth, 2020; Fu *et al*., 2023). Previous studies utilising oestrogen receptor-positive breast cancer cell lines, including MCF7 cells, have observed significant morphological alterations such as cell rounding, detachment from neighbouring cells, and loss of intercellular contact, following treatment with CBD concentrations as low as 5 µM (Shrivastava *et al.,* 2011; Sultan, Marie and Sheweita, 2018; Yan, Elbadawi and Efferth, 2020). Consistent with these findings, our data from treatment model 2, involving daily drug replacement, demonstrated a dose-dependent reduction in cell size and significant morphological changes in MCF7 cells treated with CBD alone and in combination with 2 µM Tamoxifen. Treated cells exhibited rounded morphology, decreased cell-cell adhesion, and increased intercellular spaces, indicative of cell-shrinkage and loss. These morphological changes were accompanied by a dose-dependent reduction in cell viability and increased growth inhibition across all treatment groups and time points. Using the MTT assay, Sultan, Marie and Sheweita, (2018) also showed that CBD inhibited the viability of oestrogen receptor-positive breast cancer cell lines in a dose-dependent manner by inducing apoptosis in the cells. These findings further align with previous studies demonstrating that CBD dose-dependently decreased the cell viability of not only oestrogen receptor-positive but also oestrogen receptor-negative breast cancer cell lines (Shrivastava *et al.,* 2011; Sultan, Marie and Sheweita, 2018; Dobovišek *et al*., 2022; Mokoena, George and Abrahamse, 2024).

In contrast to the single-dose treatment (model 1), the daily drug replacement regimen in model 2 maintained the cytotoxic effect of 2 µM Tamoxifen, both alone and in combination with various CBD concentrations (5, 7.5, 10 µM), over the 72-hour treatment period. This continuous drug exposure prevented cell recovery, in line with the findings by Dobovišek *et al*. (2022). Their study, utilising oestrogen receptor-positive breast cancer cell lines including T47D, demonstrated that increasing concentrations of CBD (1 – 30 µM) did not diminish Tamoxifen's efficacy. Instead, they observed a synergistic negative effect on cell viability by 48 hours, where the combined effect was greater than the sum of their individual effects. Notably, the current study using the MCF7 cell line also observed this synergistic effect. While CBD

has been studied for its potential anti-cancer properties, including its ability to modulate cell death mechanisms, its interaction with Tamoxifen in MCF7 cells requires further investigation (Seltzer *et al*., 2020; Dobovišek *et al*., 2022; Fu *et al*., 2023).

The molecular mechanisms underlying the anticancer effects of CBD and/or Tamoxifen in oestrogen receptor-positive breast cancer cells are not fully elucidated. However, CBD and other cannabinoids including tetrahydrocannabinol (THC) and cannabigerol (CBG) have been shown to interact with the endocannabinoid system in humans, which consists of cannabinoid receptors (CBRs) (Mangal *et al*., 2021; Dobovišek *et al*., 2022; **Figure 4.2**). These receptors are membrane G-protein-coupled receptors and the most prominent CBRs are cannabinoid receptor type 1 (CB1) and cannabinoid receptor type 2 (CB2). While cannabinoids, including CBD, primarily interact with these receptors, they also engage with other transmembrane proteins, such as the G protein-binding receptor 55 (GPR55). Furthermore, within the family of ion channels, transient receptor potential vanilloid receptors (TRPV1 and TRPV2) have also been identified as potential targets for cannabinoids (Seltzer *et al*., 2020; Mangal *et al*., 2021; Faiz *et al*., 2024; **Figure 4.2**).

By binding to the described receptors, CBD modulates various aspects of analgesic, metabolic and immunological functions (Kiskova *et al*., 2019; Dobovišek *et al*., 2022). Disruptions in endocannabinoid signalling have been implicated in various pathological conditions, including cancer. Several critical signalling pathways involved in cell growth, differentiation, metabolism and apoptosis interact with cannabinoid signalling (Kiskova *et al.,* 2019; Dobovišek *et al*., 2022; **Figure 4.2**). These pathways, including, AKT, EGFR and mTOR have been found to contribute to tumour development and metastasis (Almeida *et al.,* 2023; Suttithumsatid, Sukketsiri and Panichayupakaranant, 2023; **Figure 4.2**). Studies on various breast cancer subtypes have revealed that phytocannabinoids, including CBD, effectively arrest cell cycle at G0/G1 phase and induce cell death mechanisms including apoptosis and autophagy (Almeida *et al*., 2023; Suttithumsatid, Sukketsiri and Panichayupakaranant, 2023; **Figure 4.2**). Kiskova *et al.* (2019) demonstrated that CBD induces breast cancer cell death through autophagy, leading to apoptosis *in vitro*, and inhibits proliferation, invasion and angiogenesis in breast cancer cells *in vivo*. Shrivastava *et al.* (2011),

Sultan, Marie and Sheweita (2018) and Suttithumsatid, Sukketsiri and Panichayupakaranant (2023), suggested an interplay among mTOR, cyclin D, PPAR-γ and Bcl-2/caspase-3 as a mechanism of CBD-induced apoptosis in breast cancer cells.

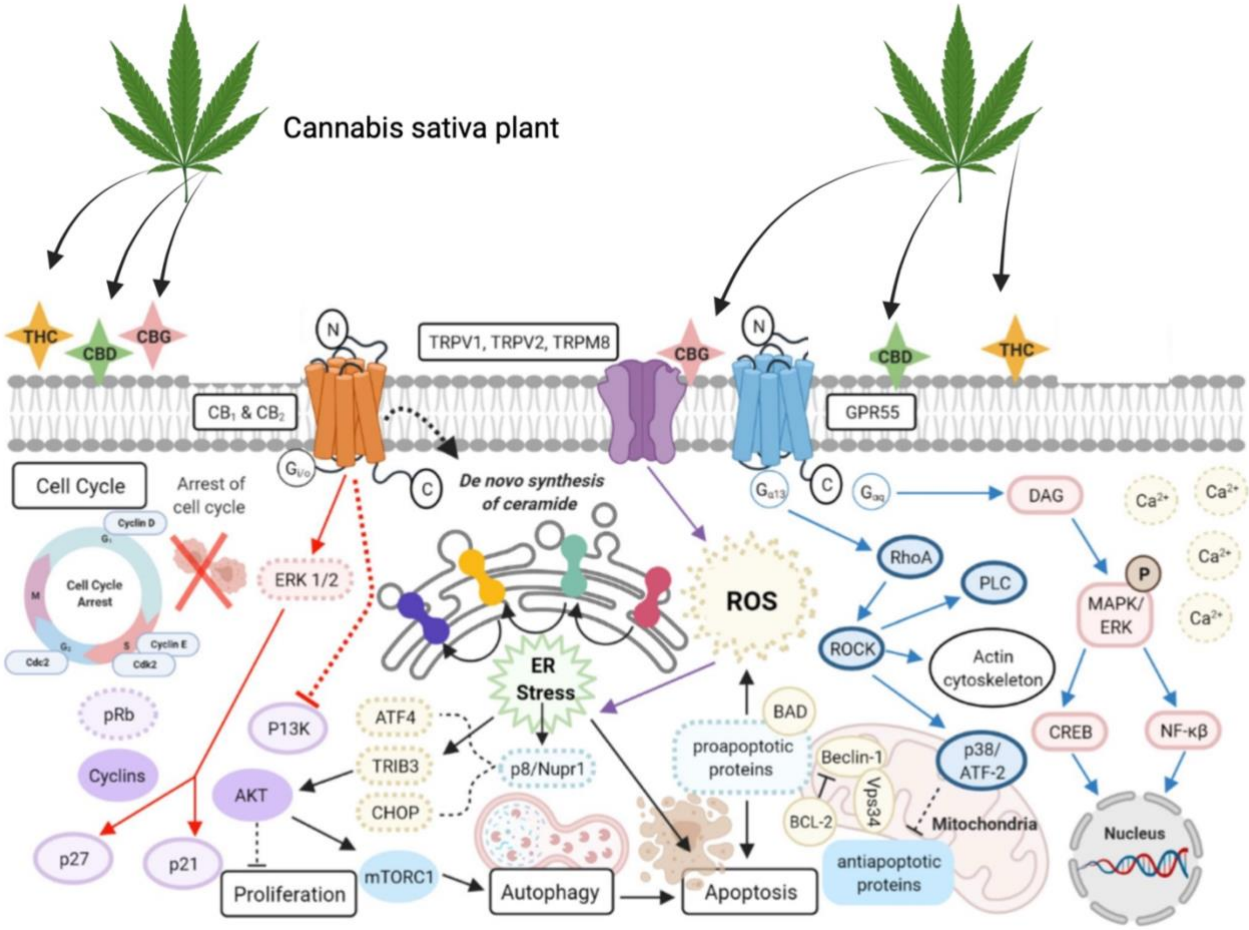


Figure 4.2: Overview of the activation and crosstalk of Cannabinoid signalling pathways. Figure illustrates the complex network signalling pathways influenced by Cannabinoids, derived from the *Cannabis sativa* plant, such as CBD. Cannabinoids can exert their effects through both cannabinoid receptors (CB1 and CB2) and non-cannabinoid receptors (such as TRPV and GPR55), modulating cellular processes like proliferation, autophagy and apoptosis. Adapted from Mangal *et al*., 2021. Created using BioRender.com.

It has been confirmed that oestrogen receptor-positive breast cancer cells express CB1 and CB2 receptors (Dobovišek *et al*., 2022). Studies have reported that Tamoxifen also exhibits moderate affinity for these receptors and acts as an inverse agonist. This process is suggested to contribute to the growth inhibitory effect of Tamoxifen in breast cancer cells (Franks *et al*., 2018; Kiskova *et al*., 2019; Dobovišek *et al*., 2022). The interaction of Tamoxifen and CBD at CBRs has been suggested to cause additive inverse effects including reducing the cell viability of oestrogen receptor-positive breast cancer cell lines (Sultan, Marie and Sheweita, 2018; Dobovišek *et al*., 2022). Additionally, Tamoxifen has been shown to induce cellular toxicity in epithelial cells, such as those found in breast tissue, by inhibiting cell proliferation and inducing apoptosis through oestrogen-receptor dependent and independent mechanisms (Franks *et al*., 2018; Sfogliarini *et al*., 2022). Taken together, these findings suggest that CBD, in combination with Tamoxifen, may offer a promising therapeutic approach for oestrogen receptor-positive breast cancer by targeting multiple signalling pathways and inducing synergistic anticancer effects.

Cell cultures are commonly used for initial evaluations of anticancer drug effectiveness (Berrouet *et al.,* 2020). These experiments provide half-maximal inhibitory concentrations (IC_{50}), which indicate drug concentrations that can inhibit tumour growth by half compared to untreated cells (Berrouet *et al*., 2020). Additionally, these drug-dose curves can inform synergistic combination therapies and drug interaction mechanisms (Tallarida, 2011; Chevereau and Bollenbach, 2015; Kahen *et al*., 2016; Berrouet *et al.,* 2020). This study's analysis of CBD concentrations (5, 7.5, 10 μM) alone or in combination with 2 μM Tamoxifen revealed lower IC_{50} values in treatment model 2 (daily drug replacement) compared to model 1 (single dose, prolonged treatment), especially after 48 and 72 hours of treatment. Comparisons of the effects of various cannabinoids including CBD, CBG, THC and cannabinol (CBN) on MCF7 cells, revealed that CBD exhibited the lowest IC_{50} values, suggesting that breast cancer cells are sensitive to CBD (Schoeman, Beukes and Frost, 2020; Alsherbiny *et al*., 2021).

Additionally, lower IC_{50} values suggest that the drug is effective at lower concentrations, potentially reducing systemic toxicity when administered to patients

(Tallarida, 2011; Chevereau and Bollenbach, 2015; Kahen *et al*., 2016; Berrouet *et a*l., 2020). For these reasons, 5 µM CBD in combination with 2 µM Tamoxifen was chosen for experimentation in this study. To induce cytotoxic effects and allow for the observation of long-term cellular responses, MCF7 cells were treated according to model 2 for a 72-hour period. This daily drug replacement approach maintains a more constant drug concentration, better reflecting *in vivo* and clinical settings (Berrouet *et al.*, 2020; Schlottmann *et al*., 2022). By determining the optimal treatment regimen on the breast cancer cells, this study established a relevant dose and duration for investigating the combinatorial effects of CBD and Tamoxifen on macrophage-cancer interactions, providing a more physiologically relevant context for the subsequent experiments.

4.3. Impact of CBD-Tamoxifen Synergy on Macrophage Behaviour

Manipulating the polarisation of tumour-associated macrophages (TAMs) towards an M1 phenotype is a promising therapeutic strategy to inhibit tumour progression (Petty and Yang, 2017; Liu *et al*., 2022; Eligini *et al*., 2023). By reducing TAM infiltration, blocking their recruitment, or inducing a phenotypic switch from M2 to M1, researchers aim to enhance anti-tumour immunity and improve treatment outcomes (Roma-Rodrigues *et al.,* 2019; Liu *et al*., 2022; Augustine, Nweke and Fru, 2022; Eligini *et al*., 2023). TAMs have emerged as a significant target for cancer immunotherapy. Their immunosuppressive and pro-tumourigenic functions make them attractive targets for novel therapeutic approaches (Jiang *et al*., 2021; Eligini *et al*., 2023). By targeting TAMs, researchers also hope to overcome the limitations of conventional therapies and develop more effective treatments for various cancers (Jiang *et al*., 2021; Eligini *et al*., 2023). In this study, we aimed to assess the synergistic effects of optimised CBD and Tamoxifen on RAW264.7 macrophages. Specifically, we investigated whether this combination treatment could induce a shift towards an M1 phenotype, thereby contributing to the anti-tumour efficacy of both drugs.

Initial experiments assessed the effect of optimised concentrations of CBD (5 µM) and Tamoxifen (2 µM), both individually and in combination, on the viability and growth of

M0 RAW264.7 macrophages. Employing a 72-hour treatment period with daily drug replacement, as previously described, ensured a more physiologically relevant assessment of the drugs against the prime target, breast cancer cells. However, Neutral red and MTT assays revealed no significant impact of CBD, Tamoxifen or their combination on macrophage viability and growth. These findings are supported by Pepe *et al*. (2021), where primary cultures of mouse peritoneal macrophages were exposed to increasing concentrations of Tamoxifen ranging from 0.001 to 10 μM. Following cell viability assessment using the MTT assay, the authors concluded that the drug concentrations were not toxic to the cells as the cell viability was not affected. Similarly, CBD has been shown to have no detrimental effects on RAW264.7 macrophage viability and growth at concentrations ranging from 0.2 μM to 20 μM CBD (Commons and Danchine *et al*., 2020). In fact, studies by Rajan *et al*. (2016) and Kim *et al*. (2023) have demonstrated a cytoprotective effect of 5 μM CBD against cell death in RAW264.7 cells, maintaining a cell viability of at least 80%.

Morphological analysis provided further insights. While untreated M0 macrophages exhibited a predominantly rounded morphology, treatment with CBD, Tamoxifen or their combination led to an increased prevalence of dendritic cells, characterised by numerous cytoplasmic extensions. These morphological features are consistent with an M1 macrophage phenotype as described previously (McWhorter *et al*., 2013; Wu *et al*., 2014; Heinrich *et al*., 2017; Li *et a*l., 2021; Liang *et al*., 2022). These observations suggest that the combination of CBD and Tamoxifen may trigger macrophage activation towards an M1-like phenotype without compromising cell viability and growth.

To further elucidate the molecular mechanisms underlying these morphological changes we performed proteomic profiling of RAW264.7 macrophages exposed to the optimised concentrations of CBD and Tamoxifen. The principal component analysis of the proteomic data revealed distinct clustering of cells treated with CBD alone, Tamoxifen alone and the combination of both drugs, suggesting that each treatment induced unique protein expression profiles in the macrophages.

A. Pathways Enriched following Treatment with 2 μM Tamoxifen

Pathway analysis of RAW264.7 macrophages exposed to 2 μM Tamoxifen revealed enrichment of proteins involved in immune responses, lipid and cholesterol metabolism.

Immune System

Tamoxifen, traditionally recognised for its role in treating oestrogen-receptor-positive breast cancer, has emerged as a multifaceted drug with potential immunomodulatory properties (Sfogliarini *et al*., 2022). While its primary mechanism of action involves targeting oestrogen receptors, recent studies have shed light on its ability to influence macrophage polarisation (Sfogliarini *et al*., 2022). Interestingly, Tamoxifen has demonstrated effectiveness against a broad spectrum of infections, including bacterial, fungal, parasitic and viral infections (Zu e*t al*., 2021; Allegretti *et al*., 2022; Sfogliarini *et al*., 2022). The antimicrobial activity of Tamoxifen likely stems from its ability to activate innate immune responses, such as enhanced phagocytosis and the production of antimicrobial peptides, characteristic features of an M1 macrophage phenotype (Zu e*t al*., 2021; Allegretti *et al*., 2022; Sfogliarini *et al*., 2022). Some studies have suggested that Tamoxifen may exert its antimicrobial effects by targeting specific cellular pathways in pathogens, such as the calmodulin-dependent signalling pathway in yeast and bacterial cells (Dolan *et al*., 2009; Butts *et al*., 2015; Sfogliarini *et al*., 2022).

This study revealed the upregulation of calcium/calmodulin-dependent protein kinase type 1 (KCC1D) in macrophages treated with Tamoxifen. KCC1D is a key regulator of cellular signalling, it is a crucial component of the calcium-calmodulin signalling pathway (Racioppi *et al*., 2017; Koga, 2024). This pathway plays a pivotal role in regulating diverse cellular functions, including immune responses in various cell types, such as T and B lymphocytes, macrophages and dendritic cells (Racioppi *et al*., 2017;

Hu *et al*., 2019; Koga, 2024). Specifically, KCC1D has been implicated in regulating various aspects of macrophage function by modulating the production and release of inflammatory cytokines such as TNF-α and IL-6 (Racioppi *et al*., 2017; Hu *et al*., 2019; Koga, 2024). This protein has also been shown to regulate cytoskeletal rearrangements and signalling pathways involved in phagocytosis, enhancing the ability of macrophages to engulf and eliminate pathogens (Racioppi *et al*., 2017; Hu *et al*., 2019; Koga, 2024). By upregulating KCC1D, the results of this study suggest that Tamoxifen may enhance the activation of macrophage functions associated with the M1 phenotype.

Further supporting the immunomodulatory abilities of Tamoxifen, this study identified the upregulation of mitogen-activated protein kinase kinase 5 (MP2K5/MKK5). MP2K5/MKK5, a key component of the mitogen-activated protein (MAP) kinase signalling pathway, is activated by upstream signals including those originating from toll-like receptors (TLRs) (Yang *et al*., 2014; Neamatallah, 2019; Hu *et al*., 2023). This pathway plays a crucial role in regulating inflammatory responses by controlling the production of cytokines such as IL-1β, IL-6 and TNF-α, in response to stimuli like bacterial lipopolysaccharides (LPS) (Yang *et al*., 2014; Neamatallah, 2019; Hu *et al*., 2023). This activation of the MAP kinase pathway, particularly through MP2K5/MKK5, contributes significantly to the amplification of inflammatory signalling within macrophages, ultimately driving M1 polarisation (Yang *et al*., 2014; Neamatallah, 2019; Hu *et al*., 2023).

Cellular Metabolism

Notably, recent studies have extended the immunomodulatory effects of Tamoxifen to include metabolic reprogramming in macrophages (Pepe *et al*., 2021; Sfogliarini e*t al*., 2022). As previously described, M1 macrophages rely on glycolysis and lipid metabolism for energy production, a metabolic shift crucial for their activation and inflammatory cytokine production (Reales-Calderon *et al*., 2014; Cao *et al*., 2023). This study revealed the upregulation of fatty acid-binding protein 5 (FABP5), which plays a role in lipid metabolism and glucose homeostasis within macrophages (Hou *et*

al., 2022; Yang *et al*., 2024). This protein facilitates the uptake, transport and metabolism of fatty acids within the cell, which can influence macrophage activation and function (Hou *et al.,* 2022; Yang *et al*., 2024). Studies show that FABP5 deficiency in macrophages can lead to altered macrophage polarisation, particularly towards an M2 phenotype (Hou *et al*., 2022; Yang *et al.,* 2024).

M1 macrophages exhibit distinct cholesterol metabolism, characterised by altered cholesterol efflux and uptake compared to M2 macrophages (Sun *et al*., 2023a). Cholesterol plays a multifaceted role in macrophage function, impacting the production of inflammatory mediators and influencing macrophage polarisation (Batista-Gonzalez *et al*., 2020; Sun *et al*., 2022a; Cao *et al*., 2023; Vassiliou and Farias-Pereira, 2023; Noble *et al*., 2024). Moreover, cholesterol is essential for maintaining cell membrane integrity and participating in crucial signalling pathways, both of which are critical for macrophage activity, including M1 functions. This study observed increased expression of key enzymes involved in the mevalonate pathway, a crucial pathway for cholesterol synthesis (Burns and Rebeck, 2010; Guerra *et al*., 2021). These proteins include farnesyl pyrophosphate synthase (FPPS), hydroxylmethylglutaryl-CoA synthase (HMCS1), diphosphomevalonate decarboxylase (MVD1), mevalonate kinase (KIME) and phosphomevalonate kinase (PMVK).

These findings collectively suggest that Tamoxifen may exert its immunomodulatory effects by modulating multiple cellular pathways, including calcium signalling, cytokine signalling and metabolic processes. This multifaceted modulation of macrophage function may contribute to the M1 phenotype and the potential therapeutic applications of Tamoxifen beyond breast cancer treatment, such as in the context of infectious diseases.

B. Pathways Enriched following Treatment with 5 µM CBD

Treatment with CBD resulted in the upregulation of proteins involved in several cellular processes including, MAP kinase and IFN-γ signalling, regulation of phagocytosis and the defence response.

MAP kinase and IFN-γ signalling

The activation of the MAP kinase pathway (also upregulated in RAW264.7 macrophages treated with Tamoxifen) and IFN-γ signalling pathway is mediated by TLR4 and JAK/STAT signalling. As previously mentioned, this is a well-established mechanism for programming macrophages to the M1 macrophage phenotype (Huang *et al*., 2018; Murugesan *et a*l., 2022). These pathways work together to promote the expression of key immune effector functions that play a role in host defence against pathogens and tumour surveillance (Wu *et al.,* 2014; Huang *et al*., 2018; Li *et al*., 2021; Murugesan *et al*., 2022). Additionally, the pathways are known to trigger the expression of several inflammatory mediators, including MHC class II molecules (CD80 and CD86), iNOS, IL-1β, IL-6 and TNF-α (Pérez and Rius-Pérez, 2022; Sfogliarini *et al*., 2022; Kim *et al.,* 2023).

MHC class II molecules, IL-1β and IL-6 play a crucial role in inflammatory responses and enhance macrophage phagocytic activity, further contributing to the M1 phenotype (Sfogliarini *et al*., 2022). The induction of iNOS contributes to inflammation and leads to the production of NO, which can directly kill pathogens (Kim *et al*., 2023). Furthermore, in addition to IL-1β and IL-6 production, the MAP kinase pathway is also involved in the production of TNF-α. This cytokine further supports the M1 macrophage phenotype as it plays a critical role in host defence responses. It can also induce cell death, both by apoptosis and necrosis (Song *et al*., 2023; Zhang and Sioud, 2023).

Notably, in other studies, CBD treatment (0.2 μM to 20 μM) of murine macrophages has been linked to an M1-like phenotype, characterised by the production of the above-mentioned inflammatory cytokines (Muthumalage and Rahman, 2019; Cohen, Gover and Schwartz, 2023; Sun *et al*., 2023). Additionally, single-cell analyses have shown that CBD can inhibit the alternative activation of macrophages (M2 phenotype). By shifting metabolic processes and targeting the PI3K-AKT pathway, CBD can rewire the TME and restore the intrinsic anti-tumour properties of macrophages (Sun *et al*., 2023; Wang *et al*., 2024).

This study demonstrated the upregulation of proteins involved in cytokine signalling and the inflammatory response, including C/EBPβ and PAI2/SerpinB2, which have been illustrated in our analysis of M1-activated macrophages. Induction of PAI2/SerpinB2 is essential during bacterial and viral infections, while C/EBPβ enhances IL-6 transcription (Reales-Calderon *et al*., 2014; Li *et al*., 2021). Other proteins include jupiter microtubule associated homolog 2 (JUPI2) and Protein S100-A13 (S10AD). Research suggests that JUPI2 can promote the inflammatory M1 macrophage phenotype by affecting gene expression related to inflammatory responses and increase immune responses against pathogens (Chen *et al*., 2024). Protein S10AD acts as a signalling molecule that can stimulate the activation of macrophages through the interaction with receptors like TLR4, subsequently triggering the production of inflammatory cytokines and chemokines (Xia *et al*., 2018; Singh and Ali, 2022).

Regulation of Phagocytosis

Proteins that were shown to be involved in phagocytosis from this study included CD63, gamma-adducin (ADDG) and complement component 1 Q subcomponent-binding protein (C1QBP). These proteins were upregulated in RAW264.7 macrophages following treatment with 5 µM CBD. CD63 is a surface marker expressed on activated macrophages and plays a role in antigen presentation. Studies suggest that CD63 may be involved in the process of phagocytosis, potentially aiding in the formation of the phagosome (Seto *et al*., 2009; Piao *et al*., 2018; Liyanage *et al*., 2021). ADDG plays an important role in maintaining the structural integrity of macrophages by regulating the actin cytoskeleton within the cell, primarily by capping the fast-growing ends of actin filaments, which is critical for cell shape, movement and phagocytosis, a key function of macrophages (Sahr *et al*., 2009; Kiang and Leung, 2018). Thus, ADDG helps control the length and dynamics of actin filaments within the macrophage, allowing it to effectively engulf and destroy pathogens (Sahr *et al*., 2009; Kiang and Leung, 2018). C1QBP plays a significant role in the immune system, particularly in the function of macrophages, by regulating their activity through interactions with the complement protein C1q, primarily influencing processes like phagocytosis and inflammation. By interacting with C1q, C1qbp can facilitate the

recognition and engulfment of apoptotic cells by macrophages (Bohlson *et al*., 2014; Wang *et al*., 2022b).

C. Pathways Enriched following Treatment with 2 µM Tamoxifen and 5 µM CBD

Protein-protein interactions in CBD-Tamoxifen treated macrophages revealed enrichment of pathways involved in the regulation of cytokine signalling , NO-mediated signal transduction and cellular metabolic processes. These pathways indicate an overlap with those observed in the individual treatments, demonstrating potential synergism between CBD and Tamoxifen.

Regulation of Cytokine Signalling

Both CBD and Tamoxifen individually demonstrated the ability to interact with the cytokine signalling pathways primarily mediated by TLR4. This trend was consistent when macrophages were exposed to the combination of both drugs, suggesting their collaborative potential in modulating inflammatory responses. Notably, in macrophages exposed to this combination treatment, we observed upregulation of proteins involving IFN-γ and NF-$\boldsymbol{\kappa}$B signalling, including Protein S10AD, calmodulin-1 (CALM1), calmodulin-2 (CALM2), calmodulin-3 (CALM3) and receptor-interacting serine/threonine-protein kinase 3 (RIPK3).

Protein S10AD, also overexpressed in RAW264.7 macrophages treated with 5 µM CBD, is a positive regulator of NF-$\boldsymbol{\kappa}$B signalling and interleukin-1alpha (IL-1α) production (Xia *et al*., 2018; Singh and Ali, 2022). NF-$\boldsymbol{\kappa}$B is a pivotal transcription factor that drives the expression of various proinflammatory mediators in M1 macrophages, including cytokines (IL-6, IL-1β, TNFα), chemokines (CCL2 and CXCL8), co-stimulatory molecules (CD80, CD86) and iNOS (produces nitric oxide) (Huang *et al*., 2018; Xia *et al*., 2018; Li *et al*., 2021; Murugesan *et a*l., 2022; Singh and Ali, 2022). While, IL-1α, a key player in innate immunity, plays a crucial role in combating pathogens (Huang *et al*., 2018; Li *et al*., 2021; Murugesan *et a*l., 2022).

CALM1, CALM2 and, CALM3 are calcium-binding proteins that regulate macrophage inflammatory responses. These proteins modulate the activity of transcription factors and signalling kinases, promoting TLR-mediated cytokine production by enhancing cellular responses to IFN-γ and activating the MAP kinase pathway (Dolan *et al*., 2009; Butts *et al*., 2015; Hussey, Limpitikul and Dick, 2023). As mentioned above, the calmodulin-dependent signalling pathway is also implicated in Tamoxifen's immunomodulatory abilities against bacterial and viral infections (Sfogliarini *et al*., 2022). RIPK3, a protein involved in programmed necrosis, can trigger inflammation by enhancing IFN-γ and NF-κB signalling (Qu *et al*., 2023; Zhou *et al*., 2024). Additionally, RIPK3 can mediate cell death by increasing ROS production, which stimulates macrophage phagocytosis (Qu *et al*., 2023; Zhou *et al*., 2024). These findings suggest a mechanism by which the combination of CBD and Tamoxifen may activate M1 macrophage functions by enhancing inflammatory cytokine signalling pathways.

NO-mediated Signal Transduction

As previously mentioned, NO is a definitive marker of M1 macrophages (Palmeri *et al*., 2020; Chen *et al*., 2023). This potent signalling molecule plays a crucial role in various cellular processes, including gene expression and the enhancement of host defence mechanisms (Connely 2003; Palmeri *et al.,* 2020; Drehmer *et a*l., 2022; Fujii and Osaki, 2023). M1 macrophages exert potent anti-tumour effects through various mechanisms including releasing cytotoxic molecules such as NO and ROS, leading to tumour cell death (Pan *et al*., 2020; Fujii and Osaki, 2023). They can also interact with dying cancer cells through efferocytosis to recruit additional immune cells and promote apoptosis in tumour cells by expressing inflammatory cytokines like IL-6 and TNF-α (Vanmeerbeek *et al.*, 2022; Fujii and Osaki, 2023; Zhang *et al*., 2024a).

The analysis of the current study revealed upregulation of ADDG and CD63, following treatment with CBD in combination with Tamoxifen (proteins also upregulated in CBD-treated macrophages). These proteins are implicated in phagocytosis, suggesting a

potential link to NO production (Kiang and Leung, 2018; Liyanage *et al*., 2021). Furthermore, we observed upregulation of metallothionein-1 (MT1) and metallothionein-2 (MT2), proteins known to mediate NO signalling (Irey *et al*., 2019; Dai *et al*., 2021). Notably, these proteins have been shown to regulate STAT1 signalling pathways, which are crucial for M1 macrophage polarisation (Irey *et al*., 2019; Dai *et al*., 2021).

Cellular Metabolic Processes

Recent studies have highlighted the profound impact of NO on macrophage metabolism (Drehmer *et al*., 2022; Fujii and Osaki, 2023). NO can induce metabolic reprogramming in M1 macrophages by inhibiting mitochondrial respiration and activating AMP-activated protein kinase (AMPK), a key regulator of cellular energy homeostasis. AMPK activation subsequently promotes glycolysis, providing the necessary energy to support the enhanced metabolic demands of activated M1 macrophages (Drehmer *et al*., 2022; Fujii and Osaki, 2023). Consistent with this metabolic reprogramming, we observed the upregulation of gamma-enolase (ENOG) in macrophages treated with the combination of CBD and Tamoxifen. ENOG is a key glycolytic enzyme, and its upregulation supports the enhanced glycolytic activity observed in M1 macrophages (Gao *et al*., 2023). Furthermore, we observed upregulation of FPPS, also upregulated in Tamoxifen-treated macrophages, and isoamyl acetate-hydrolyzing esterase 1 (IAH1). These enzymes are involved in cholesterol biosynthesis and the lipid catabolic process, respectively (Masuya *et al*., 2020; Guerra *et al*., 2021). These findings underscore the importance of both metabolic processes as alternative energy sources for M1 macrophages (Masuya *et al*., 2020; Guerra *et al*., 2021).

While the immunomodulatory effects of CBD and Tamoxifen on macrophage polarisation remain an area of active research, the findings of this study suggest that these compounds can induce a shift towards the M1 phenotype in RAW264.7 macrophages. This appears to involve the activation of multiple mechanisms. Significantly, proteomic analysis revealed the involvement of the TLR4 signalling axis

in macrophages treated with CBD and Tamoxifen, both individually and in combination. TLR4 signalling plays a crucial role in defining M1 macrophage polarisation, enhancing key functions such as phagocytosis, antigen presentation, and the production of pro-inflammatory cytokines, ultimately driving a robust immune response. Furthermore, the upregulation of several key proteins involved in immune responses and cellular metabolism, as observed in the current study, provides further insights into the mechanism underlying this M1 polarisation. These findings suggest that CBD and Tamoxifen may exert their effects by activating key signalling pathways and upregulating effector molecules, thereby effectively driving M1 macrophage polarisation and promoting a robust immune response against pathogens and tumour cells.

4.4. A Novel Role for CBD and Tamoxifen: Enhancing Macrophage Phagocytosis

Macrophage-mediated engulfment of cancer cells is a crucial component of innate anticancer immunity. Immunotherapy strategies that can enhance the phagocytic capacity of macrophages have gained significant interest (Nam *et al*., 2019; Vanmeerbeek *et al.,* 2022). To effectively elicit anti-tumour immunity, macrophages must efficiently internalise tumour-specific antigens. This process is essential for activating adaptive immune responses and ultimately leading to tumour cell elimination (Jiang *et al*., 2021; Khalaji *et al*., 2023). By monitoring the uptake of tumour cells by macrophages, researchers can evaluate the potential of different therapeutic interventions to enhance anti-tumour immunity.

To fully comprehend the tumour-modulating role of macrophages, it is crucial to assess the molecular interactions between these cells. However, the intricate nature of the TME and the diverse functions of tumour-associated macrophages have hindered *in vivo* investigations (Martinez-Martin *et al*., 2017; Mas-Rosario *et al*., 2023). Consequently, there is a growing need for *in vitro* models to study these cell-cell interactions. Cell co-culture systems have emerged as valuable tools for stimulating the TME. The current study, which combined microscopy and spectrophotometry, offers significant insights into these interactions. Although this study utilised murine

macrophages, we and others, have shown that these cells can effectively interact with and respond to human-derived cancer cells (Barra *et al.,* 2011; Martinez-Martin *et al*., 2017; Mas-Rosario *et al*., 2023).

To explore the interactions between breast cancer cells and macrophages in response to 5 μM CBD and/or 2 μM Tamoxifen, co-cultures of M0 RAW264.7 macrophages and MCF7 breast cancer cells were established and treated according to the optimised 72-hour, daily replacement treatment regimen. IFN-γ and LPS-stimulated macrophages (M1 phenotype) served as a positive control for phagocytosis (Chen *et al*., 2023; Strizova *et al*., 2023; Stavrou and Constantinidou, 2024).

Phagocytosis, a fundamental cellular process, involves the extension of pseudopodia by macrophages, which surround and internalise target particles (Onodera *et al*., 1997; Martinez-Martin *et al*., 2017). The efficiency of this process hinges on the interaction between particle surface ligands and specific receptors located on the membranes of the pseudopodia (Onodera *et al*., 1997; Martinez-Martin *et al*., 2017). The dendritic morphology of macrophages, characterised by numerous cellular extensions, significantly enhances phagocytosis by increasing the surface for receptor-ligand interactions (Onodera *et al*., 1997; McWhorter *et al*., 2013; Martinez-Martin *et al*., 2017; Zhang *et al*., 2017; Khalaji *et al*., 2023). In this study, both M0 and M1 RAW264.7 macrophages exhibited a dendritic morphology following treatment with CBD and/or Tamoxifen, consistent with previous findings (McWhorter *et al*., 2013; Wu *et al*., 2014; Heinrich *et al*., 2017; Li *et a*l., 2021; Liang *et al*., 2022; Oates *et al*., 2023). This observation suggests that the treatments may have enhanced phagocytic capacity in M0 macrophages, potentially shifting their phenotype towards a more M1-like state.

Microglia, often referred to as the brain's resident macrophages, play a critical role in maintaining homeostasis in the central nervous system (Yekhtin *et al.,* 2022). These cells are responsible for immune responses, surveillance and phagocytosis of cellular debris, and synaptic pruning. Hassan *et al.* (2014) demonstrated that CBD significantly enhanced phagocytosis in both mouse microglia and RAW264.7 macrophages. This suggests that CBD may have a broader impact on phagocytic activity across different

cell types. The mechanism underlying this effect appears to involve the transient receptor potential cation channel subfamily V member 2 and 1 (TRPV1) and (TRPV2), followed by the activation of phosphoinositide-3-kinase (PI3K). However, further research is required to fully elucidate the downstream signalling pathways involved in this process (Hassan *et al*., 2014; Yekhtin *et a*l., 2022; Martini *et al*., 2023). Other studies have demonstrated that RAW264.7 macrophages express cannabinoid receptor 1 (CB1), highlighting a potential role for the endocannabinoid system in regulating macrophage function. Upregulation of CB1 receptors may contribute to increased phagocytic activity in macrophages. However, further research is needed to assess the precise mechanisms underlying this effect (Yeisley, Arabiyat and Hahn, 2021).

Additionally, Anil *et al.* (2021) reported that CBD treatment induced macrophage polarisation and increased phagocytosis *in vitro*, accompanied by the upregulation of CD36 and FcγRII expression. CD36, a scavenger receptor, and FcγRII, a receptor for IgG-opsonised particles, play crucial roles in phagocytosis (Anil *et al*., 2021). As previously demonstrated, Fc receptors were enriched in our analysis of M1 macrophages. The FcγRII receptor binds to the Fc region in IgG antibodies that have opsonised target particles, such as bacteria, viruses or apoptotic cells. This binding triggers a cascade of intracellular signalling events that lead to the engulfment and internalisation of the target particle by the macrophage. By recognising and binging to IgG-coated particles, FcγRII enhances the efficiency of phagocytosis (Onodera *et al*., 1997; Martinez-Martin *et al*., 2017; Anil *et al*., 2021). Our analysis of M1 polarisation identified additional mechanisms involved in mediating macrophage phagocytosis, involving integrin signalling. Integrins are known to contribute to immune defence through processes like antigen presentation, phagocytosis and immunosurveillance (Bournazos, Wang and Ravetch, 2016). Notably, our analysis of macrophages treated with CBD alone and in combination with Tamoxifen further corroborate these findings. These treatments upregulated the expression of proteins crucial for phagocytosis, including CD63, ADDG and C1QBP. This suggests that CBD alone and in combination with Tamoxifen enhances phagocytic activity in RAW264.7 macrophages by modulating the expression of these key receptors and proteins, which ultimately drive M1 macrophage polarisation.

Interestingly, Tamoxifen has been shown to exhibit immunomodulatory effects beyond its traditional role in oestrogen receptor-positive breast cancer (Pepe *et al*., 2021). Studies revealed that Tamoxifen can induce oestrogen receptor alpha (ER-α) and G protein-coupled oestrogen receptor (GPER1)-independent immunomodulatory effects in macrophages, modifying cellular polarisation through nuclear factor erythroid 2-related factor 2 (NRF2) (Pepe *et al*., 2021; Sfogliarini *et al*., 2022). The transcription factor NRF2 plays a crucial role in macrophage activation. During inflammation or infection, NRF2 activation enhances bacterial clearance through increased phagocytosis and modulates the expression of inflammatory mediators, including NO and ROS, which are essential for pathogen killing (Pepe *et al*., 2021; Sfogliarini *et al*., 2022). Additionally, Tamoxifen has been observed to potentiate phagocytosis and enhance the response to LPS, leading to increased production of inflammatory cytokines such as TNF-α and IL-1β. This effect is further amplified by the activation of caspase-1, which sustains IL-1β production (Zu e*t al*., 2021; Allegretti *et al*., 2022; Sfogliarini *et al*., 2022). The proteomic analysis in this study indicated the upregulation of proteins involved in cytokine signalling pathways associated with the activation of TLR4 in cells exposed to 2 µM Tamoxifen. These pathways drive increased production of inflammatory mediators, including NO, TNF-α, IL-1β and IL-6. These findings collectively suggest that Tamoxifen may potentiate the macrophage response to pathogens and tumour cells by promoting M1 polarisation and augmenting phagocytic activity (Pepe *et al*., 2021; Sfogliarini *et al*., 2022).

Furthermore, this study observed the cytotoxic effects of CBD and/or Tamoxifen on MCF7 cells, consistent with studies suggesting that autophagy and apoptosis are key mechanisms underlying this cell death (Kisková *et al.,* 2019; Dobovišek *et al*., 2022; Suttithumsatid, Sukketsiri and Panichayupakaranant, 2023). The death of these cancer cells may release “eat-me” signals such as phosphatidylserine, which can activate macrophages (Volk *et al*., 2022; Khalaji *et al*., 2023). The proteomic analysis of M1 macrophages in this study revealed that activated M1 macrophages produce inflammatory mediators such as MHC class II molecules (CD80 and CD86), NO, TNF-α, IL-1β and IL-6, which contribute to an anti-tumour immune response (**Figure 4.3**). Notably, these macrophages can also engage in efferocytosis, a specialised form of

phagocytosis, to clear apoptotic tumour cells and recruit additional immune cells (Zhang *et al*., 2017; Ge, Huang and Yao, 2022; Vanmeerbeek *et al.,* 2022; Khalaji *et al*., 2023). These findings further support the observed phagocytic activity in co-cultures containing RAW264.7 macrophages and MCF7 breast cancer cells, suggesting a potential synergistic interaction between the cytotoxic effects of CBD and/or Tamoxifen on cancer cells and the subsequent activation of macrophage-mediated immune responses.

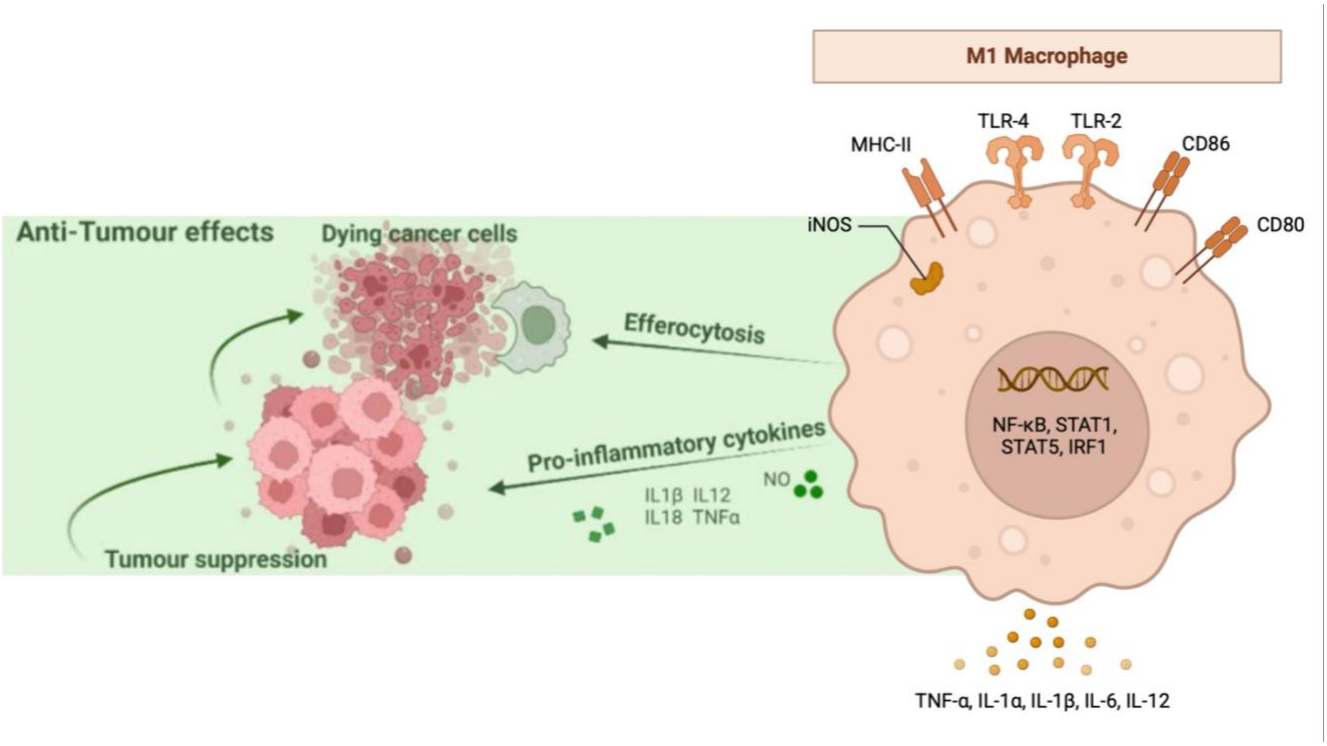


Figure 4.3: Anti-tumour effects of M1 macrophages. Activated M1 macrophages play an important role in anti-tumour immunity. They produce NO, interleukins (ILs) and TNF-α, which contribute to tumour cell killing and inflammation. M1 macrophages can engulf and eliminate dying cancer cells through a process known as efferocytosis, which also induces recruitment of other immune cells. Adapted from Vanmeerbeek *et al*., 2022. Created using BioRender.com.

Additionally, fluorescence microscopy revealed successful phagocytosis of MCF7 cells by both M0 and M1 macrophages, emphasising the importance of macrophage-mediated cancer cell clearance (Nam *et al*., 2019; Jiang *et al*., 2021). Importantly, treatment with CBD and Tamoxifen enhanced the phagocytic activity in both M0 and M1 macrophages, suggesting a potential shift towards a more potent phagocytic phenotype, even in resting macrophages (M0).

Nitrite production, a stable metabolite of nitric oxide (NO) and a hallmark of M1 macrophage activation (Palmieri *et al*., 2020; Drehmer *et al*., 2022), was significantly increased in M0 macrophage co-cultures treated with the combination of CBD and Tamoxifen compared to the untreated co-cultures. This observation confirms the synergistic effects of the two drugs in inducing M1 polarisation. As expected, co-cultures containing M1 macrophages consistently exhibited higher nitrite levels than those with M0 RAW264.7 macrophages, confirming their activated phenotype and enhanced potential for tumour clearance (Chen *et al*., 2023; Strizova *et al*., 2023; Stavrou and Constantinidou, 2024). These findings align with previous studies demonstrating higher NO production in IFN-γ/LPS treated RAW264.7 cells (M1) compared to unstimulated control groups (M0) (Aldridge *et al.,* 2008; Wang *et al*., 2015; Mas-Rosario *et al*., 2023; Jiang *et al*., 2021; Kim *et a*l., 2023).

Importantly, while CBD and/or Tamoxifen treatment did not impair the viability or growth of RAW264.7 macrophages, it significantly enhanced their functional phenotype, particularly their phagocytic and cytotoxic activity against tumour cells. These observations are supported by proteomic analysis, which revealed upregulation of proteins involved in ROS and RNS production in M1-polarised and CBD/Tamoxifen-treated macrophages. ROS and RNS production significantly enhances the phagocytic and cytotoxic capabilities of M1 macrophages, enabling them to effectively eliminate pathogens and tumour cells (Hibbs *et al*., 1988; Huang *et al*., 2012; Pérez and Rius-Pérez, 2022). Furthermore, proteomic analysis of RAW264.7 macrophages treated with the combination of CBD and Tamoxifen revealed upregulation of proteins involved in NO-mediated signal transduction, known to be crucial for phagocytosis and antimicrobial/antitumor activities (Pérez and Rius-Pérez, 2022).

These findings collectively demonstrate that the combination of CBD and Tamoxifen effectively enhances the anti-tumour functions of macrophages by promoting M1 polarisation and augmenting their phagocytic and cytotoxic capabilities, suggesting a promising therapeutic strategy for breast cancer treatment.

4.5. Conclusions

This study provides compelling evidence for the immunomodulatory and anti-cancer effects of the combination of CBD and Tamoxifen. While both agents exhibit individual immunomodulatory properties, their combined effects on macrophage function and the underlying molecular mechanisms have remained largely unexplored, highlighting the novelty of this study.

The comprehensive proteomic analysis of M1 and M2 polarised RAW264.7 macrophages performed in this study revealed significant protein expression changes that characterise these distinct phenotypes. Notably, the study identified crucial proteins involved in pathways associated with macrophage polarisation including regulation of cytokine production and signalling for M1 macrophages, and the regulation of cell adhesion and migration for M2 macrophages. These pathways have been shown to contribute to the pro-tumour and anti-tumour functions of the respective phenotypes. Importantly, this study established 48 hours as the optimal stimulation duration for inducing robust and distinct RAW264.7 M1 and M2 macrophage phenotypes *in vitro*.

Furthermore, the present study demonstrated that CBD and Tamoxifen treatment can effectively induce a shift towards the M1 phenotype in RAW264.7 macrophages without compromising cell viability. This effect appears to involve the activation of multiple mechanisms, including the TLR4 signalling pathway. Proteomic analysis revealed the upregulation of key proteins involved in immune responses, cellular metabolism, phagocytosis and the production of reactive oxygen/nitrogen species, which are crucial for M1 macrophage function and anti-tumour activity.

Ultimately, the findings of the current study demonstrate that the combination of CBD and Tamoxifen not only enhances the M1 phenotype and macrophage-mediated

tumour cell killing but also directly inhibits the growth of MCF7 breast cancer cells. This synergistic effect highlights the potential of this therapeutic combination to enhance anti-tumour immunity and improve breast cancer treatment outcomes.

4.6. Limitations of the Current Study

The research of which the current study is part, initially began during the COVID-19 pandemic, which presented significant challenges in obtaining human-derived monocytes and human macrophage cell lines (THP-1 and U937). As a result, we opted to utilise the RAW264.7 mouse macrophage cell line, a widely employed model for immunological studies (Taciak *et al*., 2018; Khabipov *et al*., 2019; Li *et al*., 2021; Shuster, 2023; Gudgeon *et al*., 2025). While cell lines offer advantages such as ease of maintenance and rapid replication, it is important to acknowledge their limitations in fully recapitulating *in vivo* conditions (Li *et al*., 2021). To address these limitations and gain deeper insights into the complex interactions within the tumour microenvironment, future research may benefit from employing more sophisticated models, including the use of volunteer-derived monocytes or macrophages, and the quantification of their phagocytic capacity. Moreover, using a non-cancerous breast epithelial cell line would also allow clarification of the impact of CBD on non-cancerous tissue. Three-dimensional cell culture systems and animal models can also provide more physiologically relevant environments, enabling a more accurate representation of tumour progression and the role of macrophages therein (Martinez-Martin *et al*., 2017; Mas-Rosario *et al.,* 2023). These complex models can also provide a better platform for assessing the efficacy of CBD and Tamoxifen in modulating macrophage behaviour and their impact on tumour growth.

References

Agyemang, D.A. (2020) *Cancer Biology Commons, Medicinal and Pharmaceutical Chemistry Commons, Natural Products Chemistry and Pharmacognosy Commons, and the Women's Health Commons Recommended Citation Recommended Citation Agyemang*, *Ursidae: The Undergraduate Research Journal at the University of Northern Colorado*. Available at: https://digscholarship.unco.edu/urjAvailableat:https://digscholarship.unco.edu/urj/vol9/iss1/2.

Aldridge, C. *et al.* (2008) "Lipopolysaccharide-Stimulated RAW 264.7 Macrophage Inducible Nitric Oxide Synthase and Nitric Oxide Production Is Decreased by an Omega-3 Fatty Acid Lipid Emulsion," *Journal of Surgical Research*, 149(2), 296–302. Available at: https://doi.org/10.1016/j.jss.2007.12.758.

Allegretti, M. *et al.* (2022) "Repurposing the estrogen receptor modulator raloxifene to treat SARS-CoV-2 infection," *Cell Death and Differentiation*. Springer Nature, 56–166. Available at: https://doi.org/10.1038/s41418-021-00844-6.

Almeida, C.F. *et al.* (2023) "Cannabidiol as a Promising Adjuvant Therapy for Estrogen Receptor-Positive Breast Tumors: Unveiling Its Benefits with Aromatase Inhibitors," *Cancers*, 15(9). Available at: https://doi.org/10.3390/cancers15092517.

Alsherbiny, M.A. *et al.* (2021) "Synergistic interactions of cannabidiol with chemotherapeutic drugs in mcf7 cells: Mode of interaction and proteomics analysis of mechanisms," *International Journal of Molecular Sciences*, 22(18). Available at: https://doi.org/10.3390/ijms221810103.

Amaral, C. *et al.* (2021) "Unveiling the mechanism of action behind the anti-cancer properties of cannabinoids in ER+ breast cancer cells: Impact on aromatase and steroid receptors," *Journal of Steroid Biochemistry and Molecular Biology*, 210. Available at: https://doi.org/10.1016/j.jsbmb.2021.105876.

Anil, S.M. *et al.* (2021) “Cannabis compounds exhibit anti-inflammatory activity in vitro in COVID-19-related inflammation in lung epithelial cells and pro-inflammatory activity in macrophages,” *Scientific Reports*, 11(1). Available at: https://doi.org/10.1038/s41598-021-81049-2.

Arzanova E, Mayrovitz HN. The Epidemiology of Breast Cancer. In: Mayrovitz HN, editor. Breast Cancer [Internet]. Brisbane (AU): Exon Publications; 2022 Aug 6. Chapter 1. PMID: 36122161.

Augustine, T.N., Nweke, E.E. and Fru, P.N. (2022) “Macrophage Polarization in the Tumor Microenvironment: Modulation and Mimicry,” in *Handbook of Cancer and Immunology*. Springer International Publishing, 1–25. Available at: https://doi.org/10.1007/978-3-030-80962-1_90-1.

Azamjah, N., Soltan-Zadeh, Y. and Zayeri, F. (2019) “Global trend of breast cancer mortality rate: A 25-year study,” *Asian Pacific Journal of Cancer Prevention*, 20(7), 2015–2020. Available at: https://doi.org/10.31557/APJCP.2019.20.7.2015.

Babar, Q. *et al.* (2023) “Targeting the tumor microenvironment: Potential strategy for cancer therapeutics,” *Biochimica et Biophysica Acta - Molecular Basis of Disease*. Elsevier B.V. Available at: https://doi.org/10.1016/j.bbadis.2023.166746.

Bai, R. and Cui, J. (2022) “Development of Immunotherapy Strategies Targeting Tumor Microenvironment Is Fiercely Ongoing,” *Frontiers in Immunology*. Frontiers Media S.A. Available at: https://doi.org/10.3389/fimmu.2022.890166.

Balce, D.R. *et al.* (2011) “Alternative activation of macrophages by IL-4 enhances the proteolytic capacity of their phagosomes through synergistic mechanisms,” *Blood*, 118(15), 4199–4208. Available at: https://doi.org/10.1182/blood-2011-01-328906.

Barra, V. *et al.* (2011) “Apoptotic cell-derived factors induce arginase II expression in murine macrophages by activating ERK5/CREB,” *Cellular and Molecular Life*

Sciences, 68(10), 1815–1827. Available at: https://doi.org/10.1007/s00018-010-0537-x.

Batista-Gonzalez, A. *et al.* (2020) “New Insights on the Role of Lipid Metabolism in the Metabolic Reprogramming of Macrophages,” *Frontiers in Immunology*, 10. Frontiers Media S.A. Available at: https://doi.org/10.3389/fimmu.2019.02993.

Behjati S, Frank MH. (2009). The effects of tamoxifen on immunity. Curr Med Chem,16(24), 3076-80. doi: 10.2174/092986709788803042. PMID: 19689284; PMCID: PMC2902982.

Berrouet, C. *et al.* (2020) “Comparison of Drug Inhibitory Effects (IC 50) in Monolayer and Spheroid Cultures,” *Bulletin of Mathematical Biology*, 82(6). Available at: https://doi.org/10.1007/s11538-020-00746-7.

Bilotta, M.T., Antignani, A. and Fitzgerald, D.J. (2022) “Managing the TME to improve the efficacy of cancer therapy,” *Frontiers in Immunology*. Frontiers Media S.A. Available at: https://doi.org/10.3389/fimmu.2022.954992.

Bohlson, S.S. *et al.* (2014) “Complement, C1Q, and C1q-related molecules regulate macrophage polarization,” *Frontiers in Immunology*. Available at: https://doi.org/10.3389/fimmu.2014.00402.

Bournazos, S., Wang, T.T. and Ravetch, J. v. (2016) “The Role and Function of Fcγ Receptors on Myeloid Cells,” *Microbiology Spectrum*, 4(6). Available at: https://doi.org/10.1128/microbiolspec.mchd-0045-2016.

Boutilier, A.J. and Elsawa, S.F. (2021) “Macrophage polarization states in the tumor microenvironment,” *International Journal of Molecular Sciences*. MDPI. Available at: https://doi.org/10.3390/ijms22136995.

Bray, F. *et al.* (2024) “Global cancer statistics 2022: GLOBOCAN estimates of incidence and mortality worldwide for 36 cancers in 185 countries,” *CA: A Cancer*

Journal for Clinicians, 74(3), 229–263. Available at: https://doi.org/10.3322/caac.21834.

Buijs, S.M. *et al.* (2023) “CBD-oil as a potential solution in case of severe tamoxifen-related side effects,” *npj Breast Cancer*, 9(1). Available at: https://doi.org/10.1038/s41523-023-00570-x.

Burns, M.P. and Rebeck, G.W. (2010) “Intracellular cholesterol homeostasis and amyloid precursor protein processing,” *Biochimica et Biophysica Acta - Molecular and Cell Biology of Lipids*, 853–859. Available at: https://doi.org/10.1016/j.bbalip.2010.03.004.

Butts, A. *et al.* (2015) “Structure-Activity Relationships for the Antifungal Activity of Selective Estrogen Receptor Antagonists Related to Tamoxifen,” *PLoS ONE*, 10(5). Available at: https://doi.org/10.1371/journal.pone.0125927.

Campos Gudiño, R., McManus, K.J. and Hombach-Klonisch, S. (2023) “Aberrant HMGA2 Expression Sustains Genome Instability That Promotes Metastasis and Therapeutic Resistance in Colorectal Cancer,” *Cancers*. Multidisciplinary Digital Publishing Institute (MDPI). Available at: https://doi.org/10.3390/cancers15061735.

Candas-Green, D. *et al.* (2020) “Dual blockade of CD47 and HER2 eliminates radioresistant breast cancer cells,” *Nature Communications*, 11(1). Available at: https://doi.org/10.1038/s41467-020-18245-7.

Cao, D. *et al.* (2021) “Potential Strategies to Improve the Effectiveness of Drug Therapy by Changing Factors Related to Tumor Microenvironment,” *Frontiers in Cell and Developmental Biology*. Frontiers Media S.A. Available at: https://doi.org/10.3389/fcell.2021.705280.

Cao, J. *et al.* (2023) “Effects of glycolysis on the polarization and function of tumor-associated macrophages (Review),” *International Journal of Oncology*, 62(6). Available at: https://doi.org/10.3892/ijo.2023.5518.

Carman, G.M. and Han, G.S. (2006) “Roles of phosphatidate phosphatase enzymes in lipid metabolism,” *Trends in Biochemical Sciences*, 694–699. Available at: https://doi.org/10.1016/j.tibs.2006.10.003.

Chen, S. *et al.* (2023) “Macrophages in immunoregulation and therapeutics,” *Signal Transduction and Targeted Therapy*. Springer Nature. Available at: https://doi.org/10.1038/s41392-023-01452-1.

Chen, X. *et al.* (2024) “JPT2 Affects Trophoblast Functions and Macrophage Polarization and Metabolism, and Acts as a Potential Therapeutic Target for Recurrent Spontaneous Abortion,” *Advanced Science*, 11(16). Available at: https://doi.org/10.1002/advs.202306359.

Chevereau, G. and Bollenbach, T. (2015) “Systematic discovery of drug interaction mechanisms,” *Molecular Systems Biology*, 11(4). Available at: https://doi.org/10.15252/msb.20156098.

Cohen, G., Gover, O. and Schwartz, B. (2023) “Phytocannabinoids Reduce Inflammation of Primed Macrophages and Enteric Glial Cells.” Available at: https://doi.org/10.20944/preprints202308.0769.v1.

Commons, D.D. and Danchine, V. (2020) *Exploring the effects of cannabidiol on RAW 264.7 macrophage Exploring the effects of cannabidiol on RAW 264.7 macrophage cell viability and inflammatory cytokine IL-6 production cell viability and inflammatory cytokine IL-6 production*. Available at: https://digitalcommons.denison.edu/studentscholarship/16.

Connelly, L. *et al.* (2003) “Macrophage endothelial nitric-oxide synthase autoregulates cellular activation and pro-inflammatory protein expression,” *Journal of Biological Chemistry*, 278(29), 26480–26487. Available at: https://doi.org/10.1074/jbc.M302238200.

Dai, H. *et al.* (2021) “Metallothionein 1: A New Spotlight on Inflammatory Diseases,” *Frontiers in Immunology*. Frontiers Media S.A. Available at: https://doi.org/10.3389/fimmu.2021.739918.

Deci, M.B. *et al.* (2019) “Carrier-Free CXCR4-Targeted Nanoplexes Designed for Polarizing Macrophages to Suppress Tumor Growth,” *Cellular and Molecular Bioengineering*, 12(5), 375–388. Available at: https://doi.org/10.1007/s12195-019-00589-w.

Deng, Y.M. *et al.* (2022) “Cannabinoid Receptor-1 suppresses M2 macrophage polarization in colorectal cancer by downregulating EGFR,” *Cell Death Discovery*, 8(1). Available at: https://doi.org/10.1038/s41420-022-01064-8.

Deretic, V. (2012) “Autophagy: An Emerging Immunological Paradigm,” *The Journal of Immunology*, 189(1), 15–20. Available at: https://doi.org/10.4049/jimmunol.1102108.

Dlamini Z. *et al*. (2023) “From Incidence to Intervention: A Comprehensive Look at Breast Cancer in South Africa”. Oncol Ther. 2024 Mar;12(1), 1-11. doi: 10.1007/s40487-023-00248-1. Epub 2023 Nov 1. PMID: 37910378; PMCID: PMC10881925.

Dobovišek, L. *et al.* (2020) “Cannabinoids and hormone receptor-positive breast cancer treatment,” *Cancers*. MDPI AG. Available at: https://doi.org/10.3390/cancers12030525.

Dobovišek, L. *et al.* (2022) “Effect of combining CBD with standard breast cancer therapeutics,” *Advances in Cancer Biology - Metastasis*, 4. Available at: https://doi.org/10.1016/j.adcanc.2022.100038.

Dolan, K. *et al.* (2009) “Antifungal activity of tamoxifen: In vitro and in vivo activities and mechanistic characterization,” *Antimicrobial Agents and Chemotherapy*, 53(8), 3337–3346. Available at: https://doi.org/10.1128/AAC.01564-08.

Domínguez-Cejudo, M.A. *et al.* (2023) “Targeting the Tumor Microenvironment in Breast Cancer: Prognostic and Predictive Significance and Therapeutic Opportunities,” *International Journal of Molecular Sciences*. Multidisciplinary Digital Publishing Institute (MDPI). Available at: https://doi.org/10.3390/ijms242316771.

Doncheva, N.T. *et al.* (2019) “Cytoscape StringApp: Network Analysis and Visualization of Proteomics Data,” *Journal of Proteome Research*, 18(2), 623–632. Available at: https://doi.org/10.1021/acs.jproteome.8b00702.

Dong, C. *et al.* (2024) “PAFAH1B3 is a KLF9 target gene that promotes proliferation and metastasis in pancreatic cancer,” *Scientific Reports*, 14(1). Available at: https://doi.org/10.1038/s41598-024-59427-3.

Dong T. *et al*. (2021) “Microglia regulate brain progranulin levels through the endocytosis/lysosomal pathway”. JCI Insight. 2021 Nov 22;6(22), 136147. doi: 10.1172/jci.insight.136147. PMID: 34618685; PMCID: PMC8663778.

Doyle, L.A. *et al.* (1998) *A multidrug resistance transporter from human MCF-7 breast cancer cells (mitoxantroneanthracyclinestransporter proteins)*. Available at: www.pnas.org.

Drehmer, D. *et al.* (2022) “Nitric oxide favours tumour-promoting inflammation through mitochondria-dependent and -independent actions on macrophages,” *Redox Biology*, 54. Available at: https://doi.org/10.1016/j.redox.2022.102350.

Du, R. *et al.* (2018) “Downregulation of annexin A3 inhibits tumor metastasis and decreases drug resistance in breast cancer,” *Cell Death and Disease*, 9(2). Available at: https://doi.org/10.1038/s41419-017-0143-z.

Elbaz M. *et al*. (2015) “Modulation of the tumor microenvironment and inhibition of EGF/EGFR pathway: novel anti-tumor mechanisms of Cannabidiol in breast cancer”.

Mol Oncol. 2015 Apr;9(4), 906-19. doi: 10.1016/j.molonc.2014.12.010. Epub 2015 Jan 19. PMID: 25660577; PMCID: PMC4387115.

Eligini, S. *et al.* (2023) “Macrophage Phenotyping in Atherosclerosis by Proteomics,” *International Journal of Molecular Sciences*. MDPI. Available at: https://doi.org/10.3390/ijms24032613.

Faiz, M.B. *et al.* (2024) “Exploring the therapeutic potential of cannabinoids in cancer by modulating signaling pathways and addressing clinical challenges,” *Discover Oncology*. Springer Science and Business Media B.V. Available at: https://doi.org/10.1007/s12672-024-01356-8.

Franks, L.N. *et al.* (2018) “The tamoxifen derivative ridaifen-B is a high affinity selective CB 2 receptor inverse agonist exhibiting anti-inflammatory and anti-osteoclastogenic effects,” *Toxicology and Applied Pharmacology*, 353, 31–42. Available at: https://doi.org/10.1016/j.taap.2018.06.009.

Fu, Z. *et al.* (2023) “Cannabidiol regulates apoptosis and autophagy in inflammation and cancer: A review,” *Frontiers in Pharmacology*. Frontiers Media S.A. Available at: https://doi.org/10.3389/fphar.2023.1094020.

Fujii, J. and Osaki, T. (2023) “Involvement of Nitric Oxide in Protecting against Radical Species and Autoregulation of M1-Polarized Macrophages through Metabolic Remodeling,” *Molecules*. MDPI. Available at: https://doi.org/10.3390/molecules28020814.

Fujiwara, T. *et al.* (2011) “Macrophage infiltration predicts a poor prognosis for human ewing sarcoma,” *American Journal of Pathology*, 179(3), 1157–1170. Available at: https://doi.org/10.1016/j.ajpath.2011.05.034.

Gao, L. *et al.* (2023) “Mediation of PKM2-dependent glycolytic and non-glycolytic pathways by ENO2 in head and neck cancer development,” *Journal of Experimental*

and Clinical Cancer Research, 42(1). Available at: https://doi.org/10.1186/s13046-022-02574-0.

García-Morales, L. *et al.* (2023) “CBD Inhibits In Vivo Development of Human Breast Cancer Tumors,” *International Journal of Molecular Sciences*, 24(17). Available at: https://doi.org/10.3390/ijms241713235.

Ge, Y., Huang, M. and Yao, Y.M. (2022) “Efferocytosis and Its Role in Inflammatory Disorders,” *Frontiers in Cell and Developmental Biology*. Frontiers Media S.A. Available at: https://doi.org/10.3389/fcell.2022.839248.

Geng, L. *et al.* (2001) *Adaptor FYB (Fyn-binding protein) regulates integrin-mediated adhesion and mediator release: Differential involvement of the FYB SH3 domain*. Available at: www.pnas.orgcgidoi10.1073pnas.191378198.

Georgila, K., Vyrla, D. and Drakos, E. (2019) “Apolipoprotein A-I (ApoA-I), immunity, inflammation and cancer,” *Cancers*. MDPI AG. Available at: https://doi.org/10.3390/cancers11081097.

Glueck, D.H. *et al.* (2008) “Exact calculations of average power for the Benjamini-Hochberg procedure,” *International Journal of Biostatistics*, 4(1). Available at: https://doi.org/10.2202/1557-4679.1103.

Gomez-Gutierrez, J.G. *et al.* (2021) “The neutral red assay can be used to evaluate cell viability during autophagy or in an acidic microenvironment in vitro,” *Biotechnic and Histochemistry*, 96(4), 302–310. Available at: https://doi.org/10.1080/10520295.2020.1802065.

González-Mariscal, I. *et al.* (2022) “Abnormal cannabidiol ameliorates inflammation preserving pancreatic beta cells in mouse models of experimental type 1 diabetes and beta cell damage,” *Biomedicine and Pharmacotherapy*, 145. Available at: https://doi.org/10.1016/j.biopha.2021.112361.

Griess, B. *et al.* (2020) “Scavenging reactive oxygen species selectively inhibits M2 macrophage polarization and their pro-tumorigenic function in part, via Stat3 suppression,” *Free Radical Biology and Medicine*, 147, 48–60. Available at: https://doi.org/10.1016/j.freeradbiomed.2019.12.018.

Gschwandtner, M., Derler, R. and Midwood, K.S. (2019) “More Than Just Attractive: How CCL2 Influences Myeloid Cell Behavior Beyond Chemotaxis,” *Frontiers in Immunology*. Frontiers Media S.A. Available at: https://doi.org/10.3389/fimmu.2019.02759.

Gudgeon, J. *et al.* (2025) “Mass spectrometry–based proteomic exploration of diverse murine macrophage cellular models,” *Life Science Alliance*, 8(1), e202402760. Available at: https://doi.org/10.26508/lsa.202402760.

Gudgeon, J., Marín-Rubio, J.L. and Trost, M. (2022) “The role of macrophage scavenger receptor 1 (MSR1) in inflammatory disorders and cancer,” *Frontiers in Immunology*. Frontiers Media S.A. Available at: https://doi.org/10.3389/fimmu.2022.1012002.

Guerra, B. *et al.* (2021) “The Mevalonate Pathway, a Metabolic Target in Cancer Therapy,” *Frontiers in Oncology*. Frontiers Media S.A. Available at: https://doi.org/10.3389/fonc.2021.626971.

Guo, M. *et al.* (2019) “Triggering MSR1 promotes JNK-mediated inflammation in IL-4-activated macrophages,” *The EMBO Journal*, 38(11). Available at: https://doi.org/10.15252/embj.2018100299.

Hao, M. *et al.* (2023) “The Interaction between Macrophages and Triple-negative Breast Cancer Cells Induces ROS-Mediated Interleukin 1α Expression to Enhance Tumorigenesis and Metastasis,” *Advanced Science*, 10(29). Available at: https://doi.org/10.1002/advs.202302857.

Hassan, M.M. *et al.* (2017) “Estrogen Replacement Reduces Risk and Increases Survival Times of Women With Hepatocellular Carcinoma,” *Clinical Gastroenterology and Hepatology*, 15(11), 1791–1799. Available at: https://doi.org/10.1016/j.cgh.2017.05.036.

Hassan, S. *et al.* (2014) “Cannabidiol enhances microglial phagocytosis via transient receptor potential (TRP) channel activation,” *British Journal of Pharmacology*, 171(9), 2426–2439. Available at: https://doi.org/10.1111/bph.12615.

He, C. *et al.* (2013) “Accelerated development of pulmonary fibrosis via Cu,Zn-superoxide dismutase-induced alternative activation of macrophages,” *Journal of Biological Chemistry*, 288(28), 20745–20757. Available at: https://doi.org/10.1074/jbc.M112.410720.

He, F., Ru, X. and Wen, T. (2020) “NRF2, a transcription factor for stress response and beyond,” *International Journal of Molecular Sciences*. MDPI AG, 1–23. Available at: https://doi.org/10.3390/ijms21134777.

He, L. *et al.* (2021) “Global characterization of macrophage polarization mechanisms and identification of M2-type polarization inhibitors,” *Cell Reports*, 37(5). Available at: https://doi.org/10.1016/j.celrep.2021.109955.

Heaster, T.M. *et al.* (2020) “Autofluorescence imaging of 3D tumor-macrophage microscale cultures resolves spatial and temporal dynamics of macrophage metabolism,” *Cancer Research*, 80(23), 5408–5423. Available at: https://doi.org/10.1158/0008-5472.CAN-20-0831.

Heinrich, F. *et al.* (2017) “Morphologic, phenotypic, and transcriptomic characterization of classically and alternatively activated canine blood-derived macrophages in vitro,” *PLoS ONE*, 12(8). Available at: https://doi.org/10.1371/journal.pone.0183572.

Hibbs, J.B. *et al.* (1988) *NITRIC OXIDE: A CYTOTOXIC ACTIVATED MACROPHAGE EFFECTOR MOLECULE*.

Hou, Y. *et al.* (2022) “FABP5 controls macrophage alternative activation and allergic asthma by selectively programming long-chain unsaturated fatty acid metabolism,” *Cell Reports*, 41(7). Available at: https://doi.org/10.1016/j.celrep.2022.111668.

Howell, A. and Howell, S.J. (2023) “Tamoxifen evolution,” *British Journal of Cancer*. Springer Nature, 421–425. Available at: https://doi.org/10.1038/s41416-023-02158-5.

Hu, J. *et al.* (2019) “Calmodulin-dependent signalling pathways are activated and mediate the acute inflammatory response of injured skeletal muscle,” *Journal of Physiology*, 597(21), 5161–5177. Available at: https://doi.org/10.1113/JP278478.

Hu, T. *et al.* (2023) “The Activation of M1 Macrophages is Associated with the JNK-m6A-p38 Axis in Chronic Obstructive Pulmonary Disease,” *International Journal of COPD*, 18, 2195–2206. Available at: https://doi.org/10.2147/COPD.S420471.

Huang, C. *et al.* (2018) “Proteomic Identification of Interferon-Induced Proteins with Tetratricopeptide Repeats as Markers of M1 Macrophage Polarization,” *Journal of Proteome Research*, 17(4), 1485–1499. Available at: https://doi.org/10.1021/acs.jproteome.7b00828.

Huang, H. *et al.* (2021) “The immunomodulatory effects of endocrine therapy in breast cancer,” *Journal of Experimental and Clinical Cancer Research*. BioMed Central Ltd. Available at: https://doi.org/10.1186/s13046-020-01788-4.

Huang, S.C.C. *et al.* (2014) “Cell-intrinsic lysosomal lipolysis is essential for alternative activation of macrophages,” *Nature Immunology*, 15(9), pp. 846–855. Available at: https://doi.org/10.1038/ni.2956.

Hussey, J.W., Limpitikul, W.B. and Dick, I.E. (2023) “Calmodulin Mutations in Human Disease,” *Channels*. Taylor and Francis Ltd. Available at: https://doi.org/10.1080/19336950.2023.2165278.

Irey, E.A. *et al.* (2019) “JAK/STAT inhibition in macrophages promotes therapeutic resistance by inducing expression of protumorigenic factors,” *Proceedings of the National Academy of Sciences of the United States of America*, 116(25), 12442–12451. Available at: https://doi.org/10.1073/pnas.1816410116.

Jaiswal, R. *et al.* (2017) “Microparticles shed from multidrug resistant breast cancer cells provide a parallel survival pathway through immune evasion,” *BMC Cancer*, 17(1). Available at: https://doi.org/10.1186/s12885-017-3102-2.

Jia, N. *et al.* (2023) “Metabolic reprogramming of proinflammatory macrophages by target delivered roburic acid effectively ameliorates rheumatoid arthritis symptoms,” *Signal Transduction and Targeted Therapy*, 8(1). Available at: https://doi.org/10.1038/s41392-023-01499-0.

Jiang, S. *et al.* (2021) “Activation of autophagy reverses gemcitabine-induced immune inhibition of RAW264.7 macrophages by promoting TNF-α, IL-6 and MHC-II expression,” *Immunologic Research*, 69(4), 352–362. Available at: https://doi.org/10.1007/s12026-021-09210-7.

Joshi, B.P. *et al.* (2018) “Surface-Modified Macrophages Facilitate Tracking of Breast Cancer-Immune Interactions,” *ACS Chemical Biology*, 13(8), 2339–2346. Available at: https://doi.org/10.1021/acschembio.8b00509.

Junker, F., Gordon, J. and Qureshi, O. (2020) “Fc Gamma Receptors and Their Role in Antigen Uptake, Presentation, and T Cell Activation,” *Frontiers in Immunology*. Frontiers Media S.A. Available at: https://doi.org/10.3389/fimmu.2020.01393.

Kahen, E. *et al.* (2016) “Identification of clinically achievable combination therapies in childhood rhabdomyosarcoma,” *Cancer Chemotherapy and Pharmacology*, 78(2), 313–323. Available at: https://doi.org/10.1007/s00280-016-3077-8.

Karp, N.A. *et al.* (2007) “Experimental and statistical considerations to avoid false conclusions in proteomics studies using differential in-gel electophoresis,” *Molecular and Cellular Proteomics*, 6(8), 1354–1364. Available at: https://doi.org/10.1074/mcp.M600274-MCP200.

Kerneur, C., Cano, C.E. and Olive, D. (2022) “Major pathways involved in macrophage polarization in cancer,” *Frontiers in Immunology*. Frontiers Media SA. Available at: https://doi.org/10.3389/fimmu.2022.1026954.

Khabipov, A. *et al.* (2019) “RAW 264.7 Macrophage Polarization by Pancreatic Cancer Cells – A Model for Studying Tumour-promoting Macrophages,” *Anticancer Research*, 39(6), pp. 2871–2882. Available at: https://doi.org/10.21873/anticanres.13416.

Khalaji, A. *et al.* (2023) “Don’t eat me/eat me signals as a novel strategy in cancer immunotherapy,” *Heliyon*. Elsevier Ltd. Available at: https://doi.org/10.1016/j.heliyon.2023.e20507.

Kiang, K.M.Y. and Leung, G.K.K. (2018) “A Review on Adducin from Functional to Pathological Mechanisms: Future Direction in Cancer,” *BioMed Research International*. Hindawi Limited. Available at: https://doi.org/10.1155/2018/3465929.

Kienesberger, P.C. *et al.* (2013) “Myocardial triacylglycerol metabolism,” *Journal of Molecular and Cellular Cardiology*, 101–110. Available at: https://doi.org/10.1016/j.yjmcc.2012.06.018.

Kim, J.H. *et al.* (2023) “In Vitro and In Vivo Anti-Inflammatory Effects of Cannabidiol Isolated from Novel Hemp (Cannabis sativa L.) Cultivar Pink Pepper,” *Molecules*, 28(18). Available at: https://doi.org/10.3390/molecules28186439.

Kisková, T. *et al.* (2019) “Future aspects for cannabinoids in breast cancer therapy,” *International Journal of Molecular Sciences*. MDPI AG. Available at: https://doi.org/10.3390/ijms20071673.

von Knethen, A. *et al.* (2007) “PPARγ1 attenuates cytosol to membrane translocation of PKCα to desensitize monocytes/macrophages,” *Journal of Cell Biology*, 176(5), 681–694. Available at: https://doi.org/10.1083/jcb.200605038.

Koga, T. (2024) “Understanding the pathogenic significance of altered calcium-calmodulin signaling in T cells in autoimmune diseases,” *Clinical Immunology*. Academic Press Inc. Available at: https://doi.org/10.1016/j.clim.2024.110177.

Kulakova, K. *et al.* (2024) “The Contribution of Macrophage Plasticity to Inflammatory Arthritis and Their Potential as Therapeutic Targets,” *Cells*. Available at: https://doi.org/10.3390/cells13181586.

Kumar, A. *et al.* (2016) “NOX2 drives M1-like microglial/macrophage activation and neurodegeneration following experimental traumatic brain injury,” *Brain, Behavior, and Immunity*, 58, 291–309. Available at: https://doi.org/10.1016/j.bbi.2016.07.158.

Kusebauch, U. *et al.* (2023) “A comprehensive spectral assay library to quantify the Halobacterium salinarum NRC-1 proteome by DIA/SWATH-MS,” *Scientific Data*, 10(1). Available at: https://doi.org/10.1038/s41597-023-02590-5.

Lai, Y. (2017) “A statistical method for the conservative adjustment of false discovery rate (q-value),” *BMC Bioinformatics*, 18. Available at: https://doi.org/10.1186/s12859-017-1474-6.

Ledderose, C. *et al.* (2018) “Purinergic P2X4 receptors and mitochondrial ATP production regulate T cell migration,” *Journal of Clinical Investigation*, 128(8), 3583–3594. Available at: https://doi.org/10.1172/JCI120972.

Lee, K.Y. (2019) “M1 and M2 polarization of macrophages: a mini-review,” *Medical Biological Science and Engineering*, 2(1), pp. 1–5. Available at: https://doi.org/10.30579/mbse.2019.2.1.1.

Lee, W.J. *et al.* (2015) “M2 macrophage polarization mediates anti-inflammatory effects of endothelial nitric oxide signaling,” *Diabetes*, 64(8), 2836–2846. Available at: https://doi.org/10.2337/db14-1668.

Li, H. *et al.* (2023) “M2 macrophages are the origin of tumor metastasis.” Available at: https://doi.org/10.21203/rs.3.rs-2381206/v1.

Li, Hongzhong *et al.* (2015) *Cyclooxygenase-2 in tumor-associated macrophages promotes breast cancer cell survival by triggering a positive-feedback loop between macrophages and cancer cells*, *Oncotarget*. Available at: www.impactjournals.com/oncotarget/.

Li, J.J., Tsang, J.Y. and Tse, G.M. (2021) “Tumor microenvironment in breast cancer—Updates on therapeutic implications and pathologic assessment,” *Cancers*. MDPI. Available at: https://doi.org/10.3390/cancers13164233.

Li, P. *et al.* (2021) “Comparative Proteomic Analysis of Polarized Human THP-1 and Mouse RAW264.7 Macrophages,” *Frontiers in Immunology*, 12. Available at: https://doi.org/10.3389/fimmu.2021.700009.

Li, P. *et al.* (2022) “Proteomic characterization of four subtypes of M2 macrophages derived from human THP-1 cells,” *Journal of Zhejiang University: Science B*, 23(5), 407–422. Available at: https://doi.org/10.1631/jzus.B2100930.

Li, T. *et al.* (2023) “Role of MEF2C in the Endothelial Cells Derived from Human Induced Pluripotent Stem Cells,” *Stem Cells*, 41(4), 341–353. Available at: https://doi.org/10.1093/stmcls/sxad005.

Liang, L. *et al.* (2022) “Sequential activation of M1 and M2 phenotypes in macrophages by Mg degradation from Ti-Mg alloy for enhanced osteogenesis,” *Biomaterials Research*, 26(1). Available at: https://doi.org/10.1186/s40824-022-00262-w.

Liu, H. *et al.* (2024) “Extracellular matrix (ECM) pathway involved in skin immune response of Cynoglossus semilaevis upon Vibrio vulnificus infection,” *Water Biology and Security*, 3(3). Available at: https://doi.org/10.1016/j.watbs.2024.100277.

Liu, L. *et al.* (2022) “An optimized flow cytometry panel for classifying macrophage polarization,” *Journal of Immunological Methods*, 511. Available at: https://doi.org/10.1016/j.jim.2022.113378.

Liyanage, D.S. *et al.* (2021) “Expression profiling, immune functions, and molecular characteristics of the tetraspanin molecule CD63 from Amphiprion clarkii,” *Developmental and Comparative Immunology*, 123. Available at: https://doi.org/10.1016/j.dci.2021.104168.

Lu, J. and Ma, L. (2020) “The role of tumor-associated macrophages in the development, metastasis and treatment of breast cancer,” *Pathology Research and Practice*. Elsevier GmbH. Available at: https://doi.org/10.1016/j.prp.2020.153085.

Luo, C., Xiao, Z.M. and Yang, W.L. (2025) “GNG2 inhibits brain metastases from colorectal cancer via PI3K/AKT/mTOR signaling pathway,” *Scientific reports*, 15(1), 1787. Available at: https://doi.org/10.1038/s41598-025-85592-0.

Ma, L. *et al.* (2024) “Research Progress on the Mechanism of the Antitumor Effects of Cannabidiol,” *Molecules*. Multidisciplinary Digital Publishing Institute (MDPI). Available at: https://doi.org/10.3390/molecules29091943.

Mangal, N. *et al.* (2021) “Cannabinoids in the landscape of cancer,” *Journal of Cancer Research and Clinical Oncology*. Springer Science and Business Media Deutschland GmbH, 2507–2534. Available at: https://doi.org/10.1007/s00432-021-03710-7.

Martinez, F.O. *et al.* (2013) “Genetic programs expressed in resting and IL-4 alternatively activated mouse and human macrophages: Similarities and differences,” *Blood*, 121(9). Available at: https://doi.org/10.1182/blood-2012-06-436212.

Martinez-Marin, D. *et al.* (2017) “Assessment of phagocytic activity in live macrophages-tumor cells co-cultures by Confocal and Nomarski Microscopy,” *Biology Methods and Protocols*. Oxford University Press. Available at: https://doi.org/10.1093/biomethods/bpx002.

Martini, S. *et al.* (2023) “Effects of Cannabidiol on Innate Immunity: Experimental Evidence and Clinical Relevance,” *International Journal of Molecular Sciences*. Multidisciplinary Digital Publishing Institute (MDPI). Available at: https://doi.org/10.3390/ijms24043125.

Mas-Rosario, J.A. *et al.* (2023) “Murine macrophage-based iNos reporter reveals polarization and reprogramming in the context of breast cancer,” *Frontiers in Oncology*, 13. Available at: https://doi.org/10.3389/fonc.2023.1151384.

Massi, P. *et al.* (2013) “Cannabidiol as potential anticancer drug,” *British Journal of Clinical Pharmacology*, 75(2), 303–312. Available at: https://doi.org/10.1111/j.1365-2125.2012.04298.x.

Masuya, T. *et al.* (2020) “Ablation of Iah1, a candidate gene for diet-induced fatty liver, does not affect liver lipid accumulation in mice,” *PLoS ONE*, 15(5). Available at: https://doi.org/10.1371/journal.pone.0233087.

Matallana-Surget, S., Leroy, B. and Wattiez, R. (2010) “Shotgun proteomics: Concept, key points and data mining,” *Expert Review of Proteomics*, 5–7. Available at: https://doi.org/10.1586/epr.09.101.

McAllister SD. *et al*. (2011) “Pathways mediating the effects of cannabidiol on the reduction of breast cancer cell proliferation, invasion, and metastasis”. Breast Cancer

Res Treat. 2011 Aug;129(1):37-47. doi: 10.1007/s10549-010-1177-4. Epub 2010 Sep 22. Erratum in: Breast Cancer Res Treat. 2012 May;133(1):401-4. PMID: 20859676; PMCID: PMC3410650.

McWhorter, F.Y. *et al.* (2013) “Modulation of macrophage phenotype by cell shape,” *Proceedings of the National Academy of Sciences of the United States of America*, 110(43), 17253–17258. Available at: https://doi.org/10.1073/pnas.1308887110.

Mehta, A.K. *et al.* (2021) “Macrophage Biology and Mechanisms of Immune Suppression in Breast Cancer,” *Frontiers in Immunology*. Frontiers Media S.A. Available at: https://doi.org/10.3389/fimmu.2021.643771.

Mendoza-Coronel, E. and Ortega, E. (2017) “Macrophage polarization modulates FcγR- and CD13-mediated phagocytosis and reactive oxygen species production, independently of receptor membrane expression,” *Frontiers in Immunology*, 8(MAR). Available at: https://doi.org/10.3389/fimmu.2017.00303.

Meyer, J.G. (2021) “Qualitative and Quantitative Shotgun Proteomics Data Analysis from Data-Dependent Acquisition Mass Spectrometry,” in *Methods in Molecular Biology*. Humana Press Inc., pp. 297–308. Available at: https://doi.org/10.1007/978-1-0716-1178-4_19.

Ming, X. *et al.* (2012) “Arginase II Promotes Macrophage Inflammatory Responses Through Mitochondrial Reactive Oxygen Species, Contributing to Insulin Resistance and Atherogenesis,” *Journal of the American Heart Association*, 1(4). Available at: https://doi.org/10.1161/jaha.112.000992.

Mishra, A. *et al.* (2021) “Metabolic reprograming confers tamoxifen resistance in breast cancer,” *Chemico-Biological Interactions*. Elsevier Ireland Ltd. Available at: https://doi.org/10.1016/j.cbi.2021.109602.

Moisand, A. *et al.* (2023) “Hormone Receptor Signaling and Breast Cancer Resistance to Anti-Tumor Immunity,” *International Journal of Molecular Sciences*. Multidisciplinary

Digital Publishing Institute (MDPI). Available at: https://doi.org/10.3390/ijms242015048.

Mokoena, D., George, B.P. and Abrahamse, H. (2024) “Cannabidiol Combination Enhances Photodynamic Therapy Effects on MCF-7 Breast Cancer Cells,” *Cells*, 13(2). Available at: https://doi.org/10.3390/cells13020187.

Munir, M.T. *et al.* (2021) “Tumor-associated macrophages as multifaceted regulators of breast tumor growth,” *International Journal of Molecular Sciences*. MDPI AG. Available at: https://doi.org/10.3390/ijms22126526.

Murray, P.J. (2017) “Macrophage Polarization,” *Annual Review of Physiology*. Annual Reviews Inc., 541–566. Available at: https://doi.org/10.1146/annurev-physiol-022516-034339.

Murugesan, G. *et al.* (2022) “Quantitative Proteomics of Polarised Macrophages Derived from Induced Pluripotent Stem Cells,” *Biomedicines*, 10(2). Available at: https://doi.org/10.3390/biomedicines10020239.

Muthumalage, T. and Rahman, I. (2019) “Cannabidiol differentially regulates basal and LPS-induced inflammatory responses in macrophages, lung epithelial cells, and fibroblasts,” *Toxicology and Applied Pharmacology*, 382. Available at: https://doi.org/10.1016/j.taap.2019.114713.

Na, Y.R. *et al.* (2013) “Cyclooxygenase-2 Inhibition Blocks M2 Macrophage Differentiation and Suppresses Metastasis in Murine Breast Cancer Model,” *PLoS ONE*, 8(5). Available at: https://doi.org/10.1371/journal.pone.0063451.

Nam, G.H. *et al.* (2019) “An optimized protocol to determine the engulfment of cancer cells by phagocytes using flow cytometry and fluorescence microscopy,” *Journal of Immunological Methods*, 470, 27–32. Available at: https://doi.org/10.1016/j.jim.2019.04.007.

Neagu, A.-N. *et al.* (2021) *Proteomics and its applications in breast cancer*, *Am J Cancer Res*. Available at: www.ajcr.us/.

Neamatallah, T. (2019) “Mitogen-Activated protein kinase pathway: A critical regulator in tumor-Associated macrophage polarization,” *Journal of Microscopy and Ultrastructure*. Wolters Kluwer Medknow Publications, 53–56. Available at: https://doi.org/10.4103/JMAU.JMAU_68_18.

Nichols, J.M. and Kaplan, B.L.F. (2020) “Immune Responses Regulated by Cannabidiol,” *Cannabis and Cannabinoid Research*, 5(1), 12–31. Available at: https://doi.org/10.1089/can.2018.0073.

Noble, J. *et al.* (2024) “Harnessing Immune Cell Metabolism to Modulate Alloresponse in Transplantation,” *Transplant International*, 37. Available at: https://doi.org/10.3389/ti.2024.12330.

Oates, T.C.L. *et al.* (2023) “Defining the proteomic landscape of cultured macrophages and their polarization continuum,” *Immunology and Cell Biology*, 101(10), pp. 947–963. Available at: https://doi.org/10.1111/imcb.12687.

O’flaherty, C. *et al.* (2020) “Protective role of peroxiredoxins against reactive oxygen species in neonatal rat testicular gonocytes,” *Antioxidants*, 9(1). Available at: https://doi.org/10.3390/antiox9010032.

Old, W.M. *et al.* (2005) “Comparison of label-free methods for quantifying human proteins by shotgun proteomics,” *Molecular and Cellular Proteomics*, 4(10), 1487–1502. Available at: https://doi.org/10.1074/mcp.M500084-MCP200.

Olivas-Aguirre, M. *et al.* (2022) “Cannabidiol on the Path from the Lab to the Cancer Patient: Opportunities and Challenges,” *Pharmaceuticals*. MDPI. Available at: https://doi.org/10.3390/ph15030366.

Onal, S. *et al.* (2020) “Breast Cancer Cells and Macrophages in a Paracrine-Juxtacrine Loop.” Available at: https://doi.org/10.1101/2020.06.16.154294.

Onitilo, AA. *et al*. (2009) “Breast cancer subtypes based on ER/PR and Her2 expression: comparison of clinicopathologic features and survival”. Clin Med Res. 2009 Jun;7(1-2):4-13. doi: 10.3121/cmr.2009.825. PMID: 19574486; PMCID: PMC2705275.

Onodera, S. *et al.* (1997) *Macrophage migration inhibitory factor induces phagocytosis of foreign particles by macrophages in autocrine and paracrine fashion*, *Immunology*.

Oshi, M. *et al.* (2020) “M1 Macrophage and M1/M2 ratio defined by transcriptomic signatures resemble only part of their conventional clinical characteristics in breast cancer,” *Scientific Reports*, 10(1). Available at: https://doi.org/10.1038/s41598-020-73624-w.

Palmieri, E.M. *et al.* (2020) “Nitric oxide orchestrates metabolic rewiring in M1 macrophages by targeting aconitase 2 and pyruvate dehydrogenase,” *Nature Communications*, 11(1). Available at: https://doi.org/10.1038/s41467-020-14433-7.

Pan, Y. *et al.* (2020) “Tumor-Associated Macrophages in Tumor Immunity,” *Frontiers in Immunology*. Frontiers Media S.A. Available at: https://doi.org/10.3389/fimmu.2020.583084.

Pan, Y. *et al.* (2022) “Cyclooxygenase-2 in adipose tissue macrophages limits adipose tissue dysfunction in obese mice,” *Journal of Clinical Investigation*, 132(9). Available at: https://doi.org/10.1172/JCI152391.

Papanicolaou, M. *et al.* (2022) “Temporal profiling of the breast tumour microenvironment reveals collagen XII as a driver of metastasis,” *Nature Communications*, 13(1). Available at: https://doi.org/10.1038/s41467-022-32255-7.

Pather, K. and Augustine, T.N. (2020) “Tamoxifen induces hypercoagulation and alterations in ERα and ERβ dependent on breast cancer sub-phenotype ex vivo,” *Scientific Reports*, 10(1). Available at: https://doi.org/10.1038/s41598-020-75779-y.

Patra, K.C. *et al.* (2013) “Hexokinase 2 is required for tumor initiation and maintenance and its systemic deletion is therapeutic in mouse models of cancer,” *Cancer Cell*, 24(2), pp. 213–228. Available at: https://doi.org/10.1016/j.ccr.2013.06.014.

Patwardhan, G.A. *et al.* (2021) “Treatment scheduling effects on the evolution of drug resistance in heterogeneous cancer cell populations,” *npj Breast Cancer*, 7(1). Available at: https://doi.org/10.1038/s41523-021-00270-4.

Pawlak, K.J. and Wiebe, J.P. (2007) “Regulation of estrogen receptor (ER) levels in MCF-7 cells by progesterone metabolites,” *Journal of Steroid Biochemistry and Molecular Biology*, 107(3–5), 172–179. Available at: https://doi.org/10.1016/j.jsbmb.2007.05.030.

Pepe, G. *et al.* (2021) “ERα-independent NRF2-mediated immunoregulatory activity of tamoxifen,” *Biomedicine and Pharmacotherapy*, 144. Available at: https://doi.org/10.1016/j.biopha.2021.112274.

Pérez, S. and Rius-Pérez, S. (2022) “Macrophage Polarization and Reprogramming in Acute Inflammation: A Redox Perspective,” *Antioxidants*. MDPI. Available at: https://doi.org/10.3390/antiox11071394.

Petty, A.J. *et al.* (2021) “Targeting tumor-associated macrophages in cancer immunotherapy,” *Cancers*. MDPI. Available at: https://doi.org/10.3390/cancers13215318.

Petty, A.J. and Yang, Y. (2017) “Tumor-associated macrophages: Implications in cancer immunotherapy,” *Immunotherapy*. Future Medicine Ltd., 289–302. Available at: https://doi.org/10.2217/imt-2016-0135.

Piao, Y.J. *et al.* (2018) *Breast cancer cell-derived exosomes and macrophage polarization are associated with lymph node metastasis*, *Oncotarget*. Available at: www.impactjournals.com/oncotarget/.

Pike, S. *et al.* (2015) “In vitro effects of tamoxifen on adipose-derived stem cells,” *Wound Repair and Regeneration*, 23(5), 728–736. Available at: https://doi.org/10.1111/wrr.12322.

Purcu, D.U. *et al.* (2022) “Effect of stimulation time on the expression of human macrophage polarization markers,” *PLoS ONE*, 17(3 March). Available at: https://doi.org/10.1371/journal.pone.0265196.

Qian, S. *et al.* (2022) “The role of BCL-2 family proteins in regulating apoptosis and cancer therapy,” *Frontiers in Oncology*. Frontiers Media S.A. Available at: https://doi.org/10.3389/fonc.2022.985363.

Qu, X. *et al.* (2023) “Macrophage RIPK3 triggers inflammation and cell death via the XBP1–Foxo1 axis in liver ischaemia–reperfusion injury,” *JHEP Reports*, 5(11). Available at: https://doi.org/10.1016/j.jhepr.2023.100879.

Racioppi, L. *et al.* (2017) “Calcium/calmodulin-dependent kinase kinase 2 regulates hematopoietic stem and progenitor cell regeneration,” *Cell Death and Disease*, 8(10). Available at: https://doi.org/10.1038/CDDIS.2017.474.

Rajan, T.S. *et al.* (2016) “Anti-inflammatory and antioxidant effects of a combination of cannabidiol and moringin in LPS-stimulated macrophages,” *Fitoterapia*, 112, 104–115. Available at: https://doi.org/10.1016/j.fitote.2016.05.008.

Rattigan, K.M. *et al.* (2018) “Metabolomic profiling of macrophages determines the discrete metabolomic signature and metabolomic interactome triggered by polarising immune stimuli,” *PLoS ONE*, 13(3). Available at: https://doi.org/10.1371/journal.pone.0194126.

Reales-Calderón, J.A. *et al.* (2014) “Proteomic characterization of human proinflammatory M1 and anti-inflammatory M2 macrophages and their response to Candida albicans,” *Proteomics*, 14(12), 1503–1518. Available at: https://doi.org/10.1002/pmic.201300508.

Remmerie, A. and Scott, C.L. (2018) “Macrophages and lipid metabolism,” *Cellular Immunology*, 330, 27–42. Available at: https://doi.org/10.1016/j.cellimm.2018.01.020.

Roma-Rodrigues, C. *et al.* (2019) “Targeting tumor microenvironment for cancer therapy,” *International Journal of Molecular Sciences*. MDPI AG. Available at: https://doi.org/10.3390/ijms20040840.

Rostami, S., Tafvizi, F. and Manjili, H.R.K. (2022) “High efficacy of tamoxifen-loaded L-lysine coated magnetic iron oxide nanoparticles in cell cycle arrest and anti-cancer activity for breast cancer therapy,” *BioImpacts*, 12(4), 301–313. Available at: https://doi.org/10.34172/bi.2021.23337.

Ruffell, D. *et al.* (2009) *A CREB-C/EBP cascade induces M2 macrophage-specific gene expression and promotes muscle injury repair*. Available at: www.pnas.orgcgidoi10.1073pnas.0908641106.

Rydén, L. *et al.* (2005) “Two years of adjuvant tamoxifen in premenopausal patients with breast cancer: A randomised, controlled trial with long-term follow-up,” *European Journal of Cancer*, 41(2), 256–264. Available at: https://doi.org/10.1016/j.ejca.2004.06.030.

Sahr, K.E. *et al.* (2009) “Targeted deletion of the γ-adducin gene (Add3) in mice reveals differences in α-adducin interactions in erythroid and nonerythroid cells,” *American Journal of Hematology*, 84(6), 354–361. Available at: https://doi.org/10.1002/ajh.21427.

Schild-Hay, L.J. *et al.* (2009) “Tamoxifen induces expression of immune response-related genes in cultured normal human mammary epithelial cells,” *Cancer Research*, 69(3), pp. 1150–1155. Available at: https://doi.org/10.1158/0008-5472.CAN-08-2806.

Schlottmann, F. *et al.* (2022) “Influence of Tamoxifen on Different Biological Pathways in Tumorigenesis and Transformation in Adipose-Derived Stem Cells, Mammary Cells and Mammary Carcinoma Cell Lines—An In Vitro Study,” *Cells*, 11(17). Available at: https://doi.org/10.3390/cells11172733.

Schoeman, R., Beukes, N. and Frost, C. (2020) “Cannabinoid combination induces cytoplasmic vacuolation in MCF-7 breast cancer cells,” *Molecules*, 25(20). Available at: https://doi.org/10.3390/molecules25204682.

Segovia-Mendoza, M. and Morales-Montor, J. (2019) “Immune tumor microenvironment in breast cancer and the participation of estrogens and its receptors into cancer physiopathology,” *Frontiers in Immunology*. Frontiers Media S.A. Available at: https://doi.org/10.3389/fimmu.2019.00348.

Seiler, K. *et al.* (2022) “Hexokinase 3 enhances myeloid cell survival via non-glycolytic functions,” *Cell Death and Disease*, 13(5). Available at: https://doi.org/10.1038/s41419-022-04891-w.

Seltzer, E.S. *et al.* (2020) “Cannabidiol (Cbd) as a promising anti-cancer drug,” *Cancers*. MDPI AG, 1–26. Available at: https://doi.org/10.3390/cancers12113203.

Senevirathne, P. *et al.* (2023) “Inhibiting NOXO1 and CYBA binding to reduce NADPH oxidase I dependent ROS damage in skin explants,” *Results in Chemistry*, 6. Available at: https://doi.org/10.1016/j.rechem.2023.101213.

Seto, S. *et al.* (2009) “Differential recruitment of CD63 and Rab7-interacting-lysosomal-protein to phagosomes containing Mycobacterium tuberculosis in macrophages,” *Microbiology and Immunology*, 54(3), 170–174. Available at: https://doi.org/10.1111/j.1348-0421.2009.00199.x.

Sfogliarini, C. *et al.* (2022) “Tamoxifen Twists Again: On and Off-Targets in Macrophages and Infections,” *Frontiers in Pharmacology*. Frontiers Media S.A. Available at: https://doi.org/10.3389/fphar.2022.879020.

Shahneh, F.Z. *et al.* (2013) “Inhibition of growth and induction of apoptosis in fibrosarcoma cell lines by echinophora platyloba DC: In vitro analysis,” *Advances in Pharmacological Sciences*, 2013. Available at: https://doi.org/10.1155/2013/512931.

Shea-Donohue, T., Zhao, A. and Antalis, T.M. (2014) “SerpinB2 mediated regulation of macrophage function during enteric infection,” *Gut microbes*, 5(2), 254–258. Available at: https://doi.org/10.4161/gmic.28093.

Sheng, W., Ji, G. and Zhang, L. (2022) “Role of macrophage scavenger receptor MSR1 in the progression of non-alcoholic steatohepatitis,” *Frontiers in Immunology*. Frontiers Media S.A. Available at: https://doi.org/10.3389/fimmu.2022.1050984.

Sheppe, A.E.F. *et al.* (2018) “PGE2 Augments Inflammasome Activation and M1 Polarization in Macrophages Infected With Salmonella Typhimurium and Yersinia enterocolitica,” *Frontiers in Microbiology*, 9. Available at: https://doi.org/10.3389/fmicb.2018.02447.

Shergalis, A.G. *et al.* (2020) “Role of the ERO1-PDI interaction in oxidative protein folding and disease,” *Pharmacology and Therapeutics*. Elsevier Inc. Available at: https://doi.org/10.1016/j.pharmthera.2020.107525.

Shi, Y. *et al.* (2020) “M1 But Not M0 Extracellular Vesicles Induce Polarization of RAW264.7 Macrophages Via the TLR4-NFκB Pathway In Vitro,” *Inflammation*, 43(5), 1611–1619. Available at: https://doi.org/10.1007/s10753-020-01236-7.

Shrivastava, A. *et al.* (2011) “Cannabidiol induces programmed cell death in breast cancer cells by coordinating the cross-talk between apoptosis and autophagy,”

Molecular Cancer Therapeutics, 10(7), 1161–1172. Available at: https://doi.org/10.1158/1535-7163.MCT-10-1100.

Shu, Y. *et al.* (2020) “M2 polarization of tumor-associated macrophages is dependent on integrin β3 via peroxisome proliferator-activated receptor-γ up-regulation in breast cancer,” *Immunology*, 160(4), 345–356. Available at: https://doi.org/10.1111/imm.13196.

Shuken, S.R. (2023) “An Introduction to Mass Spectrometry-Based Proteomics,” *Journal of Proteome Research*, 22(7), 2151–2171. Available at: https://doi.org/10.1021/acs.jproteome.2c00838.

Shuster, D. (2023) *Inflammatory Comparison of RAW 264.7 Cells, J774A.1 Cells, and Inflammatory Comparison of RAW 264.7 Cells, J774A.1 Cells, and Murine Bone Marrow-Derived Macrophages Murine Bone Marrow-Derived Macrophages*. Available at: https://digitalshowcase.lynchburg.edu/utcpDerivedMacrophages".

Silva, G.D. *et al.* (2020) “Cannabidiol in the Treatment of Epilepsy: A Focused Review of Evidence and Gaps,” *Frontiers in Neurology*. Frontiers Media S.A. Available at: https://doi.org/10.3389/fneur.2020.531939.

de Simone, G. *et al.* (2023) “Implication of metabolism in the polarization of tumor-associated-macrophages: the mass spectrometry-based point of view,” *Frontiers in Immunology*. Frontiers Media SA. Available at: https://doi.org/10.3389/fimmu.2023.1193235.

Singh, P. and Ali, S.A. (2022) “Multifunctional Role of S100 Protein Family in the Immune System: An Update,” *Cells*. MDPI. Available at: https://doi.org/10.3390/cells11152274.

Singh, R.R. and Reindl, K.M. (2021) “Glutathione s-transferases in cancer,” *Antioxidants*. MDPI. Available at: https://doi.org/10.3390/antiox10050701.

Sinha, A and Mann, M. (2021) A beginner's guide to mass spectrometry–based proteomics. *Biochem*42 (5): 64–69. doi: https://doi.org/10.1042/BIO20200057

Song, X. *et al.* (2023) "M1-Type Macrophages Secrete TNF-α to Stimulate Vascular Calcification by Upregulating CA1 and CA2 Expression in VSMCs," *Journal of Inflammation Research*, 16, 3019–3032. Available at: https://doi.org/10.2147/JIR.S413358.

Stavrou, M. and Constantinidou, A. (2024) "Tumor associated macrophages in breast cancer progression: implications and clinical relevance," *Frontiers in Immunology*. Frontiers Media SA. Available at: https://doi.org/10.3389/fimmu.2024.1441820.

Strizova, Z. *et al.* (2023) "M1/M2 macrophages and their overlaps - myth or reality?," *Clinical Science*. Portland Press Ltd, 1067–1093. Available at: https://doi.org/10.1042/CS20220531.

Sultan, A.S., Marie, M.A. and Sheweita, S.A. (2018) "Novel mechanism of cannabidiol-induced apoptosis in breast cancer cell lines," *Breast*, 41, 34–41. Available at: https://doi.org/10.1016/j.breast.2018.06.009.

Sun, Xiaoqian *et al.* (2022a) "Macrophage Polarization, Metabolic Reprogramming, and Inflammatory Effects in Ischemic Heart Disease," *Frontiers in Immunology*. Frontiers Media S.A. Available at: https://doi.org/10.3389/fimmu.2022.934040.

Sun, Xiang *et al.* (2022b) "Targeting CD44-positive ovarian cancers via engineered paclitaxel prodrug nanoparticles for enhanced chemotherapeutic efficacy," *Biomedicine and Pharmacotherapy*, 154. Available at: https://doi.org/10.1016/j.biopha.2022.113655.

Sun, X. *et al.* (2023) "Single-cell analyses reveal cannabidiol rewires tumor microenvironment via inhibiting alternative activation of macrophage and synergizes with anti-PD-1 in colon cancer," *Journal of Pharmaceutical Analysis*, 13(7), 726–744. Available at: https://doi.org/10.1016/j.jpha.2023.04.013.

Sung, H. *et al.* (2021) “Global Cancer Statistics 2020: GLOBOCAN Estimates of Incidence and Mortality Worldwide for 36 Cancers in 185 Countries,” *CA: A Cancer Journal for Clinicians*, 71(3), 209–249. Available at: https://doi.org/10.3322/caac.21660.

Suttithumsatid, W., Sukketsiri, W. and Panichayupakaranant, P. (2023) “Cannabinoids and standardized cannabis extracts inhibit migration, invasion, and induce apoptosis in MCF-7 cells through FAK/MAPK/Akt/NF-κB signaling,” *Toxicology in Vitro*, 93. Available at: https://doi.org/10.1016/j.tiv.2023.105667.

Taciak, B. *et al.* (2018) “Evaluation of phenotypic and functional stability of RAW 264.7 cell line through serial passages,” *PLoS ONE*, 13(6). Available at: https://doi.org/10.1371/journal.pone.0198943.

Tallarida, R.J. (2011) “Quantitative Methods for Assessing Drug Synergism,” *Genes and Cancer*, 1003–1008. Available at: https://doi.org/10.1177/1947601912440575.

Tan, H.Y. *et al.* (2016) “The Reactive Oxygen Species in Macrophage Polarization: Reflecting Its Dual Role in Progression and Treatment of Human Diseases,” *Oxidative Medicine and Cellular Longevity*. Hindawi Limited. Available at: https://doi.org/10.1155/2016/2795090.

Tang, F. *et al.* (2011) “RNF185, a novel mitochondrial ubiquitin E3 ligase, regulates autophagy through interaction with BNIP1,” *PLoS ONE*, 6(9). Available at: https://doi.org/10.1371/journal.pone.0024367.

Tang, Y. *et al.* (2023) “Evolution and function analysis of glycerol kinase GlpK in Pseudomonas aeruginosa,” *Biochemical and Biophysical Research Communications*, 645, pp. 30–39. Available at: https://doi.org/10.1016/j.bbrc.2022.12.060.

Tharmapalan, P. *et al.* (2019) “Mammary stem cells and progenitors: targeting the roots of breast cancer for prevention,” *The EMBO Journal*, 38(14). Available at: https://doi.org/10.15252/embj.2018100852.

Toss, MS. *et al*. (2017) “Breast conservation in ductal carcinoma in situ (DCIS): what defines optimal margins?” Histopathology. 2017 Apr;70(5):681-692. doi: 10.1111/his.13116. Epub 2016 Dec 20. PMID: 28000325.

Vanmeerbeek, I. *et al.* (2022) “The Interface of Tumour-Associated Macrophages with Dying Cancer Cells in Immuno-Oncology,” *Cells*. MDPI. Available at: https://doi.org/10.3390/cells11233890.

Vassiliou, E. and Farias-Pereira, R. (2023) “Impact of Lipid Metabolism on Macrophage Polarization: Implications for Inflammation and Tumor Immunity,” *International Journal of Molecular Sciences*. Multidisciplinary Digital Publishing Institute (MDPI). Available at: https://doi.org/10.3390/ijms241512032.

Viola, A. *et al.* (2019) “The metabolic signature of macrophage responses,” *Frontiers in Immunology*. Frontiers Media S.A. Available at: https://doi.org/10.3389/fimmu.2019.01462.

Volk, R.F. *et al.* (2022) “Proteomic characterization of phagocytic primary human monocyte-derived macrophages,” *RSC Chemical Biology*, 3(6), 783–793. Available at: https://doi.org/10.1039/d2cb00076h.

Wang, C. *et al.* (2020) “Human leukocyte antigen (HLA) and cancer immunotherapy: HLA-dependent and -independent adoptive immunotherapies,” *Annals of Blood*. AME Publishing Company. Available at: https://doi.org/10.21037/aob-20-27.

Wang, Q. *et al.* (2022) “C1QBP regulates mitochondrial plasticity to impact tumor progression and antitumor immune response,” *Frontiers in Physiology*. Frontiers Media S.A. Available at: https://doi.org/10.3389/fphys.2022.1012112.

Wang, S. *et al.* (2013) “Rapid reuptake of granzyme B leads to emperitosis: An apoptotic cell-in-cell death of immune killer cells inside tumor cells,” *Cell Death and Disease*, 4(10). Available at: https://doi.org/10.1038/cddis.2013.352.

Wang, S. *et al.* (2022a) “Metabolic Reprogramming Induces Macrophage Polarization in the Tumor Microenvironment,” *Frontiers in Immunology*. Frontiers Media S.A. Available at: https://doi.org/10.3389/fimmu.2022.840029.

Wang, W. *et al.* (2015) “Escherichia coli maltose-binding protein induces M1 polarity of RAW264.7 macrophage cells via a TLR2- and TLR4-dependent manner,” *International Journal of Molecular Sciences*, 16(5), pp. 9896–9909. Available at: https://doi.org/10.3390/ijms16059896.

Wang, X. *et al.* (2022b) “Inhibition of CEBPB Attenuates Lupus Nephritis via Regulating Pim-1 Signaling,” *Mediators of Inflammation*, 2022. Available at: https://doi.org/10.1155/2022/2298865.

Wang, Z. *et al.* (2024) “Role of natural products in tumor therapy from basic research and clinical perspectives,” *Acta Materia Medica*, 3(2). Available at: https://doi.org/10.15212/amm-2023-0050.

Wen, X.M. *et al.* (2020) “Zyxin (ZYX) promotes invasion and acts as a biomarker for aggressive phenotypes of human glioblastoma multiforme,” *Laboratory Investigation*, 100(6), 812–823.

Weiss, L. *et al*. (2007) “Cannabidiol arrests onset of autoimmune diabetes in NOD mice”. Neuropharmacology. 2008 Jan;54(1):244-9. doi: 10.1016/j.neuropharm.2007.06.029. Epub 2007 Jul 17. PMID: 17714746; PMCID: PMC2270485.

Wilson, A. and McCormick, C. (2024) “Reticulophagy and viral infection,” *Autophagy* [Preprint]. Taylor and Francis Ltd. Available at: https://doi.org/10.1080/15548627.2024.2414424.

Wu, C. *et al.* (2014) “IFN-γ Primes Macrophage Activation by Increasing Phosphatase and Tensin Homolog via Downregulation of miR-3473b,” *The Journal of Immunology*, 193(6), 3036–3044. Available at: https://doi.org/10.4049/jimmunol.1302379.

Xia, C. *et al.* (2018) “S100 proteins as an important regulator of macrophage inflammation,” *Frontiers in Immunology*. Frontiers Media S.A. Available at: https://doi.org/10.3389/fimmu.2017.01908.

Xiao, Y. and Yu, D. (2021) “Tumor microenvironment as a therapeutic target in cancer,” *Pharmacology and Therapeutics*. Elsevier Inc. Available at: https://doi.org/10.1016/j.pharmthera.2020.107753.

Xu, C. *et al.* (2023) “Protocol for detecting macrophage-mediated cancer cell phagocytosis in vitro and in vivo,” *STAR Protocols*, 4(1). Available at: https://doi.org/10.1016/j.xpro.2022.101940.

Xu, W. *et al.* (2021) “Identification of PAFAH1B3 as Candidate Prognosis Marker and Potential Therapeutic Target for Hepatocellular Carcinoma,” *Frontiers in Oncology*, 11. Available at: https://doi.org/10.3389/fonc.2021.700700.

Yadav, J. *et al.* (2021) “Recent developments in in vitro and in vivo models for improved translation of preclinical pharmacokinetics and pharmacodynamics data,” *Drug Metabolism Reviews*. Taylor and Francis Ltd., 207–233. Available at: https://doi.org/10.1080/03602532.2021.1922435.

Yan, C. *et al.* (2023) “Antitumor mechanism of cannabidiol hidden behind cancer hallmarks,” *Biochimica et Biophysica Acta - Reviews on Cancer*. Elsevier B.V. Available at: https://doi.org/10.1016/j.bbcan.2023.188905.

Yan, G., Elbadawi, M. and Efferth, T. (2020) “Multiple cell death modalities and their key features (Review),” *World Academy of Sciences Journal*. Spandidos Publications, 39–48. Available at: https://doi.org/10.3892/wasj.2020.40.

Yang, X. *et al.* (2024) “FABP5+ lipid-loaded macrophages process tumour-derived unsaturated fatty acid signal to suppress T-cell antitumour immunity,” *Journal of Hepatology* [Preprint]. Available at: https://doi.org/10.1016/j.jhep.2024.09.029.

Yang, Y. *et al.* (2014) “Functional roles of p38 mitogen-activated protein kinase in macrophage-mediated inflammatory responses,” *Mediators of Inflammation*. Hindawi Publishing Corporation. Available at: https://doi.org/10.1155/2014/352371.

Yeisley, D.J., Arabiyat, A.S. and Hahn, M.S. (2021) “Cannabidiol-Driven Alterations to Inflammatory Protein Landscape of Lipopolysaccharide-Activated Macrophages in Vitro May Be Mediated by Autophagy and Oxidative Stress,” *Cannabis and Cannabinoid Research*, 6(3), 253–263. Available at: https://doi.org/10.1089/can.2020.0109.

Yekhtin, Z. *et al.* (2022) “Differential Effects of D9 Tetrahydrocannabinol (THC)- and Cannabidiol (CBD)-Based Cannabinoid Treatments on Macrophage Immune Function In Vitro and on Gastrointestinal Inflammation in a Murine Model,” *Biomedicines*, 10(8). Available at: https://doi.org/10.3390/biomedicines10081793.

Yndart Arias, A. *et al.* (2023) “Anti-inflammatory effects of CBD in human microglial cell line infected with HIV-1,” *Scientific Reports*, 13(1). Available at: https://doi.org/10.1038/s41598-023-32927-4.

Zaiachuk, M. *et al.* (2023) “The Anti-Inflammatory Effects of Cannabis sativa Extracts on LPS-Induced Cytokines Release in Human Macrophages,” *Molecules*, 28(13). Available at: https://doi.org/10.3390/molecules28134991.

Zechner, R. *et al.* (2012) “FAT SIGNALS - Lipases and lipolysis in lipid metabolism and signaling,” *Cell Metabolism*, 279–291. Available at: https://doi.org/10.1016/j.cmet.2011.12.018.

Zhan, C. *et al.* (2023) “Antitumor therapy for breast cancer: Focus on tumor-associated macrophages and nanosized drug delivery systems,” *Cancer Medicine*. John Wiley and Sons Inc, 11049–11072. Available at: https://doi.org/10.1002/cam4.5489.

Zhang, F. *et al.* (2015) “Changes in the proteomic profile during the differential polarization status of the human monocyte-derived macrophage THP-1 cell line,” *Proteomics*, 15(4), 773–786. Available at: https://doi.org/10.1002/pmic.201300494.

Zhang, Q. and Sioud, M. (2023) “Tumor-Associated Macrophage Subsets: Shaping Polarization and Targeting,” *International Journal of Molecular Sciences*. Multidisciplinary Digital Publishing Institute (MDPI). Available at: https://doi.org/10.3390/ijms24087493.

Zhang, W. *et al.* (2024a) “Macrophage polarization in the tumor microenvironment: Emerging roles and therapeutic potentials,” *Biomedicine and Pharmacotherapy*. Elsevier Masson s.r.l. Available at: https://doi.org/10.1016/j.biopha.2024.116930.

Zhang, X. *et al.* (2024b) “Macrophages Promote Subtype Conversion and Endocrine Resistance in Breast Cancer,” *Cancers*, 16(3). Available at: https://doi.org/10.3390/cancers16030678.

Zhang, Y. *et al.* (2013) “ROS play a critical role in the differentiation of alternatively activated macrophages and the occurrence of tumor-associated macrophages,” *Cell Research*, 23(7), 898–914. Available at: https://doi.org/10.1038/cr.2013.75.

Zhang, Y. *et al.* (2017) *Tumacrophage: macrophages transformed into tumor stem-like cells by virulent genetic material from tumor cells*. Available at: www.impactjournals.com/oncotarget.

Zhao, M. *et al.* (2021) “Cytochrome p450 enzymes and drug metabolism in humans,” *International Journal of Molecular Sciences*. MDPI. Available at: https://doi.org/10.3390/ijms222312808.

Zhou, K. *et al.* (2020) “Targeting tumor-associated macrophages in the tumor microenvironment (Review),” *Oncology Letters*, 20(5). Available at: https://doi.org/10.3892/ol.2020.12097.

Zhou, Y. *et al.* (2024) “RIPK3 signaling and its role in regulated cell death and diseases,” *Cell Death Discovery*. Springer Nature. Available at: https://doi.org/10.1038/s41420-024-01957-w.

Zu, S. *et al.* (2021) “Tamoxifen and clomiphene inhibit SARS-CoV-2 infection by suppressing viral entry,” *Signal Transduction and Targeted Therapy*. Springer Nature. Available at: https://doi.org/10.1038/s41392-021-00853-4.

Appendices

Appendix A: Cell Culture Supplementary Information

A0: Ethics Waiver Certificate

UNIVERSITY OF THE WITWATERSRAND, JOHANNESBURG	HUMAN RESEARCH ETHICS COMMITTEE (MEDICAL)

Office of the Deputy Vice-Chancellor (Research & Innovation)

TO: Ms T Mackade, et al
School: Anatomical Sciences
Medical School
University

E-mail: 1692568@students.wits.ac.za

CC: Supervisor: Professor T Augustine <Tanya.Augustine @wits.ac.za>
and <HREC-Medical.ResearchOffice@wits.ac.za>

FROM: Mr Iain Burns
Human Research Ethics Committee (Medical)
Tel: 011 717 1252

E-mail: Iain.Burns@wits.ac.za

DATE: 17/06/2022

REF: *R14/49*

PROTOCOL NO: W-CBP-220617-01 (This is your ethics application study reference number. Please quote this reference number in all correspondence relating to this study)

PROJECT TITLE: *The immunoregulatory effects of macrophages on a 3-dimensional breast cancer model under Cannabidiol and Tamoxifen treatment*

Please find attached the Ethics Waiver Certificate for the above project. I hope it goes well and that an article in a recognized publication comes out of it. This will reflect well on your professional standing and contribute to the Government funding of the University.

MSWorks2000/Iain0007/ClearScanWaiver.wps

UNIVERSITY OF THE WITWATERSRAND JOHANNESBURG	HUMAN RESEARCH ETHICS COMMITTEE (MEDICAL)

Office of the Deputy Vice-Chancellor (Research & Innovation)

17/06/2022

Ref: W-CBP-220617-01

TO WHOM IT MAY CONCERN

Waiver: This certifies that the following research does not require clearance from the Human Research Ethics Committee (Medical)

Investigator: Ms T Mackade, et al
Student No. (if appropriate): 1692568
Staff No. (if appropriate):

Supervisor: Professor T Augustine

School: Anatomical Sciences
Department:
Medical School
University

Project title: *The immunoregulatory effects of macrophages on a 3-dimensional breast cancer model under Cannabidiol and Tamoxifen treatment*

Reason: In vitro laboratory study
No human participants will be involved in the study

CB Penny

Dr CB Penny
Chairperson: Human Research Ethics Committee (Medical)

Research Office Secretariat:
Third Floor, Phillip Tobias Building, corner of St Andrews and York Roads, Parktown, Johannesburg 2193
Postal address: Private Bag 3, Wits 2050
Tel Nos: +27 (0)11 717 1234/1252/2656/2700
Office E-mail: HREC-Medical.ResearchOffice@wits.ac.za
Website:
https://www.wits.ac.za/research/researcher-support/research-ethics/ethics-committees/

A1: Mycoplasma Authentication

In order to ensure that the MCF7 and RAW264.7 cell lines were not contaminated they were tested for mycoplasma. The cells were plated on coverslips at a density of 1 x 10^5 cells/well in a 24-well plate (Lasec, 662160). After 24 hours, the cells were washed twice with 0.01 M PBS, pH 7.4, and fixed with 150 µL of 4% paraformaldehyde (PFA) for 10 minutes. The fixative was removed by washing the cells twice with PBS (pH 7.4), for 5 minutes following which they were exposed to 150 µL of 0.1% Triton-X for 5 minutes and washed twice with PBS (pH 7.4), for an additional 5 minutes. The cells were then treated with 150 µL of 4',6-diamidino-2-phenylindole (DAPI) (Sigma-Aldrich, D9542) for 10 minutes and washed with PBS (pH 7.4), twice for 5 minutes. The coverslips were mounted on slides using fluoromount and viewed on the Olympus IX51 microscope using CellSense v11 software. Images were obtained at 40X magnification. Results of this study indicated that the MCF7 and RAW264.7 cell cultures were free from mycoplasma contamination as the DAPI staining was primarily localised inside the nuclei and did not stain the cytoplasmic regions (Fig. A1).

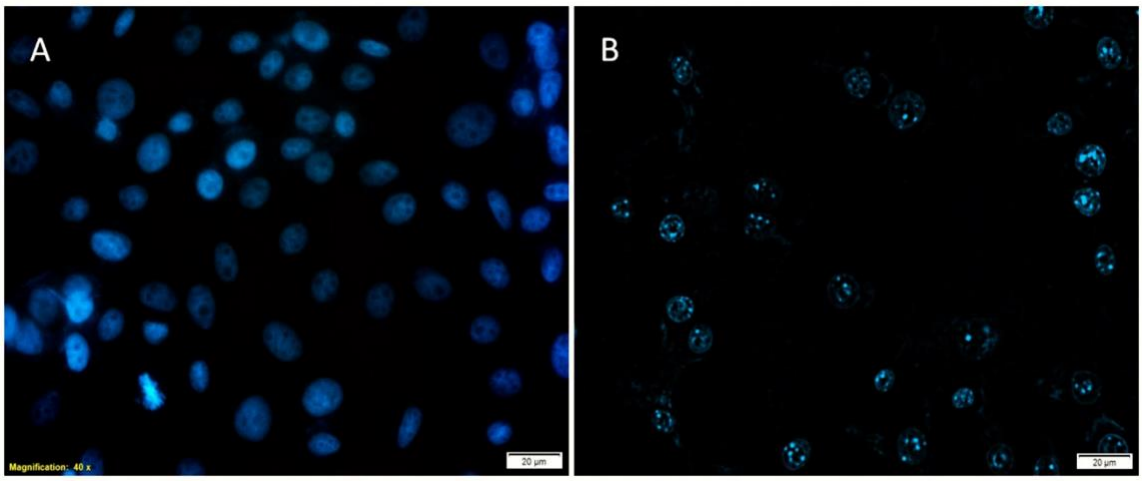


Figure A1: Representative microscopic images of DAPI-stained MCF7 and RAW264.7 cells. Micrographs **A** (MCF7 cells) and **B** (RAW264.7 cells) show DAPI-stained nuclei in both cell lines at 40X magnification (scale bar - 20 µm). The nuclei shown in A and B are highly fluorescent and there is no detectable cytoplasmic fluorescence, thus suggesting that the cell lines were not contaminated with mycoplasma.

A2. Solutions

Phosphate buffered saline (PBS) (0.1M; pH 7.40):

8 g NaCl

1.15 g Na_2HPO_4

0.2 g KCl

0.2 g KH_2PO_4

Cryopreservation media:

10% DMSO

30% DMEM

60% FBS

Appendix B: RAW264.7 Macrophage Polarisation Duration Optimisation

B1: Preparation of Stimulants

1. **M1 phenotype**

IFN-γ:

Stock solution: 500 ng/mL

Working solution: 40 ng/mL

- $C_1V_1 = C_2V_2$

  (500 ng/mL)(V_1) = (40 ng/mL)(5 mL)

  V_1 = 0.4 mL

Working Solution = 0.4 mL stock solution in 4.6 mL complete media

LPS:

Stock solution: 0.1 mg/mL

Working solution: 200 ng/mL

- $C_1V_1 = C_2V_2$

  (0.1 mg/mL)(V_1) = (0.0002 mg/ml)(5 mL)

  V_1 = 0.01 mL

Working Solution = 0.01 mLl stock solution in 4.99 mL complete media

2. M2 phenotype

IL-4:

Stock solution: 500 ng/mL

Working solution: 20 ng/mL

- $C_1V_1 = C_2V_2$

  (500 ng/mL)(V_1) = (20 ng/ml)(5 mL)

  V_1 = 0.2 mL

Working Solution = 0.2 mL stock solution in 4.8 mL complete media

B2: Griess Reagent Assay

Preparation of 100 µM Nitrite Solution

Nitrite standard solution (1.0 mL; 1.0 mM sodium nitrite in deionized water)
C1: 1,0 mM = 1000 µM
C2: 100 µM
V2 = 100 µL for 3 wells = 300 µL
C1V1 = C2V2
(1000 µM) V1 = (100 µM) (300 µL)
V1 = 30 µL

100 µM nitrite solution = 30 µL nitrite standard solutionl + 270 µL media

Preparation of Nitrite (NO_2^-) Standard Reference Curve

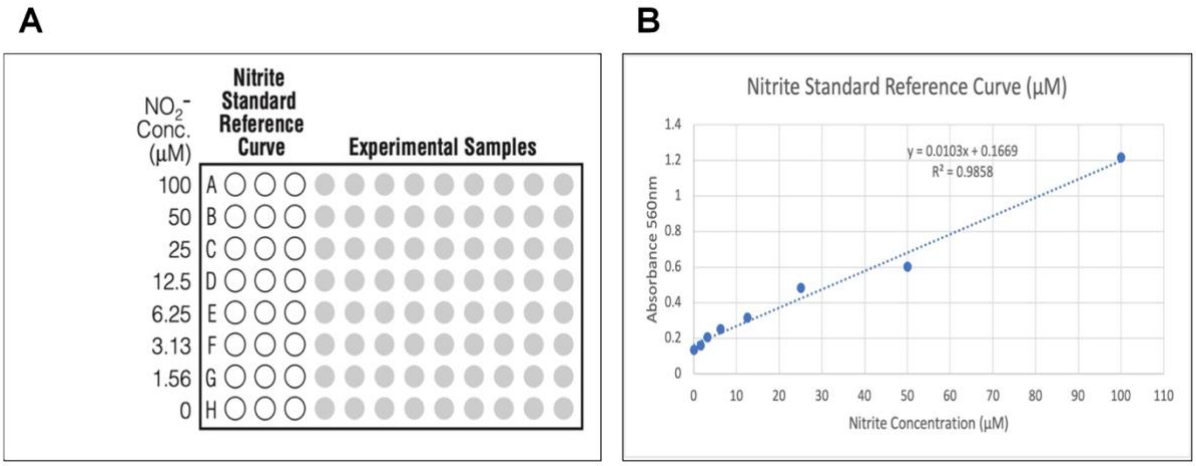


Figure B1: Nitrite Standard Reference Curve. **A)** Plate layout for nitrite standard curve. In the three wells of row A, 100 µL of 100 µM nitrite solution was added. Thereafter, six serial twofold dilutions were performed in triplicate (50 µL/well), discarding 50 µL from the 1.56 µM set of wells. Then 50 µL of the experimental samples were added to the indicated wells and were mixed with 30 µL deionized water. All wells were mixed with 20 µL of the Griess reagent (10 µL of N-(1-naphthyl) ethylenediamine (NED) and 10 µL of sulfanilic acid). **B)** Standard curve graph from which nitrite concentrations were extrapolated.

B3: Statistical Analysis – Statistica Output

RAW264.7 Nitrite Production Following Polarisation to M1 and M2 Phenotypes

Kruskal-Wallis Anova by Ranks and Post-hoc tests

24 hrs

Kruskal-Wallis ANOVA by Ranks; Nitrite concentration (µM) 24 hrs (RAW264.7 Polarisation_Griess_TM)Independent (grouping) variable: Macrophage phenotypeKruskal-Wallis test: H (2, N= 9) =1,866667 p =,3932

Depend.: Nitrite concentration (µM) 24 hrs	Code	Valid N	Sum of Ranks	Mean Rank
M0	1	3	10.00000	3.333333
M1	2	3	19.00000	6.333333
M2	3	3	16.00000	5.333333

Post-hoc

Absolute Differences between Mean Rank Approx. significant if highlighted at .05 significance level

	M0	M1	M2
M0	---	3	2
M1	3	---	1
M2	2	1	---

48 hrs

Kruskal-Wallis ANOVA by Ranks; Nitrite concentration (µM) 48 hrs (RAW264.7 Polarisation_Griess_TM)Independent (grouping) variable: Macrophage phenotypeKruskal-Wallis test: H (2, N= 9) =2,222222 p =,3292

Depend.: Nitrite concentration (µM) 48 hrs	Code	Valid N	Sum of Ranks	Mean Rank
M0	1	3	10.00000	3.333333
M1	2	3	20.00000	6.666667
M2	3	3	15.00000	5.000000

Post-hoc

Absolute Differences between Mean Rank Approx. significant if highlighted at .05 significance level

	M0	M1	M2
M0	---	3.33333333	1.66666667
M1	3.33333333	---	1.66666667
M2	1.66666667	1.66666667	---

72 hrs

Kruskal-Wallis ANOVA by Ranks; Nitrite concentration (µM) 72 hrs (RAW264.7 Polarisation_Griess_TM)Independent (grouping) variable: Macrophage phenotypeKruskal-Wallis test: H (2, N= 9) =5,600000 p =,0608

Depend.: Nitrite concentration (µM) 72 hrs	Code	Valid N	Sum of Ranks	Mean Rank
M0	1	3	6.00000	2.000000
M1	2	3	21.00000	7.000000
M2	3	3	18.00000	6.000000

Post-hoc

Absolute Differences between Mean Rank Approx. significant if highlighted at .05 significance level

	M0	M1	M2
M0	---	5	4
M1	5	---	1
M2	4	1	---

Friedman Anova by Ranks and Post-hoc test

M0

Macrophage phenotype=M0Friedman ANOVA and Kendall Coeff. of Concordance (RAW264.7 Polarisation_Griess_TM)ANOVA Chi Sqr. (N = 3, df = 2) = 4,666667 p = ,09697Coeff. of Concordance = ,77778 Aver. rank r = ,66667

Variable	Average Rank	Sum of Ranks	Mean	Std.Dev.
Nitrite concentration (µM) 24 hrs	1.000000	3.000000	9.85221	8.04936
Nitrite concentration (µM) 48 hrs	2.333333	7.000000	67.64743	61.92414
Nitrite concentration (µM) 72 hrs	2.666667	8.000000	95.43576	24.04619

Post-hoc

Absolute Differences between Average RankApprox. significant if > 1.95467632136186at .05 significance level

	Nitrite concentration (µM) 24 hrs	Nitrite concentration (µM) 48 hrs	Nitrite concentration (µM) 72 hrs
Nitrite concentration (µM) 24 hrs	---	1.333333333	1.666666667
Nitrite concentration (µM) 48 hrs	1.333333333	---	0.333333333
Nitrite concentration (µM) 72 hrs	1.666666667	0.333333333	---

M1

Macrophage phenotype=M1Friedman ANOVA and Kendall Coeff. of Concordance (RAW264.7 Polarisation_Griess_TM)ANOVA Chi Sqr. (N = 3, df = 2) = 4,666667 p = ,09697Coeff. of Concordance = ,77778 Aver. rank r = ,66667

Variable	Average Rank	Sum of Ranks	Mean	Std.Dev.
Nitrite concentration (µM) 24 hrs	1.000000	3.000000	32.8458	22.0567
Nitrite concentration (µM) 48 hrs	2.333333	7.000000	165.6485	109.0995
Nitrite concentration (µM) 72 hrs	2.666667	8.000000	184.9934	58.5254

Post-hoc

Absolute Differences between Average RankApprox. significant if > 1.95467632136186at .05 significance level

	Nitrite concentration (µM) 24 hrs	Nitrite concentration (µM) 48 hrs	Nitrite concentration (µM) 72 hrs
Nitrite concentration (µM) 24 hrs	---	1.333333333	1.666666667
Nitrite concentration (µM) 48 hrs	1.333333333	---	0.333333333
Nitrite concentration (µM) 72 hrs	1.666666667	0.333333333	---

M2

Macrophage phenotype=M2Friedman ANOVA and Kendall Coeff. of Concordance (RAW264.7 Polarisation_Griess_TM)ANOVA Chi Sqr. (N = 3, df = 2) = 6,000000 p = ,04979Coeff. of Concordance = 1,0000 Aver. rank r = 1,0000

Variable	Average Rank	Sum of Ranks	Mean	Std.Dev.
Nitrite concentration (µM) 24 hrs	1.000000	3.000000	24.9096	11.7877
Nitrite concentration (µM) 48 hrs	2.000000	6.000000	111.0997	100.8935
Nitrite concentration (µM) 72 hrs	3.000000	9.000000	177.7503	60.0594

Post-hoc

Absolute Differences between Average RankApprox. significant if > 1.95467632136186at .05 significance level

	Nitrite concentration (µM) 24 hrs	Nitrite concentration (µM) 48 hrs	Nitrite concentration (µM) 72 hrs
Nitrite concentration (µM) 24 hrs	---	1	2
Nitrite concentration (µM) 48 hrs	1	---	1
Nitrite concentration (µM) 72 hrs	2	1	---

Appendix C: Drug and Reagent Preparations for Neutral Red and MTT

C1. MCF7 CBD Optimisation

Tamoxifen (MW = 371.5 g.mol^{-1})

Stock solution: 2691.72 µM Tamoxifen

- *Dissolve 1 mg Tamoxifen in 1 ml 100% methanol (stock 1)*

  C (M) = m (g)/(MW (g.mol^{-1}) X V (L))

  C (M) = 0.001 g/(371.5 g.mol^{-1} X 0.001 L)

  C = 0.002692 M

  C = 2691.72 µM

Working solution: 4 µM Tamoxifen

- $C_1V_1 = C_2V_2$

  (2691.72 µM)(V_1) = (4 µM)(18500 µL)

  V_1 = 27.49 µL

  Tamoxifen Working Solution = 27.49 µL stock 1 in 18472.51 µL media

CBD (MW = 314.5 $g.mol^{-1}$)

Stock solution: 3179.65 µM CBD

- *Dissolve 1 mg CBD in 1 mL 100% methanol (stock 1)*

  C (M) = m (g)/(MW ($g.mol^{-1}$) X V (L))

  C (M) = 0.001 g/(314.5 $g.mol^{-1}$ X 0.001 L)

  C = 0.00317963 M

  C = 3179.65 µM

Table C1: CBD working solution calculations

10 µM CBD	15 µM CBD	20 µM CBD
$C_1V_1 = C_2V_2$ (3179.65 µM)(V_1) = (10 µM)(5500 µL) V_1 = 17.30 µL *Working solution = 17.30 µL stock 1 in 5482.70 µL media*	$C_1V_1 = C_2V_2$ (3179.65 µM)(V_1) = (10 µM)(5500 µL) V_1 = 17.30 µL *Working solution = 17.30 µL stock 1 in 5482.70 µL media*	$C_1V_1 = C_2V_2$ (3179.65 µM)(V_1) = (20 µM)(5500 µL) V_1 = 34.60 µL *Working solution = 34.60 µL stock 1 in 5464.40 µL media*

Diluent

Stock solution: 100% methanol (stock 1)

Working solution: 0.39% methanol

- $C_1V_1 = C_2V_2$

  (100%)(V_1) = (0.39%)(5500 µl)

  V_1 = 21.45 µL

  Diluent Working Solution = 21.45 µL stock 1 in 5478.55 µL media

<u>Solutions (Neutral Red and MTT)</u>

Neutral Red stock (C_f = 10 mg/mL)

0.1 g Neutral Red

0.45 g NaCl

10 ml dH_2O

Neutral Red working solution (C_f = 100 µg/mL)

150 µl NR stock

14850 µl complete media

Desorb

1% glacial acetic acid

49% dH_2O

50% ethanol

MTT Reagent (C_f = 5 mg/mL)

21.6 mg Thiazolyl Tetrazolium Bromide

4.32 ml PBS (pH 7.40)

0.1 % Triton X-100

Stock solution: 100% Triton X-100 (stock 1)

Working solution: 0.1% Triton X-100

- $C_1V_1 = C_2V_2$

  $(100\%)(V_1) = (0.1\%)(5000\ \mu L)$

  $V_1 = 5\ \mu L$

Triton X-100 Working Solution = 5 µL stock 1 in 4995 µL media

C2. RAW264.7 Neutral Red and MTT

Tamoxifen (MW = 371.5 $g.mol^{-1}$)

Stock solution: 2691.72 µM Tamoxifen

- *Dissolve 1 mg Tamoxifen in 1 mL 100% methanol (stock 1)*

  C (M) = m (g)/(MW ($g.mol^{-1}$) X V (L))

  C (M) = 0.001 g/(371.5 $g.mol^{-1}$ X 0.001 L)

  C = 0.002692 M

  C = 2691.72 µM

Working solution: 4 µM Tamoxifen

- $C_1V_1 = C_2V_2$

  $(2691.72\ \mu M)(V_1) = (4\ \mu M)(18500\ \mu Ll)$

V_1 = 27.49 µL

Tamoxifen Working Solution = 27.49 µL stock 1 in 18472.51 µL media

CBD (MW = 314.5 $g.mol^{-1}$)

Stock solution: 3179.65 µM CBD

- *Dissolve 1 mg CBD in 1 mL 100% methanol (stock 1)*

  C (M) = m (g)/(MW ($g.mol^{-1}$) X V (L))

  C (M) = 0.001 g/(314.5 $g.mol^{-1}$ X 0.001 L)

  C = 0.00317963 M

  C = 3179.65 µM

Working solution: 10 µM CBD

- $C_1V_1 = C_2V_2$

(3179.65 µM)(V_1) = (10 µM)(5500 µL)

V_1 = 17.30 µL

CBD Working Solution = 17.30 µL stock 1 in 5482.70 µL media

Diluent

Stock solution: 100% methanol (stock 1)

Working solution: 0.2% methanol

- $C_1V_1 = C_2V_2$

  (100%)(V_1) = (0.2%)(2500 µL)

  V_1 = 5 µL

  Diluent Working Solution = 5 µL stock 1 in 2495 µL media

<u>Solutions (Neutral Red and MTT)</u>

Neutral Red stock (C_f = 10 mg/mL)

0.1 g Neutral Red

0.45 g NaCl

10 ml dH_2O

Neutral Red working solution (C_f = 100 µg/mL)

150 µL NR stock

14850 µL complete media

Desorb

1% glacial acetic acid

49% dH_2O

50% ethanol

MTT Reagent (C_f = 5 mg/ml)

21.6 mg Thiazolyl Tetrazolium Bromide

4.32 mL PBS (pH 7.40)

0.2 % Triton X-100

Stock solution: 100% Triton X-100 (stock 1)

Working solution: 0.1% Triton X-100

- $C_1V_1 = C_2V_2$

  $(100\%)(V_1) = (0.1\%)(2500\ \mu L)$

  $V_1 = 2.5\ \mu L$

Triton X-100 Working Solution = 2.5 µL stock 1 in 2497.5 µL media

C3: Supplementary Information for Neutral Red and MTT Assays

IC_{50} Visuals for CBD alone and in combination with Tamoxifen

MCF7 Neutral red assay: CBD alone

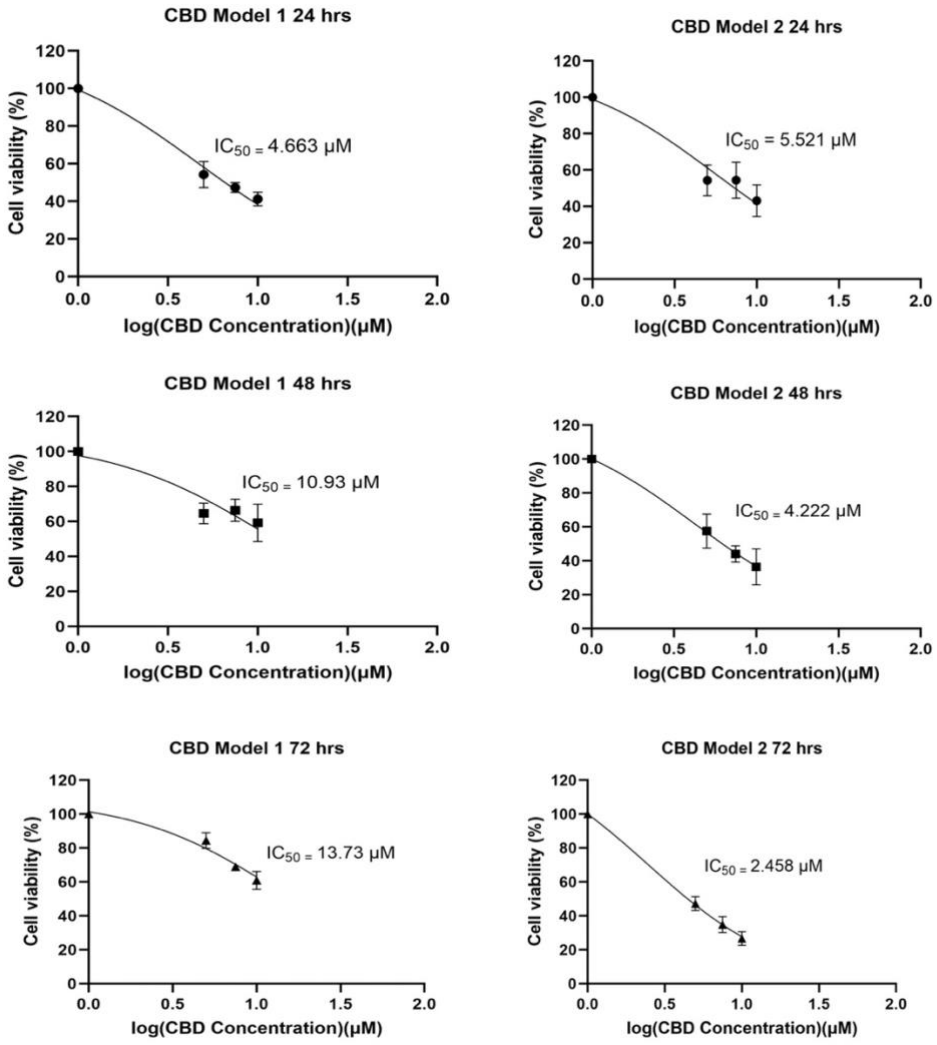


Figure C1.1: Half-maximal inhibitory (IC_{50}) concentrations of CBD alone at each time interval. Data was normalised to constrain the bottom of the curve to 0% cell viability, and IC_{50} values were calculated using GraphPad Prism Software (V10). In treatment model 1, the IC_{50} of CBD increased over time. In contrast, treatment model 2 revealed a decrease of IC_{50} values across time.

MCF7 Neutral red Assay: CBD in combination with Tamoxifen

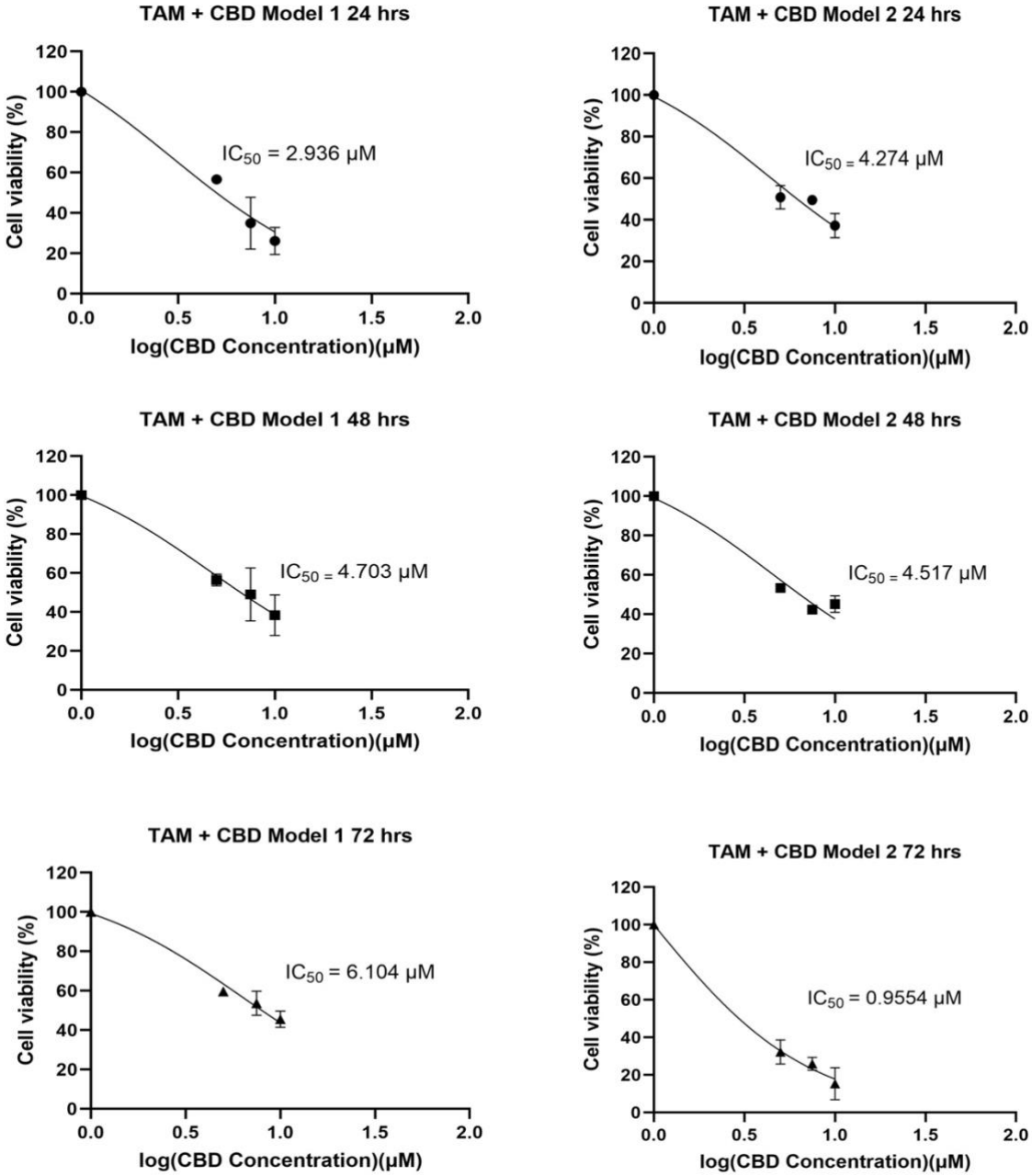


Figure C1.2: Half-maximal inhibitory (IC_{50}) concentrations of CBD combined with Tamoxifen at each time interval. Data was normalised to constrain the bottom of the curve to 0% cell viability, and IC_{50} values were calculated using GraphPad Prism Software (V10). In treatment model 1, the IC_{50} of CBD combined with Tamoxifen (TAM) increased over time. Contrastingly, IC_{50} values in treatment model 2 decreased across time. Treatment with combined Tamoxifen and CBD in model 2 at 48 hrs yielded an IC_{50} value closest to that of the 5 µM CBD concentration assessed.

MCF7 MTT assay: CBD alone

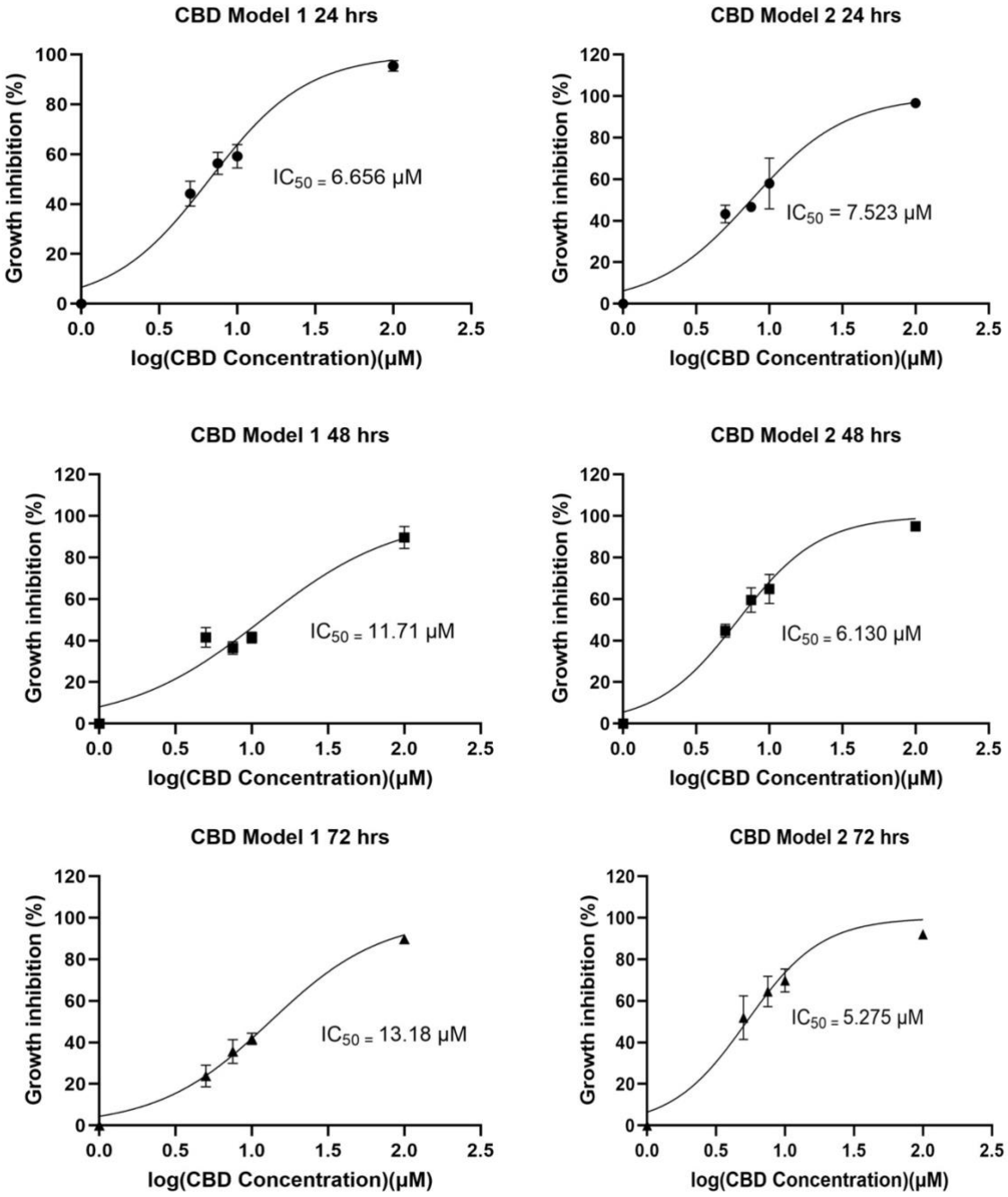


Figure C1.3: Half-maximal inhibitory (IC_{50}) concentrations of CBD alone at each time interval. The IC_{50} values were calculated using GraphPad Prism Software (V10). In treatment model 1, the IC_{50} of CBD increased over time. This contrasted treatment model 2, whereby IC_{50} values decreased across time.

MCF7 MTT assay: CBD in combination with Tamoxifen

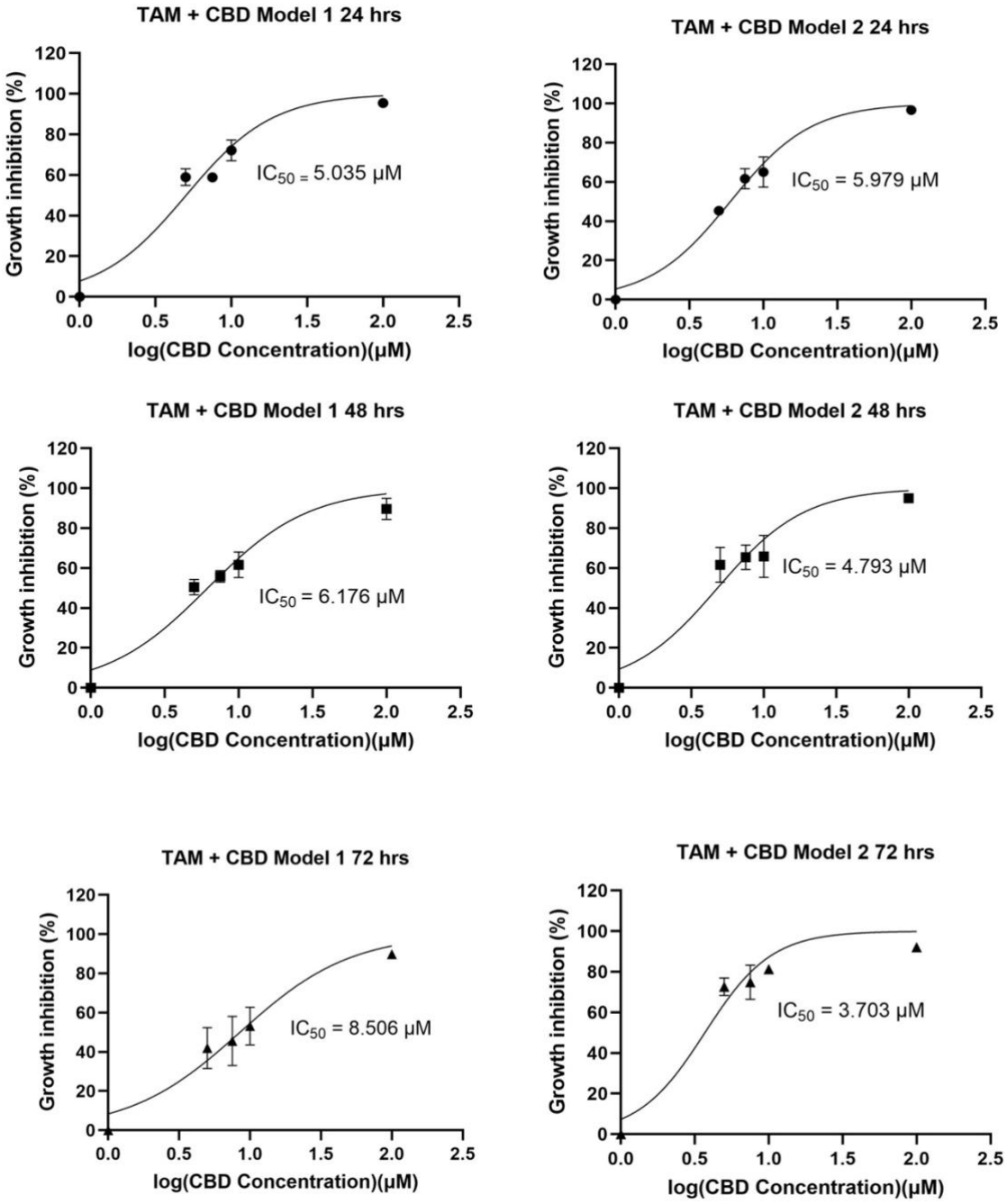


Figure C1.4: Half-maximal inhibitory (IC_{50}) concentrations of CBD combined with Tamoxifen at each time interval. Key: The IC_{50} values were calculated using GraphPad Prism Software (V10). In treatment model 1, the IC_{50} of CBD combined with Tamoxifen (TAM) increased over time. Contrastingly, IC_{50} values in treatment model 2 decreased across time.

C4: Statistical Analyses – Statistica Output

MCF7 Neutral Red assay

Model 1: Kruskal-Wallis Anova by Ranks and Post-hoc tests

24 hrs

Treatment Model=Model 1Kruskal-Wallis ANOVA by Ranks; Cell Viability (%) 24 hrs (MCF7 NR CBD Optimisation_TM)Independent (grouping) variable: TreatmentKruskal-Wallis test: H (7, N= 24) =19,66522 p =,0063

Depend.: Cell Viability (%) 24 hrs	Code	Valid N	Sum of Ranks	Mean Ranks
Diluent	1	3	69.00000	23.00000
2µM Tam	2	3	53.00000	17.66667
5µM CBD	3	3	47.00000	15.66667
7.5µM CBD	4	3	29.50000	9.83333
10µM CBD	5	3	22.50000	7.50000
5µM CBD + 2µM TAM	6	3	51.00000	17.00000
7,5µM CBD + 2µM TAM	7	3	19.00000	6.33333
10µM CBD + 2µM TAM	8	3	9.00000	3.00000

Post-Hoc

Absolute Differences between Mean Rank Approx. significant if highlighted at .05 significance level

	Diluent	2µM Tam	5µM CBD	7.5µM CBD	10µM CBD	5µM CBD + 2µM TAM	7,5µM CBD + 2µM TAM	10µM CBD + 2µM TAM
Diluent	---	5.33333333	7.33333333	13.1666667	15.5	6	16.6666667	20
2µM Tam	5.33333333	---	2	7.83333333	10.1666667	0.66666667	11.3333333	14.6666667
5µM CBD	7.33333333	2	---	5.83333333	8.16666667	1.33333333	9.33333333	12.6666667
7.5µM CBD	13.1666667	7.83333333	5.83333333	---	2.33333333	7.16666667	3.5	6.83333333
10µM CBD	15.5	10.1666667	8.16666667	2.33333333	---	9.5	1.16666667	4.5
5µM CBD + 2µM TAM	6	0.66666667	1.33333333	7.16666667	9.5	---	10.6666667	14
7,5µM CBD + 2µM TAM	16.6666667	11.3333333	9.33333333	3.5	1.16666667	10.6666667	---	3.33333333
10µM CBD + 2µM TAM	20	14.6666667	12.6666667	6.83333333	4.5	14	3.33333333	---

48 hrs

Treatment Model=Model 1Kruskal-Wallis ANOVA by Ranks; Cell Viability (%) 48 hrs (MCF7 NR CBD Optimisation_TM)Independent (grouping) variable: TreatmentKruskal-Wallis test: H (7, N= 24) =16,65333 p =,0198

Depend.: Cell Viability (%) 48 hrs	Code	Valid N	Sum of Ranks	Mean Ranks
Diluent	1	3	69.00000	23.00000
2µM Tam	2	3	48.00000	16.00000
5µM CBD	3	3	44.00000	14.66667
7.5µM CBD	4	3	48.00000	16.00000
10µM CBD	5	3	36.00000	12.00000
5µM CBD + 2µM TAM	6	3	25.00000	8.33333
7,5µM CBD + 2µM TAM	7	3	21.00000	7.00000
10µM CBD + 2µM TAM	8	3	9.00000	3.00000

Post-Hoc

Absolute Differences between Mean Rank Approx. significant if highlighted at .05 significance level

	Diluent	2µM Tam	5µM CBD	7.5µM CBD	10µM CBD	5µM CBD + 2µM TAM	7,5µM CBD + 2µM TAM	10µM CBD + 2µM TAM
Diluent	---	7	8.33333333	7	11	14.6666667	16	20
2µM Tam	7	---	1.33333333	0	4	7.66666667	9	13
5µM CBD	8.33333333	1.33333333	---	1.33333333	2.66666667	6.33333333	7.66666667	11.6666667
7.5µM CBD	7	0	1.33333333	---	4	7.66666667	9	13
10µM CBD	11	4	2.66666667	4	---	3.66666667	5	9
5µM CBD + 2µM TAM	14.6666667	7.66666667	6.33333333	7.66666667	3.66666667	---	1.33333333	5.33333333
7,5µM CBD + 2µM TAM	16	9	7.66666667	9	5	1.33333333	---	4
10µM CBD + 2µM TAM	20	13	11.6666667	13	9	5.33333333	4	---

72 hrs

Treatment Model=Model 1Kruskal-Wallis ANOVA by

Depend.: Cell Viability (%) 72 hrs	Code	Valid N	Sum of Ranks	Mean Ranks
Diluent	1	3	67.00000	22.33333
2µM Tam	2	3	61.00000	20.33333
5µM CBD	3	3	52.00000	17.33333
7.5µM CBD	4	3	42.00000	14.00000
10µM CBD	5	3	29.00000	9.66667
5µM CBD + 2µM TAM	6	3	25.00000	8.33333
7,5µM CBD + 2µM TAM	7	3	18.00000	6.00000
10µM CBD + 2µM TAM	8	3	6.00000	2.00000

Post-Hoc

Absolute Differences between Mean Rank Approx. significant if highlighted at .05 significance level

	Diluent	2µM Tam	5µM CBD	7.5µM CBD	10µM CBD	5µM CBD + 2µM TAM	7,5µM CBD + 2µM TAM	10µM CBD + 2µM TAM
Diluent	---	2	5	8.33333333	12.6666667	14	16.3333333	20.3333333
2µM Tam	2	---	3	6.33333333	10.6666667	12	14.3333333	18.3333333
5µM CBD	5	3	---	3.33333333	7.66666667	9	11.3333333	15.3333333
7.5µM CBD	8.33333333	6.33333333	3.33333333	---	4.33333333	5.66666667	8	12
10µM CBD	12.6666667	10.6666667	7.66666667	4.33333333	---	1.33333333	3.66666667	7.66666667
5µM CBD + 2µM TAM	14	12	9	5.66666667	1.33333333	---	2.33333333	6.33333333
7,5µM CBD + 2µM TAM	16.3333333	14.3333333	11.3333333	8	3.66666667	2.33333333	---	4
10µM CBD + 2µM TAM	20.3333333	18.3333333	15.3333333	12	7.66666667	6.33333333	4	---

MCF7 Model 2: Kruskal-Wallis Anova by Ranks and Post-hoc tests

24 hrs

Treatment Model=Model 2Kruskal-Wallis ANOVA by Ranks; Cell Viability (%) 24 hrs (MCF7 NR CBD Optimisation_TM)Independent (grouping) variable: TreatmentKruskal-Wallis test: H (7, N= 24) =17,53333 p =,0143

Depend.: Cell Viability (%) 24 hrs	Code	Valid N	Sum of Ranks	Mean Ranks
Diluent	1	3	69.00000	23.00000
2µM Tam	2	3	57.00000	19.00000
5µM CBD	3	3	40.00000	13.33333
7.5µM CBD	4	3	40.00000	13.33333
10µM CBD	5	3	19.00000	6.33333
5µM CBD + 2µM TAM	6	3	34.00000	11.33333
7,5µM CBD + 2µM TAM	7	3	33.00000	11.00000
10µM CBD + 2µM TAM	8	3	8.00000	2.66667

Post-Hoc

Absolute Differences between Mean Rank Approx. significant if highlighted at .05 significance level

	Diluent	2µM Tam	5µM CBD	7.5µM CBD	10µM CBD	5µM CBD + 2µM TAM	7,5µM CBD + 2µM TAM	10µM CBD + 2µM TAM
Diluent	---	4	9.666667	9.6666667	16.6666667	11.6666667	12	20.3333333
2µM Tam	4	---	5.666667	5.6666667	12.6666667	7.66666667	8	16.3333333
5µM CBD	9.66666667	5.66666667	---	0	7	2	2.33333333	10.6666667
7.5µM CBD	9.66666667	5.66666667	0	---	7	2	2.33333333	10.6666667
10µM CBD	16.6666667	12.6666667	7	7	---	5	4.66666667	3.66666667
5µM CBD + 2µM TAM	11.6666667	7.66666667	2	2	5	---	0.33333333	8.66666667
7,5µM CBD + 2µM TAM	12	8	2.333333	2.3333333	4.66666667	0.33333333	---	8.33333333
10µM CBD + 2µM TAM	20.3333333	16.3333333	10.66667	10.666667	3.66666667	8.66666667	8.33333333	---

48 hrs

Treatment Model=Model 2Kruskal-Wallis ANOVA by Ranks; Cell Viability (%) 48 hrs (MCF7 NR CBD Optimisation_TM)Independent (grouping) variable: TreatmentKruskal-Wallis test: H (7, N= 24) =18,64000 p =,0094

Depend.: Cell Viability (%) 48 hrs	Code	Valid N	Sum of Ranks	Mean Ranks
Diluent	1	3	69.00000	23.00000
2µM Tam	2	3	53.00000	17.66667
5µM CBD	3	3	51.00000	17.00000
7.5µM CBD	4	3	25.00000	8.33333
10µM CBD	5	3	13.00000	4.33333
5µM CBD + 2µM TAM	6	3	46.00000	15.33333
7,5µM CBD + 2µM TAM	7	3	17.00000	5.66667
10µM CBD + 2µM TAM	8	3	26.00000	8.66667

Post-Hoc

Absolute Differences between Mean Rank Approx. significant if highlighted at .05 significance level

	Diluent	2µM Tam	5µM CBD	7.5µM CBD	10µM CBD	5µM CBD + 2µM TAM	7,5µM CBD + 2µM TAM	10µM CBD + 2µM TAM
Diluent	---	5.33333333	6	14.666667	18.6666667	7.66666667	17.3333333	14.3333333
2µM Tam	5.33333333	---	0.666667	9.3333333	13.3333333	2.33333333	12	9
5µM CBD	6	0.66666667	---	8.6666667	12.6666667	1.66666667	11.3333333	8.33333333
7.5µM CBD	14.6666667	9.33333333	8.666667	---	4	7	2.66666667	0.33333333
10µM CBD	18.6666667	13.3333333	12.66667	4	---	11	1.33333333	4.33333333
5µM CBD + 2µM TAM	7.66666667	2.33333333	1.666667	7	11	---	9.66666667	6.66666667
7,5µM CBD + 2µM TAM	17.3333333	12	11.33333	2.6666667	1.33333333	9.66666667	---	3
10µM CBD + 2µM TAM	14.3333333	9	8.333333	0.3333333	4.33333333	6.66666667	3	---

72 hrs

Treatment Model=Model 2Kruskal-Wallis ANOVA by Ranks; Cell Viability (%) 72 hrs (MCF7 NR CBD Optimisation_TM)Independent (grouping) variable: TreatmentKruskal-Wallis test: H (7, N= 24) =20,61333 p =,0044

Depend.: Cell Viability (%) 72 hrs	Code	Valid N	Sum of Ranks	Mean Ranks
Diluent	1	3	69.00000	23.00000
2µM Tam	2	3	51.00000	17.00000
5µM CBD	3	3	59.00000	19.66667
7.5µM CBD	4	3	39.00000	13.00000
10µM CBD	5	3	23.00000	7.66667
5µM CBD + 2µM TAM	6	3	32.00000	10.66667
7,5µM CBD + 2µM TAM	7	3	19.00000	6.33333
10µM CBD + 2µM TAM	8	3	8.00000	2.66667

Post-Hoc

Absolute Differences between Mean Rank Approx. significant if highlighted at .05 significance level

	Diluent	2µM Tam	5µM CBD	7.5µM CBD	10µM CBD	5µM CBD + 2µM TAM	7,5µM CBD + 2µM TAM	10µM CBD + 2µM TAM
Diluent	---	6	3.333333	10	15.3333333	12.3333333	16.6666667	20.3333333
2µM Tam	6	---	2.666667	4	9.33333333	6.33333333	10.6666667	14.3333333
5µM CBD	3.33333333	2.66666667	---	6.6666667	12	9	13.3333333	17
7.5µM CBD	10	4	6.666667	---	5.33333333	2.33333333	6.66666667	10.3333333
10µM CBD	15.3333333	9.33333333	12	5.3333333	---	3	1.33333333	5
5µM CBD + 2µM TAM	12.3333333	6.33333333	9	2.3333333	3	---	4.33333333	8
7,5µM CBD + 2µM TAM	16.6666667	10.6666667	13.33333	6.6666667	1.33333333	4.33333333	---	3.66666667
10µM CBD + 2µM TAM	20.3333333	14.3333333	17	10.333333	5	8	3.66666667	---

MCF7 Model 1: Friedman Anova by ranks and Post-hoc tests

Diluent

Treatment=Diluent, Treatment Model=Model 1Friedman ANOVA and Kendall Coeff. of Concordance (MCF7 NR CBD Optimisation_TM)ANOVA Chi Sqr. (N = 3, df = 2) = 2,000000 p = ,36788Coeff. of Concordance = ,33333 Aver. rank r = -,1E-7

Variable	Average Rank	Sum of Ranks	Mean	Std.Dev.
Cell Viability (%) 24 hrs	1.666667	5.000000	97.8371	8.425576
Cell Viability (%) 48 hrs	2.666667	8.000000	100.4437	7.207862
Cell Viability (%) 72 hrs	1.666667	5.000000	101.4238	8.182890

Post - Hoc

Absolute Differences between Average RankApprox. significant if > 1.95467632136186at .05 significance level

	Cell Viability (%) 24 hrs	Cell Viability (%) 48 hrs	Cell Viability (%) 72 hrs
Cell Viability (%) 24 hrs	---	1	0
Cell Viability (%) 48 hrs	1	---	1
Cell Viability (%) 72 hrs	0	1	---

2uM Tam

Treatment=2µM Tam, Treatment Model=Model 1Friedman ANOVA and Kendall Coeff. of Concordance (MCF7 NR CBD Optimisation_TM)ANOVA Chi Sqr. (N = 3, df = 2) = 4,666667 p = ,09697Coeff. of Concordance = ,77778 Aver. rank r = ,66667

Variable	Average Rank	Sum of Ranks	Mean	Std.Dev.
Cell Viability (%) 24 hrs	1.333333	4.000000	58.88522	8.135328
Cell Viability (%) 48 hrs	1.666667	5.000000	66.20141	2.090127
Cell Viability (%) 72 hrs	3.000000	9.000000	92.98453	5.141595

Post - Hoc

Absolute Differences between Average RankApprox. significant if > 1.95467632136186at .05 significance level

	Cell Viability (%) 24 hrs	Cell Viability (%) 48 hrs	Cell Viability (%) 72 hrs
Cell Viability (%) 24 hrs	---	0.33333333	1.66666667
Cell Viability (%) 48 hrs	0.33333333	---	1.33333333
Cell Viability (%) 72 hrs	1.66666667	1.33333333	---

5uM CBD

Treatment=5µM CBD, Treatment Model=Model 1Friedman ANOVA and Kendall Coeff. of Concordance (MCF7 NR CBD Optimisation_TM)ANOVA Chi Sqr. (N = 3, df = 2) = 6,000000 p = ,04979Coeff. of Concordance = 1,0000 Aver. rank r = 1,0000

Variable	Average Rank	Sum of Ranks	Mean	Std.Dev.
Cell Viability (%) 24 hrs	1.000000	3.000000	54.22054	6.915466
Cell Viability (%) 48 hrs	2.000000	6.000000	64.64708	5.934467
Cell Viability (%) 72 hrs	3.000000	9.000000	84.46718	4.593768

Post - Hoc

Absolute Differences between Average RankApprox. significant if > 1.95467632136186at .05 significance level

	Cell Viability (%) 24 hrs	Cell Viability (%) 48 hrs	Cell Viability (%) 72 hrs
Cell Viability (%) 24 hrs	---	1	2
Cell Viability (%) 48 hrs	1	---	1
Cell Viability (%) 72 hrs	2	1	---

7.5uM

Treatment=7.5µM CBD, Treatment Model=Model 1Friedman ANOVA and Kendall Coeff. of Concordance (MCF7 NR CBD Optimisation_TM)ANOVA Chi Sqr. (N = 3, df = 2) = 4,666667 p = ,09697Coeff. of Concordance = ,77778 Aver. rank r = ,66667

Variable	Average Rank	Sum of Ranks	Mean	Std.Dev.
Cell Viability (%) 24 hrs	1.000000	3.000000	46.07641	2.465378
Cell Viability (%) 48 hrs	2.333333	7.000000	66.48132	6.341352
Cell Viability (%) 72 hrs	2.666667	8.000000	68.90814	0.226801

Post - Hoc

Absolute Differences between Average RankApprox. significant if > 1.95467632136186at .05 significance level

	Cell Viability (%) 24 hrs	Cell Viability (%) 48 hrs	Cell Viability (%) 72 hrs
Cell Viability (%) 24 hrs	---	1.33333333	1.66666667
Cell Viability (%) 48 hrs	1.33333333	---	0.33333333
Cell Viability (%) 72 hrs	1.66666667	0.33333333	---

10uM

Treatment=10µM CBD, Treatment Model=Model 1Friedman ANOVA and Kendall Coeff. of Concordance (MCF7 NR CBD Optimisation_TM)ANOVA Chi Sqr. (N = 3, df = 2) = 4,666667 p = ,09697Coeff. of Concordance = ,77778 Aver. rank r = ,66667

Variable	Average Rank	Sum of Ranks	Mean	Std.Dev.
Cell Viability (%) 24 hrs	1.000000	3.000000	41.23347	3.58128
Cell Viability (%) 48 hrs	2.666667	8.000000	59.22876	10.74003
Cell Viability (%) 72 hrs	2.333333	7.000000	60.91156	5.37484

Post - Hoc

Absolute Differences between Average RankApprox. significant if > 1.95467632136186at .05 significance level

	Cell Viability (%) 24 hrs	Cell Viability (%) 48 hrs	Cell Viability (%) 72 hrs
Cell Viability (%) 24 hrs	---	1.66666667	1.33333333
Cell Viability (%) 48 hrs	1.66666667	---	0.33333333
Cell Viability (%) 72 hrs	1.33333333	0.33333333	---

5uM + 2uM Tam

Treatment=5µM CBD + 2µM TAM, Treatment Model

Variable	Average Rank	Sum of Ranks	Mean	Std.Dev.
Cell Viability (%) 24 hrs	1.666667	5.000000	56.67683	2.087819
Cell Viability (%) 48 hrs	1.333333	4.000000	56.43026	3.004384
Cell Viability (%) 72 hrs	3.000000	9.000000	59.67017	1.938495

Post - Hoc

Absolute Differences between Average RankApprox. significant if > 1.95467632136186at .05 significance level

	Cell Viability (%) 24 hrs	Cell Viability (%) 48 hrs	Cell Viability (%) 72 hrs
Cell Viability (%) 24 hrs	---	0.33333333	1.33333333
Cell Viability (%) 48 hrs	0.33333333	---	1.66666667
Cell Viability (%) 72 hrs	1.33333333	1.66666667	---

7.5uM + 2uM Tam

Treatment=7,5µM CBD + 2µM TAM, Treatment Mod

Variable	Average Rank	Sum of Ranks	Mean	Std.Dev.
Cell Viability (%) 24 hrs	1.000000	3.000000	34.98828	12.80734
Cell Viability (%) 48 hrs	2.333333	7.000000	49.04723	13.59390
Cell Viability (%) 72 hrs	2.666667	8.000000	53.60695	6.09428

Post - Hoc

Absolute Differences between Average RankApprox. significant if > 1.95467632136186at .05 significance level

	Cell Viability (%) 24 hrs	Cell Viability (%) 48 hrs	Cell Viability (%) 72 hrs
Cell Viability (%) 24 hrs	---	1.33333333	1.66666667
Cell Viability (%) 48 hrs	1.33333333	---	0.33333333
Cell Viability (%) 72 hrs	1.66666667	0.33333333	---

10uM + 2uM Tam

Treatment=10µM CBD + 2µM TAM, Treatment Model=Model 1Friedman ANOVA and Kendall Coeff. of Concordance (MCF7 NR CBD Optimisation_TM)ANOVA Chi Sqr. (N = 3, df = 2) = 4,666667 p = ,09697Coeff. of Concordance = ,77778 Aver. rank r = ,66667

Variable	Average Rank	Sum of Ranks	Mean	Std.Dev.
Cell Viability (%) 24 hrs	1.000000	3.000000	26.12383	6.77088
Cell Viability (%) 48 hrs	2.333333	7.000000	38.35290	10.42093
Cell Viability (%) 72 hrs	2.666667	8.000000	45.58046	4.13575

Post - Hoc

Absolute Differences between Average RankApprox. significant if > 1.95467632136186at .05 significance level

	Cell Viability (%) 24 hrs	Cell Viability (%) 48 hrs	Cell Viability (%) 72 hrs
Cell Viability (%) 24 hrs	---	1.33333333	1.66666667
Cell Viability (%) 48 hrs	1.33333333	---	0.33333333
Cell Viability (%) 72 hrs	1.66666667	0.33333333	---

MCF7 Model 2: Friedman Anova by ranks and Post-hoc tests

Diluent

Treatment=Diluent, Treatment Model=Model 2Friedman ANOVA and Kendall Coeff. of Concordance (MCF7 NR CBD Optimisation_TM]ANOVA Chi Sqr. (N = 3, df = 2) = 4,666667 p = ,09697Coeff. of Concordance = ,77778 Aver. rank r = ,66667

Variable	Average Rank	Sum of Ranks	Mean	Std.Dev.
Cell Viability (%) 24 hrs	1.333333	4.000000	96.2306	6.601758
Cell Viability (%) 48 hrs	3.000000	9.000000	106.7344	1.853133
Cell Viability (%) 72 hrs	1.666667	5.000000	97.7983	3.634385

Post-Hoc

Absolute Differences between Average RankApprox. significant if > 1.95467632136186at .05 significance level

	Cell Viability (%) 24 hrs	Cell Viability (%) 48 hrs	Cell Viability (%) 72 hrs
Cell Viability (%) 24 hrs	---	1.66666667	0.33333333
Cell Viability (%) 48 hrs	1.66666667	---	1.33333333
Cell Viability (%) 72 hrs	0.33333333	1.33333333	---

2uM Tam

Treatment=2µM Tam, Treatment Model=Model 2Friedman ANOVA and Kendall Coeff. of Concordance (MCF7 NR CBD Optimisation_TM]ANOVA Chi Sqr. (N = 3, df = 2) = 6,000000 p = ,04979Coeff. of Concordance = 1,0000 Aver. rank r = 1,0000

Variable	Average Rank	Sum of Ranks	Mean	Std.Dev.
Cell Viability (%) 24 hrs	3.000000	9.000000	62.93520	4.649561
Cell Viability (%) 48 hrs	2.000000	6.000000	55.70426	2.545253
Cell Viability (%) 72 hrs	1.000000	3.000000	41.37810	3.450769

Post-Hoc

Absolute Differences between Average RankApprox. significant if > 1.95467632136186at .05 significance level

	Cell Viability (%) 24 hrs	Cell Viability (%) 48 hrs	Cell Viability (%) 72 hrs
Cell Viability (%) 24 hrs	---	1	2
Cell Viability (%) 48 hrs	1	---	1
Cell Viability (%) 72 hrs	2	1	---

5uM CBD

Treatment=5µM CBD, Treatment Model=Model 2Friedman ANOVA and Kendall Coeff. of Concordance (MCF7 NR CBD Optimisation_TM]ANOVA Chi Sqr. (N = 3, df = 2) = 4,666667 p = ,09697Coeff. of Concordance = ,77778 Aver. rank r = ,66667

Variable	Average Rank	Sum of Ranks	Mean	Std.Dev.
Cell Viability (%) 24 hrs	2.333333	7.000000	54.36335	8.56298
Cell Viability (%) 48 hrs	2.666667	8.000000	57.53977	10.08082
Cell Viability (%) 72 hrs	1.000000	3.000000	47.29384	4.17676

Post-Hoc

Absolute Differences between Average RankApprox. significant if > 1.95467632136186at .05 significance level

	Cell Viability (%) 24 hrs	Cell Viability (%) 48 hrs	Cell Viability (%) 72 hrs
Cell Viability (%) 24 hrs	---	0.33333333	1.33333333
Cell Viability (%) 48 hrs	0.33333333	---	1.66666667
Cell Viability (%) 72 hrs	1.33333333	1.66666667	---

7.5uM CBD

Treatment=7,5µM CBD, Treatment Model=Model 2Friedman ANOVA and Kendall Coeff. of Concordance (MCF7 NR CBD Optimisation_TM]ANOVA Chi Sqr. (N = 3, df = 2) = 4,666667 p = ,09697Coeff. of Concordance = ,77778 Aver. rank r = ,66667

Variable	Average Rank	Sum of Ranks	Mean	Std.Dev.
Cell Viability (%) 24 hrs	2.666667	8.000000	54.41599	9.898571
Cell Viability (%) 48 hrs	2.333333	7.000000	44.05334	4.784791
Cell Viability (%) 72 hrs	1.000000	3.000000	34.84382	4.664702

Post-Hoc

Absolute Differences between Average RankApprox. significant if > 1.95467632136186at .05 significance level

	Cell Viability (%) 24 hrs	Cell Viability (%) 48 hrs	Cell Viability (%) 72 hrs
Cell Viability (%) 24 hrs	---	0.33333333	1.66666667
Cell Viability (%) 48 hrs	0.33333333	---	1.33333333
Cell Viability (%) 72 hrs	1.66666667	1.33333333	---

10uM CBD

Treatment=10µM CBD, Treatment Model=Model 2Friedman ANOVA and Kendall Coeff. of Concordance (MCF7 NR CBD Optimisation_TM]ANOVA Chi Sqr. (N = 3, df = 2) = 4,666667 p = ,09697Coeff. of Concordance = ,77778 Aver. rank r = ,66667

Variable	Average Rank	Sum of Ranks	Mean	Std.Dev.
Cell Viability (%) 24 hrs	2.666667	8.000000	43.18968	8.78486
Cell Viability (%) 48 hrs	2.333333	7.000000	36.45037	10.60664
Cell Viability (%) 72 hrs	1.000000	3.000000	26.61096	4.08397

Post-Hoc

Absolute Differences between Average RankApprox. significant if > 1.95467632136186at .05 significance level

	Cell Viability (%) 24 hrs	Cell Viability (%) 48 hrs	Cell Viability (%) 72 hrs
Cell Viability (%) 24 hrs	---	0.33333333	1.66666667
Cell Viability (%) 48 hrs	0.33333333	---	1.33333333
Cell Viability (%) 72 hrs	1.66666667	1.33333333	---

5uM CBD + 2uM Tam

Treatment=5µM CBD + 2µM TAM, Treatment Model=Model 2Friedman ANOVA and Kendall Coeff. of Concordance (MCF7 NR CBD Optimisation_TM]ANOVA Chi Sqr. (N = 3, df = 2) = 4,666667 p = ,09697Coeff. of Concordance = ,77778 Aver. rank r = ,66667

Variable	Average Rank	Sum of Ranks	Mean	Std.Dev.
Cell Viability (%) 24 hrs	2.333333	7.000000	50.87374	5.631080
Cell Viability (%) 48 hrs	2.666667	8.000000	53.37814	1.648775
Cell Viability (%) 72 hrs	1.000000	3.000000	32.21288	6.458592

Post-Hoc

Absolute Differences between Average RankApprox. significant if > 1.95467632136186at .05 significance level

	Cell Viability (%) 24 hrs	Cell Viability (%) 48 hrs	Cell Viability (%) 72 hrs
Cell Viability (%) 24 hrs	---	0.33333333	1.33333333
Cell Viability (%) 48 hrs	0.33333333	---	1.66666667
Cell Viability (%) 72 hrs	1.33333333	1.66666667	---

7.5uM CBD + 2uM Tam

Treatment=7,5µM CBD + 2µM TAM, Treatment Model=Model 2Friedman ANOVA and Kendall Coeff. of Concordance (MCF7 NR CBD Optimisation_TM]ANOVA Chi Sqr. (N = 3, df = 2) = 6,000000 p = ,04979Coeff. of Concordance = 1,0000 Aver. rank r = 1,0000

Variable	Average Rank	Sum of Ranks	Mean	Std.Dev.
Cell Viability (%) 24 hrs	3.000000	9.000000	49.50562	2.207206
Cell Viability (%) 48 hrs	2.000000	6.000000	42.32204	2.158650
Cell Viability (%) 72 hrs	1.000000	3.000000	25.94431	3.436517

Post-Hoc

Absolute Differences between Average RankApprox. significant if > 1.95467632136186at .05 significance level

	Cell Viability (%) 24 hrs	Cell Viability (%) 48 hrs	Cell Viability (%) 72 hrs
Cell Viability (%) 24 hrs	---	1	2
Cell Viability (%) 48 hrs	1	---	1
Cell Viability (%) 72 hrs	2	1	---

10uM CBD + 2uM Tam

Treatment=10µM CBD + 2µM TAM, Treatment Model=Model 2Friedman ANOVA and Kendall Coeff. of Concordance (MCF7 NR CBD Optimisation_TM]ANOVA Chi Sqr. (N = 3, df = 2) = 6,000000 p = ,04979Coeff. of Concordance = 1,0000 Aver. rank r = 1,0000

Variable	Average Rank	Sum of Ranks	Mean	Std.Dev.
Cell Viability (%) 24 hrs	2.000000	6.000000	37.21968	5.853825
Cell Viability (%) 48 hrs	3.000000	9.000000	45.15998	4.214629
Cell Viability (%) 72 hrs	1.000000	3.000000	15.37154	8.523770

Post-Hoc

Absolute Differences between Average RankApprox. significant if > 1.95467632136186at .05 significance level

	Cell Viability (%) 24 hrs	Cell Viability (%) 48 hrs	Cell Viability (%) 72 hrs
Cell Viability (%) 24 hrs	---	1	1
Cell Viability (%) 48 hrs	1	---	2
Cell Viability (%) 72 hrs	1	2	---

MCF7 Mann-Whitney U Test

Diluent

	Treatment=DiluentMann-Whitney U Test (w/ continuity correction) (MCF7 NR CBD Optimisation_TM)By variable Treatment ModelMarked tests are significant at p <,05000									
variable	Rank Sum Model 1	Rank Sum Model 2	U	Z	p-value	Z adjusted	p-value	Valid N Model 1	Valid N Model 2	2*1sided exact p
Cell Viability (%) 24 hrs	12.00000	9.00000	3.000000	0.43644	0.662521	0.43644	0.662521	3	3	0.700000
Cell Viability (%) 48 hrs	7.00000	14.00000	1.000000	-1.30931	0.190431	-1.30931	0.190431	3	3	0.200000
Cell Viability (%) 72 hrs	12.00000	9.00000	3.000000	0.43644	0.662521	0.43644	0.662521	3	3	0.700000

2uM Tam

	Treatment=2µM TamMann-Whitney U Test (w/ continuity correction) (MCF7 NR CBD Optimisation_TM)By variable Treatment ModelMarked tests are significant at p <,05000									
variable	Rank Sum Model 1	Rank Sum Model 2	U	Z	p-value	Z adjusted	p-value	Valid N Model 1	Valid N Model 2	2*1sided exact p
Cell Viability (%) 24 hrs	9.00000	12.00000	3.000000	-0.436436	0.662521	-0.436436	0.662521	3	3	0.700000
Cell Viability (%) 48 hrs	15.00000	6.00000	0.000000	1.745743	0.080857	1.745743	0.080857	3	3	0.100000
Cell Viability (%) 72 hrs	15.00000	6.00000	0.000000	1.745743	0.080857	1.745743	0.080857	3	3	0.100000

5uM CBD

	Treatment=5µM CBDMann-Whitney U Test (w/ continuity correction) (MCF7 NR CBD Optimisation_TM)By variable Treatment ModelMarked tests are significant at p <,05000									
variable	Rank Sum Model 1	Rank Sum Model 2	U	Z	p-value	Z adjusted	p-value	Valid N Model 1	Valid N Model 2	2*1sided exact p
Cell Viability (%) 24 hrs	11.00000	10.00000	4.000000	0.000000	1.000000	0.000000	1.000000	3	3	1.000000
Cell Viability (%) 48 hrs	13.00000	8.00000	2.000000	0.872872	0.382734	0.872872	0.382734	3	3	0.400000
Cell Viability (%) 72 hrs	15.00000	6.00000	0.000000	1.745743	0.080857	1.745743	0.080857	3	3	0.100000

7.5uM CBD

	Treatment=7.5µM CBDMann-Whitney U Test (w/ continuity correction) (MCF7 NR CBD Optimisation_TM)By variable Treatment ModelMarked tests are significant at p <,05000									
variable	Rank Sum Model 1	Rank Sum Model 2	U	Z	p-value	Z adjusted	p-value	Valid N Model 1	Valid N Model 2	2*1sided exact p
Cell Viability (%) 24 hrs	7.00000	14.00000	1.000000	-1.30931	0.190431	-1.30931	0.190431	3	3	0.200000
Cell Viability (%) 48 hrs	15.00000	6.00000	0.000000	1.74574	0.080857	1.74574	0.080857	3	3	0.100000
Cell Viability (%) 72 hrs	15.00000	6.00000	0.000000	1.74574	0.080857	1.74574	0.080857	3	3	0.100000

10uM CBD

	Treatment=10µM CBDMann-Whitney U Test (w/ continuity correction) (MCF7 NR CBD Optimisation_TM)By variable Treatment ModelMarked tests are significant at p <,05000									
variable	Rank Sum Model 1	Rank Sum Model 2	U	Z	p-value	Z adjusted	p-value	Valid N Model 1	Valid N Model 2	2*1sided exact p
Cell Viability (%) 24 hrs	10.00000	11.00000	4.000000	0.000000	1.000000	0.000000	1.000000	3	3	1.000000
Cell Viability (%) 48 hrs	15.00000	6.00000	0.000000	1.745743	0.080857	1.745743	0.080857	3	3	0.100000
Cell Viability (%) 72 hrs	15.00000	6.00000	0.000000	1.745743	0.080857	1.745743	0.080857	3	3	0.100000

5uM CBD + 2uM Tam

	Treatment=5µM CBD + 2µM TAMMann-Whitney U Test (w/ continuity correction) (MCF7 NR CBD Optimisation_TM)By variable Treatment ModelMarked tests are significant at p <,05000									
variable	Rank Sum Model 1	Rank Sum Model 2	U	Z	p-value	Z adjusted	p-value	Valid N Model 1	Valid N Model 2	2*1sided exact p
Cell Viability (%) 24 hrs	14.00000	7.000000	1.000000	1.309307	0.190431	1.309307	0.190431	3	3	0.200000
Cell Viability (%) 48 hrs	14.00000	7.000000	1.000000	1.309307	0.190431	1.309307	0.190431	3	3	0.200000
Cell Viability (%) 72 hrs	15.00000	6.000000	0.000000	1.745743	0.080857	1.745743	0.080857	3	3	0.100000

7.5uM CBD + 2uM Tam

	Treatment=7,5µM CBD + 2µM TAMMann-Whitney U Test (w/ continuity correction) (MCF7 NR CBD Optimisation_TM)By variable Treatment ModelMarked tests are significant at p <,05000									
variable	Rank Sum Model 1	Rank Sum Model 2	U	Z	p-value	Z adjusted	p-value	Valid N Model 1	Valid N Model 2	2*1sided exact p
Cell Viability (%) 24 hrs	7.00000	14.00000	1.000000	-1.30931	0.190431	-1.30931	0.190431	3	3	0.200000
Cell Viability (%) 48 hrs	11.00000	10.00000	4.000000	0.00000	1.000000	0.00000	1.000000	3	3	1.000000
Cell Viability (%) 72 hrs	15.00000	6.00000	0.000000	1.74574	0.080857	1.74574	0.080857	3	3	0.100000

10uM CBD + 2uM Tam

	Treatment=10µM CBD + 2µM TAMMann-Whitney U Test (w/ continuity correction) (MCF7 NR CBD Optimisation_TM)By variable Treatment ModelMarked tests are significant at p <,05000									
variable	Rank Sum Model 1	Rank Sum Model 2	U	Z	p-value	Z adjusted	p-value	Valid N Model 1	Valid N Model 2	2*1sided exact p
Cell Viability (%) 24 hrs	7.00000	14.00000	1.000000	-1.30931	0.190431	-1.30931	0.190431	3	3	0.200000
Cell Viability (%) 48 hrs	9.00000	12.00000	3.000000	-0.43644	0.662521	-0.43644	0.662521	3	3	0.700000
Cell Viability (%) 72 hrs	15.00000	6.00000	0.000000	1.74574	0.080857	1.74574	0.080857	3	3	0.100000

MCF7 MTT assay

MCF7 Model 1: Kruskal-Wallis Anova by Ranks and Post-hoc tests

24 hrs

Treatment Model=Model 1Kruskal-Wallis ANOVA by Ranks; Growth Inhibition (%) 24 hrs (MCF7 MTT CBD Optimisation_TM)Independent (grouping) variable: TreatmentKruskal-Wallis test: H (9, N= 30) =26,70651 p =,0016

Depend.: Growth Inhibition (%) 24 hrs	Code	Valid N	Sum of Ranks	Mean Rank
Diluent	1	3	9.00000	3.00000
2µM Tam	2	3	17.00000	5.66667
5µM CBD	3	3	30.00000	10.00000
7.5µM CBD	4	3	48.00000	16.00000
10µM CBD	5	3	62.00000	20.66667
5µM CBD + 2µM TAM	6	3	55.00000	18.33333
7,5µM CBD + 2µM TAM	7	3	57.00000	19.00000
10µM CBD + 2µM TAM	8	3	78.00000	26.00000
SFM	9	3	22.00000	7.33333
Triton-X (0.1%)	10	3	87.00000	29.00000

Post-Hoc

Absolute Differences between Mean Rank Approx. significant if highlighted at .05 significance level

	Diluent	2µM Tam	5µM CBD	7.5µM CBD	10µM CBD	5µM CBD + 2µM TAM	7,5µM CBD + 2µM TAM	10µM CBD + 2µM TAM	SFM	Triton-X (0.1%)
Diluent	---	2.66666667	7	13	17.6666667	15.3333333	16	23	4.33333333	26
2µM Tam	2.66666667	---	4.33333333	10.3333333	15	12.6666667	13.3333333	20.3333333	1.66666667	23.33333333
5µM CBD	7	4.33333333	---	6	10.6666667	8.33333333	9	16	2.66666667	19
7.5µM CBD	13	10.3333333	6	---	4.66666667	2.33333333	3	10	8.66666667	13
10µM CBD	17.6666667	15	10.6666667	4.66666667	---	2.33333333	1.66666667	5.33333333	13.3333333	8.333333333
5µM CBD + 2µM TAM	15.3333333	12.6666667	8.33333333	2.33333333	2.33333333	---	0.66666667	7.66666667	11	10.66666667
7,5µM CBD + 2µM TAM	16	13.3333333	9	3	1.66666667	0.66666667	---	7	11.6666667	10
10µM CBD + 2µM TAM	23	20.3333333	16	10	5.33333333	7.66666667	7	---	18.6666667	3
SFM	4.33333333	1.66666667	2.66666667	8.66666667	13.3333333	11	11.6666667	18.6666667	---	21.66666667
Triton-X (0.1%)	26	23.3333333	19	13	8.33333333	10.6666667	10	3	21.6666667	---

48 hrs

Treatment Model=Model 1Kruskal-Wallis ANOVA by Ranks; Growth Inhibition (%) 48 hrs (MCF7 MTT CBD Optimisation_TM)Independent (grouping) variable: TreatmentKruskal-Wallis test: H (9, N= 30) =25,36129 p =,0026

Depend.: Growth Inhibition (%) 48 hrs	Code	Valid N	Sum of Ranks	Mean Rank
Diluent	1	3	6.00000	2.00000
2µM Tam	2	3	33.00000	11.00000
5µM CBD	3	3	39.00000	13.00000
7.5µM CBD	4	3	25.00000	8.33333
10µM CBD	5	3	41.00000	13.66667
5µM CBD + 2µM TAM	6	3	59.00000	19.66667
7,5µM CBD + 2µM TAM	7	3	70.00000	23.33333
10µM CBD + 2µM TAM	8	3	76.00000	25.33333
SFM	9	3	29.00000	9.66667
Triton-X (0.1%)	10	3	87.00000	29.00000

Post-Hoc

Absolute Differences between Mean Rank Approx. significant if highlighted at .05 significance level

	Diluent	2µM Tam	5µM CBD	7.5µM CBD	10µM CBD	5µM CBD + 2µM TAM	7,5µM CBD + 2µM TAM	10µM CBD + 2µM TAM	SFM	Triton-X (0.1%)
Diluent	---	9	11	6.33333333	11.6666667	17.6666667	21.3333333	23.3333333	7.66666667	27
2µM Tam	9	---	2	2.66666667	2.66666667	8.66666667	12.3333333	14.3333333	1.33333333	18
5µM CBD	11	2	---	4.66666667	0.66666667	6.66666667	10.3333333	12.3333333	3.33333333	16
7.5µM CBD	6.33333333	2.66666667	4.66666667	---	5.33333333	11.3333333	15	17	1.33333333	20.66666667
10µM CBD	11.6666667	2.66666667	0.66666667	5.33333333	---	6	9.66666667	11.6666667	4	15.33333333
5µM CBD + 2µM TAM	17.6666667	8.66666667	6.66666667	11.3333333	6	---	3.66666667	5.66666667	10	9.333333333
7,5µM CBD + 2µM TAM	21.3333333	12.3333333	10.3333333	15	9.66666667	3.66666667	---	2	13.6666667	5.666666667
10µM CBD + 2µM TAM	23.3333333	14.3333333	12.3333333	17	11.6666667	5.66666667	2	---	15.6666667	3.666666667
SFM	7.66666667	1.33333333	3.33333333	1.33333333	4	10	13.6666667	15.6666667	---	19.33333333
Triton-X (0.1%)	27	18	16	20.6666667	15.3333333	9.33333333	5.66666667	3.66666667	19.3333333	---

72 hrs

Treatment Model=Model 1Kruskal-Wallis ANOVA by Ranks; Growth Inhibition (%) 72 hrs (MCF7 MTT CBD Optimisation_TM)Independent (grouping) variable: TreatmentKruskal-Wallis test: H (9, N= 30) =25,42071 p =,0025

Depend.: Growth Inhibition (%) 72 hrs	Code	Valid N	Sum of Ranks	Mean Rank
Diluent	1	3	6.00000	2.00000
2µM Tam	2	3	15.00000	5.00000
5µM CBD	3	3	25.00000	8.33333
7.5µM CBD	4	3	44.00000	14.66667
10µM CBD	5	3	59.00000	19.66667
5µM CBD + 2µM TAM	6	3	55.50000	18.50000
7,5µM CBD + 2µM TAM	7	3	58.50000	19.50000
10µM CBD + 2µM TAM	8	3	74.00000	24.66667
SFM	9	3	41.00000	13.66667
Triton-X (0.1%)	10	3	87.00000	29.00000

Post-Hoc

Absolute Differences between Mean Rank Approx. significant if highlighted at .05 significance level

	Diluent	2µM Tam	5µM CBD	7.5µM CBD	10µM CBD	5µM CBD + 2µM TAM	7,5µM CBD + 2µM TAM	10µM CBD + 2µM TAM	SFM	Triton-X (0.1%)
Diluent	---	3	6.33333333	12.6666667	17.6666667	16.5	17.5	22.6666667	11.6666667	27
2µM Tam	3	---	3.33333333	9.66666667	14.6666667	13.5	14.5	19.6666667	8.66666667	24
5µM CBD	6.33333333	3.33333333	---	6.33333333	11.3333333	10.1666667	11.1666667	16.3333333	5.33333333	20.66666667
7.5µM CBD	12.6666667	9.66666667	6.33333333	---	5	3.83333333	4.83333333	10	1	14.33333333
10µM CBD	17.6666667	14.6666667	11.3333333	5	---	1.16666667	0.16666667	5	6	9.333333333
5µM CBD + 2µM TAM	16.5	13.5	10.1666667	3.83333333	1.16666667	---	1	6.16666667	4.83333333	10.5
7,5µM CBD + 2µM TAM	17.5	14.5	11.1666667	4.83333333	0.16666667	1	---	5.16666667	5.83333333	9.5
10µM CBD + 2µM TAM	22.6666667	19.6666667	16.3333333	10	5	6.16666667	5.16666667	---	11	4.333333333
SFM	11.6666667	8.66666667	5.33333333	1	6	4.83333333	5.83333333	11	---	15.33333333
Triton-X (0.1%)	27	24	20.6666667	14.3333333	9.33333333	10.5	9.5	4.33333333	15.3333333	---

MCF7 Model 2: Kruskal-Wallis Anova by Ranks and Post-hoc tests

24 hrs

Treatment Model=Model 2Kruskal-Wallis ANOVA by Ranks; Growth Inhibition (%) 24 hrs (MCF7 MTT CBD Optimisation_TM)Independent (grouping) variable: TreatmentKruskal-Wallis test: H (9, N= 30) =26,44516 p =,0017

Depend.: Growth Inhibition (%) 24 hrs	Code	Valid N	Sum of Ranks	Mean Rank
Diluent	1	3	6.00000	2.00000
2µM Tam	2	3	24.00000	8.00000
5µM CBD	3	3	41.00000	13.66667
7.5µM CBD	4	3	49.00000	16.33333
10µM CBD	5	3	59.00000	19.66667
5µM CBD + 2µM TAM	6	3	43.00000	14.33333
7,5µM CBD + 2µM TAM	7	3	68.00000	22.66667
10µM CBD + 2µM TAM	8	3	73.00000	24.33333
SFM	9	3	15.00000	5.00000
Triton-X (0.1%)	10	3	87.00000	29.00000

Post-Hoc

Absolute Differences between Mean Rank Approx. significant if highlighted at .05 significance level

	Diluent	2µM Tam	5µM CBD	7.5µM CBD	10µM CBD	5µM CBD + 2µM TAM	7,5µM CBD + 2µM TAM	10µM CBD + 2µM TAM	SFM	Triton-X (0.1%)
Diluent	---	6	11.6666667	14.3333333	17.6666667	12.3333333	20.6666667	22.3333333	3	27
2µM Tam	6	---	5.66666667	8.33333333	11.6666667	6.33333333	14.6666667	16.3333333	3	21
5µM CBD	11.6666667	5.66666667	---	2.66666667	6	0.66666667	9	10.6666667	8.66666667	15.33333333
7.5µM CBD	14.3333333	8.33333333	2.66666667	---	3.33333333	2	6.33333333	8	11.3333333	12.66666667
10µM CBD	17.6666667	11.6666667	6	3.33333333	---	5.33333333	3	4.66666667	14.6666667	9.333333333
5µM CBD + 2µM TAM	12.3333333	6.33333333	0.66666667	2	5.33333333	---	8.33333333	10	9.33333333	14.66666667
7,5µM CBD + 2µM TAM	20.6666667	14.6666667	9	6.33333333	3	8.33333333	---	1.66666667	17.6666667	6.333333333
10µM CBD + 2µM TAM	22.3333333	16.3333333	10.6666667	8	4.66666667	10	1.66666667	---	19.3333333	4.666666667
SFM	3	3	8.66666667	11.3333333	14.6666667	9.33333333	17.6666667	19.3333333	---	24
Triton-X (0.1%)	27	21	15.3333333	12.6666667	9.33333333	14.6666667	6.33333333	4.66666667	24	---

48 hrs

Treatment Model=Model 2Kruskal-Wallis ANOVA by Ranks; Growth Inhibition (%) 48 hrs (MCF7 MTT CBD Optimisation_TM)Independent (grouping) variable: TreatmentKruskal-Wallis test: H (9, N= 30) =24,12148 p =,0041

Depend.: Growth Inhibition (%) 48 hrs	Code	Valid N	Sum of Ranks	Mean Rank
Diluent	1	3	6.00000	2.00000
2µM Tam	2	3	37.00000	12.33333
5µM CBD	3	3	27.00000	9.00000
7.5µM CBD	4	3	49.00000	16.33333
10µM CBD	5	3	61.00000	20.33333
5µM CBD + 2µM TAM	6	3	59.00000	19.66667
7,5µM CBD + 2µM TAM	7	3	64.00000	21.33333
10µM CBD + 2µM TAM	8	3	60.00000	20.00000
SFM	9	3	15.00000	5.00000
Triton-X (0.1%)	10	3	87.00000	29.00000

Post-Hoc

Absolute Differences between Mean Rank Approx. significant if highlighted at .05 significance level

	Diluent	2µM Tam	5µM CBD	7.5µM CBD	10µM CBD	5µM CBD + 2µM TAM	7,5µM CBD + 2µM TAM	10µM CBD + 2µM TAM	SFM	Triton-X (0.1%)
Diluent	---	10.3333333	7	14.3333333	18.3333333	17.6666667	19.3333333	18	3	27
2µM Tam	10.3333333	---	3.33333333	4	8	7.33333333	9	7.66666667	7.33333333	16.66666667
5µM CBD	7	3.33333333	---	7.33333333	11.3333333	10.6666667	12.3333333	11	4	20
7.5µM CBD	14.3333333	4	7.33333333	---	4	3.33333333	5	3.66666667	11.3333333	12.66666667
10µM CBD	18.3333333	8	11.3333333	4	---	0.66666667	1	0.33333333	15.3333333	8.666666667
5µM CBD + 2µM TAM	17.6666667	7.33333333	10.6666667	3.33333333	0.66666667	---	1.66666667	0.33333333	14.6666667	9.333333333
7,5µM CBD + 2µM TAM	19.3333333	9	12.3333333	5	1	1.66666667	---	1.33333333	16.3333333	7.666666667
10µM CBD + 2µM TAM	18	7.66666667	11	3.66666667	0.33333333	0.33333333	1.33333333	---	15	9
SFM	3	7.33333333	4	11.3333333	15.3333333	14.6666667	16.3333333	15	---	24
Triton-X (0.1%)	27	16.6666667	20	12.6666667	8.66666667	9.33333333	7.66666667	9	24	---

72 hrs

Treatment Model=Model 2Kruskal-Wallis ANOVA by Ranks; Growth Inhibition (%) 72 hrs (MCF7 MTT CBD Optimisation_TM)Independent (grouping) variable: TreatmentKruskal-Wallis test: H (9, N= 30) =26,71183 p =,0016

Depend.: Growth Inhibition (%) 72 hrs	Code	Valid N	Sum of Ranks	Mean Rank
Diluent	1	3	6.00000	2.00000
2µM Tam	2	3	28.00000	9.33333
5µM CBD	3	3	29.00000	9.66667
7.5µM CBD	4	3	46.00000	15.33333
10µM CBD	5	3	54.00000	18.00000
5µM CBD + 2µM TAM	6	3	61.00000	20.33333
7,5µM CBD + 2µM TAM	7	3	63.00000	21.00000
10µM CBD + 2µM TAM	8	3	75.00000	25.00000
SFM	9	3	16.00000	5.33333
Triton-X (0.1%)	10	3	87.00000	29.00000

Post-Hoc

Absolute Differences between Mean Rank Approx. significant if highlighted at .05 significance level

	Diluent	2µM Tam	5µM CBD	7.5µM CBD	10µM CBD	5µM CBD + 2µM TAM	7,5µM CBD + 2µM TAM	10µM CBD + 2µM TAM	SFM	Triton-X (0.1%)
Diluent	---	7.33333333	7.66666667	13.3333333	16	18.3333333	19	23	3.33333333	27
2µM Tam	7.33333333	---	0.33333333	6	8.66666667	11	11.6666667	15.6666667	4	19.66666667
5µM CBD	7.66666667	0.33333333	---	5.66666667	8.33333333	10.6666667	11.3333333	15.3333333	4.33333333	19.33333333
7.5µM CBD	13.3333333	6	5.66666667	---	2.66666667	5	5.66666667	9.66666667	10	13.66666667
10µM CBD	16	8.66666667	8.33333333	2.66666667	---	2.33333333	3	7	12.6666667	11
5µM CBD + 2µM TAM	18.3333333	11	10.6666667	5	2.33333333	---	0.66666667	4.66666667	15	8.666666667
7,5µM CBD + 2µM TAM	19	11.6666667	11.3333333	5.66666667	3	0.66666667	---	4	15.6666667	8
10µM CBD + 2µM TAM	23	15.6666667	15.3333333	9.66666667	7	4.66666667	4	---	19.6666667	4
SFM	3.33333333	4	4.33333333	10	12.6666667	15	15.6666667	19.6666667	---	23.66666667
Triton-X (0.1%)	27	19.6666667	19.3333333	13.6666667	11	8.66666667	8	4	23.6666667	---

MCF7 Model 1: Friedman Anova by Ranks and Post-hoc tests

Diluent

Treatment=Diluent, Treatment Model=Model 1Friedman ANOVA and Kendall Coeff. of Concordance (MCF7 MTT CBD Optimisation_TM)ANOVA Chi Sqr. (N = 3, df = 2) = 4,666667 p = ,09697Coeff. of Concordance = ,77778 Aver. rank r = ,66667

Variable	Average Rank	Sum of Ranks	Mean	Std.Dev.
Growth Inhibition (%) 24 hrs	2.666667	8.000000	3.81694	1.473755
Growth Inhibition (%) 48 hrs	1.000000	3.000000	-3.10990	1.330171
Growth Inhibition (%) 72 hrs	2.333333	7.000000	1.41846	1.906266

Post-Hoc

Absolute Differences between Average RankApprox. significant if > 1.954676321368 6at .05 significance level

	Growth Inhibition (%) 24 hrs	Growth Inhibition (%) 48 hrs	Growth Inhibition (%) 72 hrs
Growth Inhibition (%) 24 hrs	---	1.66666667	0.33333333
Growth Inhibition (%) 48 hrs	1.66666667	---	1.33333333
Growth Inhibition (%) 72 hrs	0.33333333	1.33333333	---

2uM Tam

Treatment=2µM Tam, Treatment Model=Model 1Friedman ANOVA and Kendall Coeff. of Concordance (MCF7 MTT CBD Optimisation_TM)ANOVA Chi Sqr. (N = 3, df = 2) = 2,666667 p = ,26360Coeff. of Concordance = ,44444 Aver. rank r = ,16667

Variable	Average Rank	Sum of Ranks	Mean	Std.Dev.
Growth Inhibition (%) 24 hrs	2.000000	6.000000	22.43336	30.09860
Growth Inhibition (%) 48 hrs	2.666667	8.000000	38.52443	3.19240
Growth Inhibition (%) 72 hrs	1.333333	4.000000	7.08407	2.41107

Post-Hoc

Absolute Differences between Average RankApprox. significant if > 1.954676321368 6at .05 significance level

	Growth Inhibition (%) 24 hrs	Growth Inhibition (%) 48 hrs	Growth Inhibition (%) 72 hrs
Growth Inhibition (%) 24 hrs	---	0.66666667	0.66666667
Growth Inhibition (%) 48 hrs	0.66666667	---	1.33333333
Growth Inhibition (%) 72 hrs	0.66666667	1.33333333	---

5uM CBD

Treatment=5µM CBD, Treatment Model=Model 1Friedman ANOVA and Kendall Coeff. of Concordance (MCF7 MTT CBD Optimisation_TM)ANOVA Chi Sqr. (N = 3, df = 2) = 4,666667 p = ,09697Coeff. of Concordance = ,77778 Aver. rank r = ,66667

Variable	Average Rank	Sum of Ranks	Mean	Std.Dev.
Growth Inhibition (%) 24 hrs	2.666667	8.000000	44.19955	5.004640
Growth Inhibition (%) 48 hrs	2.333333	7.000000	41.58916	4.691568
Growth Inhibition (%) 72 hrs	1.000000	3.000000	23.85756	5.254361

Post-Hoc

Absolute Differences between Average RankApprox. significant if > 1.954676321368 6at .05 significance level

	Growth Inhibition (%) 24 hrs	Growth Inhibition (%) 48 hrs	Growth Inhibition (%) 72 hrs
Growth Inhibition (%) 24 hrs	---	0.33333333	1.66666667
Growth Inhibition (%) 48 hrs	0.33333333	---	1.33333333
Growth Inhibition (%) 72 hrs	1.66666667	1.33333333	---

7.5uM CBD

Treatment=7,5µM CBD, Treatment Model=Model 1Friedman ANOVA and Kendall Coeff. of Concordance (MCF7 MTT CBD Optimisation_TM)ANOVA Chi Sqr. (N = 3, df = 2) = 4,666667 p = ,09697Coeff. of Concordance = ,77778 Aver. rank r = ,66667

Variable	Average Rank	Sum of Ranks	Mean	Std.Dev.
Growth Inhibition (%) 24 hrs	3.000000	9.000000	56.41578	4.495119
Growth Inhibition (%) 48 hrs	1.666667	5.000000	36.41265	3.016827
Growth Inhibition (%) 72 hrs	1.333333	4.000000	35.60990	5.704349

Post-Hoc

Absolute Differences between Average RankApprox. significant if > 1.954676321368 6at .05 significance level

	Growth Inhibition (%) 24 hrs	Growth Inhibition (%) 48 hrs	Growth Inhibition (%) 72 hrs
Growth Inhibition (%) 24 hrs	---	1.33333333	1.66666667
Growth Inhibition (%) 48 hrs	1.33333333	---	0.33333333
Growth Inhibition (%) 72 hrs	1.66666667	0.33333333	---

10uM CBD

Treatment=10µM CBD, Treatment Model=Model 1Friedman ANOVA and Kendall Coeff. of Concordance (MCF7 MTT CBD Optimisation_TM)ANOVA Chi Sqr. (N = 3, df = 2) = 4,666667 p = ,09697Coeff. of Concordance = ,77778 Aver. rank r = ,66667

Variable	Average Rank	Sum of Ranks	Mean	Std.Dev.
Growth Inhibition (%) 24 hrs	3.000000	9.000000	61.58037	4.493878
Growth Inhibition (%) 48 hrs	1.666667	5.000000	41.41126	2.619402
Growth Inhibition (%) 72 hrs	1.333333	4.000000	41.77449	2.747334

Post-Hoc

Absolute Differences between Average RankApprox. significant if > 1.954676321368 6at .05 significance level

	Growth Inhibition (%) 24 hrs	Growth Inhibition (%) 48 hrs	Growth Inhibition (%) 72 hrs
Growth Inhibition (%) 24 hrs	---	1.33333333	1.66666667
Growth Inhibition (%) 48 hrs	1.33333333	---	0.33333333
Growth Inhibition (%) 72 hrs	1.66666667	0.33333333	---

5uM CBD + 2uM Tam

Treatment=5µM CBD + 2µM TAM, Treatment Model=Model 1Friedman ANOVA and Kendall Coeff. of Concordance (MCF7 MTT CBD Optimisation_TM)ANOVA Chi Sqr. (N = 3, df = 2) = 4,666667 p = ,09697Coeff. of Concordance = ,77778 Aver. rank r = ,66667

Variable	Average Rank	Sum of Ranks	Mean	Std.Dev.
Growth Inhibition (%) 24 hrs	3.000000	9.000000	58.97030	4.13739
Growth Inhibition (%) 48 hrs	1.666667	5.000000	50.46941	3.81363
Growth Inhibition (%) 72 hrs	1.333333	4.000000	41.98252	10.39428

Post-Hoc

Absolute Differences between Average RankApprox. significant if > 1.954676321368 6at .05 significance level

	Growth Inhibition (%) 24 hrs	Growth Inhibition (%) 48 hrs	Growth Inhibition (%) 72 hrs
Growth Inhibition (%) 24 hrs	---	1.33333333	1.66666667
Growth Inhibition (%) 48 hrs	1.33333333	---	0.33333333
Growth Inhibition (%) 72 hrs	1.66666667	0.33333333	---

7.5uM CBD + 2uM Tam

Treatment=7,5µM CBD + 2µM TAM, Treatment Model=Model 1Friedman ANOVA and Kendall Coeff. of Concordance (MCF7 MTT CBD Optimisation_TM)ANOVA Chi Sqr. (N = 3, df = 2) = 2,000000 p = ,36788Coeff. of Concordance = ,33333 Aver. rank r = -,1E-7

Variable	Average Rank	Sum of Ranks	Mean	Std.Dev.
Growth Inhibition (%) 24 hrs	2.666667	8.000000	58.84103	0.58061
Growth Inhibition (%) 48 hrs	1.666667	5.000000	55.82020	2.91883
Growth Inhibition (%) 72 hrs	1.666667	5.000000	45.51671	12.52761

Post-Hoc

Absolute Differences between Average RankApprox. significant if > 1.954676321368 6at .05 significance level

	Growth Inhibition (%) 24 hrs	Growth Inhibition (%) 48 hrs	Growth Inhibition (%) 72 hrs
Growth Inhibition (%) 24 hrs	---	1	1
Growth Inhibition (%) 48 hrs	1	---	0
Growth Inhibition (%) 72 hrs	1	0	---

10uM CBD + 2uM Tam

Treatment=10µM CBD + 2µM TAM, Treatment Model=Model 1Friedman ANOVA and Kendall Coeff. of Concordance (MCF7 MTT CBD Optimisation_TM)ANOVA Chi Sqr. (N = 3, df = 2) = 4,666667 p = ,09697Coeff. of Concordance = ,77778 Aver. rank r = ,66667

Variable	Average Rank	Sum of Ranks	Mean	Std.Dev.
Growth Inhibition (%) 24 hrs	3.000000	9.000000	72.15022	5.133546
Growth Inhibition (%) 48 hrs	1.666667	5.000000	61.64420	6.375958
Growth Inhibition (%) 72 hrs	1.333333	4.000000	53.15986	9.619628

Post-Hoc

Absolute Differences between Average RankApprox. significant if > 1.954676321368 6at .05 significance level

	Growth Inhibition (%) 24 hrs	Growth Inhibition (%) 48 hrs	Growth Inhibition (%) 72 hrs
Growth Inhibition (%) 24 hrs	---	1.33333333	1.66666667
Growth Inhibition (%) 48 hrs	1.33333333	---	0.33333333
Growth Inhibition (%) 72 hrs	1.66666667	0.33333333	---

SFM

Treatment=LC, Treatment Model=Model 1Friedman ANOVA and Kendall Coeff. of Concordance (MCF7 MTT CBD Optimisation_TM)ANOVA Chi Sqr. (N = 3, df = 2) = ,6666667 p = ,71653Coeff. of Concordance = ,11111 Aver. rank r = -,3333

Variable	Average Rank	Sum of Ranks	Mean	Std.Dev.
Growth Inhibition (%) 24 hrs	1.666667	5.000000	33.31291	13.32777
Growth Inhibition (%) 48 hrs	2.333333	7.000000	35.89656	11.89756
Growth Inhibition (%) 72 hrs	2.000000	6.000000	33.37708	9.11224

Post-Hoc

Absolute Differences between Average RankApprox. significant if > 1.954676321368 6at .05 significance level

	Growth Inhibition (%) 24 hrs	Growth Inhibition (%) 48 hrs	Growth Inhibition (%) 72 hrs
Growth Inhibition (%) 24 hrs	---	0.66666667	0.33333333
Growth Inhibition (%) 48 hrs	0.66666667	---	0.33333333
Growth Inhibition (%) 72 hrs	0.33333333	0.33333333	---

Triton-X (0.1%)

Treatment=HC, Treatment Model=Model 1Friedman ANOVA and Kendall Coeff. of Concordance (MCF7 MTT CBD Optimisation_TM)ANOVA Chi Sqr. (N = 3, df = 2) = 4,666667 p = ,09697Coeff. of Concordance = ,77778 Aver. rank r = ,66667

Variable	Average Rank	Sum of Ranks	Mean	Std.Dev.
Growth Inhibition (%) 24 hrs	3.000000	9.000000	95.45790	2.079449
Growth Inhibition (%) 48 hrs	1.333333	4.000000	89.60665	5.324247
Growth Inhibition (%) 72 hrs	1.666667	5.000000	89.76984	1.390322

Post-Hoc

Absolute Differences between Average RankApprox. significant if > 1.954676321368 6at .05 significance level

	Growth Inhibition (%) 24 hrs	Growth Inhibition (%) 48 hrs	Growth Inhibition (%) 72 hrs
Growth Inhibition (%) 24 hrs	---	1.66666667	1.33333333
Growth Inhibition (%) 48 hrs	1.66666667	---	0.33333333
Growth Inhibition (%) 72 hrs	1.33333333	0.33333333	---

MCF7 Model 2: Friedman Anova by Ranks and Post-hoc tests

Diluent

Treatment=Diluent, Treatment Model=Model 2Friedman ANOVA and Kendall Coeff. of Concordance (MCF7 MTT CBD Optimisation_TM)ANOVA Chi Sqr. (N = 3, df = 2) = ,6666667 p = ,71653Coeff. of Concordance = ,11111 Aver. rank r = -,3333

Variable	Average Rank	Sum of Ranks	Mean	Std.Dev.
Growth Inhibition (%) 24 hrs	2.000000	6.000000	2.319894	2.932348
Growth Inhibition (%) 48 hrs	2.333333	7.000000	1.708266	0.834653
Growth Inhibition (%) 72 hrs	1.666667	5.000000	1.450657	1.619494

Post-Hoc

Absolute Differences between Average RankApprox. significant if > 1,95467632136186at .05 significance level

	Growth Inhibition (%) 24 hrs	Growth Inhibition (%) 48 hrs	Growth Inhibition (%) 72 hrs
Growth Inhibition (%) 24 hrs	---	0.33333333	0.33333333
Growth Inhibition (%) 48 hrs	0.33333333	---	0.66666667
Growth Inhibition (%) 72 hrs	0.33333333	0.66666667	---

2uM Tam

Treatment=2µM Tam, Treatment Model=Model 2Friedman ANOVA and Kendall Coeff. of Concordance (MCF7 MTT CBD Optimisation_TM)ANOVA Chi Sqr. (N = 3, df = 2) = 4,666667 p = ,09697Coeff. of Concordance = ,77778 Aver. rank r = ,66667

Variable	Average Rank	Sum of Ranks	Mean	Std.Dev.
Growth Inhibition (%) 24 hrs	1.000000	3.000000	36.08999	1.98396
Growth Inhibition (%) 48 hrs	2.666667	8.000000	51.01908	10.66375
Growth Inhibition (%) 72 hrs	2.333333	7.000000	52.74067	5.00003

Post-Hoc

Absolute Differences between Average RankApprox. significant if > 1,95467632136186at .05 significance level

	Growth Inhibition (%) 24 hrs	Growth Inhibition (%) 48 hrs	Growth Inhibition (%) 72 hrs
Growth Inhibition (%) 24 hrs	---	1.66666667	1.33333333
Growth Inhibition (%) 48 hrs	1.66666667	---	0.33333333
Growth Inhibition (%) 72 hrs	1.33333333	0.33333333	---

5uM CBD

Treatment=5µM CBD, Treatment Model=Model 2Friedman ANOVA and Kendall Coeff. of Concordance (MCF7 MTT CBD Optimisation_TM)ANOVA Chi Sqr. (N = 3, df = 2) = ,6666667 p = ,71653Coeff. of Concordance = ,11111 Aver. rank r = -,3333

Variable	Average Rank	Sum of Ranks	Mean	Std.Dev.
Growth Inhibition (%) 24 hrs	1.666667	5.000000	43.29287	4.19352
Growth Inhibition (%) 48 hrs	2.000000	6.000000	44.78941	3.10856
Growth Inhibition (%) 72 hrs	2.333333	7.000000	51.91398	10.52000

Post-Hoc

Absolute Differences between Average RankApprox. significant if > 1,95467632136186at .05 significance level

	Growth Inhibition (%) 24 hrs	Growth Inhibition (%) 48 hrs	Growth Inhibition (%) 72 hrs
Growth Inhibition (%) 24 hrs	---	0.33333333	0.66666667
Growth Inhibition (%) 48 hrs	0.33333333	---	0.33333333
Growth Inhibition (%) 72 hrs	0.66666667	0.33333333	---

7.5uM CBD

Treatment=7.5µM CBD, Treatment Model=Model 2Friedman ANOVA and Kendall Coeff. of Concordance (MCF7 MTT CBD Optimisation_TM)ANOVA Chi Sqr. (N = 3, df = 2) = 4,666667 p = ,09697Coeff. of Concordance = ,77778 Aver. rank r = ,66667

Variable	Average Rank	Sum of Ranks	Mean	Std.Dev.
Growth Inhibition (%) 24 hrs	1.000000	3.000000	46.66826	2.349359
Growth Inhibition (%) 48 hrs	2.333333	7.000000	59.50753	5.929663
Growth Inhibition (%) 72 hrs	2.666667	8.000000	64.56384	7.316202

Post-Hoc

Absolute Differences between Average RankApprox. significant if > 1,95467632136186at .05 significance level

	Growth Inhibition (%) 24 hrs	Growth Inhibition (%) 48 hrs	Growth Inhibition (%) 72 hrs
Growth Inhibition (%) 24 hrs	---	1.33333333	1.66666667
Growth Inhibition (%) 48 hrs	1.33333333	---	0.33333333
Growth Inhibition (%) 72 hrs	1.66666667	0.33333333	---

10uM CBD

Treatment=10µM CBD, Treatment Model=Model 2Friedman ANOVA and Kendall Coeff. of Concordance (MCF7 MTT CBD Optimisation_TM)ANOVA Chi Sqr. (N = 3, df = 2) = 2,666667 p = ,26360Coeff. of Concordance = ,44444 Aver. rank r = ,16667

Variable	Average Rank	Sum of Ranks	Mean	Std.Dev.
Growth Inhibition (%) 24 hrs	1.333333	4.000000	57.94381	12.24699
Growth Inhibition (%) 48 hrs	2.000000	6.000000	64.85310	7.04278
Growth Inhibition (%) 72 hrs	2.666667	8.000000	69.83113	5.50982

Post-Hoc

Absolute Differences between Average RankApprox. significant if > 1,95467632136186at .05 significance level

	Growth Inhibition (%) 24 hrs	Growth Inhibition (%) 48 hrs	Growth Inhibition (%) 72 hrs
Growth Inhibition (%) 24 hrs	---	0.66666667	1.33333333
Growth Inhibition (%) 48 hrs	0.66666667	---	0.66666667
Growth Inhibition (%) 72 hrs	1.33333333	0.66666667	---

5uM CBD + 2uM Tam

Treatment=5µM CBD + 2µM TAM, Treatment Model=Model 2Friedman ANOVA and Kendall Coeff. of Concordance (MCF7 MTT CBD Optimisation_TM)ANOVA Chi Sqr. (N = 3, df = 2) = 6,000000 p = ,04979Coeff. of Concordance = 1,0000 Aver. rank r = 1,0000

Variable	Average Rank	Sum of Ranks	Mean	Std.Dev.
Growth Inhibition (%) 24 hrs	1.000000	3.000000	45.32903	2.137282
Growth Inhibition (%) 48 hrs	2.000000	6.000000	61.60971	8.777666
Growth Inhibition (%) 72 hrs	3.000000	9.000000	72.60712	4.348623

Post-Hoc

Absolute Differences between Average RankApprox. significant if > 1,95467632136186at .05 significance level

	Growth Inhibition (%) 24 hrs	Growth Inhibition (%) 48 hrs	Growth Inhibition (%) 72 hrs
Growth Inhibition (%) 24 hrs	---	1	2
Growth Inhibition (%) 48 hrs	1	---	1
Growth Inhibition (%) 72 hrs	2	1	---

7.5uM CBD+ 2uM Tam

Treatment=7.5µM CBD + 2µM TAM, Treatment Model=Model 2Friedman ANOVA and Kendall Coeff. of Concordance (MCF7 MTT CBD Optimisation_TM)ANOVA Chi Sqr. (N = 3, df = 2) = 6,000000 p = ,04979Coeff. of Concordance = 1,0000 Aver. rank r = 1,0000

Variable	Average Rank	Sum of Ranks	Mean	Std.Dev.
Growth Inhibition (%) 24 hrs	1.000000	3.000000	61.61709	5.098791
Growth Inhibition (%) 48 hrs	2.000000	6.000000	65.43903	6.106903
Growth Inhibition (%) 72 hrs	3.000000	9.000000	74.83860	8.423846

Post-Hoc

Absolute Differences between Average RankApprox. significant if > 1,95467632136186at .05 significance level

	Growth Inhibition (%) 24 hrs	Growth Inhibition (%) 48 hrs	Growth Inhibition (%) 72 hrs
Growth Inhibition (%) 24 hrs	---	1	2
Growth Inhibition (%) 48 hrs	1	---	1
Growth Inhibition (%) 72 hrs	2	1	---

10uM CBD + 2uM Tam

Treatment=10µM CBD + 2µM TAM, Treatment Model=Model 2Friedman ANOVA and Kendall Coeff. of Concordance (MCF7 MTT CBD Optimisation_TM)ANOVA Chi Sqr. (N = 3, df = 2) = 4,666667 p = ,09697Coeff. of Concordance = ,77778 Aver. rank r = ,66667

Variable	Average Rank	Sum of Ranks	Mean	Std.Dev.
Growth Inhibition (%) 24 hrs	1.333333	4.000000	65.02543	7.77302
Growth Inhibition (%) 48 hrs	1.666667	5.000000	65.82518	10.56461
Growth Inhibition (%) 72 hrs	3.000000	9.000000	81.29643	2.08287

Post-Hoc

Absolute Differences between Average RankApprox. significant if > 1,95467632136186at .05 significance level

	Growth Inhibition (%) 24 hrs	Growth Inhibition (%) 48 hrs	Growth Inhibition (%) 72 hrs
Growth Inhibition (%) 24 hrs	---	0.33333333	1.66666667
Growth Inhibition (%) 48 hrs	0.33333333	---	1.33333333
Growth Inhibition (%) 72 hrs	1.66666667	1.33333333	---

SFM

Treatment=LC, Treatment Model=Model 2Friedman ANOVA and Kendall Coeff. of Concordance (MCF7 MTT CBD Optimisation_TM)ANOVA Chi Sqr. (N = 3, df = 2) = 2,000000 p = ,36788Coeff. of Concordance = ,33333 Aver. rank r = -,1E-7

Variable	Average Rank	Sum of Ranks	Mean	Std.Dev.
Growth Inhibition (%) 24 hrs	1.666667	5.000000	27.06454	5.00308
Growth Inhibition (%) 48 hrs	1.666667	5.000000	21.32399	15.18927
Growth Inhibition (%) 72 hrs	2.666667	8.000000	37.49328	2.66508

Post-Hoc

Absolute Differences between Average RankApprox. significant if > 1,95467632136186at .05 significance level

	Growth Inhibition (%) 24 hrs	Growth Inhibition (%) 48 hrs	Growth Inhibition (%) 72 hrs
Growth Inhibition (%) 24 hrs	---	0	1
Growth Inhibition (%) 48 hrs	0	---	1
Growth Inhibition (%) 72 hrs	1	1	---

Triton-X (-0.1%)

Treatment=HC, Treatment Model=Model 2Friedman ANOVA and Kendall Coeff. of Concordance (MCF7 MTT CBD Optimisation_TM)ANOVA Chi Sqr. (N = 3, df = 2) = 6,000000 p = ,04979Coeff. of Concordance = 1,0000 Aver. rank r = 1,0000

Variable	Average Rank	Sum of Ranks	Mean	Std.Dev.
Growth Inhibition (%) 24 hrs	3.000000	9.000000	96.66333	1.018830
Growth Inhibition (%) 48 hrs	2.000000	6.000000	95.09253	2.299978
Growth Inhibition (%) 72 hrs	1.000000	3.000000	92.03294	1.049763

Post-Hoc

Absolute Differences between Average RankApprox. significant if > 1,95467632136186at .05 significance level

	Growth Inhibition (%) 24 hrs	Growth Inhibition (%) 48 hrs	Growth Inhibition (%) 72 hrs
Growth Inhibition (%) 24 hrs	---	1	2
Growth Inhibition (%) 48 hrs	1	---	1
Growth Inhibition (%) 72 hrs	2	1	---

MCF7 Mann-Whitney U Test

Diluent

Treatment=DiluentMann-Whitney U Test (w/ continuity correction) (MCF7 MTT CBD Optimisation_TM)By variable Treatment ModelMarked tests are significant at p <,05000

variable	Rank Sum Model 1	Rank Sum Model 2	U	Z	p-value	Z adjusted	p-value	Valid N Model 1	Valid N Model 2	2*1sided exact p
Growth Inhibition (%) 24 hrs	12.00000	9.00000	3.000000	0.43644	0.662521	0.43644	0.662521	3	3	0.700000
Growth Inhibition (%) 48 hrs	6.00000	15.00000	0.000000	-1.74574	0.080857	-1.77123	0.076523	3	3	0.100000
Growth Inhibition (%) 72 hrs	11.00000	10.00000	4.000000	0.00000	1.000000	0.00000	1.000000	3	3	1.000000

2uM Tam

Treatment=2µM TamMann-Whitney U Test (w/ continuity correction) (MCF7 MTT CBD Optimisation_TM)By variable Treatment ModelMarked tests are significant at p <,05000

variable	Rank Sum Model 1	Rank Sum Model 2	U	Z	p-value	Z adjusted	p-value	Valid N Model 1	Valid N Model 2	2*1sided exact p
Growth Inhibition (%) 24 hrs	10.00000	11.00000	4.000000	0.00000	1.000000	0.00000	1.000000	3	3	1.000000
Growth Inhibition (%) 48 hrs	7.00000	14.00000	1.000000	-1.30931	0.190431	-1.30931	0.190431	3	3	0.200000
Growth Inhibition (%) 72 hrs	6.00000	15.00000	0.000000	-1.74574	0.080857	-1.74574	0.080857	3	3	0.100000

5uM CBD

Treatment=5µM CBDMann-Whitney U Test (w/ continuity correction) (MCF7 MTT CBD Optimisation_TM)By variable Treatment ModelMarked tests are significant at p <,05000

variable	Rank Sum Model 1	Rank Sum Model 2	U	Z	p-value	Z adjusted	p-value	Valid N Model 1	Valid N Model 2	2*1sided exact p
Growth Inhibition (%) 24 hrs	12.00000	9.00000	3.000000	0.43644	0.662521	0.43644	0.662521	3	3	0.700000
Growth Inhibition (%) 48 hrs	7.00000	14.00000	1.000000	-1.30931	0.190431	-1.32842	0.184040	3	3	0.200000
Growth Inhibition (%) 72 hrs	6.00000	15.00000	0.000000	-1.74574	0.080857	-1.74574	0.080857	3	3	0.100000

7.5uM CBD

Treatment=7.5µM CBDMann-Whitney U Test (w/ continuity correction) (MCF7 MTT CBD Optimisation_TM)By variable Treatment ModelMarked tests are significant at p <,05000

variable	Rank Sum Model 1	Rank Sum Model 2	U	Z	p-value	Z adjusted	p-value	Valid N Model 1	Valid N Model 2	2*1sided exact p
Growth Inhibition (%) 24 hrs	15.00000	6.00000	0.00	1.74574	0.080857	1.74574	0.080857	3	3	0.100000
Growth Inhibition (%) 48 hrs	6.00000	15.00000	0.00	-1.74574	0.080857	-1.74574	0.080857	3	3	0.100000
Growth Inhibition (%) 72 hrs	6.00000	15.00000	0.00	-1.74574	0.080857	-1.74574	0.080857	3	3	0.100000

10uM CBD

Treatment=10µM CBDMann-Whitney U Test (w/ continuity correction) (MCF7 MTT CBD Optimisation_TM)By variable Treatment ModelMarked tests are significant at p <,05000

variable	Rank Sum Model 1	Rank Sum Model 2	U	Z	p-value	Z adjusted	p-value	Valid N Model 1	Valid N Model 2	2*1sided exact p
Growth Inhibition (%) 24 hrs	11.00000	10.00000	4.000000	0.00000	1.000000	0.00000	1.000000	3	3	1.000000
Growth Inhibition (%) 48 hrs	6.00000	15.00000	0.000000	-1.74574	0.080857	-1.74574	0.080857	3	3	0.100000
Growth Inhibition (%) 72 hrs	6.00000	15.00000	0.000000	-1.74574	0.080857	-1.74574	0.080857	3	3	0.100000

5uM CBD + 2uM Tam

Treatment=5µM CBD + 2µM TAMMann-Whitney U Test (w/ continuity correction) (MCF7 MTT CBD Optimisation_TM)By variable Treatment ModelMarked tests are significant at p <,05000

variable	Rank Sum Model 1	Rank Sum Model 2	U	Z	p-value	Z adjusted	p-value	Valid N Model 1	Valid N Model 2	2*1sided exact p
Growth Inhibition (%) 24 hrs	15.00000	6.00000	0.000000	1.74574	0.080857	1.74574	0.080857	3	3	0.100000
Growth Inhibition (%) 48 hrs	7.00000	14.00000	1.000000	-1.30931	0.190431	-1.32842	0.184040	3	3	0.200000
Growth Inhibition (%) 72 hrs	6.00000	15.00000	0.000000	-1.74574	0.080857	-1.74574	0.080857	3	3	0.100000

7.5uM CBD + 2uM Tam

Treatment=7,5µM CBD + 2µM TAMMann-Whitney U Test (w/ continuity correction) (MCF7 MTT CBD Optimisation_TM)By variable Treatment ModelMarked tests are significant at p <,05000

variable	Rank Sum Model 1	Rank Sum Model 2	U	Z	p-value	Z adjusted	p-value	Valid N Model 1	Valid N Model 2	2*1sided exact p
Growth Inhibition (%) 24 hrs	9.000000	12.00000	3.000000	-0.43644	0.662521	-0.43644	0.662521	3	3	0.700000
Growth Inhibition (%) 48 hrs	6.000000	15.00000	0.000000	-1.74574	0.080857	-1.74574	0.080857	3	3	0.100000
Growth Inhibition (%) 72 hrs	6.000000	15.00000	0.000000	-1.74574	0.080857	-1.74574	0.080857	3	3	0.100000

10uM CBD + 2uM Tam

Treatment=10µM CBD + 2µM TAMMann-Whitney U Test (w/ continuity correction) (MCF7 MTT CBD Optimisation_TM)By variable Treatment ModelMarked tests are significant at p <,05000

variable	Rank Sum Model 1	Rank Sum Model 2	U	Z	p-value	Z adjusted	p-value	Valid N Model 1	Valid N Model 2	2*1sided exact p
Growth Inhibition (%) 24 hrs	13.00000	8.00000	2.000000	0.87287	0.382734	0.87287	0.382734	3	3	0.400000
Growth Inhibition (%) 48 hrs	8.00000	13.00000	2.000000	-0.87287	0.382734	-0.87287	0.382734	3	3	0.400000
Growth Inhibition (%) 72 hrs	6.00000	15.00000	0.000000	-1.74574	0.080857	-1.74574	0.080857	3	3	0.100000

SFM

Treatment=LCMann-Whitney U Test (w/ continuity correction) (MCF7 MTT CBD Optimisation_TM)By variable Treatment ModelMarked tests are significant at p <,05000

variable	Rank Sum Model 1	Rank Sum Model 2	U	Z	p-value	Z adjusted	p-value	Valid N Model 1	Valid N Model 2	2*1sided exact p
Growth Inhibition (%) 24 hrs	12.00000	9.00000	3.000000	0.436436	0.662521	0.436436	0.662521	3	3	0.700000
Growth Inhibition (%) 48 hrs	13.00000	8.00000	2.000000	0.872872	0.382734	0.872872	0.382734	3	3	0.400000
Growth Inhibition (%) 72 hrs	10.00000	11.00000	4.000000	0.000000	1.000000	0.000000	1.000000	3	3	1.000000

Triton-X (0.1%)

Treatment=HCMann-Whitney U Test (w/ continuity correction) (MCF7 MTT CBD Optimisation_TM)By variable Treatment ModelMarked tests are significant at p <,05000

variable	Rank Sum Model 1	Rank Sum Model 2	U	Z	p-value	Z adjusted	p-value	Valid N Model 1	Valid N Model 2	2*1sided exact p
Growth Inhibition (%) 24 hrs	9.000000	12.00000	3.000000	-0.43644	0.662521	-0.43644	0.662521	3	3	0.700000
Growth Inhibition (%) 48 hrs	8.000000	13.00000	2.000000	-0.87287	0.382734	-0.87287	0.382734	3	3	0.400000
Growth Inhibition (%) 72 hrs	7.000000	14.00000	1.000000	-1.30931	0.190431	-1.30931	0.190431	3	3	0.200000

RAW264.7: Neutral Red assay

Kruskal-Wallis Anova by Ranks and Post-hoc tests

Depend.: Cell Viability (%) 72 hrs	Kruskal-Wallis ANOVA by Ranks; Cell Viability (%) 72 hrs (RAW264.7 NR_TM)Independent (grouping) variable: TreatmentKruskal-Wallis test: H (3, N= 12) =2,589744 p =,4593															
	Code	Valid N	Sum of Ranks	Mean Rank												
DILUENT	1	3	28.00000	9.333333												
2µM TAM	2	3	17.00000	5.666667												
5µM CBD	3	3	15.00000	5.000000												
5µM CBD + 2µM TAM	4	3	18.00000	6.000000												
Post-Hoc																
	Absolute Differences between Mean Rank Approx. significant if highlighted at .05 significance level															
	DILUENT	2µM TAM	5µM CBD	5µM CBD + 2µM TAM												
DILUENT	---	3.66666667	4.33333333	3.33333333												
2µM TAM	3.66666667	---	0.66666667	0.33333333												
5µM CBD	4.33333333	0.66666667	---	1												
5µM CBD + 2µM TAM	3.33333333	0.33333333	1	---												

RAW264.7: MTT assay

Kruskal-Wallis Anova by Ranks and Post-hoc tests

	Kruskal-Wallis ANOVA by Ranks; Growth Inhibition (%) 72 hrs (RAW264.7 MTT_TM)Independent (grouping) variable: TreatmentKruskal-Wallis test: H (5, N= 18) =12,32164 p =,0306															
Depend.: Growth Inhibition (%) 72 hrs	Code	Valid N	Sum of Ranks	Mean Rank												
DILUENT	1	3	14.00000	4.66667												
2µM TAM	2	3	21.00000	7.00000												
5µM CBD	3	3	22.00000	7.33333												
5µM CBD + 2µM TAM	4	3	21.00000	7.00000												
SFM	5	3	42.00000	14.00000												
Triton-X (0.1%)	6	3	51.00000	17.00000												
Post-Hoc																
	Absolute Differences between Mean Rank Approx. significant if highlighted at .05 significance level															
	DILUENT	2µM TAM	5µM CBD	5µM CBD + 2µM TAM	LC	HC										
DILUENT	---	2.33333333	2.66666667	2.33333333	9.33333333	12.3333333										
2µM TAM	2.33333333	---	0.33333333	0	7	10										
5µM CBD	2.66666667	0.33333333	---	0.33333333	6.66666667	9.66666667										
5µM CBD + 2µM TAM	2.33333333	0	0.33333333	---	7	10										
SFM	9.33333333	7	6.66666667	7	---	3										
Triton-X (0.1%)	12.3333333	10	9.66666667	10	3	---										

Appendix D: Proteome Profiling

D1: Cross Run Global Normalisation

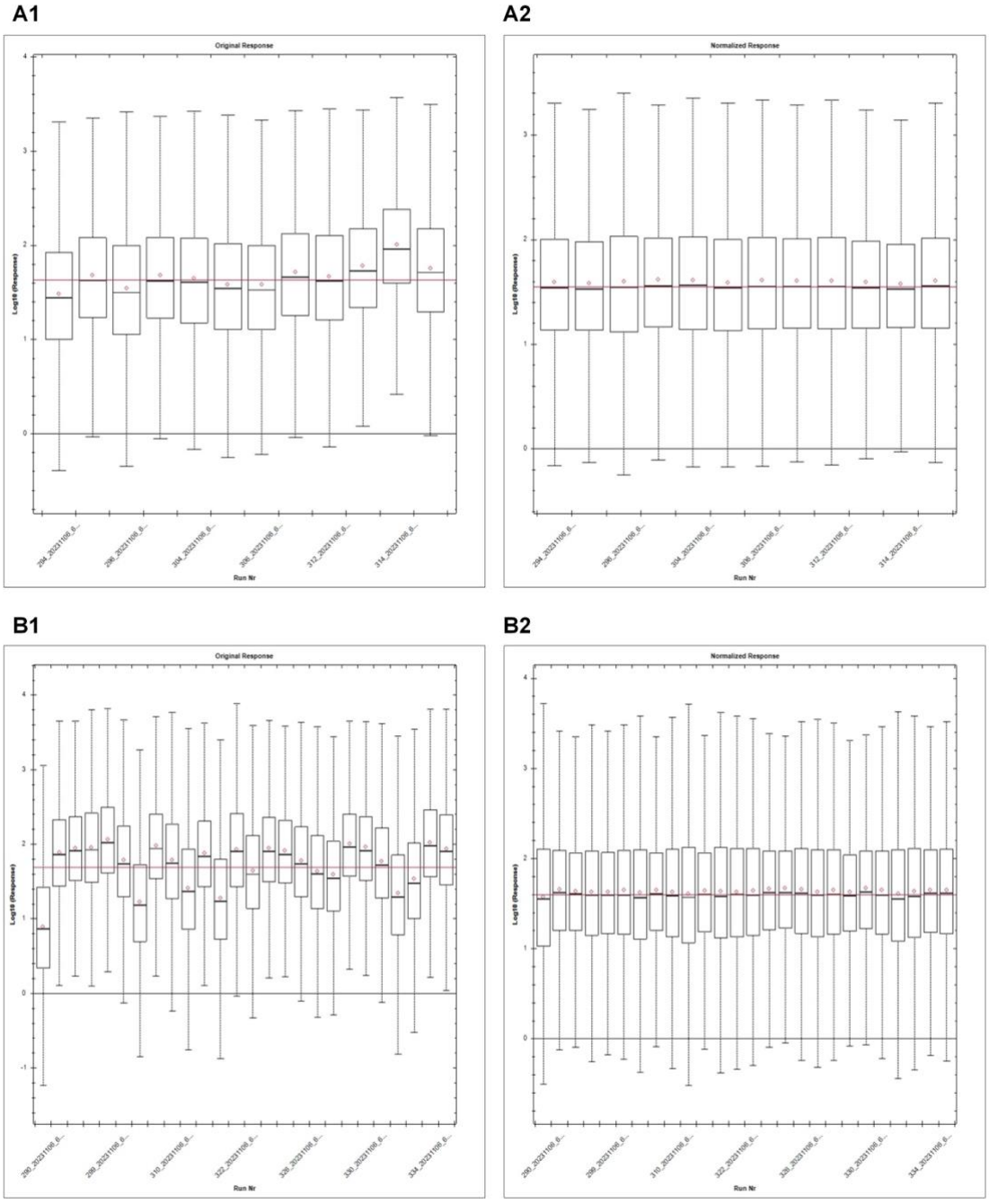


Figure D1: Cross Run Global Normalisation. Individual runs were normalised using the median quantities of all peptides selected for normalisation. This was performed to reduce noise in the data, to ensure that variations in protein signal intensities were due to biological differences rather than technical artifacts. **(A)** Normalisation of peptides from RAW264.7 cells treated with CBD and/or Tamoxifen, **(A1)** original response and **(A2)** normalised response. **(B)** Normalisation of peptides from RAW264.7 macrophages stimulated to M1 and M2 phenotypes, **(B1)** original response and **(B2)** normalised response.

D2: Quality and Technical Control Evaluation

To ensure data accuracy, reliability and reproducibility, samples from polarised macrophages (M0, M1 and M2) and those treated with optimised CBD and Tamoxifen were pooled separately (P1 and P2, respectively) and used as technical and quality controls. These control samples were utilised to monitor instrument performance, identify potential technical issues and assess the overall quality of the data.

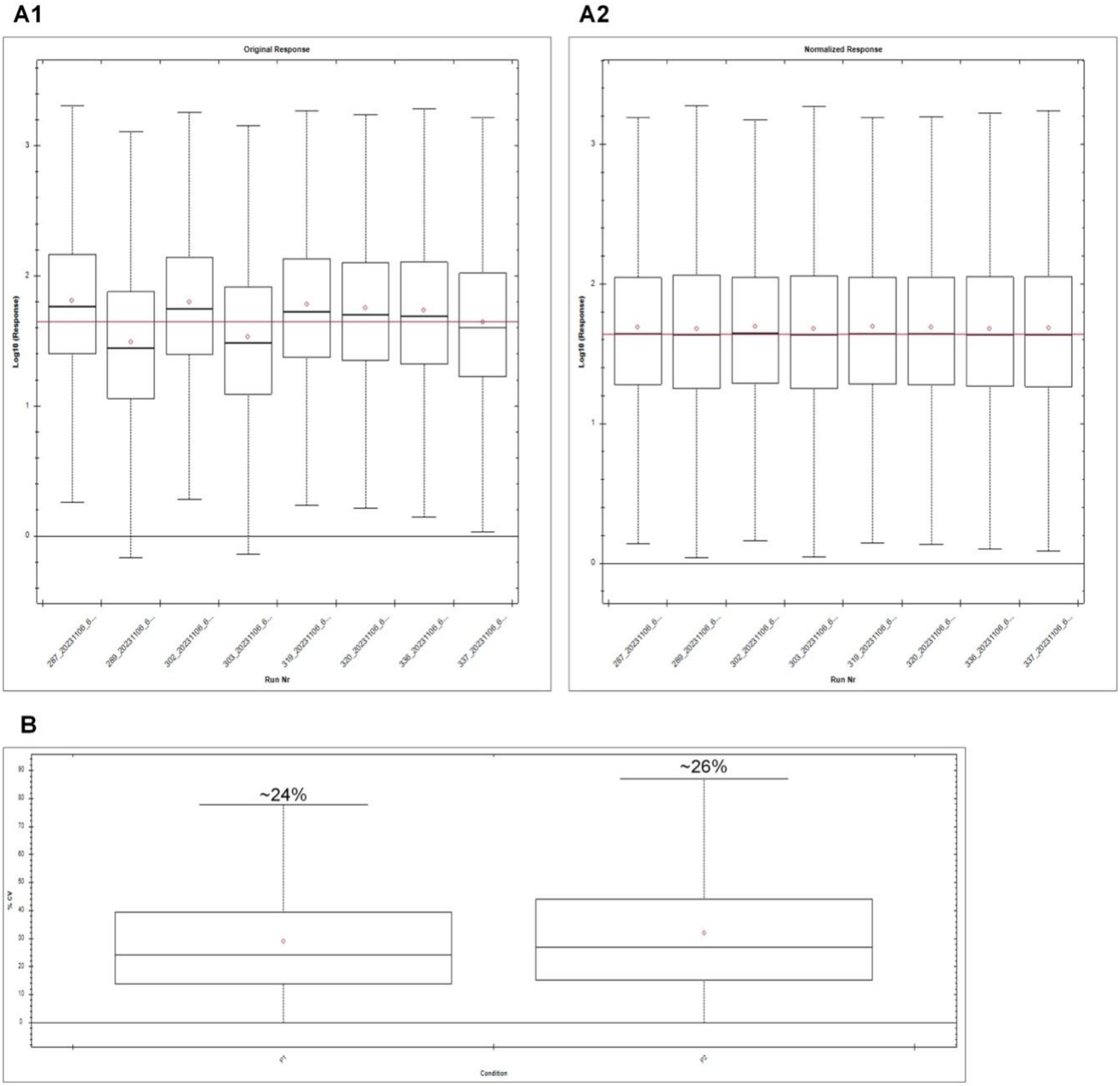


Figure D2: Quality and technical control evaluation. (A) shows original and normalized responses in pooled samples. **(B)** Box and whisker plot showing coefficient of variation percentages (CV%) of pooled samples; X-axis – condition (P1/P2), y-axis CV%. P1 - RAW264.7 macrophages polarised to M1 and M2 phenotypes; P2 - cells treated with CBD and/or Tamoxifen. The observed CV% values are close to 20%, indicating a relatively low level of variability within the data.

Appendix E: Assessment of the Phagocytic Capacity of RAW264.7 Macrophages in Response to Optimised Tamoxifen and CBD Treatment

E1: Optimisation of CellTracker Green Dye Concentration and Co-culture Ratio

Optimisation of Celltracker green CMFDA dye concentration

CellTracker Green, a nontoxic fluorescent probe, is widely used to track cell movement, location, proliferation and migration in living cells (Piccinini *et al.,* 2015; Nam *et al*., 2019; Thermofisher Scientific, C2925). This dye readily crosses cell membranes and remains retained within the cells, even during cell division and the fluorescence persists for at least 72 hours (Piccinini *et al.,* 2015; Nam *et al*., 2019; Thermofisher Scientific, C2925). To determine the optimal concentration and incubation time of the dye, MCF7 breast cancer cells were seeded in 24-well plates at a density of 1 x 10^5 cells/well and labelled with various concentrations of CellTracker green (1 µM, 2.5 µM and 5 µM) for different durations (30 – 60 minutes). The cells were incubated in complete media. Thereafter, the breast cancer cells were washed with PBS, pH 7.4, and visualised using an Olympus IX51 microscope with CellSense V11 software, at a wavelength of 488 nm. Microscopic evaluation revealed sufficient staining and fluorescence across all concentrations and timepoints. However, cells labelled with 1 µM exhibited background staining, while those labelled with 2.5 µM and 5 µM displayed minimal background fluorescence. To minimise potential artifacts and maintain normal cellular physiology, we opted for the sub-optimal concentration of 2.5 µM and a 60 minute incubation period, ensuring adequate staining while avoiding excessive dye loading (**Figure E1**).

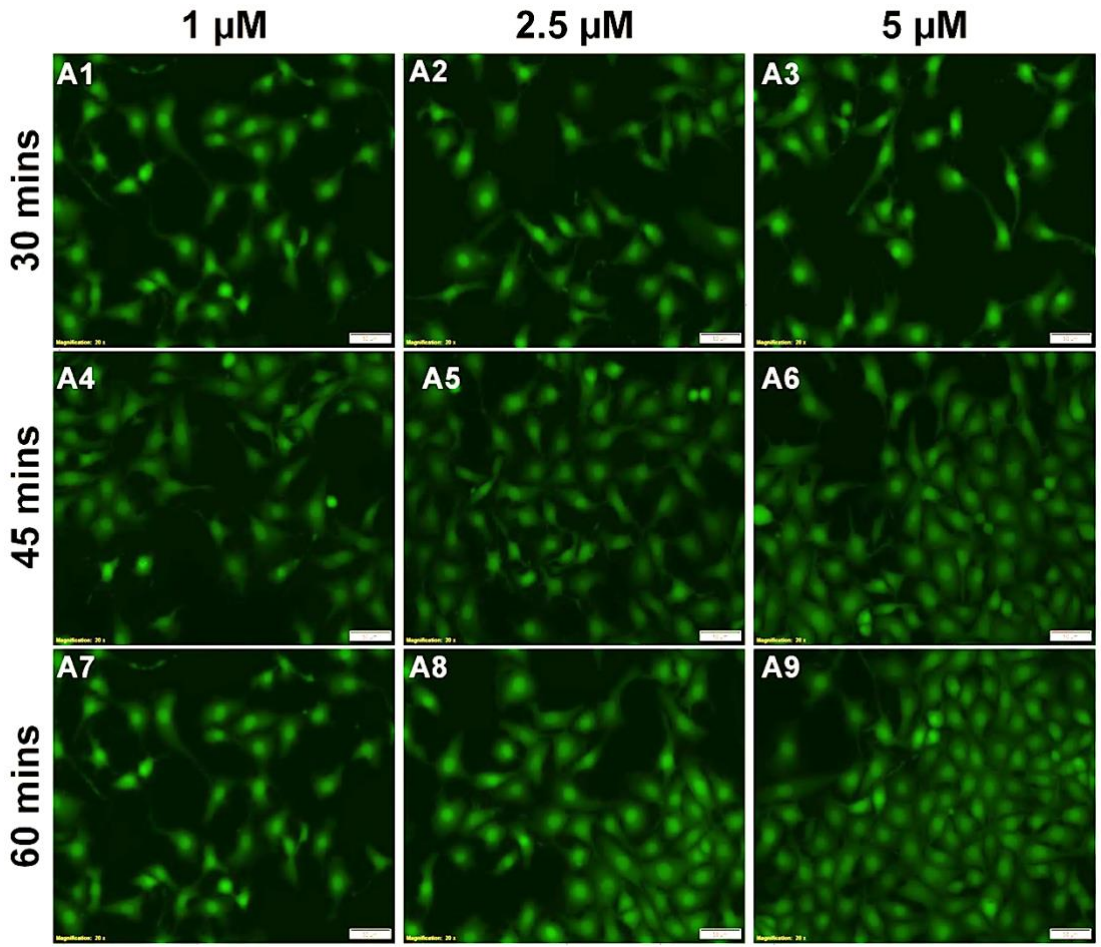


Figure E1: Fluorescence microscopic images illustrating staining of MCF7 breast cancer cells with the CellTracker green CMFDA dye. MCF7 cells were stained with CellTracker green at different concentrations (1 µM, 2.5 µM and 5 µM) for different durations (30, 45 and 60 minutes). **A1-3)** shows cells stained for 30 minutes at the various concentrations; **A4-6)** shows cells stained for 45 minutess at the various concentrations **A7-9)** shows cells stained for 60 minutes at the various concentrations. All the cells showed positive staining for the CellTracker green dye across all concentrations and time points. Images captured at 20X magnification (scale bar – 50 µm), at a wavelength of 488 nm.

Optimisation of MCF7 and RAW264.7 Co-culture Ratio

The use of co-culture systems have proven invaluable in studying the interactions between tumour cells and the microenvironment (Kaemmerer *et al*., 2016). While there is limited information on 2-dimensional co-culture systems involving MCF7 cells and RAW264.7 macrophages, the optimal cell ratio is highly dependent on the specific assay being conducted (Wang *et al*., 2013; Jaiswal *et al*., 2017; Joshi *et al*., 2018; Candas-Green *et al*., 2020; Sun *et al*., 2022a). To optimise the RAW264.7:MCF7 co-culture ratio for our experiments, we tested various ratios (1:1 and 1:2) and monitored the co-cultures for 72 hours. The MCF7 cells were incubated with CellTracker green at a concentration of 2.5 µM for 60 minutes in 24-well plates and were subsequently co-cultured with M0 RAW264.7 cells according to ratios shown in **Table E**. The co-cultures were incubated in complete media and monitored every 24 hours for a duration of 72 hours, using an Olympus IX51 microscope with CellSense V11 software, at a wavelength of 488 nm. A 1:1 ratio was found to be optimal, as the higher ratio of 1:2 led to over-confluency of MCF7 cells, hindering the observation of cell-cell interactions and compromising cell viability by 72 hours. Given our optimised treatment duration for Tamoxifen and/or CBD (72 hours), the 1:1 co-culture ratio was chosen for subsequent experiments to facilitate the study of interactions between MCF7 breast cancer cells and RAW264.7 macrophages (**Figure E2**).

Table E: Cell ratios for MCF7 and RAW264.7 co-cultures

Co-culture ratio	RAW264.7 cells/well	MCF7 cells/well
1:1	5×10^4	5×10^4
1:2	1×10^5	2×10^5

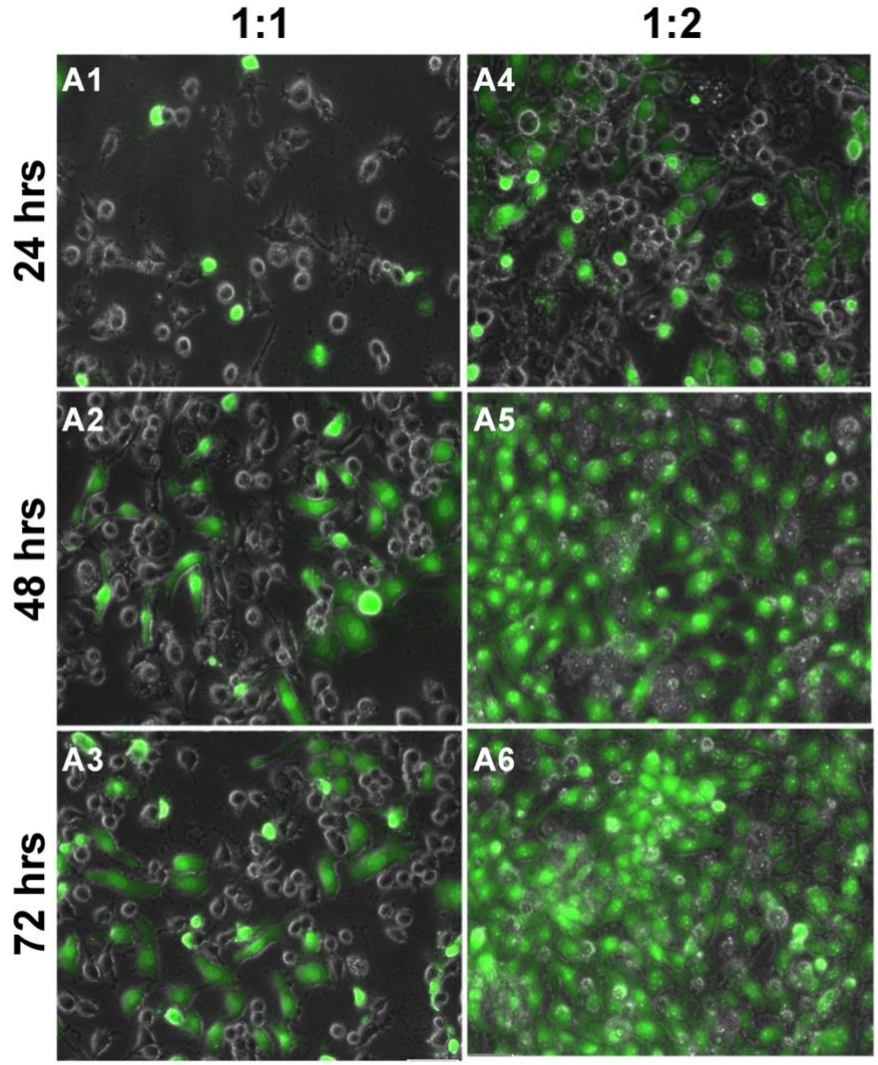


Figure E2: Fluorescence microscopic images showing RAW264.7:MCF7 co-culture ratios at different time intervals. MCF7 cells were labelled with CellTracker green and incubated at different ratios (RAW264.7:MCF7; 1:1 and 1:2) with RAW264.7 macrophages over 72 hours. **A1-3)** shows a 1:1 co-culture ratio of RAW264.7:MCF7 cells observed over 72 hrs. **A4-6)** shows a 1:2 co-culture ratio of RAW264.7:MCF7 cells observed over 72 hours. A 1:2 ratio led to over-confluency of MCF7 cells by 48 hours. Images captured at 20X magnification (scale bar – 50 µm), at a wavelength of 488 nm.

Preparation of CellTracker green dye

Preparation of 10 mM CellTracker Green stock solution

Stock solution: 1 mg (MW= 464.9g/mol)

1. Need 10 mM stock solution (C1= 10000µM)
   Dissolve in DMSO
2. C=m/MWV
   V=m/CMW
   V= (0.001 g)/(0.01 M)(464.9 g/mol)
   V= 0.000215 L (0.215 mL)
   V=215.1ul DMSO

To make 10 mM stock of Cell Tracker, add 215.1 ulL 00% DMSO to 0.001g (1 mg) Cell Tracker powder.

Preparation of CellTracker Green working solutions in serum free media

Working solution: 1.0 µM, 2.5 µM, 5 µM

- Final volume = 300 µL/well X 6-wells/concentration = 1800 µl (~2000 µL)

- **1.0 µM**
  C1V1 = C2V2
  (10000 µM)V1 = (1,0 µM)(2000 µL)
  V1 = 0,2 µL

Working solution = 0,2 µl stock 1 + 1999,8 µL serum free DMEM

- **2.5 µM**
  C1V1 = C2V2
  (10000 µM)V1 = (2,5 µM)(2000 µL)
  V1 = 0,5 µL

Working solution = 0,5 µL stock 1 + 1999,5 µL serum free DMEM

- **5 µM**
  C1V1 = C2V2
  (10000 µM)V1 = (5 µM)(2000 µL)
  V1 = 1 µL

Working solution = 1 µL stock 1 + 1999 µL serum free DMEM

E2: Statistical Analysis – Statistica Output

Phagocytic assay – Nitrite production analysis

Kruskal-Wallis Anova by Ranks and Post-hoc tests

M0

Macrophage phenotype=M0Kruskal-Wallis ANOVA by Ranks; Nitrite concentration (µM) 72 hrs (Phagocytic assay_TM)Independent (grouping) variable: TreatmentKruskal-Wallis test: H (4, N= 15) =11,53333 p =,0212

Depend.: Nitrite concentration (µM) 72 hrs	Code	Valid N	Sum of Ranks	Mean Rank
Media control	1	3	8.00000	2.66667
Diluent control	2	3	13.00000	4.33333
2µM TAM	3	3	27.00000	9.00000
5µM CBD	4	3	33.00000	11.00000
2µM TAM + 5µM CBD	5	3	39.00000	13.00000

Post-hoc

Absolute Differences between Mean Rank Approx. significant if highlighted at .05 significance level

	Media control	Diluent control	2µM TAM	5µM CBD	2µM TAM + 5µM CBD
Media control	---	1.66666667	6.33333333	8.33333333	10.3333333
Diluent control	1.66666667	---	4.66666667	6.66666667	8.66666667
2µM TAM	6.33333333	4.66666667	---	2	4
5µM CBD	8.33333333	6.66666667	2	---	2
2µM TAM + 5µM CBD	10.3333333	8.66666667	4	2	---

M1

Macrophage phenotype=M1Kruskal-Wallis ANOVA by Ranks; Nitrite concentration (µM) 72 hrs (Phagocytic assay_TM)Independent (grouping) variable: TreatmentKruskal-Wallis test: H (4, N= 15) =7,900000 p =,0953

Depend.: Nitrite concentration (µM) 72 hrs	Code	Valid N	Sum of Ranks	Mean Rank
Media control	1	3	20.00000	6.66667
Diluent control	2	3	17.00000	5.66667
2µM TAM	3	3	15.00000	5.00000
5µM CBD	4	3	26.00000	8.66667
2µM TAM + 5µM CBD	5	3	42.00000	14.00000

Post-hoc

Absolute Differences between Mean Rank Approx. significant if highlighted at .05 significance level

	Media control	Diluent control	2µM TAM	5µM CBD	2µM TAM + 5µM CBD
Media control	---	1	1.66666667	2	7.33333333
Diluent control	1	---	0.66666667	3	8.33333333
2µM TAM	1.66666667	0.66666667	---	3.66666667	9
5µM CBD	2	3	3.66666667	---	5.33333333
2µM TAM + 5µM CBD	7.33333333	8.33333333	9	5.33333333	---

Mann-Whitney U Test

Media control

Treatment=Media controlMann-Whitney U Test (w/ continuity correction) (Phagocytic assay_TM)By variable Macrophage phenotypeMarked tests are significant at p <,05000

variable	Rank Sum M0	Rank Sum M1	U	Z	p-value	Z adjusted	p-value	Valid N M0	Valid N M1	2*1sided exact p
Nitrite concentration (µM) 72 hrs	6.000000	15.00000	0.00	-1.74574	0.080857	-1.74574	0.080857	3	3	0.100000

Diluent control

Treatment=Diluent controlMann-Whitney U Test (w/ continuity correction) (Phagocytic assay_TM)By variable Macrophage phenotypeMarked tests are significant at p <,05000

variable	Rank Sum M0	Rank Sum M1	U	Z	p-value	Z adjusted	p-value	Valid N M0	Valid N M1	2*1sided exact p
Nitrite concentration (µM) 72 hrs	6.000000	15.00000	0.00	-1.74574	0.080857	-1.74574	0.080857	3	3	0.100000

2uM Tamoxifen

Treatment=2µM TAMMann-Whitney U Test (w/ continuity correction) (Phagocytic assay_TM)By variable Macrophage phenotypeMarked tests are significant at p <,05000

variable	Rank Sum M0	Rank Sum M1	U	Z	p-value	Z adjusted	p-value	Valid N M0	Valid N M1	2*1sided exact p
Nitrite concentration (µM) 72 hrs	6.000000	15.00000	0.00	-1.74574	0.080857	-1.74574	0.080857	3	3	0.100000

5uM CBD

Treatment=5µM CBDMann-Whitney U Test (w/ continuity correction) (Phagocytic assay_TM)By variable Macrophage phenotypeMarked tests are significant at p <,05000

variable	Rank Sum M0	Rank Sum M1	U	Z	p-value	Z adjusted	p-value	Valid N M0	Valid N M1	2*1sided exact p
Nitrite concentration (µM) 72 hrs	6.000000	15.00000	0.00	-1.74574	0.080857	-1.74574	0.080857	3	3	0.100000

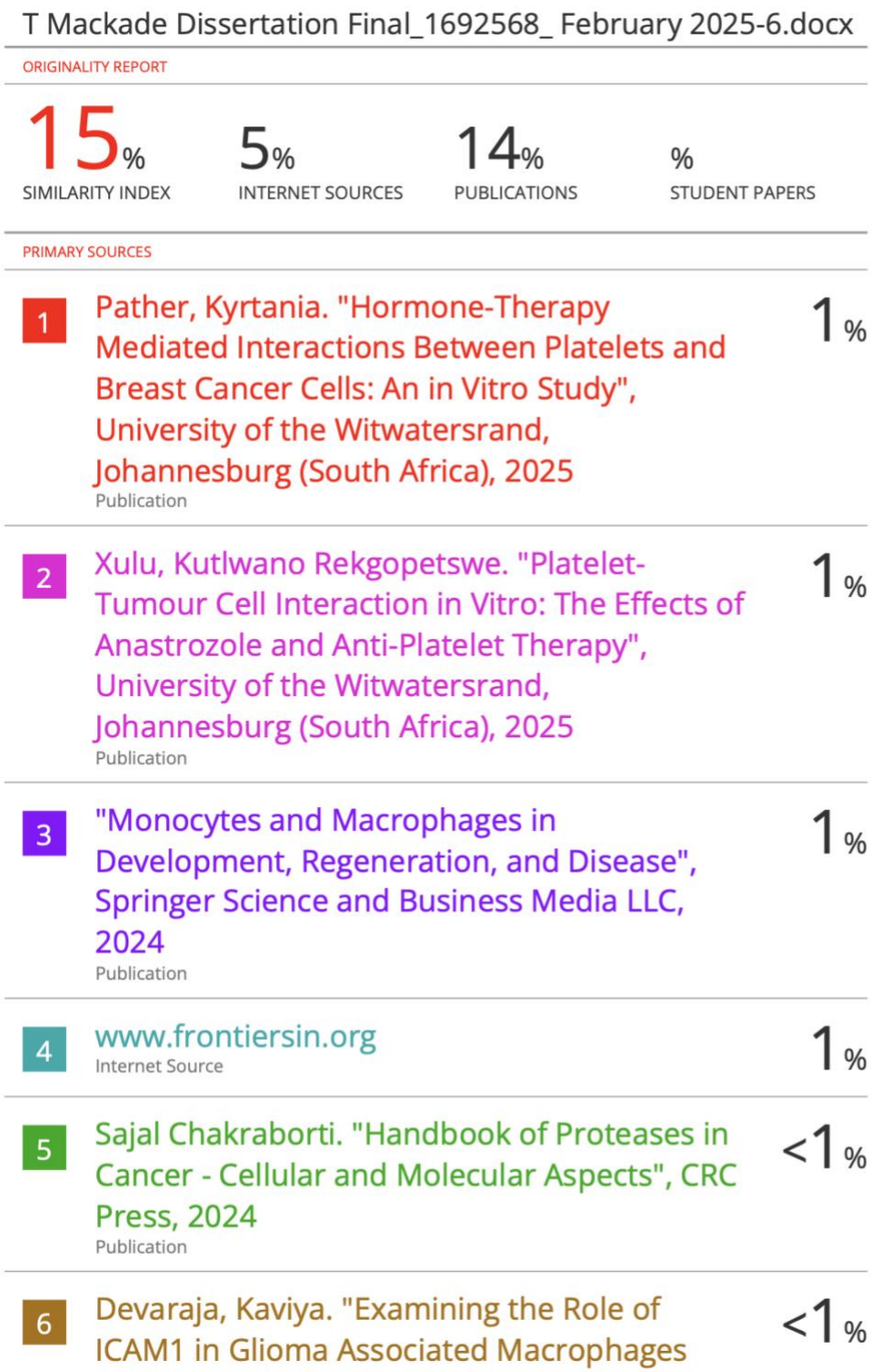
2uM Tamoxifen + 5uM CBD

Treatment=2µM TAM + 5µM CBDMann-Whitney U Test (w/ continuity correction) (Phagocytic assay_TM)By variable Macrophage phenotypeMarked tests are significant at p <,05000

variable	Rank Sum M0	Rank Sum M1	U	Z	p-value	Z adjusted	p-value	Valid N M0	Valid N M1	2*1sided exact p
Nitrite concentration (µM) 72 hrs	6.000000	15.00000	0.00	-1.74574	0.080857	-1.74574	0.080857	3	3	0.100000

Appendix F: Additional Supplementary Information

F1: Turn-it in Report



T Mackade Dissertation Final_1692568_ February 2025-6.docx

ORIGINALITY REPORT

15%	5%	14%	%
SIMILARITY INDEX	INTERNET SOURCES	PUBLICATIONS	STUDENT PAPERS

PRIMARY SOURCES

1	Pather, Kyrtania. "Hormone-Therapy Mediated Interactions Between Platelets and Breast Cancer Cells: An in Vitro Study", University of the Witwatersrand, Johannesburg (South Africa), 2025 Publication	1%
2	Xulu, Kutlwano Rekgopetswe. "Platelet-Tumour Cell Interaction in Vitro: The Effects of Anastrozole and Anti-Platelet Therapy", University of the Witwatersrand, Johannesburg (South Africa), 2025 Publication	1%
3	"Monocytes and Macrophages in Development, Regeneration, and Disease", Springer Science and Business Media LLC, 2024 Publication	1%
4	www.frontiersin.org Internet Source	1%
5	Sajal Chakraborti. "Handbook of Proteases in Cancer - Cellular and Molecular Aspects", CRC Press, 2024 Publication	<1%
6	Devaraja, Kaviya. "Examining the Role of ICAM1 in Glioma Associated Macrophages	<1%

F2: Protein list of differentially expressed proteins in M1 and M2 polarised RAW264.7 macrophages compared to M0 ('-' indicates downregulated and no sign indicates upregulated)

Comparison (group1/group2)	Protein names	Protein descriptions	AVG Log2 Ratio	q-value
M1 48 / M0 48	SYN1	Synapsin-1	6,89098	0,00192
M1 48 / M0 48	PAI2	Plasminogen activator inhibitor 2, macrophage	5,44409	0,00208
M1 48 / M0 48	RBNS5	Rabenosyn-5	4,60853	0,00114
M1 48 / M0 48	ARGI2	Arginase-2, mitochondrial	4,38196	0,00179
M1 48 / M0 48	KCD12	BTB/POZ domain-containing protein KCTD12	3,99461	0,00028
M1 48 / M0 48	BASP1	Brain acid soluble protein 1	3,91755	0,00100
M1 48 / M0 48	IL1RA	Interleukin-1 receptor antagonist protein	3,52666	0,00537
M1 48 / M0 48	PGH2	Prostaglandin G/H synthase 2	3,48130	0,00250
M1 48 / M0 48	CEBPB	CCAAT/enhancer-binding protein beta	3,24039	0,00430
M1 48 / M0 48	IRG1	Cis-aconitate decarboxylase	3,23326	0,00064
M1 48 / M0 48	RANT	GTP-binding nuclear protein Ran, testis-specific isoform	3,16081	0,00875
M1 48 / M0 48	GLPK	Glycerol kinase	3,15481	0,00337
M1 48 / M0 48	UPP1	Uridine phosphorylase 1	3,12512	0,00267
M1 48 / M0 48	SN	Sialoadhesin	2,91100	0,00162
M1 48 / M0 48	RPGF5	Rap guanine nucleotide exchange factor 5	2,83053	0,00384
M1 48 / M0 48	GPNMB	Transmembrane glycoprotein NMB	2,78647	0,00218
M1 48 / M0 48	PAI1	Plasminogen activator inhibitor 1	2,78010	0,00068
M1 48 / M0 48	SQOR	Sulfide:quinone oxidoreductase, mitochondrial	2,73658	0,00433
M1 48 / M0 48	S28A2	Sodium/nucleoside cotransporter 2	2,72307	0,00260
M1 48 / M0 48	CDD	Cytidine deaminase	2,71665	0,00158
M1 48 / M0 48	ATF6B	Cyclic AMP-dependent transcription factor ATF-6 beta	2,65882	0,00622
M1 48 / M0 48	PRDX5	Peroxiredoxin-5, mitochondrial	2,49659	0,00126
M1 48 / M0 48	S15A3	Solute carrier family 15 member 3	2,46223	0,00373
M1 48 / M0 48	GAPR1	Golgi-associated plant pathogenesis-related protein 1	2,42503	0,00155

M1 48 / M0 48	IFI5B	Interferon-activable protein 205-B	2,38422	0,00290
M1 48 / M0 48	LTMD1	LETM1 domain-containing protein 1	2,37118	0,00086
M1 48 / M0 48	IF2B2	Insulin-like growth factor 2 mRNA-binding protein 2	2,35941	0,00557
M1 48 / M0 48	LANC3	LanC-like protein 3	2,34736	0,00287
M1 48 / M0 48	DHRS1	Dehydrogenase/reductase SDR family member 1	2,34330	0,00439
M1 48 / M0 48	IF2B3	Insulin-like growth factor 2 mRNA-binding protein 3	2,30675	0,00407
M1 48 / M0 48	MISSL	MAPK-interacting and spindle-stabilizing protein-like	2,29616	0,00846
M1 48 / M0 48	ANXA8	Annexin A8	2,24435	0,00371
M1 48 / M0 48	FCGR3	Low affinity immunoglobulin gamma Fc region receptor III	2,18157	0,00531
M1 48 / M0 48	MSTN1	Musculoskeletal embryonic nuclear protein 1	2,16684	0,00292
M1 48 / M0 48	PITM1	Membrane-associated phosphatidylinositol transfer protein 1	2,15992	0,00074
M1 48 / M0 48	P2RX4	P2X purinoceptor 4	2,14957	0,00874
M1 48 / M0 48	AMPN	Aminopeptidase N	2,14065	0,00224
M1 48 / M0 48	ASSY	Argininosuccinate synthase	2,12411	0,00191
M1 48 / M0 48	CATC	Dipeptidyl peptidase 1	2,12353	0,00101
M1 48 / M0 48	ALBU	Albumin	2,08081	0,00167
M1 48 / M0 48	SC61G	Protein transport protein Sec61 subunit gamma	2,07628	0,00097
M1 48 / M0 48	CCL9	C-C motif chemokine 9	2,06302	0,00515
M1 48 / M0 48	TNR6	Tumor necrosis factor receptor superfamily member 6	2,05989	0,00225
M1 48 / M0 48	HMGA2	High mobility group protein HMGI-C	2,05409	0,00335
M1 48 / M0 48	OASL1	2'-5'-oligoadenylate synthase-like protein 1	2,04347	0,00217
M1 48 / M0 48	MRP	MARCKS-related protein	2,03906	0,00026
M1 48 / M0 48	XYLT2	Xylosyltransferase 2	2,03072	0,00167
M1 48 / M0 48	RN149	E3 ubiquitin-protein ligase RNF149	2,02346	0,00369
M1 48 / M0 48	GBG2	Guanine nucleotide-binding protein G(I)/G(S)/G(O) subunit gamma-2	2,02324	0,00191
M1 48 / M0 48	VMA21	Vacuolar ATPase assembly integral	1,99046	0,00821

		membrane protein Vma21		
M1 48 / M0 48	PA1B3	Platelet-activating factor acetylhydrolase IB subunit alpha1	1,97446	0,00245
M1 48 / M0 48	XCT	Cystine/glutamate transporter	1,96827	0,00205
M1 48 / M0 48	F162A	Protein FAM162A	1,96261	0,00315
M1 48 / M0 48	ATX1	Ataxin-1	1,96234	0,00095
M1 48 / M0 48	SODM	Superoxide dismutase [Mn], mitochondrial	1,95892	0,00462
M1 48 / M0 48	ARF4	ADP-ribosylation factor 4	1,95422	0,00409
M1 48 / M0 48	STOM	Stomatin	1,95305	0,00119
M1 48 / M0 48	GDPD1	Lysophospholipase D GDPD1	1,95292	0,00243
M1 48 / M0 48	S38A7	Sodium-coupled neutral amino acid transporter 7	1,94540	0,00298
M1 48 / M0 48	SRC	Proto-oncogene tyrosine-protein kinase Src	1,92230	0,00298
M1 48 / M0 48	PBIP1	Pre-B-cell leukemia transcription factor-interacting protein 1	1,90155	0,00447
M1 48 / M0 48	SCRB1	Scavenger receptor class B member 1	1,90015	0,00638
M1 48 / M0 48	GBG12	Guanine nucleotide-binding protein G(I)/G(S)/G(O) subunit gamma-12	1,89404	0,00599
M1 48 / M0 48	SP110	Sp110 nuclear body protein	1,88799	0,00753
M1 48 / M0 48	TX264	Testis-expressed protein 264 homolog	1,88337	0,00554
M1 48 / M0 48	FCGR2	Low affinity immunoglobulin gamma Fc region receptor II	1,87349	0,00035
M1 48 / M0 48	TOM6	Mitochondrial import receptor subunit TOM6 homolog	1,86542	0,00278
M1 48 / M0 48	PLD3	5'-3' exonuclease PLD3	1,85224	0,00193
M1 48 / M0 48	CHCH2	Coiled-coil-helix-coiled-coil-helix domain-containing protein 2	1,84353	0,00125
M1 48 / M0 48	CD003	Uncharacterized protein C4orf3 homolog	1,82255	0,00553
M1 48 / M0 48	TTP	mRNA decay activator protein ZFP36	1,81596	0,00758
M1 48 / M0 48	MEF2C	Myocyte-specific enhancer factor 2C	1,81149	0,00240
M1 48 / M0 48	B2L11	Bcl-2-like protein 11	1,80309	0,00812
M1 48 / M0 48	NCOA6	Nuclear receptor coactivator 6	1,79449	0,00250
M1 48 / M0 48	T106A	Transmembrane protein 106A	1,78653	0,00322
M1 48 / M0 48	MPEG1	Macrophage-expressed gene 1 protein	1,78216	0,00539

M1 48 / M0 48	FIL1L	Filamin A-interacting protein 1-like	1,77286	0,00026
M1 48 / M0 48	NaN	NaN	1,76935	0,00228
M1 48 / M0 48	CEIP2	Cell surface hyaluronidase	1,76593	0,00218
M1 48 / M0 48	B2CL1	Bcl-2-like protein 1	1,75257	0,00239
M1 48 / M0 48	CCL2	C-C motif chemokine 2	1,74255	0,00368
M1 48 / M0 48	PHLA1	Pleckstrin homology-like domain family A member 1	1,74210	0,00739
M1 48 / M0 48	C42S2	CDC42 small effector protein 2	1,72850	0,00641
M1 48 / M0 48	CY24A	Cytochrome b-245 light chain	1,72482	0,00207
M1 48 / M0 48	SCMC1	Mitochondrial adenyl nucleotide antiporter SLC25A24	1,72228	0,00208
M1 48 / M0 48	HMOX1	Heme oxygenase 1	1,71446	0,00634
M1 48 / M0 48	PLIN2	Perilipin-2	1,71118	0,00181
M1 48 / M0 48	LRC25	Leucine-rich repeat-containing protein 25	1,70270	0,00074
M1 48 / M0 48	VTI1B	Vesicle transport through interaction with t-SNAREs homolog 1B	1,68089	0,00927
M1 48 / M0 48	MINY1	Ubiquitin carboxyl-terminal hydrolase MINDY-1	1,67216	0,00806
M1 48 / M0 48	SP100	Nuclear autoantigen Sp-100	1,66208	0,00701
M1 48 / M0 48	IFT22	Intraflagellar transport protein 22 homolog	1,66037	0,00975
M1 48 / M0 48	CATL1	Procathepsin L	1,65697	0,00237
M1 48 / M0 48	SQSTM	Sequestosome-1	1,65441	0,00133
M1 48 / M0 48	GBA1	Lysosomal acid glucosylceramidase	1,65216	0,00490
M1 48 / M0 48	DAD1	Dolichyl-diphosphooligosaccharide--protein glycosyltransferase subunit DAD1	1,65104	0,00197
M1 48 / M0 48	NDRG1	Protein NDRG1	1,64474	0,00309
M1 48 / M0 48	SNX18	Sorting nexin-18	1,63295	0,00249
M1 48 / M0 48	SC61B	Protein transport protein Sec61 subunit beta	1,62564	0,00111
M1 48 / M0 48	NPC2	NPC intracellular cholesterol transporter 2	1,62428	0,00574
M1 48 / M0 48	ANXA3	Annexin A3	1,62302	0,00895
M1 48 / M0 48	IFM3	Interferon-induced transmembrane protein 3	1,61997	0,00837
M1 48 / M0 48	NUDT8	Mitochondrial coenzyme A diphosphatase NUDT8	1,61300	0,00465
M1 48 / M0 48	SRXN1	Sulfiredoxin-1	1,61066	0,00191

M1 48 / M0 48	EDEM2	ER degradation-enhancing alpha-mannosidase-like protein 2	1,59374	0,00808
M1 48 / M0 48	NUCB2	Nucleobindin-2	1,59055	0,00788
M1 48 / M0 48	PKHN1	Probable pleckstrin homology domain-containing family N member 1	1,58109	0,00305
M1 48 / M0 48	ISG15	Ubiquitin-like protein ISG15	1,57360	0,00946
M1 48 / M0 48	GCSH	Glycine cleavage system H protein, mitochondrial	1,57295	0,00161
M1 48 / M0 48	ZYX	Zyxin	1,56178	0,00187
M1 48 / M0 48	FCGR1	High affinity immunoglobulin gamma Fc receptor I	1,51954	0,00228
M1 48 / M0 48	SYPL1	Synaptophysin-like protein 1	1,51024	0,00931
M1 48 / M0 48	VAMP3	Vesicle-associated membrane protein 3	1,50315	0,00591
M1 48 / M0 48	MYH11	Myosin-11	1,48215	0,00827
M1 48 / M0 48	CCDB1	Cyclin-D1-binding protein 1	1,47708	0,00543
M1 48 / M0 48	ABHEB	Putative protein-lysine deacylase ABHD14B	1,47548	0,00625
M1 48 / M0 48	HXK3	Hexokinase-3	1,47289	0,00222
M1 48 / M0 48	DTX2	Probable E3 ubiquitin-protein ligase DTX2	1,47037	0,00239
M1 48 / M0 48	BAK	Bcl-2 homologous antagonist/killer	1,45872	0,00564
M1 48 / M0 48	AKTS1	Proline-rich AKT1 substrate 1	1,45868	0,00667
M1 48 / M0 48	GOLI	E3 ubiquitin-protein ligase RNF130	1,44053	0,00633
M1 48 / M0 48	STX6	Syntaxin-6	1,43453	0,00733
M1 48 / M0 48	IF2B1	Insulin-like growth factor 2 mRNA-binding protein 1	1,43295	0,00065
M1 48 / M0 48	SAP3	Ganglioside GM2 activator	1,43243	0,00095
M1 48 / M0 48	TOIP2	Torsin-1A-interacting protein 2	1,42542	0,00334
M1 48 / M0 48	RETR3	Reticulophagy regulator 3	1,42218	0,00038
M1 48 / M0 48	FYB1	FYN-binding protein 1	1,42101	0,00540
M1 48 / M0 48	PRS33	Serine protease 33	1,41510	0,00692
M1 48 / M0 48	CATD	Cathepsin D	1,41137	0,00730
M1 48 / M0 48	T106B	Transmembrane protein 106B	1,41109	0,00035
M1 48 / M0 48	RFIP1	Rab11 family-interacting protein 1	1,40489	0,00328
M1 48 / M0 48	A4	Amyloid-beta precursor protein	1,38497	0,00203

M1 48 / M0 48	ITB2	Integrin beta-2	1,38495	0,00513
M1 48 / M0 48	CD44	CD44 antigen	1,38225	0,00139
M1 48 / M0 48	IRGQ	Immunity-related GTPase family Q protein	1,38103	0,00624
M1 48 / M0 48	SNG1	Synaptogyrin-1	1,37409	0,00317
M1 48 / M0 48	DHR11	Dehydrogenase/reductase SDR family member 11	1,36392	0,00092
M1 48 / M0 48	ITM2C	Integral membrane protein 2C	1,35504	0,00432
M1 48 / M0 48	RN185	E3 ubiquitin-protein ligase RNF185	1,34662	0,01000
M1 48 / M0 48	VATE1	V-type proton ATPase subunit E 1	1,34369	0,00668
M1 48 / M0 48	RAB3D	Ras-related protein Rab-3D	1,34298	0,00936
M1 48 / M0 48	KSYK	Tyrosine-protein kinase SYK	1,34233	0,00095
M1 48 / M0 48	ABCA1	Phospholipid-transporting ATPase ABCA1	1,34213	0,00540
M1 48 / M0 48	VATL	V-type proton ATPase 16 kDa proteolipid subunit c	1,34109	0,00683
M1 48 / M0 48	NUDT7	Peroxisomal coenzyme A diphosphatase NUDT7	1,33816	0,00898
M1 48 / M0 48	TM38B	Trimeric intracellular cation channel type B	1,33458	0,00983
M1 48 / M0 48	QPCT	Glutaminyl-peptide cyclotransferase	1,33101	0,00349
M1 48 / M0 48	NCPR	NADPH--cytochrome P450 reductase	1,32492	0,00068
M1 48 / M0 48	HA1L	H-2 class I histocompatibility antigen, L-D alpha chain	1,32262	0,00070
M1 48 / M0 48	MRP5	ATP-binding cassette sub-family C member 5	1,32161	0,00097
M1 48 / M0 48	RHBD2	Rhomboid domain-containing protein 2	1,32134	0,00161
M1 48 / M0 48	FND3A	Fibronectin type-III domain-containing protein 3A	1,31865	0,00044
M1 48 / M0 48	TXTP	Tricarboxylate transport protein, mitochondrial	1,31690	0,00473
M1 48 / M0 48	APOBR	Apolipoprotein B receptor	1,31632	0,00441
M1 48 / M0 48	RETR1	Reticulophagy regulator 1	1,30519	0,00530
M1 48 / M0 48	CD166	CD166 antigen	1,30231	0,00271
M1 48 / M0 48	TACAN	Ion channel TACAN	1,29581	0,00542
M1 48 / M0 48	F177A	Protein FAM177A1	1,29248	0,00686
M1 48 / M0 48	SUMF1	Formylglycine-generating enzyme	1,28387	0,00553
M1 48 / M0 48	TAP2	Antigen peptide transporter 2	1,28360	0,00028

M1 48 / M0 48	S35A2	UDP-galactose translocator	1,27662	0,00952
M1 48 / M0 48	LRC8C	Volume-regulated anion channel subunit LRRC8C	1,26702	0,00513
M1 48 / M0 48	MILK2	MICAL-like protein 2	1,26662	0,00413
M1 48 / M0 48	DYST	Dystonin	1,26254	0,00454
M1 48 / M0 48	S27A4	Long-chain fatty acid transport protein 4	1,25984	0,00187
M1 48 / M0 48	JTB	Protein JTB	1,24927	0,00505
M1 48 / M0 48	NaN	NaN	1,24638	0,00060
M1 48 / M0 48	CO039	Uncharacterized protein C15orf39 homolog	1,24494	0,00494
M1 48 / M0 48	MMSA	Methylmalonate-semialdehyde dehydrogenase [acylating], mitochondrial	1,23631	0,00565
M1 48 / M0 48	AMRP	Alpha-2-macroglobulin receptor-associated protein	1,23578	0,00912
M1 48 / M0 48	STX12	Syntaxin-12	1,23438	0,00759
M1 48 / M0 48	HPGDS	Hematopoietic prostaglandin D synthase	1,22777	0,00337
M1 48 / M0 48	AGRE1	Adhesion G protein-coupled receptor E1	1,22445	0,00107
M1 48 / M0 48	GCH1	GTP cyclohydrolase 1	1,21864	0,00087
M1 48 / M0 48	CCNY	Cyclin-Y	1,21050	0,00297
M1 48 / M0 48	4F2	4F2 cell-surface antigen heavy chain	1,20970	0,00569
M1 48 / M0 48	HS74L	Heat shock 70 kDa protein 4L	1,20941	0,00446
M1 48 / M0 48	LXN	Latexin	1,20234	0,00764
M1 48 / M0 48	AR6P1	ADP-ribosylation factor-like protein 6-interacting protein 1	1,20228	0,00649
M1 48 / M0 48	PCAT2	Lysophosphatidylcholine acyltransferase 2	1,19967	0,00739
M1 48 / M0 48	IFI4	Interferon-activable protein 204	1,19839	0,00458
M1 48 / M0 48	NaN	NaN	1,19288	0,00933
M1 48 / M0 48	STX8	Syntaxin-8	1,19283	0,00187
M1 48 / M0 48	LPP	Lipoma-preferred partner homolog	1,18910	0,00006
M1 48 / M0 48	MARF1	Meiosis regulator and mRNA stability factor 1	1,18852	0,00706
M1 48 / M0 48	FABP4	Fatty acid-binding protein, adipocyte	1,18490	0,00954
M1 48 / M0 48	MAIP1	m-AAA protease-interacting protein 1, mitochondrial	1,18408	0,00924
M1 48 / M0 48	ITAM	Integrin alpha-M	1,18273	0,00151

M1 48 / M0 48	MIC27	MICOS complex subunit Mic27	1,18008	0,00816
M1 48 / M0 48	ATRN	Attractin	1,17343	0,00284
M1 48 / M0 48	SAMN1	SAM domain-containing protein SAMSN-1	1,17225	0,00290
M1 48 / M0 48	GBP3	Guanylate-binding protein 3	1,17192	0,00186
M1 48 / M0 48	TAP1	Antigen peptide transporter 1	1,17104	0,00027
M1 48 / M0 48	LRCH4	Leucine-rich repeat and calponin homology domain-containing protein 4	1,17008	0,00090
M1 48 / M0 48	SNP23	Synaptosomal-associated protein 23	1,16758	0,00893
M1 48 / M0 48	ERO1A	ERO1-like protein alpha	1,16745	0,00070
M1 48 / M0 48	IFI2	Interferon-activable protein 202	1,16641	0,00132
M1 48 / M0 48	GAB2	GRB2-associated-binding protein 2	1,15336	0,00283
M1 48 / M0 48	NCEH1	Neutral cholesterol ester hydrolase 1	1,15300	0,00228
M1 48 / M0 48	DCAF5	DDB1- and CUL4-associated factor 5	1,14744	0,00448
M1 48 / M0 48	TUSC3	Tumor suppressor candidate 3	1,14005	0,00780
M1 48 / M0 48	NICA	Nicastrin	1,13935	0,00030
M1 48 / M0 48	PPT1	Palmitoyl-protein thioesterase 1	1,13489	0,00171
M1 48 / M0 48	SCPDL	Saccharopine dehydrogenase-like oxidoreductase	1,13197	0,00375
M1 48 / M0 48	VATG1	V-type proton ATPase subunit G 1	1,12357	0,00805
M1 48 / M0 48	SAP	Prosaposin	1,12004	0,00398
M1 48 / M0 48	S23A2	Solute carrier family 23 member 2	1,11783	0,00242
M1 48 / M0 48	ATP5L	ATP synthase subunit g, mitochondrial	1,11666	0,00168
M1 48 / M0 48	PO2F2	POU domain, class 2, transcription factor 2	1,11515	0,00799
M1 48 / M0 48	GLRX1	Glutaredoxin-1	1,11275	0,00466
M1 48 / M0 48	IRAK3	Interleukin-1 receptor-associated kinase 3	1,11268	0,00070
M1 48 / M0 48	F117B	Protein FAM117B	1,10641	0,00228
M1 48 / M0 48	HIG1A	HIG1 domain family member 1A, mitochondrial	1,10565	0,00228
M1 48 / M0 48	SCRB2	Lysosome membrane protein 2	1,10522	0,00397
M1 48 / M0 48	ATP8	ATP synthase protein 8	1,10508	0,00094
M1 48 / M0 48	ESYT1	Extended synaptotagmin-1	1,09962	0,00513
M1 48 / M0 48	ZDHC3	Palmitoyltransferase ZDHHC3	1,09715	0,00173

M1 48 / M0 48	TPSN	Tapasin	1,09273	0,00308
M1 48 / M0 48	GNS	N-acetylglucosamine-6-sulfatase	1,08824	0,00904
M1 48 / M0 48	RHOB	Rho-related GTP-binding protein RhoB	1,08734	0,00176
M1 48 / M0 48	ATP5S	ATP synthase subunit s, mitochondrial	1,07774	0,00138
M1 48 / M0 48	3HIDH	3-hydroxyisobutyrate dehydrogenase, mitochondrial	1,07661	0,00068
M1 48 / M0 48	GDE1	Glycerophosphodiester phosphodiesterase 1	1,07485	0,00316
M1 48 / M0 48	LRRF1	Leucine-rich repeat flightless-interacting protein 1	1,07270	0,00453
M1 48 / M0 48	TI17B	Mitochondrial import inner membrane translocase subunit Tim17-B	1,07146	0,00151
M1 48 / M0 48	LACC1	Purine nucleoside phosphorylase LACC1	1,06693	0,00825
M1 48 / M0 48	ERRFI	ERBB receptor feedback inhibitor 1	1,06036	0,00083
M1 48 / M0 48	EAF1	ELL-associated factor 1	1,05717	0,00306
M1 48 / M0 48	REEP5	Receptor expression-enhancing protein 5	1,05667	0,00401
M1 48 / M0 48	ITA5	Integrin alpha-5	1,05646	0,00296
M1 48 / M0 48	TOIP1	Torsin-1A-interacting protein 1	1,05593	0,00076
M1 48 / M0 48	ITAL	Integrin alpha-L	1,04827	0,00371
M1 48 / M0 48	TGM2	Protein-glutamine gamma-glutamyltransferase 2	1,04783	0,00161
M1 48 / M0 48	M17L2	Mpv17-like protein 2	1,04772	0,00952
M1 48 / M0 48	LYRM4	LYR motif-containing protein 4	1,04329	0,00692
M1 48 / M0 48	TRPV2	Transient receptor potential cation channel subfamily V member 2	1,04292	0,00056
M1 48 / M0 48	SLAI2	SLAIN motif-containing protein 2	1,04183	0,00717
M1 48 / M0 48	AK1A1	Aldo-keto reductase family 1 member A1	1,04080	0,00660
M1 48 / M0 48	PLXA1	Plexin-A1	1,03761	0,00055
M1 48 / M0 48	TOM1	Target of Myb1 membrane trafficking protein	1,03715	0,00141
M1 48 / M0 48	PGH1	Prostaglandin G/H synthase 1	1,03138	0,00745
M1 48 / M0 48	ASPH	Aspartyl/asparaginyl beta-hydroxylase	1,02836	0,00394
M1 48 / M0 48	LTOR1	Ragulator complex protein LAMTOR1	1,02796	0,00130
M1 48 / M0 48	CDK13	Cyclin-dependent kinase 13	1,02531	0,00218

M1 48 / M0 48	GSTP1	Glutathione S-transferase P 1	1,02463	0,00430
M1 48 / M0 48	TOM22	Mitochondrial import receptor subunit TOM22 homolog	1,02218	0,00930
M1 48 / M0 48	JUPI1	Jupiter microtubule associated homolog 1	1,01769	0,00075
M1 48 / M0 48	S10AB	Protein S100-A11	1,01752	0,00461
M1 48 / M0 48	PARP3	Protein mono-ADP-ribosyltransferase PARP3	1,01722	0,00076
M1 48 / M0 48	DGKH	Diacylglycerol kinase eta	1,01585	0,00677
M1 48 / M0 48	OSTC	Oligosaccharyltransferase complex subunit OSTC	1,01532	0,00568
M1 48 / M0 48	ANXA4	Annexin A4	1,01263	0,00977
M1 48 / M0 48	CHP1	Calcineurin B homologous protein 1	1,01074	0,00190
M1 48 / M0 48	NLRX1	NLR family member X1	1,00894	0,00265
M1 48 / M0 48	IRGM1	Immunity-related GTPase family M protein 1	1,00683	0,00089
M1 48 / M0 48	SHPS1	Tyrosine-protein phosphatase non-receptor type substrate 1	1,00621	0,00518
M1 48 / M0 48	MSRE	Macrophage scavenger receptor types I and II	1,00581	0,00169
M1 48 / M0 48	SCAM1	Secretory carrier-associated membrane protein 1	1,00491	0,00393
M1 48 / M0 48	ANXA6	Annexin A6	1,00427	0,00118
M1 48 / M0 48	RFOX2	RNA binding protein fox-1 homolog 2	1,00186	0,00018
M1 48 / M0 48	CATB	Cathepsin B	1,00155	0,00473
M1 48 / M0 48	PAFA2	Platelet-activating factor acetylhydrolase 2, cytoplasmic	1,00121	0,00269
M1 48 / M0 48	WIPF1	WAS/WASL-interacting protein family member 1	1,00108	0,00392
M1 48 / M0 48	PCNP	PEST proteolytic signal-containing nuclear protein	1,00066	0,00054
M1 48 / M0 48	ADSSP	Adipose-secreted signaling protein	-1,00150	0,00867
M1 48 / M0 48	GLYC	Serine hydroxymethyltransferase, cytosolic	-1,00294	0,00498
M1 48 / M0 48	CADM1	Cell adhesion molecule 1	-1,00436	0,00289
M1 48 / M0 48	FOXJ3	Forkhead box protein J3	-1,00645	0,00554
M1 48 / M0 48	ABI2	Abl interactor 2	-1,00958	0,00582
M1 48 / M0 48	BRD1	Bromodomain-containing protein 1	-1,01130	0,00972

M1 48 / M0 48	MCM5	DNA replication licensing factor MCM5	-1,01201	0,00151
M1 48 / M0 48	AAR2	Protein AAR2 homolog	-1,01239	0,00067
M1 48 / M0 48	EIF3C	Eukaryotic translation initiation factor 3 subunit C	-1,01424	0,00225
M1 48 / M0 48	CIRBP	Cold-inducible RNA-binding protein	-1,01901	0,00707
M1 48 / M0 48	DIM1	Probable dimethyladenosine transferase	-1,01916	0,00310
M1 48 / M0 48	CND2	Condensin complex subunit 2	-1,01959	0,00129
M1 48 / M0 48	MOG1	Ran guanine nucleotide release factor	-1,02151	0,00208
M1 48 / M0 48	FBSP1	F-box/SPRY domain-containing protein 1	-1,02589	0,00981
M1 48 / M0 48	EIF3D	Eukaryotic translation initiation factor 3 subunit D	-1,02590	0,00399
M1 48 / M0 48	TRI16	Tripartite motif-containing protein 16	-1,03042	0,00268
M1 48 / M0 48	AURKB	Aurora kinase B	-1,03240	0,00162
M1 48 / M0 48	ANC2	Anaphase-promoting complex subunit 2	-1,03388	0,00709
M1 48 / M0 48	CND1	Condensin complex subunit 1	-1,03483	0,00728
M1 48 / M0 48	WDHD1	WD repeat and HMG-box DNA-binding protein 1	-1,03658	0,00976
M1 48 / M0 48	IFG15	Torsin-1A-interacting protein 2, isoform IFRG15	-1,04117	0,00805
M1 48 / M0 48	ANM7	Protein arginine N-methyltransferase 7	-1,04294	0,00125
M1 48 / M0 48	NSUN5	28S rRNA (cytosine-C(5))-methyltransferase	-1,04330	0,00192
M1 48 / M0 48	RFA1	Replication protein A 70 kDa DNA-binding subunit	-1,04501	0,00891
M1 48 / M0 48	PRPS1	Ribose-phosphate pyrophosphokinase 1	-1,04548	0,00736
M1 48 / M0 48	ACBP	Acyl-CoA-binding protein	-1,05458	0,00549
M1 48 / M0 48	RS7	Small ribosomal subunit protein eS7	-1,05517	0,00070
M1 48 / M0 48	FANCI	Fanconi anemia group I protein homolog	-1,06026	0,00796
M1 48 / M0 48	HIRP3	HIRA-interacting protein 3	-1,06216	0,00249
M1 48 / M0 48	HMGB3	High mobility group protein B3	-1,06479	0,00307
M1 48 / M0 48	TWF2	Twinfilin-2	-1,06701	0,00863
M1 48 / M0 48	TFDP1	Transcription factor Dp-1	-1,06856	0,00472
M1 48 / M0 48	NACAM	Nascent polypeptide-associated complex	-1,07610	0,00064

		subunit alpha, muscle-specific form		
M1 48 / M0 48	ENOPH	Enolase-phosphatase E1	-1,08028	0,00120
M1 48 / M0 48	LIPL	Lipoprotein lipase	-1,08290	0,00175
M1 48 / M0 48	THA11	THAP domain-containing protein 11	-1,08631	0,00939
M1 48 / M0 48	FA32A	Protein FAM32A	-1,08845	0,00929
M1 48 / M0 48	SPEE	Spermidine synthase	-1,09187	0,00092
M1 48 / M0 48	FBX42	F-box only protein 42	-1,09848	0,00107
M1 48 / M0 48	IRF2	Interferon regulatory factor 2	-1,09860	0,00589
M1 48 / M0 48	DNLI1	DNA ligase 1	-1,09992	0,00003
M1 48 / M0 48	DNPH1	2'-deoxynucleoside 5'-phosphate N-hydrolase 1	-1,10043	0,00653
M1 48 / M0 48	TBPL1	TATA box-binding protein-like 1	-1,10241	0,00279
M1 48 / M0 48	MTND	Acireductone dioxygenase	-1,10242	0,00062
M1 48 / M0 48	ASF1A	Histone chaperone ASF1A	-1,10444	0,00601
M1 48 / M0 48	EMAL3	Echinoderm microtubule-associated protein-like 3	-1,10492	0,00132
M1 48 / M0 48	PEBB	Core-binding factor subunit beta	-1,10554	0,00418
M1 48 / M0 48	SMC4	Structural maintenance of chromosomes protein 4	-1,10868	0,00077
M1 48 / M0 48	EWS	RNA-binding protein EWS	-1,10899	0,00569
M1 48 / M0 48	HELLS	Lymphocyte-specific helicase	-1,11041	0,00223
M1 48 / M0 48	PRP17	Pre-mRNA-processing factor 17	-1,11459	0,00595
M1 48 / M0 48	CEP76	Centrosomal protein of 76 kDa	-1,11872	0,00651
M1 48 / M0 48	PRI1	DNA primase small subunit	-1,12414	0,00008
M1 48 / M0 48	EIF1	Eukaryotic translation initiation factor 1	-1,12483	0,00179
M1 48 / M0 48	DNMT1	DNA (cytosine-5)-methyltransferase 1	-1,13213	0,00017
M1 48 / M0 48	TTL12	Tubulin--tyrosine ligase-like protein 12	-1,13593	0,00297
M1 48 / M0 48	PK1IP	p21-activated protein kinase-interacting protein 1	-1,14296	0,00255
M1 48 / M0 48	KT3K	Ketosamine-3-kinase	-1,15123	0,00304
M1 48 / M0 48	RASA3	Ras GTPase-activating protein 3	-1,15229	0,00061
M1 48 / M0 48	ENV2	Retrovirus-related Env polyprotein from Fv-4 locus	-1,15569	0,00280

M1 48 / M0 48	SMYD3	Histone-lysine N-methyltransferase SMYD3	-1,15975	0,00064
M1 48 / M0 48	HINT1	Adenosine 5'-monophosphoramidase HINT1	-1,16086	0,00891
M1 48 / M0 48	SSNA1	Microtubule nucleation factor SSNA1	-1,16377	0,00983
M1 48 / M0 48	KS6A1	Ribosomal protein S6 kinase alpha-1	-1,17227	0,00168
M1 48 / M0 48	WDR73	WD repeat-containing protein 73	-1,17595	0,00997
M1 48 / M0 48	RPF1	Ribosome production factor 1	-1,17613	0,00425
M1 48 / M0 48	AHSA1	Activator of 90 kDa heat shock protein ATPase homolog 1	-1,17697	0,00806
M1 48 / M0 48	IN80D	INO80 complex subunit D	-1,17899	0,00635
M1 48 / M0 48	FPPS	Farnesyl pyrophosphate synthase	-1,17917	0,00341
M1 48 / M0 48	RASF1	Ras association domain-containing protein 1	-1,18308	0,00692
M1 48 / M0 48	DNA2	DNA replication ATP-dependent helicase/nuclease DNA2	-1,18449	0,00320
M1 48 / M0 48	SZT2	KICSTOR complex protein SZT2	-1,18547	0,00204
M1 48 / M0 48	PP2AA	Serine/threonine-protein phosphatase 2A catalytic subunit alpha isoform	-1,18573	0,00952
M1 48 / M0 48	TYSY	Thymidylate synthase	-1,18797	0,00467
M1 48 / M0 48	FEM1B	Protein fem-1 homolog B	-1,19325	0,00098
M1 48 / M0 48	DDX28	Probable ATP-dependent RNA helicase DDX28	-1,19707	0,00113
M1 48 / M0 48	CTCF	Transcriptional repressor CTCF	-1,20401	0,00369
M1 48 / M0 48	PHF14	PHD finger protein 14	-1,20495	0,00350
M1 48 / M0 48	RAD18	E3 ubiquitin-protein ligase RAD18	-1,21386	0,00075
M1 48 / M0 48	SPB8	Serpin B8	-1,21670	0,00228
M1 48 / M0 48	CDK6	Cyclin-dependent kinase 6	-1,22162	0,00356
M1 48 / M0 48	AVIL	Advillin	-1,23083	0,00158
M1 48 / M0 48	CAF1A	Chromatin assembly factor 1 subunit A	-1,24157	0,00574
M1 48 / M0 48	TTC33	Tetratricopeptide repeat protein 33	-1,24166	0,00036
M1 48 / M0 48	PSTK	L-seryl-tRNA(Sec) kinase	-1,24275	0,00167
M1 48 / M0 48	H12	Histone H1.2	-1,25068	0,00947
M1 48 / M0 48	HMCS1	Hydroxymethylglutaryl-CoA synthase, cytoplasmic	-1,25116	0,00939

M1 48 / M0 48	JKIP3	Janus kinase and microtubule-interacting protein 3	-1,26482	0,00717
M1 48 / M0 48	IFRD2	Interferon-related developmental regulator 2	-1,26637	0,00601
M1 48 / M0 48	SMYD2	N-lysine methyltransferase SMYD2	-1,27227	0,00521
M1 48 / M0 48	ILKAP	Integrin-linked kinase-associated serine/threonine phosphatase 2C	-1,28017	0,00120
M1 48 / M0 48	CAF1B	Chromatin assembly factor 1 subunit B	-1,28239	0,00479
M1 48 / M0 48	SYVC	Valine--tRNA ligase	-1,28279	0,00018
M1 48 / M0 48	RNH2B	Ribonuclease H2 subunit B	-1,29413	0,00153
M1 48 / M0 48	SERC3	Serine incorporator 3	-1,30145	0,00884
M1 48 / M0 48	EKI1	Ethanolamine kinase 1	-1,30267	0,00639
M1 48 / M0 48	5NTC	Cytosolic purine 5'-nucleotidase	-1,30463	0,00077
M1 48 / M0 48	IPO8	Importin-8	-1,30696	0,00060
M1 48 / M0 48	PUR1	Amidophosphoribosyltransferase	-1,30946	0,00181
M1 48 / M0 48	PIAS1	E3 SUMO-protein ligase PIAS1	-1,31366	0,00900
M1 48 / M0 48	BRX1	Ribosome biogenesis protein BRX1 homolog	-1,31897	0,00678
M1 48 / M0 48	H2A2C	Histone H2A type 2-C	-1,32180	0,00966
M1 48 / M0 48	RBM3	RNA-binding protein 3	-1,32383	0,00157
M1 48 / M0 48	SURF2	Surfeit locus protein 2	-1,34279	0,00210
M1 48 / M0 48	CIP2A	Protein CIP2A	-1,34370	0,00071
M1 48 / M0 48	TYDP1	Tyrosyl-DNA phosphodiesterase 1	-1,35343	0,00020
M1 48 / M0 48	RBL1	Retinoblastoma-like protein 1	-1,35360	0,00071
M1 48 / M0 48	CCND1	G1/S-specific cyclin-D1	-1,36477	0,00966
M1 48 / M0 48	SPC25	Kinetochore protein Spc25	-1,36668	0,00181
M1 48 / M0 48	HMGB2	High mobility group protein B2	-1,37370	0,00262
M1 48 / M0 48	ITA4	Integrin alpha-4	-1,38472	0,00006
M1 48 / M0 48	GPN3	GPN-loop GTPase 3	-1,38946	0,00459
M1 48 / M0 48	ZWILC	Protein zwilch homolog	-1,38965	0,00632
M1 48 / M0 48	MOB2	MOB kinase activator 2	-1,40438	0,00126
M1 48 / M0 48	PRPS2	Ribose-phosphate pyrophosphokinase 2	-1,42057	0,00249
M1 48 / M0 48	H31	Histone H3.1	-1,42470	0,00106
M1 48 / M0 48	FADS1	Acyl-CoA (8-3)-desaturase	-1,43358	0,00390
M1 48 / M0 48	RO60	RNA-binding protein Ro60	-1,43455	0,00674

M1 48 / M0 48	BTF3	Transcription factor BTF3	-1,43470	0,00101
M1 48 / M0 48	UHRF1	E3 ubiquitin-protein ligase UHRF1	-1,43622	0,00144
M1 48 / M0 48	TYY1	Transcriptional repressor protein YY1	-1,44272	0,00018
M1 48 / M0 48	VRK1	Serine/threonine-protein kinase VRK1	-1,44453	0,00192
M1 48 / M0 48	PTPS	6-pyruvoyl tetrahydrobiopterin synthase	-1,44642	0,00030
M1 48 / M0 48	QTRT2	Queuine tRNA-ribosyltransferase accessory subunit 2	-1,46542	0,00190
M1 48 / M0 48	TFEB	Transcription factor EB	-1,47075	0,00074
M1 48 / M0 48	ABEC1	C->U-editing enzyme APOBEC-1	-1,50191	0,00268
M1 48 / M0 48	NADK	NAD kinase	-1,52053	0,00095
M1 48 / M0 48	CP51A	Lanosterol 14-alpha demethylase	-1,53570	0,00253
M1 48 / M0 48	S19A1	Reduced folate transporter	-1,55294	0,00426
M1 48 / M0 48	GSDME	Gasdermin-E	-1,56042	0,00760
M1 48 / M0 48	CDK1	Cyclin-dependent kinase 1	-1,59720	0,00009
M1 48 / M0 48	MOT10	Monocarboxylate transporter 10	-1,62065	0,00627
M1 48 / M0 48	MOFA1	MORF4 family-associated protein 1	-1,63817	0,00469
M1 48 / M0 48	DCTD	Deoxycytidylate deaminase	-1,64043	0,00894
M1 48 / M0 48	KIF15	Kinesin-like protein KIF15	-1,64101	0,00057
M1 48 / M0 48	SCD2	Stearoyl-CoA desaturase 2	-1,65224	0,00396
M1 48 / M0 48	ZFAN1	AN1-type zinc finger protein 1	-1,65642	0,00054
M1 48 / M0 48	RNH2C	Ribonuclease H2 subunit C	-1,65982	0,00116
M1 48 / M0 48	TIDC1	Complex I assembly factor TIMMDC1, mitochondrial	-1,67009	0,00838
M1 48 / M0 48	CRIP1	Cysteine-rich protein 1	-1,71478	0,00060
M1 48 / M0 48	KBTBB	Kelch repeat and BTB domain-containing protein 11	-1,72972	0,00027
M1 48 / M0 48	AASD1	Alanyl-tRNA editing protein Aarsd1	-1,77799	0,00036
M1 48 / M0 48	KITH	Thymidine kinase, cytosolic	-1,79556	0,00095
M1 48 / M0 48	CKS2	Cyclin-dependent kinases regulatory subunit 2	-1,81790	0,00638
M1 48 / M0 48	GPR84	G-protein coupled receptor 84	-1,83137	0,00384
M1 48 / M0 48	RCC2	Protein RCC2	-1,85140	0,00232

M1 48 / M0 48	ZN787	Zinc finger protein 787	-1,95234	0,00100
M1 48 / M0 48	RIR1	Ribonucleoside-diphosphate reductase large subunit	-1,97962	0,00511
M1 48 / M0 48	CKS1	Cyclin-dependent kinases regulatory subunit 1	-2,02064	0,00614
M1 48 / M0 48	SYTC2	Threonine--tRNA ligase 2, cytoplasmic	-2,10000	0,00526
M1 48 / M0 48	CNBP	CCHC-type zinc finger nucleic acid binding protein	-2,19657	0,00060
M1 48 / M0 48	H2B1B	Histone H2B type 1-B	-2,25862	0,00192
M2 48 / M0 48	SYN1	Synapsin-1	5,38702	0,00111
M2 48 / M0 48	PAI2	Plasminogen activator inhibitor 2, macrophage	3,91975	0,00279
M2 48 / M0 48	BASP1	Brain acid soluble protein 1	3,18181	0,00237
M2 48 / M0 48	ALBU	Albumin	3,11655	0,00142
M2 48 / M0 48	CDD	Cytidine deaminase	3,09312	0,00639
M2 48 / M0 48	RBNS5	Rabenosyn-5	3,07706	0,00118
M2 48 / M0 48	ARGI2	Arginase-2, mitochondrial	2,93873	0,00521
M2 48 / M0 48	SQSTM	Sequestosome-1	2,72671	0,00508
M2 48 / M0 48	IL1RA	Interleukin-1 receptor antagonist protein	2,59830	0,00256
M2 48 / M0 48	IRG1	Cis-aconitate decarboxylase	2,53340	0,00008
M2 48 / M0 48	KCD12	BTB/POZ domain-containing protein KCTD12	2,38526	0,00062
M2 48 / M0 48	B2CL1	Bcl-2-like protein 1	2,37264	0,00656
M2 48 / M0 48	ERO1A	ERO1-like protein alpha	2,36306	0,00530
M2 48 / M0 48	UPP1	Uridine phosphorylase 1	2,31621	0,00164
M2 48 / M0 48	PGH2	Prostaglandin G/H synthase 2	2,29487	0,00167
M2 48 / M0 48	PRDX5	Peroxiredoxin-5, mitochondrial	2,17823	0,00240
M2 48 / M0 48	GSTP1	Glutathione S-transferase P 1	2,16407	0,00565
M2 48 / M0 48	GLMP	Glycosylated lysosomal membrane protein	2,11780	0,00456
M2 48 / M0 48	ARSA	Arylsulfatase A	2,01199	0,00218
M2 48 / M0 48	GLPK	Glycerol kinase	1,94858	0,00261
M2 48 / M0 48	SQOR	Sulfide:quinone oxidoreductase, mitochondrial	1,88889	0,00197
M2 48 / M0 48	CEBPB	CCAAT/enhancer-binding protein beta	1,87334	0,00133
M2 48 / M0 48	LANC3	LanC-like protein 3	1,86417	0,00090
M2 48 / M0 48	CHCH2	Coiled-coil-helix-coiled-coil-helix domain-containing protein 2	1,85561	0,00315

M2 48 / M0 48	XCT	Cystine/glutamate transporter	1,84449	0,00239
M2 48 / M0 48	MRP	MARCKS-related protein	1,84389	0,00239
M2 48 / M0 48	GPNMB	Transmembrane glycoprotein NMB	1,83729	0,00161
M2 48 / M0 48	FRIH	Ferritin heavy chain	1,82936	0,00574
M2 48 / M0 48	HMGA2	High mobility group protein HMGI-C	1,78553	0,00210
M2 48 / M0 48	COPT2	Protein SLC31A2	1,77749	0,00853
M2 48 / M0 48	MEF2C	Myocyte-specific enhancer factor 2C	1,77726	0,00363
M2 48 / M0 48	SN	Sialoadhesin	1,77104	0,00248
M2 48 / M0 48	ZYX	Zyxin	1,76624	0,00119
M2 48 / M0 48	PBIP1	Pre-B-cell leukemia transcription factor-interacting protein 1	1,72254	0,00068
M2 48 / M0 48	MISSL	MAPK-interacting and spindle-stabilizing protein-like	1,69084	0,00114
M2 48 / M0 48	FCGR3	Low affinity immunoglobulin gamma Fc region receptor III	1,68068	0,00183
M2 48 / M0 48	NUDT7	Peroxisomal coenzyme A diphosphatase NUDT7	1,68055	0,00497
M2 48 / M0 48	SODM	Superoxide dismutase [Mn], mitochondrial	1,67903	0,00026
M2 48 / M0 48	IKBA	NF-kappa-B inhibitor alpha	1,67270	0,00329
M2 48 / M0 48	NUCB2	Nucleobindin-2	1,66175	0,00261
M2 48 / M0 48	NDRG1	Protein NDRG1	1,65967	0,00636
M2 48 / M0 48	AMPN	Aminopeptidase N	1,65557	0,00061
M2 48 / M0 48	GBG2	Guanine nucleotide-binding protein G(I)/G(S)/G(O) subunit gamma-2	1,64877	0,00017
M2 48 / M0 48	DYN1	Dynamin-1	1,61999	0,00849
M2 48 / M0 48	K1C16	Keratin, type I cytoskeletal 16	1,61296	0,00572
M2 48 / M0 48	ICAL	Calpastatin	1,58448	0,00305
M2 48 / M0 48	F117B	Protein FAM117B	1,58143	0,00648
M2 48 / M0 48	GBG12	Guanine nucleotide-binding protein G(I)/G(S)/G(O) subunit gamma-12	1,56161	0,00232
M2 48 / M0 48	HXK3	Hexokinase-3	1,53511	0,00214
M2 48 / M0 48	IF2B2	Insulin-like growth factor 2 mRNA-binding protein 2	1,53033	0,00217
M2 48 / M0 48	DPH6	Diphthine--ammonia ligase	1,51927	0,00127
M2 48 / M0 48	TX264	Testis-expressed protein 264 homolog	1,51499	0,00157

M2 48 / M0 48	RPGF5	Rap guanine nucleotide exchange factor 5	1,51298	0,00322
M2 48 / M0 48	SC61B	Protein transport protein Sec61 subunit beta	1,47330	0,00017
M2 48 / M0 48	ANXA3	Annexin A3	1,46555	0,00163
M2 48 / M0 48	HMGN2	Non-histone chromosomal protein HMG-17	1,46526	0,00753
M2 48 / M0 48	BRI3B	BRI3-binding protein	1,46210	0,00012
M2 48 / M0 48	ARF4	ADP-ribosylation factor 4	1,44848	0,00011
M2 48 / M0 48	B2L11	Bcl-2-like protein 11	1,44469	0,00335
M2 48 / M0 48	EAF1	ELL-associated factor 1	1,43896	0,00675
M2 48 / M0 48	TP8L2	Tumor necrosis factor alpha-induced protein 8-like protein 2	1,43851	0,00100
M2 48 / M0 48	NPC2	NPC intracellular cholesterol transporter 2	1,43445	0,00083
M2 48 / M0 48	QPCT	Glutaminyl-peptide cyclotransferase	1,42474	0,00155
M2 48 / M0 48	UBQL1	Ubiquilin-1	1,41946	0,00347
M2 48 / M0 48	B2MG	Beta-2-microglobulin	1,41786	0,00063
M2 48 / M0 48	CHSP1	Calcium-regulated heat stable protein 1	1,41340	0,00974
M2 48 / M0 48	PAI1	Plasminogen activator inhibitor 1	1,40959	0,00197
M2 48 / M0 48	PCNP	PEST proteolytic signal-containing nuclear protein	1,37934	0,00042
M2 48 / M0 48	PTGR1	Prostaglandin reductase 1	1,37584	0,00073
M2 48 / M0 48	LMBD1	Lysosomal cobalamin transport escort protein LMBD1	1,37348	0,00452
M2 48 / M0 48	GSH0	Glutamate--cysteine ligase regulatory subunit	1,35534	0,00635
M2 48 / M0 48	PLP2	Proteolipid protein 2	1,34676	0,00026
M2 48 / M0 48	ATX1	Ataxin-1	1,34160	0,00044
M2 48 / M0 48	MSRE	Macrophage scavenger receptor types I and II	1,33251	0,00175
M2 48 / M0 48	NaN	NaN	1,32312	0,00388
M2 48 / M0 48	DHRS1	Dehydrogenase/reductase SDR family member 1	1,30870	0,00253
M2 48 / M0 48	CY24A	Cytochrome b-245 light chain	1,30666	0,00084
M2 48 / M0 48	NTAL	Linker for activation of T-cells family member 2	1,30426	0,00198
M2 48 / M0 48	NDKA	Nucleoside diphosphate kinase A	1,28649	0,00595
M2 48 / M0 48	DHR11	Dehydrogenase/reductase SDR family member 11	1,28396	0,00181
M2 48 / M0 48	MILK2	MICAL-like protein 2	1,28199	0,00125

M2 48 / M0 48	NUDT8	Mitochondrial coenzyme A diphosphatase NUDT8	1,27784	0,00304
M2 48 / M0 48	RGS1	Regulator of G-protein signaling 1	1,26606	0,00871
M2 48 / M0 48	FRIL1	Ferritin light chain 1	1,26037	0,00252
M2 48 / M0 48	SASH1	SAM and SH3 domain-containing protein 1	1,26031	0,00024
M2 48 / M0 48	FYB1	FYN-binding protein 1	1,23977	0,00062
M2 48 / M0 48	GRPE1	GrpE protein homolog 1, mitochondrial	1,23948	0,00134
M2 48 / M0 48	PDCD6	Programmed cell death protein 6	1,23253	0,00510
M2 48 / M0 48	S10AA	Protein S100-A10	1,22754	0,00168
M2 48 / M0 48	KGD4	Alpha-ketoglutarate dehydrogenase component 4	1,22524	0,00414
M2 48 / M0 48	DERPC	Decreased expression in renal and prostate cancer protein	1,22066	0,00283
M2 48 / M0 48	XYLT2	Xylosyltransferase 2	1,21903	0,00305
M2 48 / M0 48	AMPD3	AMP deaminase 3	1,21698	0,00190
M2 48 / M0 48	STOM	Stomatin	1,21325	0,00163
M2 48 / M0 48	LRRF1	Leucine-rich repeat flightless-interacting protein 1	1,20701	0,00017
M2 48 / M0 48	SYPL1	Synaptophysin-like protein 1	1,19320	0,00064
M2 48 / M0 48	CGL	Cystathionine gamma-lyase	1,18626	0,00095
M2 48 / M0 48	PO2F2	POU domain, class 2, transcription factor 2	1,18516	0,00209
M2 48 / M0 48	SYAP1	Synapse-associated protein 1	1,18258	0,00393
M2 48 / M0 48	BST1	ADP-ribosyl cyclase/cyclic ADP-ribose hydrolase 2	1,17710	0,00489
M2 48 / M0 48	SCMC1	Mitochondrial adenyl nucleotide antiporter SLC25A24	1,17594	0,00099
M2 48 / M0 48	TM199	Transmembrane protein 199	1,17461	0,00262
M2 48 / M0 48	ASSY	Argininosuccinate synthase	1,17431	0,00198
M2 48 / M0 48	TOIP2	Torsin-1A-interacting protein 2	1,17304	0,00569
M2 48 / M0 48	SAMN1	SAM domain-containing protein SAMSN-1	1,15956	0,00302
M2 48 / M0 48	SAP	Prosaposin	1,15722	0,00613
M2 48 / M0 48	CNOT9	CCR4-NOT transcription complex subunit 9	1,15571	0,00270
M2 48 / M0 48	T106A	Transmembrane protein 106A	1,15389	0,00388
M2 48 / M0 48	LXN	Latexin	1,15219	0,00032

M2 48 / M0 48	S28A2	Sodium/nucleoside cotransporter 2	1,14766	0,00191
M2 48 / M0 48	LPP	Lipoma-preferred partner homolog	1,14705	0,00825
M2 48 / M0 48	A4	Amyloid-beta precursor protein	1,14380	0,00036
M2 48 / M0 48	PRDX1	Peroxiredoxin-1	1,14377	0,00077
M2 48 / M0 48	AF1Q	Protein AF1q	1,14244	0,00727
M2 48 / M0 48	GRN	Progranulin	1,14079	0,00021
M2 48 / M0 48	APOBR	Apolipoprotein B receptor	1,13462	0,00038
M2 48 / M0 48	MYH11	Myosin-11	1,13168	0,00047
M2 48 / M0 48	IRAK3	Interleukin-1 receptor-associated kinase 3	1,12948	0,00087
M2 48 / M0 48	CD37L	Hsp90 co-chaperone Cdc37-like 1	1,12298	0,00725
M2 48 / M0 48	ITAM	Integrin alpha-M	1,11717	0,00159
M2 48 / M0 48	ZNRF2	E3 ubiquitin-protein ligase ZNRF2	1,11336	0,00127
M2 48 / M0 48	GDPD1	Lysophospholipase D GDPD1	1,11258	0,00356
M2 48 / M0 48	SC22B	Vesicle-trafficking protein SEC22b	1,11145	0,00008
M2 48 / M0 48	T22D4	TSC22 domain family protein 4	1,11008	0,00049
M2 48 / M0 48	CD44	CD44 antigen	1,10809	0,00292
M2 48 / M0 48	MINY1	Ubiquitin carboxyl-terminal hydrolase MINDY-1	1,10578	0,00372
M2 48 / M0 48	CLN5	Ceroid-lipofuscinosis neuronal protein 5 homolog	1,10422	0,00855
M2 48 / M0 48	WIPF1	WAS/WASL-interacting protein family member 1	1,10203	0,00129
M2 48 / M0 48	VTI1B	Vesicle transport through interaction with t-SNAREs homolog 1B	1,10022	0,00021
M2 48 / M0 48	DYST	Dystonin	1,09783	0,00116
M2 48 / M0 48	PLSL	Plastin-2	1,09626	0,00031
M2 48 / M0 48	AP4AT	AP-4 complex accessory subunit Tepsin	1,09519	0,00916
M2 48 / M0 48	LTOR2	Ragulator complex protein LAMTOR2	1,08833	0,00039
M2 48 / M0 48	MAAI	Maleylacetoacetate isomerase	1,08717	0,00826
M2 48 / M0 48	VTI1A	Vesicle transport through interaction with t-SNAREs homolog 1A	1,08623	0,00662
M2 48 / M0 48	PKHN1	Probable pleckstrin homology domain-containing family N member 1	1,08534	0,00302
M2 48 / M0 48	BAG1	BAG family molecular chaperone regulator 1	1,07925	0,00518

M2 48 / M0 48	RIPL2	RILP-like protein 2	1,07772	0,00058
M2 48 / M0 48	MTX1	Metaxin-1	1,07141	0,00078
M2 48 / M0 48	ACBD5	Acyl-CoA-binding domain-containing protein 5	1,07082	0,00677
M2 48 / M0 48	DAAM1	Disheveled-associated activator of morphogenesis 1	1,07075	0,00008
M2 48 / M0 48	SORCN	Sorcin	1,07009	0,00027
M2 48 / M0 48	HMGA1	High mobility group protein HMG-I/HMG-Y	1,06902	0,00327
M2 48 / M0 48	NUP62	Nuclear pore glycoprotein p62	1,06849	0,00492
M2 48 / M0 48	RAB3A	Ras-related protein Rab-3A	1,06089	0,00941
M2 48 / M0 48	ISC2A	Isochorismatase domain-containing protein 2A	1,05844	0,00161
M2 48 / M0 48	IFT22	Intraflagellar transport protein 22 homolog	1,05570	0,00204
M2 48 / M0 48	CHMP6	Charged multivesicular body protein 6	1,05392	0,00882
M2 48 / M0 48	NCF4	Neutrophil cytosol factor 4	1,05117	0,00049
M2 48 / M0 48	CATD	Cathepsin D	1,05044	0,00488
M2 48 / M0 48	NUCB1	Nucleobindin-1	1,04938	0,00030
M2 48 / M0 48	4F2	4F2 cell-surface antigen heavy chain	1,04747	0,00283
M2 48 / M0 48	P2RX4	P2X purinoceptor 4	1,04500	0,00566
M2 48 / M0 48	MACIR	Macrophage immunometabolism regulator	1,04278	0,00590
M2 48 / M0 48	SDHF2	Succinate dehydrogenase assembly factor 2, mitochondrial	1,04089	0,00399
M2 48 / M0 48	ETFR1	Electron transfer flavoprotein regulatory factor 1	1,03399	0,00963
M2 48 / M0 48	PPAL	Lysosomal acid phosphatase	1,03388	0,00023
M2 48 / M0 48	ASM3A	Acid sphingomyelinase-like phosphodiesterase 3a	1,03344	0,00197
M2 48 / M0 48	CATB	Cathepsin B	1,03299	0,00026
M2 48 / M0 48	ASPG	N(4)-(beta-N-acetylglucosaminyl)-L-asparaginase	1,03126	0,00249
M2 48 / M0 48	TI17B	Mitochondrial import inner membrane translocase subunit Tim17-B	1,02947	0,00305
M2 48 / M0 48	DEGS1	Sphingolipid delta(4)-desaturase DES1	1,02817	0,00228
M2 48 / M0 48	AKTS1	Proline-rich AKT1 substrate 1	1,02687	0,00053

M2 48 / M0 48	TOIP1	Torsin-1A-interacting protein 1	1,02578	0,00032
M2 48 / M0 48	GPSM3	G-protein-signaling modulator 3	1,02331	0,00459
M2 48 / M0 48	3HIDH	3-hydroxyisobutyrate dehydrogenase, mitochondrial	1,01752	0,00226
M2 48 / M0 48	RISC	Retinoid-inducible serine carboxypeptidase	1,00972	0,00071
M2 48 / M0 48	SNAA	Alpha-soluble NSF attachment protein	1,00820	0,00187
M2 48 / M0 48	MIC27	MICOS complex subunit Mic27	1,00394	0,00301
M2 48 / M0 48	VP37A	Vacuolar protein sorting-associated protein 37A	1,00371	0,00761
M2 48 / M0 48	FANCI	Fanconi anemia group I protein homolog	-1,00267	0,00224
M2 48 / M0 48	ALKB5	RNA demethylase ALKBH5	-1,00270	0,00086
M2 48 / M0 48	CCD25	Coiled-coil domain-containing protein 25	-1,00328	0,00423
M2 48 / M0 48	PUR6	Bifunctional phosphoribosylaminoimidazole carboxylase/phosphoribosylaminoimidazole succinocarboxamide synthetase	-1,00727	0,00363
M2 48 / M0 48	RASA3	Ras GTPase-activating protein 3	-1,01139	0,00070
M2 48 / M0 48	WDR48	WD repeat-containing protein 48	-1,01224	0,00059
M2 48 / M0 48	CRBN	Protein cereblon	-1,01541	0,00494
M2 48 / M0 48	GLD2	Poly(A) RNA polymerase GLD2	-1,02054	0,00591
M2 48 / M0 48	RM02	Large ribosomal subunit protein uL2m	-1,02245	0,00017
M2 48 / M0 48	ZN106	Zinc finger protein 106	-1,02311	0,00236
M2 48 / M0 48	CD109	CD109 antigen	-1,03073	0,00839
M2 48 / M0 48	RL18	Large ribosomal subunit protein eL18	-1,03334	0,00097
M2 48 / M0 48	RS11	Small ribosomal subunit protein uS17	-1,03474	0,00103
M2 48 / M0 48	PCNA	Proliferating cell nuclear antigen	-1,04020	0,00074
M2 48 / M0 48	TTC33	Tetratricopeptide repeat protein 33	-1,04472	0,00322
M2 48 / M0 48	PAAT	ATPase PAAT	-1,05280	0,00780
M2 48 / M0 48	RL26	Large ribosomal subunit protein uL24	-1,05742	0,00133
M2 48 / M0 48	TOP2A	DNA topoisomerase 2-alpha	-1,05787	0,00272
M2 48 / M0 48	GRSF1	G-rich sequence factor 1	-1,05831	0,00763
M2 48 / M0 48	SEM4A	Semaphorin-4A	-1,06035	0,00030
M2 48 / M0 48	ORC6	Origin recognition complex subunit 6	-1,07386	0,00277

M2 48 / M0 48	GLNA	Glutamine synthetase	-1,07628	0,00196
M2 48 / M0 48	NSA2	Ribosome biogenesis protein NSA2 homolog	-1,07686	0,00021
M2 48 / M0 48	FBX42	F-box only protein 42	-1,07744	0,00237
M2 48 / M0 48	TBC31	TBC1 domain family member 31	-1,08284	0,00674
M2 48 / M0 48	KIF23	Kinesin-like protein KIF23	-1,08345	0,00502
M2 48 / M0 48	NFAM1	NFAT activation molecule 1	-1,08571	0,00312
M2 48 / M0 48	RM18	Large ribosomal subunit protein uL18m	-1,09220	0,00559
M2 48 / M0 48	STMN1	Stathmin	-1,09476	0,00307
M2 48 / M0 48	CDYL	Chromodomain Y-like protein	-1,09543	0,00149
M2 48 / M0 48	S20A1	Sodium-dependent phosphate transporter 1	-1,09615	0,00638
M2 48 / M0 48	ZNHI3	Zinc finger HIT domain-containing protein 3	-1,09659	0,00685
M2 48 / M0 48	DALD3	DALR anticodon-binding domain-containing protein 3	-1,10075	0,00808
M2 48 / M0 48	ABEC1	C->U-editing enzyme APOBEC-1	-1,10088	0,00550
M2 48 / M0 48	DNLI1	DNA ligase 1	-1,10113	0,00047
M2 48 / M0 48	RS6	Small ribosomal subunit protein eS6	-1,10271	0,00428
M2 48 / M0 48	CBX8	Chromobox protein homolog 8	-1,10648	0,00788
M2 48 / M0 48	RECQ4	ATP-dependent DNA helicase Q4	-1,11047	0,00666
M2 48 / M0 48	LRC41	Leucine-rich repeat-containing protein 41	-1,11905	0,00057
M2 48 / M0 48	TF3C5	General transcription factor 3C polypeptide 5	-1,12596	0,00027
M2 48 / M0 48	RL21	Large ribosomal subunit protein eL21	-1,13271	0,00079
M2 48 / M0 48	IF140	Intraflagellar transport protein 140 homolog	-1,13277	0,00159
M2 48 / M0 48	STEEP	STING ER exit protein	-1,13725	0,00126
M2 48 / M0 48	KIN17	DNA/RNA-binding protein KIN17	-1,15384	0,00528
M2 48 / M0 48	KI67	Proliferation marker protein Ki-67	-1,15434	0,00020
M2 48 / M0 48	HMCS1	Hydroxymethylglutaryl-CoA synthase, cytoplasmic	-1,15468	0,00310
M2 48 / M0 48	I5P2	Type II inositol 1,4,5-trisphosphate 5-phosphatase	-1,15743	0,00441
M2 48 / M0 48	TFE2	Transcription factor E2-alpha	-1,17787	0,00686
M2 48 / M0 48	TTK	Dual specificity protein kinase TTK	-1,18352	0,00079
M2 48 / M0 48	MGME1	Mitochondrial genome maintenance exonuclease 1	-1,18457	0,00172

M2 48 / M0 48	CTCF	Transcriptional repressor CTCF	-1,19416	0,00306
M2 48 / M0 48	UHRF1	E3 ubiquitin-protein ligase UHRF1	-1,19417	0,00219
M2 48 / M0 48	CEP76	Centrosomal protein of 76 kDa	-1,20267	0,00417
M2 48 / M0 48	AASD1	Alanyl-tRNA editing protein Aarsd1	-1,20330	0,00113
M2 48 / M0 48	DNMT1	DNA (cytosine-5)-methyltransferase 1	-1,20621	0,00018
M2 48 / M0 48	PLK1	Serine/threonine-protein kinase PLK1	-1,22618	0,00264
M2 48 / M0 48	CALRL	Calcitonin gene-related peptide type 1 receptor	-1,22686	0,00166
M2 48 / M0 48	CIP2A	Protein CIP2A	-1,24215	0,00100
M2 48 / M0 48	KIF15	Kinesin-like protein KIF15	-1,25428	0,00202
M2 48 / M0 48	CP51A	Lanosterol 14-alpha demethylase	-1,25672	0,00504
M2 48 / M0 48	RTF2	Replication termination factor 2	-1,25839	0,00634
M2 48 / M0 48	STK19	Serine/threonine-protein kinase 19	-1,26356	0,00056
M2 48 / M0 48	DDX28	Probable ATP-dependent RNA helicase DDX28	-1,26655	0,00077
M2 48 / M0 48	PI4KB	Phosphatidylinositol 4-kinase beta	-1,26899	0,00257
M2 48 / M0 48	PAR12	Protein mono-ADP-ribosyltransferase PARP12	-1,27316	0,00070
M2 48 / M0 48	TYDP1	Tyrosyl-DNA phosphodiesterase 1	-1,27431	0,00038
M2 48 / M0 48	GPR84	G-protein coupled receptor 84	-1,28676	0,00553
M2 48 / M0 48	GPN3	GPN-loop GTPase 3	-1,32904	0,00662
M2 48 / M0 48	CRLS1	Cardiolipin synthase (CMP-forming)	-1,33547	0,00431
M2 48 / M0 48	RL40	Ubiquitin-ribosomal protein eL40 fusion protein	-1,33620	0,00160
M2 48 / M0 48	RCC2	Protein RCC2	-1,34017	0,00248
M2 48 / M0 48	NAA40	N-alpha-acetyltransferase 40	-1,34533	0,00451
M2 48 / M0 48	KBTBB	Kelch repeat and BTB domain-containing protein 11	-1,35639	0,00042
M2 48 / M0 48	CK5P1	Mitochondrial tRNA methylthiotransferase CDK5RAP1	-1,35800	0,00283
M2 48 / M0 48	FADS1	Acyl-CoA (8-3)-desaturase	-1,37059	0,00236
M2 48 / M0 48	JKIP3	Janus kinase and microtubule-interacting protein 3	-1,37419	0,00325
M2 48 / M0 48	HELLS	Lymphocyte-specific helicase	-1,37793	0,00156

M2 48 / M0 48	TAP26	Thyroid transcription factor 1-associated protein 26	-1,38450	0,00638
M2 48 / M0 48	RN123	E3 ubiquitin-protein ligase RNF123	-1,47252	0,00342
M2 48 / M0 48	RGL1	Ral guanine nucleotide dissociation stimulator-like 1	-1,49509	0,00164
M2 48 / M0 48	S19A1	Reduced folate transporter	-1,52521	0,00587
M2 48 / M0 48	SCD2	Stearoyl-CoA desaturase 2	-1,52943	0,00480
M2 48 / M0 48	RIR1	Ribonucleoside-diphosphate reductase large subunit	-1,54358	0,00692
M2 48 / M0 48	WDR90	WD repeat-containing protein 90	-1,57419	0,00349
M2 48 / M0 48	BUB1B	Mitotic checkpoint serine/threonine-protein kinase BUB1 beta	-1,57736	0,00772
M2 48 / M0 48	LZTR1	Leucine-zipper-like transcriptional regulator 1	-1,61080	0,00357
M2 48 / M0 48	NUCG	Endonuclease G, mitochondrial	-1,63164	0,00243
M2 48 / M0 48	CGAS	Cyclic GMP-AMP synthase	-1,63544	0,00326
M2 48 / M0 48	CNBP	CCHC-type zinc finger nucleic acid binding protein	-1,64654	0,00162
M2 48 / M0 48	CDK1	Cyclin-dependent kinase 1	-1,68847	0,00004
M2 48 / M0 48	B3GL2	UDP-GalNAc:beta-1,3-N-acetylgalactosaminyltransferase 2	-1,69306	0,00126
M2 48 / M0 48	CLM8	CMRF35-like molecule 8	-1,75280	0,00542
M2 48 / M0 48	H31	Histone H3.1	-1,76413	0,00076
M2 48 / M0 48	ZNF22	Zinc finger protein 22	-1,77894	0,00007
M2 48 / M0 48	PLTP	Phospholipid transfer protein	-1,88680	0,00161
M2 48 / M0 48	CEP78	Centrosomal protein of 78 kDa	-1,92045	0,00249
M2 48 / M0 48	PTMS	Parathymosin	-2,11354	0,00019
M2 48 / M0 48	MTHSD	Methenyltetrahydrofolate synthase domain-containing protein	-2,14097	0,00436
M2 48 / M0 48	LRC58	Leucine-rich repeat-containing protein 58	-3,29486	0,00301

F3: Protein list of differentially expressed proteins in M0 RAW264.7 macrophages following treatment with Tamoxifen (RT), CBD (RCB) and combination of both (RTCB), compared to untreated cells (RDC – diluent control ('-' indicates downregulated and no sign indicates upregulated)

Comparison (group1/group2)	Protein names	Protein descriptions	AVG Log2 Ratio	q-value
RT / RDC	CA174	UPF0688 protein C1orf174 homolog	2,33213	0,00721
RT / RDC	4EBP1	Eukaryotic translation initiation factor 4E-binding protein 1	1,88724	0,00502
RT / RDC	MVD1	Diphosphomevalonate decarboxylase	1,64784	0,00033
RT / RDC	FPPS	Farnesyl pyrophosphate synthase	1,52978	0,00112
RT / RDC	THIC	Acetyl-CoA acetyltransferase, cytosolic	1,49460	0,00055
RT / RDC	FABP5	Fatty acid-binding protein 5	1,45004	0,00265
RT / RDC	HMCS1	Hydroxymethylglutaryl-CoA synthase, cytoplasmic	1,37452	0,00269
RT / RDC	NaN	NaN	1,36632	0,00639
RT / RDC	CA052	UPF0690 protein C1orf52 homolog	1,31893	0,00082
RT / RDC	SPS2	Selenide, water dikinase 2	1,30116	0,00518
RT / RDC	AASD1	Alanyl-tRNA editing protein Aarsd1	1,28908	0,00243
RT / RDC	IF4E3	Eukaryotic translation initiation factor 4E type 3	1,26583	0,00481
RT / RDC	RIR1	Ribonucleoside-diphosphate reductase large subunit	1,20381	0,00708
RT / RDC	RCC2	Protein RCC2	1,20194	0,00326
RT / RDC	CKS1	Cyclin-dependent kinases regulatory subunit 1	1,20007	0,00852
RT / RDC	CRADD	Death domain-containing protein CRADD	1,17644	0,00499
RT / RDC	IDHC	Isocitrate dehydrogenase [NADP] cytoplasmic	1,17556	0,00158
RT / RDC	HAGHL	Hydroxyacylglutathione hydrolase-like protein	1,11655	0,00816
RT / RDC	ABCE1	ATP-binding cassette sub-family E member 1	1,11555	0,00502
RT / RDC	CNBP	CCHC-type zinc finger nucleic acid binding protein	1,11388	0,00303
RT / RDC	KIME	Mevalonate kinase	1,10793	0,00960
RT / RDC	ARP19	cAMP-regulated phosphoprotein 19	1,09953	0,00735
RT / RDC	DUT	Deoxyuridine 5'-triphosphate nucleotidohydrolase	1,09843	0,00539
RT / RDC	PCY2	Ethanolamine-phosphate cytidylyltransferase	1,08790	0,00477

RT / RDC	CLIC6	Chloride intracellular channel protein 6;Chloride intracellular channel protein 5	1,08696	0,00280
RT / RDC	KCC1D	Calcium/calmodulin-dependent protein kinase type 1D	1,08504	0,00554
RT / RDC	DPYL2	Dihydropyrimidinase-related protein 2	1,06346	0,00130
RT / RDC	MP2K5	Dual specificity mitogen-activated protein kinase kinase 5	1,04998	0,00526
RT / RDC	APT	Adenine phosphoribosyltransferase	1,03630	0,00406
RT / RDC	NACAM	Nascent polypeptide-associated complex subunit alpha, muscle-specific form	1,02154	0,00391
RT / RDC	PMVK	Phosphomevalonate kinase	1,00641	0,00253
RT / RDC	PDK1	[Pyruvate dehydrogenase (acetyl-transferring)] kinase isozyme 1, mitochondrial	-1,00634	0,00844
RT / RDC	AMACR	Alpha-methylacyl-CoA racemase	-1,01101	0,00518
RT / RDC	NBR1	Next to BRCA1 gene 1 protein	-1,01187	0,00184
RT / RDC	NMNA3	Nicotinamide/nicotinic acid mononucleotide adenylyltransferase 3	-1,03552	0,00531
RT / RDC	RM41	Large ribosomal subunit protein mL41	-1,03625	0,00680
RT / RDC	BAK	Bcl-2 homologous antagonist/killer	-1,04100	0,00823
RT / RDC	F177A	Protein FAM177A1	-1,04231	0,00366
RT / RDC	CD5	T-cell surface glycoprotein CD5	-1,04455	0,00735
RT / RDC	PTSS2	Phosphatidylserine synthase 2	-1,04565	0,00462
RT / RDC	COR2A	Coronin-2A	-1,05742	0,00611
RT / RDC	TPST2	Protein-tyrosine sulfotransferase 2	-1,06193	0,00448
RT / RDC	PGLT1	Protein O-glucosyltransferase 1	-1,06749	0,00276
RT / RDC	ECM1	Extracellular matrix protein 1	-1,07738	0,00045
RT / RDC	CD003	Uncharacterized protein C4orf3 homolog	-1,08292	0,00222
RT / RDC	VKORL	Vitamin K epoxide reductase complex subunit 1-like protein 1	-1,08422	0,00694
RT / RDC	CACB2	Voltage-dependent L-type calcium channel subunit beta-2	-1,09878	0,00477
RT / RDC	GLPK	Glycerol kinase	-1,10624	0,00376
RT / RDC	MFSD5	Molybdate-anion transporter	-1,10864	0,00859
RT / RDC	CD14	Monocyte differentiation antigen CD14	-1,11260	0,00813

RT / RDC	RT18C	Small ribosomal subunit protein bS18m	-1,11311	0,00841
RT / RDC	TFR1	Transferrin receptor protein 1	-1,11386	0,00381
RT / RDC	SRC	Proto-oncogene tyrosine-protein kinase Src	-1,11417	0,00606
RT / RDC	PLXA1	Plexin-A1	-1,11682	0,00497
RT / RDC	IF44L	Interferon-induced protein 44-like	-1,11949	0,00678
RT / RDC	GXLT1	Glucoside xylosyltransferase 1	-1,12105	0,00764
RT / RDC	SURF4	Surfeit locus protein 4	-1,13369	0,00985
RT / RDC	DEN11	DENN domain-containing protein 11	-1,13820	0,00083
RT / RDC	DHRS1	Dehydrogenase/reductase SDR family member 1	-1,14594	0,00848
RT / RDC	KLRA2	Killer cell lectin-like receptor 2	-1,14699	0,00154
RT / RDC	NICA	Nicastrin	-1,16127	0,00502
RT / RDC	SUSD6	Sushi domain-containing protein 6	-1,19258	0,00754
RT / RDC	CLN5	Ceroid-lipofuscinosis neuronal protein 5 homolog	-1,19979	0,00137
RT / RDC	PLCD	1-acyl-sn-glycerol-3-phosphate acyltransferase delta	-1,20441	0,00603
RT / RDC	LTOR2	Ragulator complex protein LAMTOR2	-1,22072	0,00164
RT / RDC	CD47	Leukocyte surface antigen CD47	-1,22574	0,00781
RT / RDC	CP27A	Sterol 26-hydroxylase, mitochondrial	-1,22695	0,00374
RT / RDC	LYRM7	Complex III assembly factor LYRM7	-1,22827	0,00230
RT / RDC	GNS	N-acetylglucosamine-6-sulfatase	-1,23674	0,00980
RT / RDC	TMX4	Thioredoxin-related transmembrane protein 4	-1,23769	0,00573
RT / RDC	GALT3	Polypeptide N-acetylgalactosaminyltransferase 3	-1,24765	0,00582
RT / RDC	B2CL1	Bcl-2-like protein 1	-1,24975	0,00516
RT / RDC	ITIH2	Inter-alpha-trypsin inhibitor heavy chain H2	-1,25392	0,00830
RT / RDC	ST7	Suppressor of tumorigenicity 7 protein	-1,26212	0,00995
RT / RDC	REEP5	Receptor expression-enhancing protein 5	-1,26442	0,00207
RT / RDC	ABHD5	1-acylglycerol-3-phosphate O-acyltransferase ABHD5	-1,26990	0,00371
RT / RDC	S23A2	Solute carrier family 23 member 2	-1,28660	0,00637
RT / RDC	TGFB1	Transforming growth factor beta-1 proprotein	-1,29111	0,00929
RT / RDC	AGAL	Alpha-galactosidase A	-1,30984	0,00843
RT / RDC	BASP1	Brain acid soluble protein 1	-1,30995	0,00342

RT / RDC	ANTR2	Anthrax toxin receptor 2	-1,34012	0,00229
RT / RDC	RBPMS	RNA-binding protein with multiple splicing	-1,34474	0,00161
RT / RDC	ATP5S	ATP synthase subunit s, mitochondrial	-1,34783	0,00604
RT / RDC	ANXA3	Annexin A3	-1,37358	0,00678
RT / RDC	SC6A4	Sodium-dependent serotonin transporter	-1,39262	0,00856
RT / RDC	QPCTL	Glutaminyl-peptide cyclotransferase-like protein	-1,40697	0,00710
RT / RDC	FIS1	Mitochondrial fission 1 protein	-1,42813	0,00696
RT / RDC	GA2L2	GAS2-like protein 2	-1,44641	0,00325
RT / RDC	SAP3	Ganglioside GM2 activator	-1,45042	0,00269
RT / RDC	NPC2	NPC intracellular cholesterol transporter 2	-1,45205	0,00655
RT / RDC	PDCD6	Programmed cell death protein 6	-1,45489	0,00282
RT / RDC	GBG12	Guanine nucleotide-binding protein G(I)/G(S)/G(O) subunit gamma-12	-1,45824	0,00767
RT / RDC	SLPI	Antileukoproteinase	-1,47525	0,00188
RT / RDC	SSRA	Translocon-associated protein subunit alpha	-1,48077	0,00243
RT / RDC	CCL9	C-C motif chemokine 9	-1,48919	0,00723
RT / RDC	SYPM	Probable proline--tRNA ligase, mitochondrial	-1,50758	0,00944
RT / RDC	IFI2	Interferon-activable protein 202	-1,51550	0,00929
RT / RDC	PAI1	Plasminogen activator inhibitor 1	-1,53067	0,00972
RT / RDC	RM51	Large ribosomal subunit protein mL51	-1,53675	0,00647
RT / RDC	ANXA6	Annexin A6	-1,55455	0,00716
RT / RDC	MARK4	MAP/microtubule affinity-regulating kinase 4	-1,55545	0,00454
RT / RDC	DCOR	Ornithine decarboxylase	-1,56629	0,00188
RT / RDC	LAMP2	Lysosome-associated membrane glycoprotein 2	-1,57273	0,00869
RT / RDC	VIME	Vimentin	-1,59698	0,00448
RT / RDC	FXL17	F-box/LRR-repeat protein 17	-1,60155	0,00150
RT / RDC	IL1RA	Interleukin-1 receptor antagonist protein	-1,62441	0,00483
RT / RDC	HIUH	5-hydroxyisourate hydrolase	-1,62521	0,00360
RT / RDC	F162A	Protein FAM162A	-1,65162	0,00882
RT / RDC	BST1	ADP-ribosyl cyclase/cyclic ADP-ribose hydrolase 2	-1,78864	0,00034
RT / RDC	PGH2	Prostaglandin G/H synthase 2	-1,91648	0,00158
RT / RDC	NOS2	Nitric oxide synthase, inducible	-1,92711	0,00776

RT / RDC	DCA17	DDB1- and CUL4-associated factor 17	-1,98515	0,00133
RT / RDC	SMTN	Smoothelin	-2,02300	0,00689
RT / RDC	IL36G	Interleukin-36 gamma	-2,05719	0,00816
RT / RDC	UPP1	Uridine phosphorylase 1	-2,12402	0,00281
RT / RDC	ASAH1	Acid ceramidase	-2,70838	0,00969
RCB / RDC	CD63	CD63 antigen	3,66335	0,00492
RCB / RDC	LY6E	Lymphocyte antigen 6E	3,50681	0,00969
RCB / RDC	THIOM	Thioredoxin, mitochondrial	2,75667	0,00989
RCB / RDC	NHP2	H/ACA ribonucleoprotein complex subunit 2	2,41345	0,00404
RCB / RDC	RBM43	RNA-binding protein 43	2,37319	0,00207
RCB / RDC	S10AD	Protein S100-A13	2,37201	0,00587
RCB / RDC	UB2E3	Ubiquitin-conjugating enzyme E2 E3;Ubiquitin-conjugating enzyme E2 E2	2,03474	0,00171
RCB / RDC	KCAB1	Voltage-gated potassium channel subunit beta-1	2,03391	0,00678
RCB / RDC	KAT1	Kynurenine--oxoglutarate transaminase 1	2,00286	0,00892
RCB / RDC	TXD17	Thioredoxin domain-containing protein 17	1,85086	0,00124
RCB / RDC	CA052	UPF0690 protein C1orf52 homolog	1,73727	0,00302
RCB / RDC	POMP	Proteasome maturation protein	1,67512	0,00356
RCB / RDC	FRIL1	Ferritin light chain 1	1,58951	0,00045
RCB / RDC	C1QBP	Complement component 1 Q subcomponent-binding protein, mitochondrial	1,47576	0,00576
RCB / RDC	HAP28	28 kDa heat- and acid-stable phosphoprotein	1,44721	0,00971
RCB / RDC	LAT4	Large neutral amino acids transporter small subunit 4	1,43584	0,00406
RCB / RDC	CF418	Cilia- and flagella-associated protein 418	1,42613	0,00477
RCB / RDC	PEX19	Peroxisomal biogenesis factor 19	1,41715	0,00691
RCB / RDC	RBM42	RNA-binding protein 42	1,38930	0,00688
RCB / RDC	CEBPD	CCAAT/enhancer-binding protein delta	1,37224	0,00477
RCB / RDC	EF1B	Elongation factor 1-beta	1,36646	0,00813
RCB / RDC	ICAL	Calpastatin	1,34742	0,00142
RCB / RDC	AN32E	Acidic leucine-rich nuclear phosphoprotein 32 family member E	1,32731	0,00624
RCB / RDC	PAI2	Plasminogen activator inhibitor 2, macrophage	1,28083	0,00133
RCB / RDC	ENOG	Gamma-enolase	1,24997	0,00694
RCB / RDC	DAB2	Disabled homolog 2	1,23905	0,00253
RCB / RDC	JUPI2	Jupiter microtubule associated homolog 2	1,20365	0,00573

RCB / RDC	TTC1	Tetratricopeptide repeat protein 1	1,16422	0,00789
RCB / RDC	NUP62	Nuclear pore glycoprotein p62	1,15522	0,00481
RCB / RDC	TM192	Transmembrane protein 192	1,14473	0,00299
RCB / RDC	EPN2	Epsin-2	1,10635	0,00669
RCB / RDC	ARP19	cAMP-regulated phosphoprotein 19	1,10497	0,00460
RCB / RDC	DTD2	D-aminoacyl-tRNA deacylase 2	1,10404	0,00694
RCB / RDC	PHP14	14 kDa phosphohistidine phosphatase	1,10255	0,00389
RCB / RDC	NUBP1	Cytosolic Fe-S cluster assembly factor NUBP1	1,09906	0,00683
RCB / RDC	CHSP1	Calcium-regulated heat stable protein 1	1,09225	0,00230
RCB / RDC	ADDG	Gamma-adducin	1,09078	0,00608
RCB / RDC	UB2FA	NEDD8-conjugating enzyme UBE2F	1,07169	0,00653
RCB / RDC	RBMS1	RNA-binding motif, single-stranded-interacting protein 1	1,05897	0,00717
RCB / RDC	GPX1	Glutathione peroxidase 1	1,05224	0,00675
RCB / RDC	SET	Protein SET	1,02844	0,00490
RCB / RDC	TXNL1	Thioredoxin-like protein 1	1,02776	0,00624
RCB / RDC	NF2IP	NFATC2-interacting protein	1,02613	0,00889
RCB / RDC	CAMP1	Calmodulin-regulated spectrin-associated protein 1	1,02079	0,00080
RCB / RDC	ZRAB2	Zinc finger Ran-binding domain-containing protein 2	1,01936	0,00063
RCB / RDC	NEMP1	Nuclear envelope integral membrane protein 1	1,01627	0,00873
RCB / RDC	BAG1	BAG family molecular chaperone regulator 1	1,01511	0,00536
RCB / RDC	LAGE3	EKC/KEOPS complex subunit Lage3	1,00326	0,00993
RCB / RDC	DDX31	Probable ATP-dependent RNA helicase DDX31	-1,00387	0,00585
RCB / RDC	CHSS1	Chondroitin sulfate synthase 1	-1,00572	0,00498
RCB / RDC	MON1A	Vacuolar fusion protein MON1 homolog A	-1,01640	0,00498
RCB / RDC	NBR1	Next to BRCA1 gene 1 protein	-1,04032	0,00386
RCB / RDC	PGAP1	GPI inositol-deacylase	-1,06613	0,00909
RCB / RDC	CEBOS	Protein CEBPZOS	-1,09922	0,00730
RCB / RDC	PYRG2	CTP synthase 2	-1,13403	0,00161
RCB / RDC	CP27A	Sterol 26-hydroxylase, mitochondrial	-1,15385	0,00492
RCB / RDC	RUXE	Small nuclear ribonucleoprotein E	-1,15961	0,00988
RCB / RDC	ATR	Serine/threonine-protein kinase ATR	-1,16728	0,00483

RCB / RDC	ITIH2	Inter-alpha-trypsin inhibitor heavy chain H2	-1,19895	0,00934
RCB / RDC	BAF	Barrier-to-autointegration factor	-1,21731	0,00491
RCB / RDC	SSRA	Translocon-associated protein subunit alpha	-1,23274	0,00678
RCB / RDC	S23A2	Solute carrier family 23 member 2	-1,23608	0,00670
RCB / RDC	ANKH	Progressive ankylosis protein	-1,25012	0,00497
RCB / RDC	RBPMS	RNA-binding protein with multiple splicing	-1,32386	0,00386
RCB / RDC	OSTC	Oligosaccharyltransferase complex subunit OSTC	-1,34379	0,00201
RCB / RDC	GPS2	G protein pathway suppressor 2	-1,35588	0,00723
RCB / RDC	RL38	Large ribosomal subunit protein eL38	-1,37873	0,00876
RCB / RDC	SAP30	Histone deacetylase complex subunit SAP30	-1,40176	0,00844
RCB / RDC	NUD19	Acyl-coenzyme A diphosphatase NUDT19	-1,40542	0,00947
RCB / RDC	FADS2	Acyl-CoA 6-desaturase	-1,58395	0,00146
RCB / RDC	R12BB	RNA-binding protein 12B-B;RNA-binding protein 12B-A	-1,58519	0,00398
RCB / RDC	IFM2	Interferon-induced transmembrane protein 2	-1,60337	0,00873
RCB / RDC	METL9	Protein-L-histidine N-pros-methyltransferase	-1,62807	0,00712
RCB / RDC	H12	Histone H1.2	-1,66390	0,00128
RCB / RDC	RN185	E3 ubiquitin-protein ligase RNF185	-1,66721	0,00449
RCB / RDC	TAP26	Thyroid transcription factor 1-associated protein 26	-1,74208	0,00216
RCB / RDC	S6A12	Sodium- and chloride-dependent betaine transporter	-1,78696	0,00542
RCB / RDC	CX7A2	Cytochrome c oxidase subunit 7A2, mitochondrial	-1,97385	0,00674
RCB / RDC	S10A6	Protein S100-A6	-3,51440	0,00512
RCB / RDC	H2A2C	Histone H2A type 2-C	-6,79863	0,00231
RTCB / RDC	DCA17	DDB1- and CUL4-associated factor 17	3,67877	0,00981
RTCB / RDC	CD63	CD63 antigen	3,19224	0,00467
RTCB / RDC	LY6E	Lymphocyte antigen 6E	3,10907	0,00620
RTCB / RDC	THIOM	Thioredoxin, mitochondrial	2,97749	0,00823
RTCB / RDC	PP2AA	Serine/threonine-protein phosphatase 2A catalytic subunit alpha isoform	2,19492	0,00034
RTCB / RDC	RBM43	RNA-binding protein 43	2,17485	0,00291
RTCB / RDC	NHP2	H/ACA ribonucleoprotein complex subunit 2	2,11211	0,00015
RTCB / RDC	MT1	Metallothionein-1	2,05327	0,00487

RTCB / RDC	KCAB1	Voltage-gated potassium channel subunit beta-1	1,94888	0,00100
RTCB / RDC	UB2E3	Ubiquitin-conjugating enzyme E2 E3;Ubiquitin-conjugating enzyme E2 E2	1,93320	0,00096
RTCB / RDC	CIRBP	Cold-inducible RNA-binding protein	1,80708	0,00180
RTCB / RDC	TXD17	Thioredoxin domain-containing protein 17	1,77267	0,00095
RTCB / RDC	S10AD	Protein S100-A13	1,75609	0,00512
RTCB / RDC	POMP	Proteasome maturation protein	1,61301	0,00182
RTCB / RDC	CA052	UPF0690 protein C1orf52 homolog	1,56798	0,00875
RTCB / RDC	AN32E	Acidic leucine-rich nuclear phosphoprotein 32 family member E	1,53404	0,00984
RTCB / RDC	FRIL1	Ferritin light chain 1	1,52129	0,00135
RTCB / RDC	CALM1	Calmodulin-1;Calmodulin-2;Calmodulin-3	1,44219	0,00158
RTCB / RDC	PEX19	Peroxisomal biogenesis factor 19	1,44180	0,00696
RTCB / RDC	MT2	Metallothionein-2	1,36676	0,00232
RTCB / RDC	CF418	Cilia- and flagella-associated protein 418	1,34419	0,00397
RTCB / RDC	ACTS	Actin, alpha skeletal muscle	1,33227	0,00630
RTCB / RDC	NACAM	Nascent polypeptide-associated complex subunit alpha, muscle-specific form	1,21475	0,00246
RTCB / RDC	NUBP1	Cytosolic Fe-S cluster assembly factor NUBP1	1,20045	0,00720
RTCB / RDC	FPPS	Farnesyl pyrophosphate synthase	1,16469	0,00406
RTCB / RDC	PSMF1	Proteasome inhibitor PI31 subunit	1,16332	0,00256
RTCB / RDC	CHSP1	Calcium-regulated heat stable protein 1	1,14005	0,00243
RTCB / RDC	THIO	Thioredoxin	1,13684	0,00604
RTCB / RDC	ENOG	Gamma-enolase	1,11999	0,00454
RTCB / RDC	ADDG	Gamma-adducin	1,11157	0,00517
RTCB / RDC	ABI3	ABI gene family member 3	1,10706	0,00373
RTCB / RDC	ARP19	cAMP-regulated phosphoprotein 19	1,10683	0,00843
RTCB / RDC	RIPK3	Receptor-interacting serine/threonine-protein kinase 3	1,09722	0,00842
RTCB / RDC	CEBPD	CCAAT/enhancer-binding protein delta	1,08944	0,00670
RTCB / RDC	IAH1	Isoamyl acetate-hydrolyzing esterase 1 homolog	1,05145	0,00708
RTCB / RDC	CAMP1	Calmodulin-regulated spectrin-associated protein 1	1,04925	0,00855

RTCB / RDC	HAP28	28 kDa heat- and acid-stable phosphoprotein	1,02855	0,00647
RTCB / RDC	ABHEB	Putative protein-lysine deacylase ABHD14B	1,02096	0,00543
RTCB / RDC	TTC1	Tetratricopeptide repeat protein 1	1,01897	0,00664
RTCB / RDC	JUPI2	Jupiter microtubule associated homolog 2	1,01419	0,00916
RTCB / RDC	TXNL1	Thioredoxin-like protein 1	1,00834	0,00158
RTCB / RDC	NEMP1	Nuclear envelope integral membrane protein 1	1,00277	0,00468
RTCB / RDC	PTN18	Tyrosine-protein phosphatase non-receptor type 18	1,00229	0,00646
RTCB / RDC	PGLT1	Protein O-glucosyltransferase 1	-1,00147	0,00317
RTCB / RDC	GAS7	Growth arrest-specific protein 7	-1,02053	0,00493
RTCB / RDC	ATF7	Cyclic AMP-dependent transcription factor ATF-7	-1,02147	0,00691
RTCB / RDC	GTPB6	Putative GTP-binding protein 6	-1,02612	0,00797
RTCB / RDC	DCP1B	mRNA-decapping enzyme 1B	-1,02977	0,00133
RTCB / RDC	COX5A	Cytochrome c oxidase subunit 5A, mitochondrial	-1,03181	0,00823
RTCB / RDC	ANKH	Progressive ankylosis protein	-1,03413	0,00689
RTCB / RDC	FIG4	Polyphosphoinositide phosphatase	-1,03652	0,00892
RTCB / RDC	SSXT	Protein SSXT	-1,04455	0,00554
RTCB / RDC	HIUH	5-hydroxyisourate hydrolase	-1,04527	0,00342
RTCB / RDC	CO3	Complement C3	-1,08550	0,00929
RTCB / RDC	SAP30	Histone deacetylase complex subunit SAP30	-1,11898	0,00953
RTCB / RDC	NMNA3	Nicotinamide/nicotinic acid mononucleotide adenylyltransferase 3	-1,16734	0,00572
RTCB / RDC	OXSM	3-oxoacyl-[acyl-carrier-protein] synthase, mitochondrial	-1,20340	0,00256
RTCB / RDC	RT18C	Small ribosomal subunit protein bS18m	-1,22113	0,00694
RTCB / RDC	NBR1	Next to BRCA1 gene 1 protein	-1,24026	0,00231
RTCB / RDC	R12BB	RNA-binding protein 12B-B;RNA-binding protein 12B-A	-1,27346	0,00674
RTCB / RDC	TEFM	Transcription elongation factor, mitochondrial	-1,33341	0,00772
RTCB / RDC	GPR84	G-protein coupled receptor 84	-1,35852	0,00779
RTCB / RDC	ATR	Serine/threonine-protein kinase ATR	-1,36428	0,00503
RTCB / RDC	VA0D2	V-type proton ATPase subunit d 2	-1,39046	0,00929

RTCB / RDC	PD1L1	Programmed cell death 1 ligand 1	-1,51839	0,00929
RTCB / RDC	S23A2	Solute carrier family 23 member 2	-1,56558	0,00567
RTCB / RDC	RBPMS	RNA-binding protein with multiple splicing	-1,58889	0,00137
RTCB / RDC	MAP12	Methionine aminopeptidase 1D, mitochondrial	-1,61832	0,00706
RTCB / RDC	RN185	E3 ubiquitin-protein ligase RNF185	-1,64415	0,00681
RTCB / RDC	PPA5	Tartrate-resistant acid phosphatase type 5	-1,66127	0,00828
RTCB / RDC	TAP26	Thyroid transcription factor 1-associated protein 26	-1,81256	0,00096
RTCB / RDC	CX7A2	Cytochrome c oxidase subunit 7A2, mitochondrial	-1,85539	0,00691
RTCB / RDC	RN222	RING finger protein 222	-1,89082	0,00796
RTCB / RDC	PPT1	Palmitoyl-protein thioesterase 1	-2,00412	0,00876
RTCB / RDC	S10A6	Protein S100-A6	-2,62804	0,00604
RTCB / RDC	H2A2C	Histone H2A type 2-C	-6,15470	0,00253